

## Durham E-Theses

---

### *Global evaluation of Os and Ca marine isotope stratigraphy and U-Pb geochronology of the OAE 2*

DU VIVIER, ALICE,DIANA,CHARLOTTE

#### How to cite:

---

DU VIVIER, ALICE,DIANA,CHARLOTTE (2014) *Global evaluation of Os and Ca marine isotope stratigraphy and U-Pb geochronology of the OAE 2*, Durham theses, Durham University. Available at Durham E-Theses Online: <http://etheses.dur.ac.uk/10649/>

#### Use policy

---

The full-text may be used and/or reproduced, and given to third parties in any format or medium, without prior permission or charge, for personal research or study, educational, or not-for-profit purposes provided that:

- a full bibliographic reference is made to the original source
- a [link](#) is made to the metadata record in Durham E-Theses
- the full-text is not changed in any way

The full-text must not be sold in any format or medium without the formal permission of the copyright holders.

Please consult the [full Durham E-Theses policy](#) for further details.

---

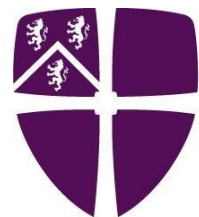
# Global evaluation of Os and Ca marine isotope stratigraphy and U-Pb geochronology of the OAE 2

Alice Diana Charlotte Du Vivier

A thesis submitted in partial fulfilment of the requirements for the degree of Doctor  
of Philosophy at Durham University

Department of Earth Sciences  
Durham University

March 2014



**Alice Diana Charlotte Du Vivier**

**Global evaluation of Os and Ca marine isotope stratigraphy and U-Pb geochronology of the OAE 2**

**Abstract**

Oceanic anoxic events occur in response to significant climate perturbations. This study focuses on the late Cretaceous OAE 2, which occurred across the Cenomanian-Turonian boundary (CTB), ~93.9 Ma. Multiple isotope proxies have reviewed the implications of palaeocirculation, volcanism and climate change to assess the driving mechanism(s) associated with global anoxia. Utilising geochemistry and geochronology (Os, Ca and U-Pb) this study provides a greater understanding of palaeoclimate conditions and assesses the global extent of anoxia. Hitherto, analyses have focussed on sections in and around the proto-North Atlantic. Herein, high-resolution  $^{187}\text{Os}/^{188}\text{Os}$  isotope stratigraphy from 8 globally representative sections is presented; Portland #1 core, Site 1260, Wunstorf, Vocontian Basin, Furlo, Site 530, Yezo Group, and Great Valley Sequence. The Re-Os system is sensitive to regional and global variation in seawater chemistry on the order of the residence time of Os due to ocean inputs: radiogenic Os from continental weathering and unradiogenic Os from hydrothermal inputs. The initial  $^{187}\text{Os}/^{188}\text{Os}$  ( $\text{Os}_i$ ) profiles present a globally ubiquitous trend: radiogenic Os values are attenuated by unradiogenic Os for ~200 kyr, which then gradually return to radiogenic Os. Minor discrepancies illustrate the sensitivity of local water masses as a function of basin connectivity and global sea level; i.e., Portland, Great Valley Sequence and Yezo Group (temporally restricted basins) vs. Site 1260 and Site 530 (open ocean).

Furthermore, a temporal framework is developed from existing ages (from the Western Interior, USA) and new U-Pb zircon geochronology (Yezo Group, Japan) to quantify the duration of OAE 2 and volcanic activity at the Caribbean LIP. Age models are applied and support the revision of the stratigraphic position of the OAE 2 onset and the CTB in the Yezo Group. The integration of the Western Interior and Pacific geochronology quantitatively verifies that the OAE 2 was globally synchronous occurring at  $\sim 94.4 \text{ Ma} \pm 0.15 \text{ Ma}$ .

In addition, marine  $\delta^{44}\text{Ca}$  records from 4 global OAE 2 sections are presented. The seawater mixing models reveal that  $\delta^{44}\text{Ca}$  values show no appreciable change to riverine or hydrothermal influx. Herein, I quantitatively demonstrate that fractionation is a parameter for  $\delta^{44}\text{Ca}$  isotopic variation at Portland and Pont d'Issole, which may be attributed to diagenetic reactions in the marl-rich lithology leading to site-specific fractionation. Therefore, marine  $\delta^{44}\text{Ca}$  profiles are different in each section as a function of varying fractionation factor. Ca isotope systematics are highly complex and so further work is crucial in order to develop our understanding of other parameters and to establish which, if any, is the most influential.

## Table of contents

Abstract	ii
Table of contents	iii-vii
List of Tables	viii-ix
List of Figures	x-xi
Declaration	xii
Acknowledgements	xiii-xv
<b>Chapter 1 Introduction</b>	<b>1</b>
1. Thesis rational	2
1.1. Oceanic Anoxic Events	2
1.2. Osmium isotope stratigraphy	7
1.3. Application of U-Pb zircon geochronology	11
1.4. Marine calcium isotope stratigraphy	13
1.5. Chapter Synopsis	17
1.5.1. Chapter 2: Marine $^{187}\text{Os}/^{188}\text{Os}$ isotope stratigraphy reveals the interaction of volcanism and ocean circulation during Oceanic Anoxic Event 2	17
1.5.2. Chapter 3: Pacific $^{187}\text{Os}/^{188}\text{Os}$ isotope chemistry and U-Pb geochronology: Implications for global synchronicity of OAE 2	19
1.5.3. Chapter 4: Calcium isotope stratigraphy across the Cenomanian-Turonian OAE 2: Implications on the controls of marine Ca isotope composition	21
1.5.4. Chapter 5: Conclusion and Future work	23
1.6. Synopsis	23
References	25
<b>Chapter 2 Marine <math>^{187}\text{Os}/^{188}\text{Os}</math> isotope stratigraphy reveals the interaction of volcanism and ocean circulation during Oceanic Anoxic Event 2</b>	<b>34</b>
1. Introduction	35
2. OAE 2 section geology	38
2.1. Portland #1 Core, Colorado, USA	38
2.2. Wunstorf, NW Germany	40

2.3. Vocontian Basin (Pont d'Issole and Vergons), SE France	42
2.4. DSDP Site 530, Hole 530A, South Atlantic	43
2.5. ODP Site 1260, Hole 1260B, Demerara Rise and Furlo, Italy	44
3. Methods	45
3.1. Sampling Protocol	45
3.2. Re-Os Isotope analysis of organic-rich sediments (ORS)	46
3.3. Organic $\delta^{13}\text{C}$ analytical protocol	48
3.4. OAE 2 correlation	51
3.5. Initial $^{187}\text{Os}/^{188}\text{Os}$ ( $\text{Os}_i$ )	54
4. Results	54
4.1. Re-Os Abundance	54
4.2. $^{187}\text{Os}/^{188}\text{Os}$ isotope stratigraphy	55
5. Discussion	58
5.1. Heterogeneous seawater $^{187}\text{Os}/^{188}\text{Os}$ prior to OAE 2	58
5.1.1. Implications of basin connectivity	59
5.1.2. Implications of enhanced weathering rates	60
5.2. Caribbean Large Igneous Province and OAE 2	61
5.3. Hiatuses identified during the CTBI	64
5.4. Palaeocirculation across OAE 2	65
6. Conclusions	66
References	67

**Chapter 3 Pacific  $^{187}\text{Os}/^{188}\text{Os}$  isotope chemistry and U-Pb geochronology: implications for global synchronicity of OAE 2** **88**

1. Introduction	89
2. Geological setting and stratigraphy	93
2.1. Yezo Group (YG), Hokkaido, Japan	93
2.2. Great Valley Sequence (GVS), California, USA	98
3. Sampling and Analytical methodology	101
3.1. Sampling and preparation	101
3.2. Re-Os geochemistry	101
3.3. Initial $^{187}\text{Os}/^{188}\text{Os}$ ( $\text{Os}_i$ )	103
3.4. U-Pb zircon geochronology	103

3.4.1. Zircon Mineral Separation	104
3.4.2. U-Pb Zircon ID-TIMS	106
4. Results	107
4.1. Re-Os Abundance	107
4.2. Initial osmium (Os <sub>i</sub> )	107
4.2.1. Os <sub>i</sub> stratigraphy of the Yezo Group, Japan	108
4.2.2. Os <sub>i</sub> stratigraphy of the Great Valley Sequence, USA	108
4.3. U-Pb analysis	109
5. Discussion	115
5.1. OAE 2 correlation	115
5.2. Temporal framework	122
5.3. Interpreted Os <sub>i</sub> correlation based on the integrated timescale model and age model	126
5.3.1. Correlation of OAE 2 interval	126
5.3.2. Pre-OAE 2 Yezo Group section, western Pacific	128
5.4. Great Valley Sequence, eastern Pacific	130
5.5. Longevity of the Caribbean Large Igneous Province	134
6. Summary	135
References	136

## **Chapter 4 Calcium isotope stratigraphy across the Cenomanian-Turonian OAE**

<b>2: Implication on the controls of marine Ca isotope composition</b>	<b>147</b>
1. Introduction	148
1.1. Previous marine $\delta^{44}\text{Ca}$ isotope OAE 2	153
2. Location and Geological background	154
2.1. Portland 1 Core, Colorado, USA	154
2.2. Pont d'Issole, SE France	157
2.3. Yezo Group section, Hokkaido, Japan	158
2.4. Eastbourne, UK	159
3. Methods	162
3.1. Sample preparation	162
3.2. Analytical protocol	162
3.3. Section correlation	163

4. Results	164
4.1. Portland #1 core $\delta^{44}\text{Ca}$ values	164
4.2. Pont d'Issole $\delta^{44}\text{Ca}$ values	165
4.3. Yezo Group $\delta^{44}\text{Ca}$ values	165
4.4. Eastbourne $\delta^{44}\text{Ca}$ values	167
5. Discussion	167
5.1. Analytical comparison and justification	167
5.2. Relationship between marine $\delta^{44}\text{Ca}$ and other isotope proxies	170
5.3. Evolution of $\delta^{44}\text{Ca}$ isotope composition, seawater mixing model	173
5.3.1. Model parameters and steady-state simulation	173
5.3.2. Hydrothermal influx model simulation	176
5.3.3. Riverine influx model simulation	180
5.3.4. Fractionation factor model simulation	181
5.4. Further variables of marine $\delta^{44}\text{Ca}$ composition	183
5.4.1. Precipitation and ocean acidification (seawater pH)	184
5.4.2. Diagenesis and lithology	187
5.4.3. Temperature	190
6. Summary	191
References	193
<b>Chapter 5 Conclusion</b>	<b>207</b>
1. Overview	208
2. Global marine $^{187}\text{Os}/^{188}\text{Os}$ isotope stratigraphy reveals the interaction of volcanism and ocean circulation during Oceanic Anoxic Event 2	208
2.1. Introduction	209
2.2. Temporal framework	211
2.3. Implications of $^{187}\text{Os}/^{188}\text{Os}$ profiles	212
2.4. Revised correlation and application of $^{187}\text{Os}/^{188}\text{Os}$ isotope stratigraphy	214
3. Calcium isotope stratigraphy across the Cenomanian-Turonian OAE 2: Implication on the controls of marine Ca isotope composition	215
3.1. Introduction: Isotopic proxies and the OAE 2	215
3.2. Qualitative observations and implications	217

3.3. Quantitative observations and implications	218
4. Future research and implications	221
5. Application of $^{187}\text{Os}/^{188}\text{Os}$ isotope stratigraphy to petroleum geology	224
References	226
<b>Appendix I: Highwood River, Alberta, Canada</b>	<b>231</b>
1. Introduction	232
2. Geological background	233
3. Results	235
3.1. $\text{Os}_i$ isotope stratigraphy	235
4. Discussion	236
5. Conclusions and future work	238
References	238

## List of Tables

### Chapter 2 Marine $^{187}\text{Os}/^{188}\text{Os}$ isotope stratigraphy reveals the interaction of volcanism and ocean circulation during Oceanic Anoxic Event 2

<b>Table 2.1a</b> $\delta^{13}\text{C}_{\text{org}}$ data for Portland #1 Core, Colorado, USA (Sageman et al., 2006)	75
<b>Table 2.1b</b> $\delta^{13}\text{C}_{\text{org}}$ data for Wunstorf, NW Germany (this study)	76
<b>Table 2.1c</b> $\delta^{13}\text{C}_{\text{org}}$ data for ODP Site 1260, Hole 1260B, Demerara Rise (Forster et al., 2007)	77
<b>Table 2.1d</b> $\delta^{13}\text{C}_{\text{org}}$ data for Vocontian Basin (Pont d'Issole and Vergons), SE France (Jarvis et al., 2011)	78
<b>Table 2.1e</b> $\delta^{13}\text{C}_{\text{org}}$ data for Furlo, Italy (Jenkyns et al., 2007)	79
<b>Table 2.1f</b> $\delta^{13}\text{C}_{\text{org}}$ data for DSDP Site 530A, South Atlantic (Forster et al., 2008)	80
<b>Table 2.2a</b> Re-Os data for samples for the CTB, from Portland #1 Core, Colorado, USA	81
<b>Table 2.2b</b> Re-Os data for samples for the CTB, from Wunstorf, NW Germany	82
<b>Table 2.2c</b> Additional Re-Os data for samples for the CTB, from ODP Site 1260, Hole 1260B, Demerara Rise	83
<b>Table 2.2d</b> Re-Os data for samples for the CTB, from Vocontian Basin (Pont d'Issole and Vergons), SE France	84
<b>Table 2.2e</b> Additional Re-Os data for samples for the CTB, from Furlo, Italy	85
<b>Table 2.2f</b> Re-Os data for samples for the CTB, from DSDP Site 530A, South Atlantic	86
<b>Table 2.3</b> Re-Os data for USGS Std. SDO-1	87
<b>Table 2.4</b> Age of datum levels A, B and C to calculate the Linear sedimentation rate to derive the integrated timescale	53

### Chapter 3 Pacific $^{187}\text{Os}/^{188}\text{Os}$ isotope chemistry and U-Pb geochronology: implications for global synchronicity of OAE 2

<b>Table 3.1</b> SDO-1 geochemical data	143
<b>Table 3.2a</b> Re-Os data for geochemical analysis of Yezo Group section, Japan	143

<b>Table 3.2b</b> Re-Os data for geochemical analysis of the Great Valley Sequence, California, USA	144
<b>Table 3.3a</b> U-Pb Zircon CA-ID-TIMS data for tuff horizons throughout the Cenomanian-Turonian boundary interval, Yezo Group, Japan	111
<b>Table 3.3b</b> U-Pb Zircon CA-ID-TIMS summary data for volcanic tuff horizons throughout the CTBI, Yezo Group, Japan	113
<b>Table 3.4</b> DOP and $\delta^{13}\text{C}_{\text{wood}}$ for the Yezo Group section, Japan and the Great Valley Sequence, California, USA	145
<b>Table 3.5</b> Calculation of Linear Sedimentation Rate to derive the temporal framework	124
<b>Table 3.6</b> Data for the OxCal age-depth model (Fig. 3.6B) vs. stratigraphic height (m)	146
<b>Chapter 4 Calcium isotope stratigraphy across the Cenomanian-Turonian OAE 2: Implication on the controls of marine Ca isotope composition</b>	
<b>Table 4.1a</b> $\delta^{44}\text{Ca}$ (sw) values and $\text{CaCO}_3$ abundances for Portland #1 Core, USA, during the CTBI	203
<b>Table 4.1b</b> $\delta^{44}\text{Ca}$ (sw) values and $\text{CaCO}_3$ abundances for Pont d'Issole, SE France, during the CTBI	204
<b>Table 4.1c</b> $\delta^{44}\text{Ca}$ (sw) values and $\text{CaCO}_3$ abundances for Yezo Group, Japan, during the CTBI	204
<b>Table 4.1d</b> $\delta^{44}\text{Ca}$ (sw) values and $\text{CaCO}_3$ abundances for Eastbourne, UK, during the CTBI	205
<b>Table 4.2</b> Standard data run throughout each section of analysis to monitor precision	206
<b>Table 4.3</b> Symbols and values for parameters used in the seawater mixing model	175
<b>Appendix I: Highwood River, Alberta, Canada</b>	
<b>Appendix Table 1</b> Re-Os geochemical data for Highwood River section, Alberta Canada	240
<b>Appendix Table 2</b> $\delta^{13}\text{C}_{\text{org}}$ data for Highwood River section, Alberta, Canada	241

## List of Figures

### Chapter 1 Introduction

- Figure 1.1** Global distribution of OAE 2 sites during the late Cretaceous. 3
- Figure 1.2** Palaeomap of the late Cretaceous. 4
- Figure 1.3** Image of the Portland #1 core. 5
- Figure 1.4** Schematic cross-section of the input and output sources of  $^{187}\text{Os}/^{188}\text{Os}$ . 9
- Figure 1.5** Schematic cross-section of the inputs and outputs of marine  $\delta^{44}\text{Ca}$ . 14

### Chapter 2 Marine $^{187}\text{Os}/^{188}\text{Os}$ isotope stratigraphy reveals the interaction of volcanism and ocean circulation during Oceanic Anoxic Event 2

- Figure 2.1** Palaeogeographic map of the CTB showing locations of analysed sites. 38
- Figure 2.2**  $\delta^{13}\text{C}_{\text{org}}$  (black) and  $\text{Os}_i$  (red) vs. stratigraphic height/depth. 50
- Figure 2.3**  $\text{Os}_i$  data calculated at 93.90 Ma relative to chemostratigraphically integrated timescale (kyr). 57
- Figure 2.4** Palaeocirculation pattern during the Cenomanian-Turonian boundary interval. 66

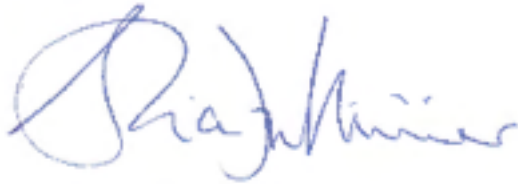
### Chapter 3 Pacific $^{187}\text{Os}/^{188}\text{Os}$ isotope chemistry and U-Pb geochronology: implications for global synchronicity of OAE 2

- Figure 3.1** Palaeogeographic map illustrating sample locations. 90
- Figure 3.2** Stratigraphic column for Yezo Group, Japan and Great Valley Sequence, California, USA. 97
- Figure 3.3**  $\delta^{13}\text{C}_{\text{wood}}$  and  $\delta^{13}\text{C}_{\text{org}}$  section correlation. 100
- Figure 3.4** Illustrates the stratigraphic height of the U-Pb dated tuff horizons from the Yezo Group, Japan on the  $\text{Os}_i$  (red) and  $\delta^{13}\text{C}$  (black) profiles. 105
- Figure 3.5** Lithostratigraphy and biostratigraphy of the Yezo Group section, Japan with CA-ID-TIMS  $^{206}\text{Pb}/^{238}\text{U}$  single zircon and interpreted weighted mean ages. 112
- Figure 3.6** Lithostratigraphy and Tuff ID of the Yezo Group section (A) vs. OxCal age-depth model (B) vs. Chemostratigraphy of the Yezo Group section (C). 114

<b>Figure 3.7</b> Global correlation of $\delta^{13}\text{C}_{\text{org}}$ and $\delta^{13}\text{C}_{\text{wood}}$ (black) and $\text{Os}_i$ (red) vs. stratigraphic height (m).	118
<b>Figure 3.8</b> Degree of Pyritization (DOP) vs. $\text{Os}_i$ in Yezo Group, Japan and Great Valley Sequence, California, USA.	121
<b>Figure 3.9</b> $\text{Os}_i$ profiles from Yezo Group (black) and Portland #1 Core (grey) vs. temporal timescale (kyr).	125
<b>Figure 3.10</b> $\text{Os}_i$ vs. temporal timescale (kyr).	132
<b>Chapter 4 Calcium isotope stratigraphy across the Cenomanian-Turonian OAE</b>	
<b>2: Implication on the controls of marine Ca isotope composition</b>	
<b>Figure 4.1</b> Palaeogeographic map of the late Cretaceous.	152
<b>Figure 4.2</b> Section stratigraphy.	156
<b>Figure 4.3</b> Stratigraphic correlation of $\delta^{13}\text{C}$ vs. stratigraphic height.	161
<b>Figure 4.4</b> $\delta^{44/40}\text{Ca}$ vs. stratigraphic height.	166
<b>Figure 4.5</b> $\delta^{44/42}\text{Ca}$ from Eastbourne and South Ferriby, UK and conversion of $\delta^{44/40}\text{Ca}$ to $\delta^{44/42}\text{Ca}$ (this study).	169
<b>Figure 4.6</b> $\delta^{44}\text{Ca}$ and $\text{Os}_i$ vs. stratigraphic height.	171
<b>Figure 4.7</b> Seawater mixing models.	178
<b>Figure 4.8</b> $\text{CaCO}_3$ (red) and $\delta^{44}\text{Ca}$ (black) vs. stratigraphic height.	189
<b>Chapter 5 Conclusion</b>	
<b>Figure 5.1</b> Palaeomap of the late Cretaceous.	210
<b>Figure 5.2</b> Shows analytical vs. numerically derived curves.	219
<b>Figure 5.3</b> Palaeomap of the late Cretaceous, sites proposed for future work are in pink.	221
<b>Figure 5.4</b> Distinct $\text{Os}_i$ isotope profile of CTBI and after radiogenic growth.	225
<b>Appendix I: Highwood River, Alberta, Canada</b>	
<b>Appendix Figure 1</b> Palaeogeographic map of the late Cretaceous	235
<b>Appendix Figure 2</b> $\text{Os}_i$ data (red) with $\delta^{13}\text{C}_{\text{org}}$ (black and grey) vs. stratigraphic height (m)	236

**Declaration**

I declare that this thesis, which I submit for the degree of Doctor of Philosophy at Durham University, is my own work and unlike any other submitted here or at any other institution.



*Alice D. C. Du Vivier*

*Durham University*

*2<sup>nd</sup> March, 2014*

The copyright of this thesis rests with the author. No quotation should be published without the author's written consent and information derived from it should be acknowledged.

## **Acknowledgements**

So here I am ...finally finished!

I have been very lucky to undertake a project that has involved being in the outdoors so much and experiencing the beauty of the World around us, while travelling to many spectacular locations for fieldwork. As a result I have clocked up thousands of miles... ~127 k to be precise. I have enjoyed the wonderful landscapes, culture and people in all the countries I have visited. Travelling has enlightened me and it is something that I have come to love. Firstly therefore, I would like to thank all those who helped me during my fieldwork. Brad Sageman in Colorado, Darren Gröcke and Silke Voigt in Germany, Ian Jarvis in France, Reishi Takashima in Japan, and Guy Plint in Canada.

The luxury of travelling around so much and collecting so many samples however did mean that upon returning to Durham I have needed to spend months in the lab and hours on the Triton. Despite that, the lab work is something that I have particularly enjoyed. The need to be meticulous and organised has given me great satisfaction and invaluable data sets. I would like to thank Chris Ottley, Jo Peterkin, and Joanna Hesselink, who all taught and helped me in the labs.

In addition to working at Durham I have worked at NIGL at the BGS in Keyworth. Thank you to Dan Condon for his support and Nicola Atkinson for her help in the lab there. I also had a fantastic experience at Northwestern University in Evanston, Illinois, where I went to undertake lab work for Ca isotopes. It was interesting and fun working in a different environment and getting a flavour for the American system, their classes and their work ethic. Thank you to Greg Lehn and Grace Andrews for educating me and overall making it such a fun time.

An important thank you goes to the organisations whose funding has made my many excursions possible. I received a grant from the Geologists' Association for fieldwork in Colorado. I was awarded a grant from the Timothy Jefferson Field Research Fund, through the Geological Society for fieldwork in Japan. For the lab work that I carried out at Northwestern, I was granted a student research grant from the International Association of Geochemists. The project as a whole was in part funded by a NERC small grant. We also receive a grant from the NERC Isotope

Geosciences Facilities Steering Committee to undertake the U-Pb zircon geochronology analysis at NIGL.

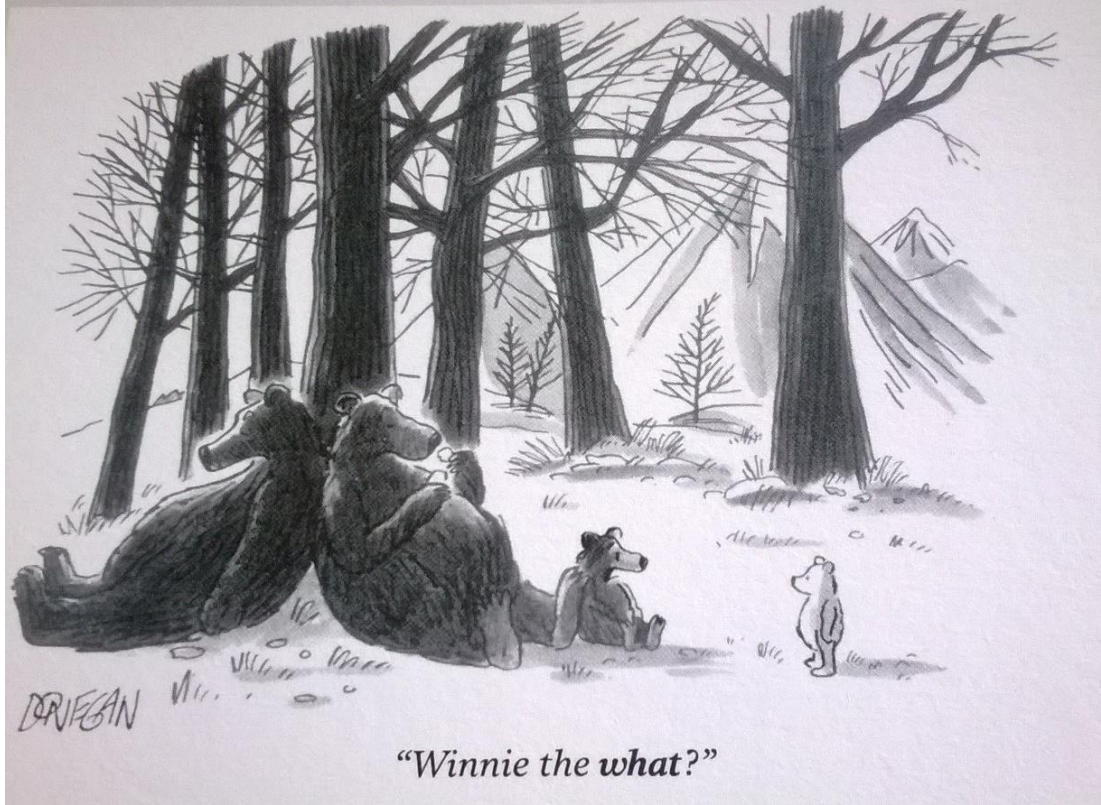
I would like to thank Mark Allen, Dave Selby, Jonny Imber and Bob Holdsworth for giving me the opportunity to teach on many fieldtrips: the Lake District, Assynt and in America. I have thoroughly enjoyed them all, particularly Assynt, which must be one of the most beautiful places on Earth. A particular highlight was being involved on the 4<sup>th</sup> year trip to the SW USA. We had such an amazing time, and as well as demonstrating we all learned a huge amount courtesy of James Baldini, Jon Davidson, Dave Selby and Richie Brown. I am so grateful and lucky to have shared such an experience and happy times with Harriet Ridley and Pete Tollan. Thank you to them for many happy memories in sensational and breath taking surroundings.

I would like to thank all those who have responded with such patience to my emails checking theories, facts and figures, and apologies to all those who I emailed too much... Dan Condon, Brad Sageman and Andy Jacobson in particular, who are no doubt relieved that I am finally finished.

When I started my PhD I lacked confidence in giving presentations. Over the last 3 years I have had to give a number of presentations at conferences, both international and departmental, which has helped me to overcome my nerves, believe in the work that I have produced and in myself. I would like to thank Dave Selby for helping me to do this by believing in me. Dave has been a fantastic supervisor from start to finish. I have definitely learned the most from him and I want to thank him so much for his endless support, help and encouragement that he has given me. Thank you for being my field assistant, teaching me in the lab and endeavouring to give me feedback more quickly than I would have thought possible. Thank you to my examiners, Mark Allen and Hugh Jenkyns. I thoroughly enjoyed my Viva and I am so grateful for such kind comments and good feedback on my work.

Finally thank you to all my friends, who have supported me throughout my PhD and wished me lots of luck to the finish, especially Josephine Mackintosh, Oliver Mankowski, Will Dyott, Owen Davis, Nicholas Rooke, Sophia Gerth, Hannah Jones, Harriet Ridley and Pete Tollan, I look forward to celebrating with you all. Most importantly, thank you to my family, my nearest and dearest, my Mummy and Daddy and John; I couldn't have done it without you. I hope I have made you proud.

“...always remember. You are braver than you believe, stronger than you seem and smarter than you think.” – Winnie-the-Pooh.



“Winnie the *what?*”

# ***1*** Introduction

## **1. Thesis rationale**

### *1.1. Oceanic Anoxic Events*

Oceanic Anoxic Events (OAEs) stereotype distinct episodes of pelagic organic-rich sediment deposition that occurred across intervals of approximately one million years during the Jurassic and Cretaceous periods. Schlanger et al. (1976) characterised these occurrences as episodes “during which global marine waters were relatively depleted in oxygen, and deposition of organic matter, derived from both terrestrial and planktonic sources, was widespread”. They suggested, “bacterial consumption of this organic matter favoured the development of poorly oxygenated mid- to late Cretaceous waters in which many of the characteristic facies of the Period were deposited.”

This thesis focuses on the OAE 2, which occurred across the Cenomanian-Turonian boundary (CTB) ~93.90 Ma. The main questions that I address are:

- 1) What ocean-atmosphere processes were responsible for driving OAE 2 to become synchronously widespread in multiple basinal environments in the world’s oceans?
- 2) Can key stages and the duration of OAE 2 be quantitatively constrained?
- 3) Was OAE 2 a truly ‘global’ event?

The abundance of organic-rich material deposited during an anoxic event provides valuable information on the global stratigraphic record and as such there have been many studies that evaluate the distribution, structure and composition of organic-rich sediments (ORS), which aim to assess the depositional processes responsible for the development of anoxia. In some cases ORS have economic potential as a source for the generation of petroleum deposits, e.g., the Angola Basin.

However, this study focuses on the palaeoclimatic implications of the depositional record.

Numerous sections worldwide (Fig 1.1) have undergone analyses to identify the potential characteristic features of OAE 2.

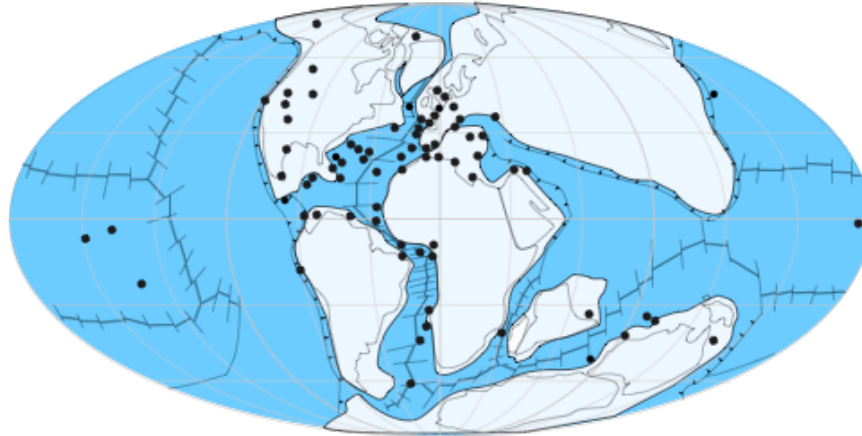


**Figure 1.1 Global distribution of OAE 2 sites during the late Cretaceous** (modified from Trabucho-Alexandre et al., 2010).

The palaeomap illustrates the concentration of OAE 2 sites studied throughout the Atlantic, Tethys and Western Interior basins. The study of OAE 2 is limited in the Pacific Ocean and throughout much of the southern Hemisphere. As such this global study of the OAE 2 includes 2 sections of the proto-Pacific (Yezo Group, Hokkaido, Japan and Great Valley Sequence, California, USA), and one from the proto-South Atlantic (DSDP Site 530; Fig. 1.2).

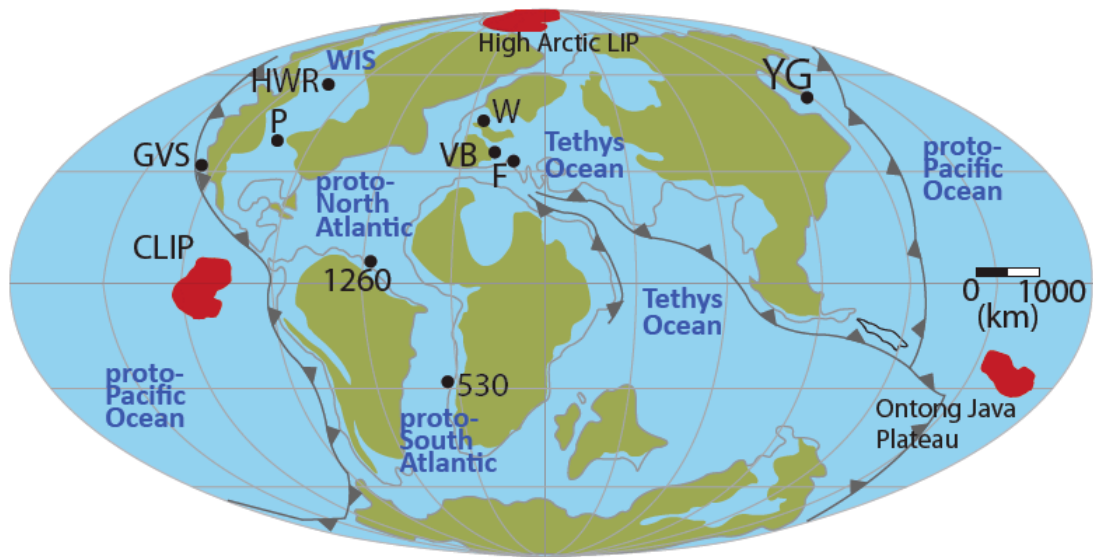


**Figure 1.2 Palaeomap of the late Cretaceous.** The sites analysed in this thesis are; P – Portland #1 Core, GVS – Great Valley Sequence, 1260 – ODP Site 1260 Demerara Rise, 530 – DSDP Site 530, W – Wunstorf, VB- Vocontian Basin, F – Furlo, YG – Yezo Group, HWR – Highwood River (Appendix). The location of the Caribbean (CLIP) and High Arctic Large Igneous Province, and the Ontong Java Plateau are marked on in red.

OAE 2 is characterised by organic-rich marl/shales, which have been deposited and preserved, and interbedded by lighter marl/limestone. The distribution, abundance and consistency of biozones are commonly limited and there is little bioturbation, which restricts the reliability of correlation based purely on biostratigraphy. As such, biostratigraphy is combined with lithostratigraphy and  $\delta^{13}\text{C}$  isotope chemostratigraphy to identify the onset of oceanic anoxic events, which are typically characterised by a 2 – 4‰ excursion in the  $\delta^{13}\text{C}_{\text{org}}$  and  $\delta^{13}\text{C}_{\text{carb}}$  record.



**Figure 1.3 Image of the Portland #1 core.** Illustrates a characteristic lithological sequence of OAE 2.

OAE 2 sections are identified by a multitude of disciplines: perturbations in the marine carbon isotope record, extinctions in the biostratigraphic record and the deposition of organic-rich sediments (Fig. 1.3). Since the classification of OAEs there has been an increase in the analysis of isotopic proxies to evaluate the relationship of multiple factors influencing the ocean and the atmosphere at the time of formation, which facilitate our understanding of the mid- to late Cretaceous environment. Other proxies include neodymium, strontium, phosphorus,  $TEX_{86}$ , calcium, osmium, lead, lithium and uranium (Arthur et al., 1987; Kerr, 1998; McArthur et al., 2004; Forster et al., 2007; MacLeod et al., 2008; Turgeon and Creaser, 2008; Voigt et al., 2008; Montoya-Pino et al., 2010; Blättler et al., 2011; Kuroda et al., 2011; Mort et al., 2011; Martin et al., 2012; Pogge von Strandmann et al., 2013, Zheng et al., 2013). Although the OAE 2 has been well studied, the driving mechanisms remain poorly constrained, as is the onset and global extent. The proposed mechanisms responsible for driving oceanic anoxia are enhanced

volcanism and CO<sub>2</sub> output, increased land and sea surface temperatures, an accelerated hydrological cycle, sea level rise and increased rates of ocean circulation, and changes in nutrient supply and productivity (Jenkyns, 1980; Arthur et al., 1987; Arthur and Sageman, 1994; Erbacher et al., 1996; Jones and Jenkyns, 2001; Mort et al., 2007; Forster et al., 2007; Turgeon and Creaser, 2008; Jenkyns, 2010; Martin et al., 2012).

A climatic shift and transgressive pulse are associated processes driving OAE 2 (Jenkyns, 1980; Schlanger et al., 1987; Jenkyns, 2010). The late Cretaceous was particularly warm, with atmospheric and sea surface temperatures reaching a maximum that has not been recorded since ( $\geq 33^\circ$ ; Clarke and Jenkyns, 1999; Jenkyns et al., 2004; Forster et al., 2007). The high temperatures were responsible for an accelerated hydrological cycle, which led to an increase in global weathering and the influx of nutrients into the ocean. In addition, the contemporaneous sea-level change over the CTB interval mobilised organic-rich terrestrial material to the sea and enhanced marine productivity (Jenkyns, 1980; Haq et al., 1988; Erbacher et al., 1996; Leckie et al., 2002; Pearce et al., 2009). The abundance of organic-rich material led to large-scale burial of organic matter, which accelerated the drawdown of  $p\text{CO}_2$  that began to saturate the ocean and increase the capacity of the oxygen minimum zone (OMZ, Erbacher et al., 1996). The combined effect of transgression and the subsequent expansion of the OMZ led to the widespread development of anoxia. The positive excursion in the  $\delta^{13}\text{C}$  isotope record identifies the climatic perturbation, the most significant of all OAEs (Schlanger et al., 1987; Jenkyns, 1980; Keller and Pardo, 2004; Erbacher et al., 2005; Gale et al., 2005; Grosheny et al., 2006; Jarvis et al., 2006; Voigt et al., 2008; Takashima et al., 2011).

### *1.2. Osmium isotope stratigraphy*

As the abundance of organic-rich material in seawater escalates during OAE 2, ORS are readily deposited. Rhenium and osmium are sequestered simultaneously into ORS during accumulation. Though we are unclear of the exact mechanism involved during rhenium and osmium sequestration, it is considered that under oxygen limiting conditions the Re-Os system becomes insoluble and ORS are typically enriched in Re (tens of ppb) and Os (tens to hundreds of ppt) relative to the continental crust (~ 1.26; Esser & Turekian, 1993; Colodner et al., 1993; Crusius et al., 1996). Sequestration is thought to occur just below the sediment-water interface by diffusion, reducing pore water to the solid phase (Colodner, 1991). Evidence from other redox sensitive elements such as Ni and Mo suggest that Re and Os enrichment in ORS is a function of sedimentation rate (Lewan and Maynard, 1982; Kendall et al., 2009). However, recent work in riverine systems has shown that Re-Os are present in sediments in an oxic water column, and where Re-Os abundances are below crustal levels they are hydrogenous and isochronous (Cumming et al., 2012).

Following organic capture, the Re-Os systematics are not disturbed by post-depositional effects such as diagenesis, hydrocarbon maturation and low-grade metamorphism (Rooney et al., 2010). However, evidence from veining infers that the systematics are affected by high temperature fluid flow (Selby et al., 2003; Lawley and Selby, 2012). Consequently the Re-Os system can be utilised as a geochronometer, combined with biostratigraphy, to calibrate geological timescales (e.g., the Devonian-Mississippian boundary of the Exshaw Formation, Selby and Creaser, 2005; Selby et al., 2009). The isochron method yields the initial  $^{187}\text{Os}/^{188}\text{Os}$  composition ( $\text{Os}_i$ ) at the time of deposition, but this can also be directly calculated

using the present day Re and Os isotope ratios and the  $^{187}\text{Re}$  decay constant (Selby and Creaser, 2005; Kendall et al., 2004).

An evaluation of  $\text{Os}_i$  provides valuable information on the geochemistry of seawater that reflects the variable inputs of osmium associated with continental weathering, meteoritic impact, and hydrothermal alteration (Fig. 1.4; Ravizza & Turekian, 1992; Peucker-Ehrenbrink et al., 1995; Cohen et al., 1999). Our understanding is that the  $^{187}\text{Os}/^{188}\text{Os}$  isotope composition of seawater is predominantly controlled by two end-member Os isotope components: weathered continental crust ( $\sim 1.4$ ) and mantle inputs (0.13) (Fig. 1.4; Peucker-Ehrenbrink and Ravizza, 2000). These end-member values, coupled with the short residence time of Os in seawater ( $\leq 10$  kyr; Oxburgh, 2001), make  $^{187}\text{Os}/^{188}\text{Os}$  values excellent chemostratigraphic monitors for global stratigraphy (Turgeon and Creaser, 2008; Cohen et al., 1999; Cohen, 2004; Bottini et al., 2012). Furthermore, the evolution of seawater chemistry is indicative of palaeoclimatic and palaeoceanographic changes in the geological record (Ravizza and Turekian, 1992; Ravizza and Esser, 1993; Peucker-Ehrenbrink and Ravizza, 2000; Cohen, 2004), particularly across the CTB where there is evidence for accelerated continental weathering and an abundance of submarine volcanic activity (Sinton and Duncan, 1997; Snow et al., 2005; Frijia and Parente, 2008; Turgeon and Creaser, 2008).

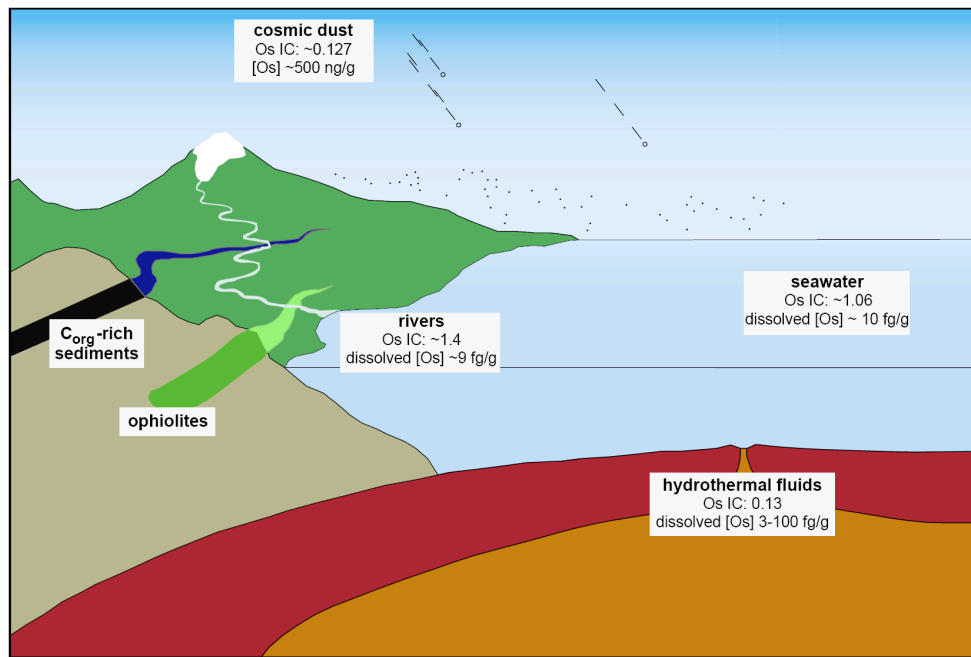


**Figure 1.4 Schematic cross-section of the input and output sources of  $^{187}\text{Os}/^{188}\text{Os}$  (modified from Peucker-Ehrenbrink and Ravizza, 2000).**

Magmatism is a significant driving force for modifications in  $^{187}\text{Os}/^{188}\text{Os}$  seawater chemistry (Cohen et al., 1999; Peucker-Ehrenbrink et al., 1995; Cohen & Coe, 2002; Snow et al., 2005; Ravizza & Peucker-Ehrenbrink, 2003; Turgeon & Creaser, 2008; and Robinson et al., 2009). However, the isotopic signature depends on the style of volcanism: terrestrial (Peucker-Ehrenbrink et al. 1995; Peucker-Ehrenbrink & Ravizza, 2000; Ravizza & Peucker-Ehrenbrink, 2003; Robinson et al., 2009) or submarine (Cohen & Coe, 2002, 2007; Robinson et al., 2009). Unradiogenic  $\text{Os}_i$  are a direct indicator of submarine volcanism, however as figure 1.4 suggests, submarine volcanism is not the only mechanism for the addition of unradiogenic Os. Cosmic dust with equally low isotope composition,  $\sim 0.127$ , has the potential to simultaneously affect the isotope composition of seawater (Peucker-Ehrenbrink & Ravizza, 2000). Despite this, there is no evidence of an extra-terrestrial impact during OAE 2 (i.e., no iridium spike), which excludes the implications of a meteorite impact on seawater chemistry at this time.

The OAE 2 is associated with volcanic activity from the Caribbean Large Igneous Province (LIP). Evidence from a previous OAE 2  $Os_i$  study suggests that the events were contemporaneous (Turgeon and Creaser, 2008). Furthermore, the evaluation of  $Os_i$  isotope stratigraphy across the Triassic-Jurassic boundary (Cohen and Coe, 2002; Cohen, 2004) and the OAE 1a (Tejada et al., 2009; Bottini et al., 2012) provide tenable evidence to support the synchronicity of OAE development and magmatism. Therefore establishing  $Os_i$  profiles of ORS from multiple sites across the CTB interval will provide a valuable understanding of the mechanism(s) that initiate OAE 2 and quantify changes in global processes throughout the CTB interval.

The previous study concluded that the onset of the event was initiated by volcanism at the Caribbean LIP based on the synchronicity of the  $Os_i$  profile with the start of the OAE 2 (Turgeon and Creaser, 2008). However, they did not consider the importance of the interval prior to the onset of OAE 2, as well as the trend to radiogenic  $Os_i$  values after the unradiogenic interval, which yield important implications for the CTB interval. In particular, the heterogeneous  $^{187}Os/^{188}Os$  isotope composition prior to the onset of OAE 2 is indicative of a more complicated relationship between the oceanic and atmospheric environments during the development of anoxia. In addition, the duration and cessation of volcanic activity can be quantitatively constrained from the  $Os_i$  profile. Therefore, a global assessment of depositional environments, including the representative section of the GSSP section (Sageman et al., 2006), the European reference section (Voigt et al., 2008) and two proto-Pacific sections (Takashima et al., 2011), reveal more detailed implications of global Os isotope stratigraphy than previously considered.

### *1.3. Application of U-Pb zircon geochronology*

Geochronology (U-Pb, Ar-Ar) of volcanogenic tuff horizons across the CTB plus Bayesian astrochronology, constrains a number of stratigraphic horizons, notably the CTB at ~93.90 Ma specifically from the Portland #1 core (Meyers et al., 2012). In sections that are unconstrained beyond bio- and lithostratigraphy, the temporal framework of the Portland #1 core facilitates the correlation of OAE 2 stratigraphic horizons. In Chapter 3 I apply the U-Pb dating technique to constrain the age of five volcanic tuff horizons from the Yezo Group section, Japan, in order to facilitate and improve the correlation of OAE 2. In addition, the U-Pb dates are used to evaluate the global synchronicity of the OAE 2, which is hypothesised for this event. A previous study produced two dates for tuff horizons in the YG section (Quidelleur et al., 2011). However, the recent study on the GSSP section (Meyers et al., 2012), which combines U-Pb, Ar-Ar and Bayesian stratigraphy, has deemed these ages correlatively untenable due to poor precision inherent of the LA-ICP-MS methodology and incorrect stratigraphic integration of ages (Chapter 3).

The U-Pb technique is a well-established chronological tool; the refractory and durable nature of zircons means that despite volcanic material being altered to clay at the time of deposition, the crystals retain indicators that are representative of time. The analysis of two chronometers ( $^{238}\text{U}$ - $^{206}\text{Pb}$  and  $^{235}\text{U}$ - $^{207}\text{Pb}$ ) in one mineral provides information on closed system behaviour, i.e. radioactive decay as a function of time. Furthermore the detection of nominal open system behaviour can be inferred, i.e., Pb loss and/or inheritance. Significant developments in ID-TIMS have led to increased precision (Mattinson, 2005); elemental mapping of zircon structures and features has enabled grain selection and abrasion of the least fractured crystals, removing the outer rim of the crystal to avoid radiation contamination and Pb loss,

analytical blanks have been lowered and improved isotopic measurements with more efficient ionisation of single crystals, and the evaluation of the accuracy of uranium decay constants. Advances in pre-treatment techniques, thermal annealing and leaching, have proven to effectively eliminate Pb loss, with any remaining effects of Pb loss recognised by high-precision ID-TIMS and data points excluded from the calculation of the final age (Mattinson, 2005). The precision of ID-TIMS has been lowered to 0.1 – 0.3% and similarly the uncertainties have been reduced by analysing large numbers of zircons per sample and restricting analysis to single grains or fragments is the most proficient way to correct for inheritance problems.

Geochronology studies have typically relied upon the  $^{40}\text{Ar}/^{39}\text{Ar}$  technique because obtaining zircons, for U-Pb analysis, from K-rich felsic tuffs was difficult and their abundance in bentonite horizons is low (Obradovich et al., 1993). However, there has been significant improvement on accuracy and precision of dating tuff horizons, which was facilitated by the development of the EARTHTIME double spike tracer solutions ( $^{233}\text{U}$ - $^{235}\text{U}$ - $^{202}\text{Pb}$  and  $^{233}\text{U}$ - $^{235}\text{U}$ - $^{205}\text{Pb}$ ), which also helped reduce the uncertainty of mass fractionation associated with the measurements of isotope ratios (ET2535; Condon et al., *in review*; McLean et al., *in review*).

Obtaining high precision U-Pb dates for tuff horizons throughout the Yezo Group will quantitatively constrain the section and develop the first time correlative section for the proto-Pacific Ocean during the OAE 2. Moreover, combining the new U-Pb dates with the age-depth model (Bronk Ramsey, 2008) permits the projection of ages from Portland #1 core and the Yezo Group section on to the  $\text{Os}_i$  profiles and consequently facilitates inter-basin correlation.

#### *1.4. Marine calcium isotope stratigraphy*

The evaluation of global Os isotope stratigraphy across the OAE 2 assesses the driving mechanisms for the onset of anoxia. In order to quantify the mechanisms (e.g., weathering, productivity or volcanism) influencing seawater chemistry during the CTBI it is necessary to evaluate an number of isotope systems to yield a comprehensive understanding of the ocean and atmosphere conditions during the OAE 2 interval. One of the more recent isotope systems to be evaluated as a potential proxy for the evolution of seawater chemistry across the OAE 2 is calcium (Blättler et al., 2011). Ca is a mobile element and is therefore able to move between and within multiple geochemical reservoirs; e.g., lithosphere, hydrosphere, biosphere and atmosphere, as part of the Ca cycle. In seawater, Ca is recorded as  $\delta^{44}\text{Ca}/^{40}\text{Ca}$ , denoted as  $\delta^{44}\text{Ca}$ . The  $\delta^{44}\text{Ca}$  isotope composition of marine carbonates has been proposed as a proxy of chemical weathering and a key element involved in the long-term carbon cycle and the marine calcium budget (De La Rocha and DePaolo, 2000; Gussone et al., 2003, 2005, 2006; DePaolo, 2004; Fantle and DePaolo, 2005; Farkaš et al., 2007b; Blättler et al., 2012; Holmden et al., 2012; Fantle and Tipper, 2013).

The systematics for changing  $\delta^{44}\text{Ca}$  isotopic composition are dependent on variations in mass balance to and from the seawater through inputs: rivers ( $-1.03\text{‰}$ ) and MORs ( $-0.95\text{‰}$ ), and outputs: carbonate sedimentation (De La Rocha and DePaolo, 2000; Schmitt et al., 2003; Fantle et al., 2010; Blättler et al., 2012; Holmden et al., 2012; Fantle and Tipper, 2013; Fig. 1.5), as a function of the isotopic evolution of these inputs and outputs (Fantle and DePaolo, 2005; Sime et al., 2007). Over tens of millions of years the Ca isotopes are believed to be relatively resistant to diagenetic alteration, in comparison to a number of other proxies (Fantle and De Paolo, 2006), which would therefore enhance the capabilities of Ca isotopes over

million year time scales. However, on the order of the Ca residence time ( $\sim 0.5 - 1$  Ma; Schmitt et al., 2003; Farkaš et al., 2007a; Fantle and Tipper, 2013), the influence of diagenesis on the evolution of  $\delta^{44}\text{Ca}$  in seawater is a more prevalent possibility, which is not well constrained (Mitchell et al., 1997; Fantle, 2010; Fantle and Tipper, 2013).

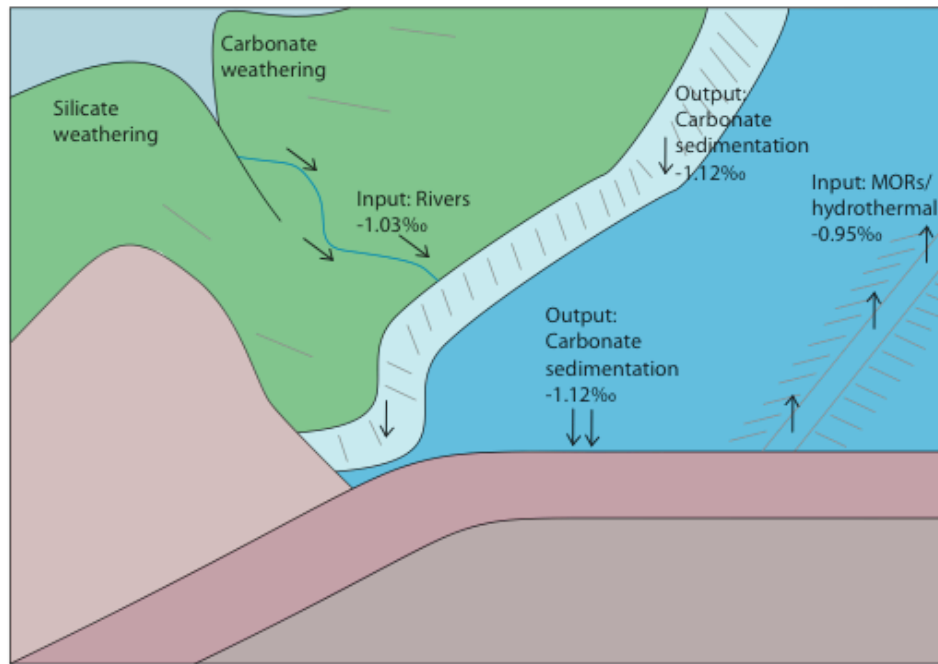


**Figure 1.5 Schematic cross-section of the inputs and outputs of marine  $\delta^{44}\text{Ca}$ .**

The marine  $\delta^{44}\text{Ca}$  isotope system is relatively poorly understood. A multitude of studies have aimed to answer a number of outstanding questions with regard to what the Ca isotopic record is directly controlled by and recording (Nägler et al., 2000; Gussone et al., 2003, 2005, 2006; Lemarchand et al., 2004; Böhm et al., 2006; Langer et al., 2007; Griffith et al., 2008b; Fantle and Tipper; 2013). Unlike isotopic records of Li, Mo, Nd, Os, Pb, Sr, U and trace metals (for example; Kerr, 1998; Snow et al., 2005; van Bentum et al., 2009; Frijia and Parente, 2008; MacLeod et al., 2008; Jenkyns, 2010; Montoya-Pino et al., 2010; Kuroda et al., 2011; Pogge von Strandmann et al., 2013; Du Vivier et al., 2014; Chapter 2, 3, this thesis) where the

isotopic variation of seawater is a function of known end-member inputs and outputs (Peucker-Ehrenbrink and Ravizza, 2000; McArthur et al., 2004), the isotopic variation of the  $\delta^{44}\text{Ca}$  isotope record cannot be attributed exclusively to changes in the isotopic composition of 2 end-members mixing (Griffith et al., 2008a; Fantle and Tipper, 2013). Hitherto, analysis indicates that differentiating between the primary inputs based on simple end-member mixing is very difficult since the end-members have nearly identical  $\delta^{44}\text{Ca}$  values ( $-0.95\%$ , hydrothermal and  $-1.03\%$ , riverine; Holmden et al., 2012), which offer little isotopic leverage for driving distinguishable variations in the Ca isotope composition of seawater (Schmitt et al., 2003; Holmden et al., 2012). In particular, during an episode of significant ocean and atmosphere perturbation driven by global warming and volcanic activity, such as the OAE 2. Furthermore, the interpretation of Ca isotopes is complicated by kinematic fractionation and mass dependent fractionation (Gussone et al., 2003; Fantle et al., 2010). Consequently, due to the lack of variability, it has been assumed that the  $\delta^{44}\text{Ca}$  values respond to changes in fractionation factor due to an imbalance in the scale of input/output fluxes (De La Rocha and DePaolo, 2000; Blättler et al., 2011; Fantle and Tipper, 2013). The fractionation factor is a function of carbonate precipitation, which is primarily dependent on  $\text{CaCO}_3$  mineralogy (DePaolo, 2004; Blättler et al., 2012; Holmden et al., 2012; Fantle and Tipper, 2013; Ockert et al., 2013).

Additionally, as a result of the lack of isotopic leverage between the two end-members, there are a number of parameters to consider during the assessment of  $\delta^{44}\text{Ca}$  values that potentially influence the evolution of  $\delta^{44}\text{Ca}$  ratios in seawater during deposition, which could be environmental and/or biological (e.g., chemical composition, precipitation, temperature, salinity, lithology/ carbonate mineralogy,

growth rate, and post-deposition diagenesis; De La Rocha and DePaolo, 2000; Farkaš et al., 2007b; Fantle, 2010; Blättler et al., 2012; Fantle and Tipper, 2013).

Multiple isotopic analyses of OAE 2 reveal a synchronous shift in isotope composition with the onset of the OAE 2 (e.g.,  $\delta^{13}\text{C}$ , Li, Mo, Nd, Os, Pb, P, Sr, U and trace metals; Schlanger et al., 1987; Kerr, 1998; Clarke and Jenkyns, 1999; McArthur et al., 2004; Snow et al., 2005; Frijia and Parente, 2008; Turgeon and Creaser, 2008; Macleod et al., 2008; Tsandev and Slomp, 2009; van Bentum et al., 2009; Jenkyns, 2010; Montoya-Pino et al., 2010; Kuroda et al., 2011; Mort et al., 2011; Pogge von Strandmann et al., 2013; Du Vivier et al., 2014; Chapter 2, 3, this thesis). A previous OAE 2 study (Blättler et al., 2011) revealed that the  $\delta^{44/42}\text{Ca}$  isotope excursion was also synchronous with the onset of OAE 2. They generated oceanic box models, which inferred that the variation in the  $\delta^{44/42}\text{Ca}$  isotope record was caused by large weathering flux imbalances to the global ocean, and was not a result of temperature and diagenetic factors and/or inputs from submarine volcanic activity did not appreciably affect the marine calcium isotope budget. However, the subtle trend makes justification of the negative excursion in each data set particularly difficult to discern.

As indicated above, quantitative experimental data interpreted from seawater mixing models suggest that hydrothermal inputs are not sufficient to change the seawater  $\delta^{44}\text{Ca}$  ratios (Schmitt et al., 2003; Amini et al., 2008; Tipper et al., 2010; Blättler et al., 2011), despite the temporal coincidence between the variation in  $\delta^{44}\text{Ca}$  values synchronous with the onset of OAE 2 and the putative indication to hydrothermal inputs contemporaneous with the OAE 2. In Chapter 4, I evaluate  $\delta^{44}\text{Ca}$  records from 4 global sections to determine if the perturbations in the marine  $^{187}\text{Os}/^{188}\text{Os}$  record (of Chapters 2 and 3) were replicated in the  $\delta^{44}\text{Ca}$  record and if an

analogous cause of isotopic change is tenable in both systems. Through the utilisation of seawater mixing models, quantitative analysis simulates profiles of variable  $\delta^{44}\text{Ca}$  values in order to determine the mechanism which best replicates the variation in  $\delta^{44}\text{Ca}$  values compared to the record established in nature.

### *1.5. Chapter synopsis*

The research in this thesis is presented in paper format. Each paper (chapter) represents a complete study, which builds a global record for both marine Os and marine Ca, contributing to the catalogue of isotopic proxies used to evaluate the OAE 2. The following sections of this introductory chapter provide a synopsis of the chapters within this thesis.

#### *1.5.1. Chapter 2: Marine $^{187}\text{Os}/^{188}\text{Os}$ isotope stratigraphy reveals the interaction of volcanism and ocean circulation during Oceanic Anoxic Event 2*

The chapter presents a version of the paper published in *Earth Planetary Science Letters*, **389**, 23-33, 2014; co-authored by David Selby, Bradley Sageman, Ian Jarvis, Darren Gröcke, and Silke Voigt.

The chapter presents high-resolution osmium (Os) isotope stratigraphy across the Cenomanian-Turonian Boundary Interval from 6 sections for four transcontinental settings producing a record of seawater chemistry that demonstrates regional variability as a function of terrestrial and hydrothermal inputs, revealing the impact of palaeoenvironmental processes. In every section the  $^{187}\text{Os}/^{188}\text{Os}$  profiles show a comparable trend; radiogenic values in the lead up to Oceanic Anoxic Event 2 (OAE 2); an abrupt unradiogenic trend at the onset of OAE 2; an unradiogenic

interval during the first part of OAE 2; and a return to radiogenic values towards the end of the event, above the Cenomanian-Turonian boundary. The unradiogenic trend in  $^{187}\text{Os}/^{188}\text{Os}$  is synchronous in all sections. Previous work suggests that activity at the Caribbean LIP (Large Igneous Province) was the source of unradiogenic Os across the OAE 2 and possibly an instigator of anoxia in the oceans. Here I assess this hypothesis and consider the influence of activity from other LIPs, such as the High Arctic LIP.

A brief shift to high radiogenic  $^{187}\text{Os}/^{188}\text{Os}$  values occurred in the Western Interior Seaway before the onset of OAE 2. I evaluate this trend and suggest that a combination of factors collectively played critical roles in the initiation of OAE 2; differential input of nutrients from continental and volcanogenic sources, coupled with efficient palaeocirculation of the global ocean and epeiric seas, enhanced productivity due to higher nutrient availability, which permitted penecontemporaneous transport of continental and LIP-derived nutrients to trans-equatorial basins.

I undertook sample collection from the Portland #1 core, Wunstorf core, Vocontian Basin (outcrop) and Site 530 (core), and analysed and processed all samples for  $^{187}\text{Os}/^{188}\text{Os}$  isotope composition at Durham University. I wrote the manuscript and compiled figures; improved by comments from Selby, Sageman, Jarvis and Voigt. Selby, Sageman, Jarvis, Gröcke and Voigt helped with sample collection at outcrop. Gröcke and Voigt analysed  $\delta^{13}\text{C}_{\text{org}}$  from Wunstorf, in Durham and Hanover, respectively. The USGS core repository (CO) and H. Jenkyns (Oxford) supplied additional samples from ODP Site 1260 and Furlo, respectively.

*1.5.2. Chapter 3: Pacific  $^{187}\text{Os}/^{188}\text{Os}$  isotope chemistry and U-Pb geochronology: Implications for global synchronicity of OAE 2*

A version of this chapter will be submitted to Earth Planetary Science Letters; co-authored by David Selby, Daniel Condon, Reishi Takashima and Hiroshi Nishi.

The marine realm across the Cenomanian-Turonian boundary interval records the OAE 2. This event has been studied using a number of geochemical proxies (e.g.,  $\delta^{13}\text{C}$ , Os, Sr, Nd, Pb, U) at several sites from the proto-Atlantic. In contrast, there are limited studies from the proto-Pacific. I present initial osmium isotope stratigraphy ( $\text{Os}_i$ ) from two proto-Pacific sites: the Yezo Group (YG) section, Hokkaido, Japan, and the Great Valley Sequence (GVS), California, USA; to evaluate the Os seawater chemistry of the proto-Pacific with that of the Western Interior Seaway, Tethys and proto-Atlantic. In addition, I present U-Pb zircon ID-TIMS geochronology from 5 volcanic tuff horizons of the Yezo Group section to facilitate basinal integration and to quantitatively constrain the duration of events across the Cenomanian-Turonian boundary interval.

For the YG section the  $\text{Os}_i$  prior to OAE 2 are radiogenic and heterogeneous ( $\sim 0.55 - 0.85$ ). Synchronous with the OAE 2 onset the  $\text{Os}_i$  abruptly become unradiogenic and remain homogenous ( $\sim 0.20 - 0.30$ ) before showing a gradual return to more radiogenic  $\text{Os}_i$  ( $\sim 0.70$ ) throughout the middle to late OAE 2. The  $\text{Os}_i$  data and U-Pb age(s) combined, revise the stratigraphic position of the onset of OAE 2 in the YG section. The bed marking the onset of OAE 2 is  $\sim 24$  m higher than previously considered based solely on the  $\delta^{13}\text{C}_{\text{wood}}$  analysis, which is supported by the U-Pb age for HK017 of  $94.436 \pm 0.14$  Ma (adjacent to the onset of OAE 2) that agrees with the interpolated age of the onset  $\sim 94.38 \pm 0.15$  Ma, within uncertainty. In addition, I develop an age-depth model based on the  $^{206}\text{Pb}/^{238}\text{U}$  ages to facilitate the

integration of  $Os_i$  profiles between the YG and the Portland core. In contrast, the  $Os_i$  profile from the GVS is disparate to the YG profile and those of several proto-Atlantic and Tethys locations. The heterogeneous  $Os_i$  values in the GVS suggest that seawater chemistry was influenced interchangeably by both unradiogenic and radiogenic Os, which infers that the  $Os_i$  isotope composition is readily sensitive to regional variability and responds within <20 kyr to changes in ocean chemistry. The continuous inflections in the  $Os_i$  data suggest there is frequent alternation between continental flux and hydrothermal pulses to the palaeobasin due to the proximity to the Caribbean LIP.

Furthermore, the application of a temporal framework generates a quantitative model, from which the timing and onset of OAE 2 is derived and the duration of activity at the Caribbean LIP is estimated. The model illustrates the synchronous onset of OAE 2 and the contemporaneous activity at the Caribbean LIP in the  $Os_i$  profiles from trans-Pacific sections, which concur with  $Os_i$  profiles from OAE 2 sections worldwide (Chapter 2, this thesis).

I undertook sample collection from the Yezo Group section during fieldwork in Hokkaido, Japan, helped by Takashima and Selby. Samples from the Great Valley Sequence, California, USA were provided by Nishi. I analysed and processed all samples for  $^{187}Os/^{188}Os$  isotope composition at Durham University. The volcanic tuff horizons were also collected from the Yezo Group during fieldwork in Japan. I extracted zircons from the tuff samples for U-Pb zircon geochronology at NIGL BGS, Keyworth. I observed part of each stage of the analytical protocol for U-Pb zircon ID-TIMS, which was done by Nicola Atkinson at NIGL. Condon provided the U-Pb ages and facilitated with the OxCal age-depth model. I wrote the manuscript and compiled figures; improved by comments from Selby, Condon and Takashima.

*1.5.3. Chapter 4: Calcium isotope stratigraphy across the Cenomanian-Turonian OAE 2: Implications on the controls of marine Ca isotope composition*

A version of this chapter will be submitted *Geochimica et Cosmochimica Acta*; co-authored by Andrew Jacobson, Gregory Lehn, David Selby and Bradley Sageman.

This chapter presents a high-precision  $\delta^{44/40}\text{Ca}$  ( $\delta^{44}\text{Ca}$ ) isotope composition ( $2\sigma$  SD =  $\pm 0.04\%$ ) record for three OAE 2 sections from the Portland #1 core; the Pont d'Issole section, SE France; and the Yezo Group section, Japan; and new data for selected samples from Eastbourne, and compares with existing data for Eastbourne (previously analysed by Blättler et al., 2011). Evidence suggests that the isotopic leverage from inputs is insufficient to differentiate the factor driving long-term variability in the Ca isotope composition. Whereas the affect of fractionation factor as a result of the removal of Ca from the ocean through carbonate deposition is shown to have sufficient leverage on the variability of  $\delta^{44}\text{Ca}$  values.

A previous study represented  $\delta^{44/42}\text{Ca}$  values against numerical models coupled with Sr isotope curves, which were utilised to interpret the factors influencing the seawater chemistry (Blättler et al., 2011). The study infers that a transient negative excursion in the marine  $\delta^{44/42}\text{Ca}$  isotope composition across the onset of the OAE 2 is indicative to an increase in weathering influx (Blättler et al., 2011). However, the  $\delta^{44}\text{Ca}$  values from this study reveal a positive excursion that is synchronous with the onset of OAE 2, after which the  $\delta^{44}\text{Ca}$  values gradually return to pre-OAE 2 values.

Qualitative observations of the positive trend in the  $\delta^{44}\text{Ca}$  values suggest that the variation may be sensitive to an increase in hydrothermal flux, which is globally

contemporaneous with activity at submarine LIPs based on evidence from Os isotope stratigraphy (Chapters 2 and 3, this thesis) and other isotope proxies and trace metals, which may suggest that Ca and Sr are decoupled in seawater chemistry for this period of time. In spite of this, I utilise seawater mixing models to simulate changes in  $\delta^{44}\text{Ca}$  values, in order to determine the dominant factor driving  $\delta^{44}\text{Ca}$  variation. The models are derived from a non-steady-state permitting the mass and residence time of Ca in seawater to vary in order to maintain a mass-balance and return to steady state over time. The models demonstrate no appreciable variation in  $\delta^{44}\text{Ca}$  values in response to hydrothermal influx or weathering influx. The best imitation of the  $\delta^{44}\text{Ca}$  record from Portland and Pont d'Issole is inferred from the model that simulates a variable fractionation factor. In addition, I interpret the discrepancy of the trends between this study and Blättler et al. (2011).

The contrasting marine  $\delta^{44}\text{Ca}$  profiles suggest that fractionation is influenced by the lithology of the sequence stratigraphy and therefore the positive excursion at Portland and Pont d'Issole is an artefact of site-specific mineralogical variation (Ockert et al., 2013). In this study I discuss the influence of fractionation factor determined by site-specific lithology and express the complexities of the marine  $\delta^{44}\text{Ca}$  isotopic system through the discussion of multiple parameters, which need to be constrained before conclusive interpretation of  $\delta^{44}\text{Ca}$  profiles can be made. The variation in fractionation factor may also be interpreted as consistent with ocean acidification, which subsequently influences the depositional composition. Whereby the increase in submarine volcanic activity, contemporaneous with the onset of OAE 2, elevates the abundance of dissolved  $\text{CO}_2$  in the oceans and thus increases carbonate dissolution as the pH of the seawater decreases. Ultimately, the variability in  $\delta^{44}\text{Ca}$  values is a function of changing fractionation factor in response to

decreasing carbonate precipitation, stimulated by a change in seawater chemistry that is driven by volcanism.

I undertook sample collection from the Portland #1 core, Pont d'Issole section and the Yezo Group section. I spent 5 weeks at Northwestern University to process and analyse all samples for  $\delta^{44}\text{Ca}$  for the Portland #1 core. Samples from Pont d'Issole and the Yezo Group were subsequently processed and analysed by Lehn at Northwestern. All  $^{187}\text{Os}/^{188}\text{Os}$  isotope compositions were processed at Durham University (Chapters 2 and 3). I wrote the manuscript and compiled the figures. Jacobson provided the seawater mixing model. Selby, Jacobson, Lehn and Sageman provided constructive comments on the manuscript as a whole.

#### *1.5.4. Chapter 5: Conclusions and Future work*

This chapter summarises the main conclusions and implications of this thesis and documents future work that could be undertaken to address any outstanding issues associated with this project area.

#### *1.6. Synopsis*

This thesis aims to investigate marine Os and Ca isotope stratigraphy of organic-rich deposits, with the intention of improving our understanding of the late Cretaceous through the analysis of multiple global OAE 2 sections. The  $\delta^{13}\text{C}$  isotope curves, that characterise OAEs, have been combined with new high-resolution  $\text{Os}_i$  isotope profiles to better understand the relationship between the ocean-atmosphere systems during a turbulent interval of the geological past. Re-Os provide a unique tool to infer the global extent of the OAE 2, to assess the mechanism(s) driving fluctuations in seawater  $^{187}\text{Os}/^{188}\text{Os}$  and quantitatively determine the change in flux

to the oceans, and by inference assess the changeability of palaeocirculation associated with OAE 2. The fluctuation of  $\text{Os}_i$  data suggests that  $^{187}\text{Os}/^{188}\text{Os}$  isotope stratigraphy might provide a more dynamic fingerprint for seawater chemistry during the OAE 2 (and other OAEs) compared to the  $\delta^{13}\text{C}$  isotope data. Therefore the  $\text{Os}_i$  profiles facilitate section correlation and can quantitatively constrain the duration of volcanism associated with the OAE 2. The U-Pb zircon geochronology of volcanogenic tuff horizons enable stratigraphic integration of a Pacific OAE 2 section with the GSSP section and confirm the validity of the globally synchronous OAE 2.

The application of marine  $\delta^{44}\text{Ca}$  to elucidate the Ca cycle during the CTBI combined with seawater mixing models shows that the input required to change the Ca isotopic composition of the ocean, riverine and/or hydrothermal, is insufficient during the OAE 2. I use seawater mixing models to simulate the causes of  $\delta^{44}\text{Ca}$  isotopic variation. The simulated models for increased hydrothermal and riverine influx both show no appreciable change in  $\delta^{44}\text{Ca}$  values and reveal that fractionation factor drives the variability of seawater  $\delta^{44}\text{Ca}$  ratios. Fractionation factor is dependent on the carbonate composition of the sediment precipitating. I illustrate the relationship between modelled fractionation factor and data recorded and conclude that instantaneously changing the fractionation factor at the onset, consistent with a change in lithology, produces a positive excursion in the  $\delta^{44}\text{Ca}$  record at Portland and Pont d'Issole; however, there are a number of other depositional and post depositional factors associated with the fractionation factor that must be considered. Overall, I suggest that Ca isotope systematics are complex and the marine  $\delta^{44}\text{Ca}$  profiles are regionally disparate on a global scale as a function of varying

fractionation factor. Further work is crucial in order to develop our understanding and to establish which parameter(s), if any, is the most influential.

## REFERENCES

- Amini, M., Eisenhauer, A., Böhm, F., Fietzke, J., Bach, W., Garbe-Schonberg, D., Rosner, M., Bock, B., Lackschewitz, K.S., Hauff, F., 2008. Calcium isotope ( $^{844/40}\text{Ca}$ ) fractionation along hydrothermal pathways, Logatchev field (Mid-Atlantic Ridge, 14°45'N). *Geochim. Cosmochim. Acta* 72, 4107-4122.
- Arthur, M. A., Sageman, B.B., 1994. Marine black shales: Depositional mechanisms and environments of ancient deposits. *Annu. Rev. Earth Planet. Sci.* 22, 499-551.
- Arthur, M. A., Schlanger, S. O., Jenkyns, H. C., 1987. The Cenomanian/Turonian Oceanic Anoxic Event, II: Palaeoceanographic controls on organic matter production and preservation, in *Marine Petroleum Source Rocks*, edited by J. Brooks and A. J. Fleet, *Geol. Soc. London Spec. Publ.*, 26, 401–420.
- Blättler, C. L., Jenkyns, H. C., Reynard, L. M., Henderson, G. M., 2011. Significant increases in global weathering during Oceanic Anoxic Events 1a and 2 indicated by calcium isotopes. *Earth Planet. Sci. Letts.* 309, 77-88.
- Blättler, C.L., Henderson, G.M., Jenkyns, H.C., 2012. Explaining the Phanerozoic Ca isotope history of seawater. *Geology* 40, 843-846.
- Böhm, F., Gussone, N., Eisenhauer, A., Dullo, W.-C., Reynaud, S., Paytan, A., 2006. Ca isotope fractionation in modern corals. *Geochim. Cosmochim. Acta* 70, 4452–4462.
- Bottini, C., Cohen, A. S., Erba, E., Jenkyns, H. C., & Coe, A. L., 2012. Osmium-isotope evidence for volcanism, weathering, and ocean mixing during the early Aptian OAE 1a. *Geology*, 40(7), 583-586.
- Bronk Ramsey, C., 2008. Deposition models for chronological records. *Quaternary Science Reviews* 27, 42-60.
- Clarke, L. J., Jenkyns, H. C., 1999. New oxygen isotope evidence for long-term Cretaceous climatic change in the Southern Hemisphere. *Geology* 27, 8; 699-702.
- Cohen, A. S., 2004. The rhenium-osmium isotope system: Applications to geochronological and palaeoenvironmental problems. *Journal of the Geological Society London* 161, 729-734.
- Cohen, A., Coe, A., 2002. New geochemical evidence for the onset of volcanism in the Central Atlantic magmatic province and the environmental change at the Triassic–Jurassic boundary. *Geology* 30, 267–270

- Cohen, A., Coe, A., 2007. The impact of the Central Atlantic Magmatic Province on climate and on the Sr- and Os-isotope evolution of seawater. *Palaeogeog. Palaeoclimatol. Paleocol.* 244, 374–390.
- Cohen, A.S., Coe, A.L., Bartlett, J.M. & Hawkesworth, C.J. 1999. Precise Re–Os ages of organic-rich mudrocks and the Os isotope composition of Jurassic seawater. *Earth Planet. Sci. Lett.* 167, 159-173.
- Colodner, D., 1991. The marine geochemistry of rhenium, iridium and platinum, Ph.D. Thesis. MIT/WHOI Joint Program in Oceanography.
- Colodner, D., Sachs, J., Ravizza, G., Turekian, K.K., Edmond, J., Boyle, E., 1993. The geochemical cycle of rhenium: A reconnaissance, *Earth Planet. Sci. Lett.* 117, 205–221.
- Condon, D.J., others, a., in-review. Metrology and Traceability of U-Pb Isotope Dilution Geochronology (EARTHTIME Tracer Calibration Part I). *Geochem. Geophys. Geosyst.*
- Crusius, J., Calvert, S., Pedersen, T., Sage, D., 1996. Rhenium and molybdenum enrichments in sediments as indicators of oxic, suboxic and sulfidic conditions of deposition. *Earth Planet. Sci. Lett.* 145, 65-78.
- Cumming, V.M., Selby, D., Lillis, P.G., 2012. Re–Os geochronology of the lacustrine Green River Formation: Insights into direct depositional dating of lacustrine successions, Re–Os systematics and paleocontinental weathering. *Earth Planet. Sci. Lett.* 359-360, 194-205.
- De La Rocha, C.L., DePaolo, D.J., 2000. Isotopic evidence for variations in the marine calcium cycle over the Cenozoic. *Science* 289, 1176–1178.
- DePaolo, D.J., 2004. Calcium isotopic variations produced by biological, kinetic, radiogenic and nucleosynthetic processes. *Rev. Mineral. Geochem.* 55, 255–288.
- Du Vivier, A.D.C., Selby, D., Sageman, B.B., Jarvis, I., Grocke, D.R., Voigt, S., 2014. Marine  $^{187}\text{Os}/^{188}\text{Os}$  isotope stratigraphy reveals the interaction of volcanism and ocean circulation during Oceanic Anoxic Event 2. *Earth Planet. Sci. Lett.* 389, 23-33.
- Erbacher, J., Friedrich, O., Wilson, P. A., Birch, H., Mutterlose, J., 2005. Stable organic carbon isotope stratigraphy across Oceanic Anoxic Event 2 of Demerara Rise, western tropical Atlantic. *Geochem., Geophys. Geosyst.* 6, Q06010, doi:10.1029/2004GC000850.
- Erbacher, J., Thurow, J., Littke, R., 1996. Evolution patterns of radiolaria and organic matter variations: A new approach to identify sea-level changes in mid-Cretaceous pelagic environments. *Geology*, 24, 499-502.

- Esser, B.K. & Turekian, K.K. 1993. Anthropogenic osmium in coastal deposits. *Environ. Sci. Tech.* 27, 2719–2724.
- Fantle M.S., DePaolo D.J., 2006. Sr isotopes and pore fluid chemistry in carbonate sediment of the Ontong Java Plateau: Calcite recrystallization rates and evidence for a rapid rise in seawater Mg over the last 10 million years. *Geochim. Cosmochim. Acta* 70(15), 3883–3904.
- Fantle, M.S., 2010. Evaluating the Ca isotope proxy. *Am. J. Sci.* 310, 194–230.
- Fantle, M.S., DePaolo, D.J., 2005. Variations in the marine Ca cycle over the past 20 million years. *Earth Planet. Sci. Lett.* 237, 102–117.
- Fantle, M.S., Tipper, E.T., 2013. Calcium isotopes in the global biogeochemical Ca cycle: Implications for development of a Ca isotope proxy. *Earth-Science Reviews* doi:10.1016/j.earscirev.2013.10.004
- Farkaš, J., Böhm, F., Wallmann, K., Blenkinsop, J., Eisenhauer, A., Van Geldern, R., Veizer, J., 2007b. Calcium isotope record of Phanerozoic oceans: Implications for chemical evolution of seawater and its causative mechanisms. *Geochim. Cosmochim. Acta* 71(21), 5117-5134.
- Farkaš, J., Buhl, D., Blenkinsop, J., Veizer, J., 2007a. Evolution of the oceanic calcium cycle during the late Mesozoic: Evidence from  $\delta^{44/40}\text{Ca}$  of marine skeletal carbonates. *Earth Planet. Sci. Lett.* 253(1), 96-111.
- Forster, A., Schouten, S., Moriya, K., Wilson, P.A., Sinninghe Damsté, J.S., 2007. Tropical warming and intermittent cooling during the Cenomanian/Turonian oceanic anoxic event 2: Sea surface temperature records from the equatorial Atlantic. *Paleoceanography*, 22, PA1219. doi:10.1029/2006PA001349.
- Frijia, G., Parente, M., 2008. Strontium isotope stratigraphy in the upper Cenomanian shallow-water carbonates of the southern Apennines: Short-term perturbations of marine  $^{87}\text{Sr}/^{86}\text{Sr}$  during the oceanic anoxic event 2. *Palaeogeog. Palaeoclimatol. Palaeoecol.* 261, 15-29.
- Gale, A.S., Kennedy, W.J., Voigt, S., Walaszczyk, I., 2005. Stratigraphy of the Upper Cenomanian-Lower Turonian Chalk succession at Eastbourne, Sussex, UK.: ammonites, inoceramid bivalves and stable carbon isotopes. *Cretaceous Research* 26, 3, 460 – 487.
- Griffith, E.M., Paytan, A., Caldeira, K., Bullen, T.D., Thomas, E., 2008a. A dynamic marine calcium cycle during the past 28 million years. *Science* 322, 1671–1674.
- Griffith, E.M., Paytan, A., Kozdon, R., Eisenhauer, A., Ravelo, A.C., 2008b, Influences on the fractionation of calcium isotopes in planktonic foraminifera: *Earth and Planetary Science Lett.* 268, 124–136, doi:10.1016/j.epsl.2008.01.006

- Grosheny, D., Beaudoin, B., Morel, L., Desmares, D., 2006. High-resolution biostratigraphy and chemostratigraphy of the Cenomanian/Turonian boundary event in the Vocontian Basin, southeast France. *Cretaceous Research* 27, 629-640.
- Gussone, N., Böhm, F., Eisenhauer, A., Dietzel, M., Heuser, A., Teichert, B.M.A., Reitner, J., Worheide, G., Dullo, W.-C., 2005. Calcium isotope fractionation in calcite and aragonite. *Geochim. Cosmochim. Acta* 69, 4485-4494.
- Gussone, N., Eisenhauer, A., Heuser, A., Dietzel, M., Bock, B., Böhm, F., Spero, H.J., Lea, D.W., Buma, J., Nägler, T.F., 2003. Model for kinetic effects on calcium isotope fractionation ( $\delta^{44}\text{Ca}$ ) in inorganic aragonite and cultured planktonic foraminifera. *Geochim. Cosmochim. Acta* 67, 1375–1382.
- Gussone, N., Langer, G., Thoms, S., Nehrke, G., Eisenhauer, A., Riebesell, U., Wefer, G., 2006. Cellular calcium pathways and isotope fractionation in *Emiliana huxleyi*. *Geology* 34, 625–628.
- Haq, B.U., Hardenbol, J., Vail, P.A., 1988. Mesozoic and Cenozoic chronostratigraphy and cycles of sea-level change, in *Sea-Level Changes: An Integrated Approach*, edited by C.K. Wilgus et al., Spec. Publ. Soc. Econ. Plaeontol. Mineral. 42, 71-108.
- Holmden, C., Papanastassiou, D.A., Blanchon, P., Evans, S., 2012.  $\delta^{44/40}\text{Ca}$  variability in shallow water carbonates and the impact of submarine groundwater discharge on Ca-cycling in marine environments. *Geochim. Cosmochim. Acta* 83, 179–194.
- Jarvis, I., Gale, A. S., Jenkyns, H. C., Pearce, M. A., 2006. Secular variation in Late Cretaceous carbon isotopes: a new  $\delta^{13}\text{C}$  carbonate reference curve for the Cenomanian – Campanian (99.6 – 70.6 Ma). *Geol. Mag.* 143, 561 – 608.
- Jenkyns, H.C., 1980. Cretaceous anoxic events: from continents to oceans. *J. Geol. Soc. London* 137, 171–188.
- Jenkyns, H.C., 2010. Geochemistry of oceanic anoxic events. *Geochem. Geophys. Geosys.* 11(3).
- Jenkyns, H.C., Forster, A., Schouten, S., Sinninghe Damste, J.S., 2004. High temperatures in the Late Cretaceous Arctic Ocean. *Nature* 432, 888 -892.
- Jones, C. E., Jenkyns, H. C., 2001. Seawater strontium isotopes, oceanic anoxic events, and seafloor hydrothermal activity in the Jurassic and Cretaceous. *Am. J. Sci.*, 301, 112 – 149.
- Keller, G., Pardo, A., 2004. Age and paleoenvironment of the Cenomanian/Turonian global stratotype section and point at Pueblo, Colorado. *Mar. Micropaleontol.* 51, 95–128.
- Kendall, B., Creaser, R. A., Ross, G.M., Selby, D., 2004. Constraints on the timing of Marinoan “Snowball Earth” glaciation by  $^{187}\text{Re}$ – $^{187}\text{Os}$  dating of a Neoproterozoic, post-glacial black shale in Western Canada. *Earth Planet. Sci. Letts.* 222, 729–740.

- Kendall, B., Creaser, R. A., Gordon, G. W., Anbar, A. D., 2009. Re-Os and Mo isotope systematics of black shales from the Middle Proterozoic Velkerri and Wollongorang Formations, McArthur Basin, northern Australia. *Geochim. Cosmochim. Acta* 73, 2534-2558.
- Kerr, A.C., 1998. Oceanic plateau formation: a cause of mass extinction and black shale deposition around the Cenomanian–Turonian boundary? *J. Geol. Soc.* 155, 619-626.
- Kuroda, J., Tanimizu, M., Hori, R.S., Suzuki, K., Ogawa, N.O., Tejada, M.L., Ohkouchi, N., 2011. Lead isotopic record of Barremian–Aptian marine sediments: Implications for large igneous provinces and the Aptian climatic crisis. *Earth Planet. Sci. Lett.* 307, 126-134.
- Langer, G., Gussone, N., Nehrke, G., Riebesell, U., Eisenhauer, A., and Thoms, S., 2007, Calcium isotope fractionation during coccolith formation in *Emiliana huxleyi*: Independence of growth and calcification rate: *Geochemistry, Geophysics, Geosystems*, v. 8, Q05007, doi:10.1029/2006GC001422.
- Lawley, C.J.M., Selby, D., 2012. Re-Os Geochronology of Quartz Enclosed Ultra-fine Molybdenite: Implications for Ore Geochronology. *Economic Geology* 107, 1499-1506.
- Leckie, R. M., Bralower, T. J., Cashman, R., 2002. Oceanic anoxic events and plankton evolution: Biotic response to tectonic forcing during the mid-Cretaceous. *Paleocean*, 17, 3.
- Lemarchand, D., Wasserburg, G.T., Papanastassiou, D.A., 2004. Rate-controlled calcium isotope fractionation in synthetic calcite: *Geochim. Cosmochim. Acta* 68, 4665–4678, doi:10.1016/j.gca.2004.05.029.
- Lewan, M.D., Maynard, J.B., 1982, Factors controlling enrichment of vanadium and nickel in the bitumen of organic sedimentary rocks. *Geochim. Cosmochim. Acta* 46, 2547-2560.
- MacLeod, K. G., Marin, E. E., Blair, S. W., 2008. Nd excursions across the Cretaceous oceanic anoxia event 2 (Cenomanian-Turonian) in the tropical North Atlantic. *Geology* 36, 811-814.
- Martin, E. E., MacLeod, K. G., Jimenez Berrocoso, A., Bourbon, E., 2012. Water mass circulation on Demerara Rise during the Late Cretaceous based on Nd isotopes. *Earth Planet. Sci. Lett.*, 327-328, 111-120.
- Mattinson, J.M., 2005. Zircon U-Pb chemical abrasion (“CA-TIMS”) method: combined annealing and multi-step partial dissolution analysis for improved precision and accuracy of zircon ages. *Chem. Geol.* 220, 47–66.

- McArthur, J.M., Howarth, R.J., Bailey, T., 2004. Strontium isotope stratigraphy. In: Gradstein, F., Ogg, J., Smith, A., (Eds.) A Geological Time Scale 2004. Cambridge University Press, Cambridge, U.K., pp. 96–105.
- McLean, N., Others, in-review. Evaluating Uncertainties in the Calibration of Isotopic Reference Materials and Multi-Element Isotopic Tracers (EARTHTIME Tracer Calibration Part II). *Geochemistry Geophysics Geosystems*.
- Meyers, S.R., Siewert, S.E., Singer, B.S., Sageman, B.B., Condon, D.J., Obradovich, J.D., Jicha, B.R., Sawyer, D.A., 2012. Intercalibration of radioisotopic and astrochronologic time scales for the Cenomanian-Turonian boundary interval, Western Interior Basin, USA. *Geology* 40, 7-10.
- Mitchell, S.F., Ball, J.D., Crowley, S.F., Marshall, J.D., Paul, C.R., Veltkamp, C.J., Samir, A. 1997. Isotope data from Cretaceous chalks and foraminifera: Environmental or diagenetic signals? *Geology* 25, 691-694.
- Montoya-Pino, C., Weyer, S., Anbar, A.D., Pross, J., Oschmann, W., van de Schootbrugge, B., Arz, H.W., 2010. Global enhancement of ocean anoxia during Oceanic Anoxic vent 2: A quantitative approach using U isotopes. *Geology* 38, 315-318.
- Mort, H., Jacquat, O., Adatte, T., Steinmann, P., Follmi, K., Matera, V., Berner, Z., Stuben, D., 2007. The Cenomanian/Turonian anoxic event at the Bonarelli Level in Italy and Spain: enhanced productivity and/or better preservation? *Cretaceous Research* 28, 597 - 612.
- Mort, H. P., Adatte, T., Follmi, K. B., Keller, G., Steinmann, P., Matera, V., Berner, Z., Stüben, D., 2011. Phosphorus and the roles of productivity and nutrient recycling during Oceanic Anoxic Event 2. *Geology*, 35, 6; 483-486.
- Nägler, T.F., Eisenhauer, A., Müller, A., Hemleben, C., Kramers, J., 2000. The  $\delta^{44}\text{Ca}$ -temperature calibration on fossil and cultured Globigerinoides sacculifer: New tool for reconstruction of past sea surface temperatures: *Geochem. Geophys. Geosys.* 1, 1052, doi:10.1029/2000GC000091.
- Obradovich, J. 1993. The Evolution of the Western Interior Basin, Geological Association of Canada, Special Paper 39, 379-396.
- Ockert, C., Gussone, N., Kaufhold, S., Teichert, B.M.A., 2013. Isotope fractionation during Ca exchange on clay minerals in a marine environment. *Geochim. Cosmochim. Acta*, 112, 374-388.
- Oxburgh, R., 2001, Residence time of osmium in the oceans. *Geochemistry, Geophysics, Geosystems* 2, 2000GC000104.
- Pearce, M.A., Jarvis, I., Tocher, B.A., 2009. The Cenomanian–Turonian boundary event, OAE2 and palaeoenvironmental change in epicontinental seas: New insights from

- the dinocyst and geochemical records. *Palaeogeog. Palaeoclimatol. Palaeoecol.* 280, 207–234.
- Peucker-Ehrenbrink, B., Ravizza, G., 2000. The marine osmium isotope record. *Terra Nova* 12, 205-219.
- Peucker-Ehrenbrink, B., Ravizza, G., Hofman, A.W., 1995. The marine  $^{187}\text{Os}/^{188}\text{Os}$  record of the past 80 million years. *Earth Planet. Sci. Lett.* 130, 155–167.
- Pogge von Strandmann, P.A.E., Jenkyns, H.C., Woodfine, R.G., 2013. Lithium isotope evidence for enhanced weathering during Oceanic Anoxic Event 2. *Nature Geoscience*, doi:10.1083/NGE01875
- Quidelleur, X., Paquette, J.L., Fiet, N., Takashima, R., Tiepolo, M., Desmares, D., Nishi, H., Grosheny, D., 2011. New U-Pb (ID-TIMS and LA-ICPMS) and  $^{40}\text{Ar}/^{39}\text{Ar}$  geochronological constraints of the Cretaceous geologic time scale calibration from Hokkaido (Japan). *Chem. Geol.* 286, 72-83.
- Ravizza, G., Esser, B.K., 1993. A possible link between the seawater osmium isotope record and weathering of ancient sedimentary organic matter. *Chem. Geol.* 107, 255-258
- Ravizza, G., Peucker-Ehrenbrink, B., 2003. Chemostratigraphic evidence of Deccan volcanism from the marine osmium isotope record. *Science* 302, 1392–1395.
- Ravizza, G., Turekian, K.K., 1992. The osmium isotopic composition of organic rich marine sediments. *Earth Planet. Sci. Lett.* 110, 1-6.
- Robinson, N., Ravizza, G., Coccioni, R., Peucker-Ehrenbrink, B., Norris, R., 2009. A high-resolution marine  $^{187}\text{Os}/^{188}\text{Os}$  record for the late Maastrichtian: Distinguishing the chemical fingerprints of Deccan volcanism and the KP impact event. *Earth Planet Sci. Lett.* 281, 159–168.
- Rooney, A.D., Selby, D., Houzay, J-P., Renne, P.R 2010. Re-Os geochronology of Mesoproterozoic sediments from the Taoudeni basin, Mauritania: Implications for basin-wide correlations, supercontinent reconstruction and Re-Os systematics of organic-rich sediments. *Earth Planet. Sci. Lett.* 289, 486-496.
- Sageman, B.B., Meyers, S.R., Arthur, M.A., 2006. Orbital time scale and new C-isotope record for Cenomanian–Turonian boundary stratotype. *Geology* 34, 125–128.
- Schlanger, S.O., Arthur, M.A., Jenkyns, H.C., Scholle, P.A. 1987. The Cenomanian/Turonian Oceanic Anoxic Event, I. Stratigraphy and distribution of organic carbon-rich beds and the marine  $\delta^{13}\text{C}$  excursion. In: Brooks, J. & Fleet, A.J. (eds) *Marine Petroleum Source Rocks*. Geological Society London, Spec. Publ., 26, 371–399.
- Schmitt, A.-D., Chabaux, F., Stille, P., 2003. The calcium riverine and hydrothermal isotopic fluxes and the oceanic calcium mass balance. *Earth Planet. Sci. Lett.* 6731, 1–16.

- Selby, D., Creaser, R.A., 2003. Re-Os geochronology of organic rich sediments: an evaluation of organic matter analysis methods. *Chem. Geol.* 200, 225–240.
- Selby, D., Creaser, R.A., Heaman, L.M., Hart, C.J.R., 2003. Re-Os and U-Pb geochronology of the Clear Creek, Dublin Gulch and Mactung deposits, Tombstone Gold Belt, Canada: Absolute timing relationships between plutonism and mineralization. *Canadian Journal of Earth Sciences* 40, 1839-1852.
- Selby, D., Creaser, R.A., 2005. Direct radiometric dating of hydrocarbon deposits using rhenium-osmium isotopes: *Science* 308, 1293–1295, doi: 10.1126/science.1111081.
- Selby, D., Mutterlose, J., Condon, D.J., 2009. U–Pb and Re–Os geochronology of the Aptian/Albian and Cenomanian/Turonian stage boundaries: Implications for timescale calibration, osmium isotope seawater composition and Re–Os systematics in organic-rich sediments. *Chem. Geol.* 265, 394 – 409.
- Sime, N.G., De La Rocha, C.L., Tipper, E.T., Tripathi, A., Galy, A., Bickle, M.J., 2007. Interpreting the Ca isotope record of marine biogenic carbonates. *Geochim. Cosmochim. Acta* 71, 3979–3989.
- Sinton, C. W., Duncan, R. A., 1997. Potential links between ocean plateau volcanism and global ocean anoxia and the Cenomanian-Turonian boundary. *Econ. Geol.*, 92, 836-842.
- Snow, L. J., Duncan, R. A., Bralower, T. J., 2005. Trace element abundances in the Rock Canyon Anticline, Pueblo, Colorado, marine sedimentary section and their relationship to Caribbean plateau construction and oxygen anoxic event 2. *Paleoceanography* 20, doi:10.1029/2004PA001093.
- Takashima, R., Nishi, H., Yamanaka, T., Tomosugi, T., Fernando, A.G., Tanabe, K., Moriya, K., Kawabe, F., Hayashi, K., 2011. Prevailing oxic environments in the Pacific Ocean during the mid-Cretaceous Oceanic Anoxic Event 2. *Nature Comms.* 2:234 DOI:10.1038/ncomms1233.
- Tejada, M.L.G., Suzuki, K., Kuroda, J., Coccioni, R., Mahoney, J.J., Ohkouchi, N., Tatsumi, Y., 2009. Ontong Java Plateau eruption as a trigger for the early Aptian oceanic anoxic event. *Geology* 37, 855-858.
- Tipper, E.T., Gaillardet, J., Galy, A., Louvat, P., Bickle, M.J., Capmas, F., 2010. Calcium isotope ratios in the World's largest rivers: a constraint on the maximum imbalance of oceanic calcium fluxes. *Glob. Biogeochem. Cycles* 24, GB3019. doi.org/10.1029/2009GB003574.
- Trabucho-Alexandre, J., Tuenter, E., Henstra, G.A., van der Zwan, K.J., van de Wal, R.S.W., Dijkstra, H.A., de Boer, P.L., 2010. The mid-Cretaceous North Atlantic nutrient trap: Black shales and OAEs. *Paleoceanography* 25, PA4201, doi:10.1029/2010PA001925.

- Tsandev, I., Slomp, C. P., 2009. Modelling phosphorus cycling and carbon burial during Cretaceous Oceanic Anoxic Events. *Earth Planet. Sci. Lett.*
- Turgeon, S.C., Creaser, R.A., 2008. Cretaceous Anoxic Event 2 triggered by a massive magmatic episode. *Nature* 454, 323–326.
- van Bentum, E.C., Hetzel, A., Brumsack, H.J., Forster, A., Reichart, G.J., Sinninghe Damsté, J.S., 2009. Reconstruction of water column anoxia in the equatorial Atlantic during the Cenomanian–Turonian oceanic anoxic event using biomarker and trace metal proxies. *Palaeogeog. Palaeoclimatol. Palaeoecol.* 280, 489-498.
- Voigt, S., Erbacher, J., Mutterlose, J., Weiss, W., Westerhold, T., Wiese, F., Wilmsen, M., Wonik, T., 2008. The Cenomanian-Turonian of the Wunstorf section (North Germany): global stratigraphic reference section and new orbital time scale for Oceanic Anoxic Event 2. *Newsl. Stratigr.* 43, 65-89.
- Zheng X-Y., Jenkyns, H.C., Gale, A.S., Ward, D.J., Henderson, G.M., 2013. Changing ocean circulation and hydrothermal inputs during Oceanic Anoxic Event 2 (Cenomanian-Turonian): Evidence from Nd-isotopes in the European shelf sea. *Earth Planet. Sci. Lett.* <http://dx.doi.org/10.1016/j.epsl.2013.05.053i>

# 2

## **Marine $^{187}\text{Os}/^{188}\text{Os}$ isotope stratigraphy reveals the interaction of volcanism and ocean circulation during Oceanic Anoxic Event 2**

A version of this chapter has been published in *Earth and Planetary Science Letters*, **389, 23-33, 2014**; co-authored by David Selby of Durham University, Bradley Sageman of Northwestern University, Ian Jarvis of Kingston University London, Darren Gröcke of Durham University, and Silke Voigt of Goethe-University Frankfurt.

### **1. Introduction**

The Cenomanian-Turonian boundary (CTB) OAE 2 records an extensive period of global anoxia, represented worldwide by sections containing organic-rich marine sedimentary rocks. Strata marking the onset of OAE 2 are globally correlated by a 2 to 4‰ positive excursion in the carbon stable isotope composition of organic matter ( $\delta^{13}\text{C}_{\text{org}}$ ) and marine carbonates ( $\delta^{13}\text{C}_{\text{carb}}$ ), which are interpreted to reflect the onset of massive organic carbon burial and widespread oxygen deficiency in the oceans (Jenkyns, 1980; Schlanger et al., 1987). The OAE 2 has been studied using numerous proxies (e.g. carbon, strontium, osmium, calcium, neodymium, lithium, uranium,  $\text{TEX}_{86}$  and phosphorus; Arthur et al., 1987; McArthur et al., 2004; Forster et al., 2007; Mort et al., 2007; MacLeod et al., 2008; Turgeon and Creaser, 2008; Voigt et al., 2008; Montoya-Pino et al., 2010; Blättler et al., 2011; Pogge von Strandmann et al., 2013; Zheng et al., 2013) to determine the driving mechanisms for organic carbon burial and anoxia. Among the processes thought to play a role are: enhanced volcanism and  $\text{CO}_2$  output; increased land and sea surface temperatures; an accelerated hydrological cycle, sea level rise and increased rates of ocean circulation; and changes in nutrient supply and productivity. These have all been supported by different proxy studies (e.g. Jenkyns, 1980; Arthur et al., 1987; Arthur and Sageman, 1994; Mort et al., 2007; Turgeon and Creaser, 2008; Martin et al., 2012).

In this study, we present high-resolution initial osmium isotope ( $^{187}\text{Os}/^{188}\text{Os}$ ;  $\text{Os}_i$ ) stratigraphy of the upper Cenomanian to lower Turonian from 4 transcontinental sections, and the  $\text{Os}_i$  data from two previously analysed representative sections of the proto-North Atlantic and Tethyan margin (Fig. 2.1; ODP Site 1260 and Furlo; Turgeon and Creaser 2008) with additional analysis to enhance resolution. These data are predominantly controlled by the mass balance of two end-member Os

isotope components: weathered continental crust (~1.4) and mantle inputs (0.13) attributed to enhanced submarine volcanism (Peucker-Ehrenbrink and Ravizza, 2000). This, coupled with the short residence time of Os in seawater ( $\leq 10$  kyr; Oxburgh, 2001), makes  $^{187}\text{Os}/^{188}\text{Os}$  composition an excellent monitor of palaeoceanographic changes in the geological record (Peucker-Ehrenbrink and Ravizza, 2000; Cohen, 2004), particularly across the CTB where there is evidence for accelerated weathering, as well as evidence of submarine volcanic activity (Snow et al., 2005; Frijia and Parente, 2008; Turgeon and Creaser, 2008; Pogge van Strandmann et al., 2013).

Analysis of osmium isotope trends recorded from different sites provides information about changes in these inputs to the marine realm, as well as the interconnectivity of oceanic water masses with epeiric seas. The  $\text{Os}_i$  data reported from the previous study show similar profiles, and suggest that for at least ~700 kyr of the late Cenomanian-early Turonian the ocean basins were relatively well connected. The  $\text{Os}_i$  data also show that a major pulse of volcanism interpreted to be associated with activity from Large Igneous Provinces (LIPs), i.e., Caribbean and High Arctic (Fig. 2.1; Snow et al., 2005; Tegner et al., 2011) occurred at or just prior to the onset of OAE 2. However, the High Arctic LIP is largely understudied due to lack of exposure. Since constraints on timing and duration of activity from LIP volcanism are ambiguous (Tegner et al., 2011; Zheng et al., 2013), we associate the  $\text{Os}_i$  data presented here with activity from the better temporally constrained Caribbean LIP (Turgeon and Creaser, 2008).

The  $\text{Os}_i$  stratigraphic profiles across the CTB in this study are from (Fig. 2.1): the Portland #1 core, which is representative of the Global Stratotype Section and Point (GSSP) near Pueblo, Colorado (Western Interior Seaway (WIS); Kennedy et

al., 2000); the Wunstorff core in Germany, a representative section in the NW European pelagic shelf sea (Voigt et al., 2008); the Vocontian Basin, south east France (Western Tethys; Grosheny et al., 2006; Jarvis et al., 2011); and DSDP Site 530 (proto-South Atlantic; Forster et al., 2008). The Portland #1 core has the most refined temporal control for the studied interval based on detailed biostratigraphy, new radioisotopic dating, astrochronology, and chemostratigraphy (Sageman et al., 2006; Meyers et al., 2012a; Ma et al., 2014), and provides a critical framework for global correlation. The Wunstorff core has a similarly good age control based on bio-, chemo-, and cyclostratigraphy and can be correlated to the Portland #1 core succession (Voigt et al., 2008). Based on the GSSP time scale, and confirmed by additional estimates from different OAE 2 sites, the duration of the  $\delta^{13}\text{C}$  isotope excursion that characterises the OAE 2 is between 500-600 kyr (Meyers et al., 2012b).

In this study we investigate the  $\text{Os}_i$  stratigraphy of multiple sections over an interval of  $\sim 1.8$  Myr from the late Cenomanian to the early Turonian and demonstrate that  $\text{Os}_i$  values show some differences prior to OAE 2 depending on geographic location and depositional setting. These variations are interpreted to reflect differential water mass exchange between epeiric settings and the open ocean modulated by sea-level change, as well as changes in terrigenous weathering rates due to enhanced global warming, which may have also affected nutrient fluxes and primary production levels. These results suggest that epeiric seas, like the WIS or the European shelf sea, may have played an important role in the driving mechanism for OAE 2.

Additionally, we show that in comparison to the pre-OAE 2 interval, the syn-OAE 2  $\text{Os}_i$  values from Site 1260 and Furlo combined with Portland, Wunstorff, the

Vocontian Basin and Site 530 are remarkably similar. Coupled with the new geochronology from the WIS (Meyers et al., 2012a) a refined timing for the onset and duration of LIPs and its temporal association with OAE 2 is developed. Furthermore, our interpretation of the  $\text{Os}_i$  profile concurs with the hypothesis of increased ocean circulation based on analysis of neodymium (Nd) isotopes (Martin et al., 2012; Zheng et al., 2013).

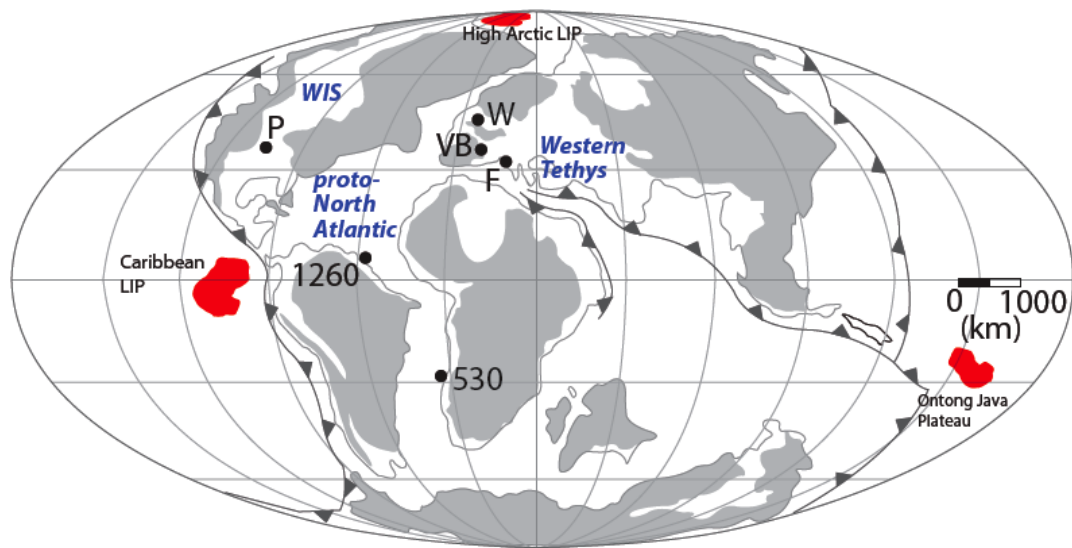


**Figure 2.1 Palaeogeographic map of the CTB showing locations of analysed sites.** P – Portland and Pueblo GSSP; 1260 – ODP Site 1260, Demerara Rise; W – Wunstorf; VB – Vocontian Basin; F – Furlo; 530 – DSDP Site 530. The location of the Caribbean LIP and High Arctic LIP (Large Igneous Province) are also shown.

## 2. OAE 2 section geology

### 2.1. Portland #1 Core, Colorado, USA

The studied interval was sampled from the USGS Portland #1 core ( $32^{\circ} 22.6$  'N,  $105^{\circ} 01.3$  'W; Dean and Arthur, 1998; Meyers et al., 2001; Fig. 2.1). This core was taken about 40 km west of the site near Pueblo, CO that was ratified as the

GSSP for the CTB (Kennedy et al., 2005), and its stratigraphy has been correlated, essentially bed for bed, to the GSSP section (Sageman et al., 2006). The Pueblo region was ratified as the GSSP site because the boundary interval contains abundant biostratigraphic index taxa, several options for geochronologic calibration, shows no obvious signs of condensation or significant disconformity, and has various stratigraphic markers that can be correlated over tens of thousands of square km (Hattin, 1971; Elder et al., 1994; Kennedy et al., 2005).

Within the Portland core, the Cenomanian-Turonian Boundary Interval (CTBI) was studied in a 17.7 m-thick section of the Bridge Creek Limestone (~12 m) and Hartland Shale (~12.6 m) Members of the Greenhorn Formation (Cobban and Scott, 1972). These units include organic-rich calcareous shales and rhythmically interbedded couplets of shale and fossiliferous biomicritic limestone. The stratigraphy is also characterised by four bentonite units of 1 to 20 cm that have been regionally correlated (Elder, 1988). Recent sanidine  $^{40}\text{Ar}/^{39}\text{Ar}$  and zircon  $^{206}\text{Pb}/^{238}\text{U}$  geochronology integrated with astrochronology constrain the CTB at  $93.90 \pm 0.15$  Ma (Meyers et al., 2012a). The CTBI contains a variety of fossil taxa useful for biostratigraphy (e.g., Gale et al., 1993; Kennedy et al., 2000, 2005; Keller and Pardo, 2004; Keller et al., 2004; Cobban et al., 2006) some of which have intercontinental distributions; however, their transcontinental synchronicity is limited. The dominant foraminifera species spanning the CTBI are *Rotalipora cushmani*, *Whiteinella archaeocretacea* and *Helvetoglobotruncana helvetica* (Eicher and Worstell, 1970). The FO (first occurrence) of the ammonite *Watinoceras devonense* (Fig. 2.2; Kennedy et al., 2000) marks the basal Turonian, recorded at the base of bed 86 of the Bridge Creek Limestone (Meyers et al., 2001; bed numbers are based on Cobban and Scott, 1972). The FO of *W. devonense* coincides with the FO of *Mytiloides*

*puebloensis* (Kennedy et al., 2000), which can be traced through both Tethyan and Boreal regions (Kennedy et al., 2005).

The onset of OAE 2 is identified by an abrupt 2-3‰ VPDB  $\delta^{13}\text{C}_{\text{org}}$  positive shift from values of  $\sim -27\text{‰}$  in the upper Hartland Shale, 4.3 m below the CTB (Fig. 2.2; Table 2.1a; Sageman et al., 2006). The positive excursion is characteristic of the isotopic response during OAE 2 and, although many localities record increased organic carbon deposition at this level (e.g., Tsikos et al., 2004), sites within the WIS do not. Here the onset is characterised by organic-poor interbedded limestones and shales that are generally bioturbated. Shale interbeds in the upper half of the OAE 2 interval, however, do become enriched in TOC in the WIS. The end of OAE 2 is expressed by a gradual fall in  $\delta^{13}\text{C}_{\text{org}}$  back to  $\sim -27\text{‰}$  (Sageman et al., 2006).

A high-resolution time scale for the study interval has been developed in recent years based on integration of new radioisotopic dates and astrochronological methods (Meyers et al., 2001, 2012a; Sageman et al., 2006; Ma et al., 2014). The astrochronological techniques yield a more accurate interpolation of time for the intervals between dated tuff horizons because they include evolutive assessment of changes in linear sedimentation rate (not corrected for compaction). Both radioisotopic and astrochronologic methods indicate a duration for OAE 2 of  $\sim 600$  kyr measured from the  $\delta^{13}\text{C}_{\text{org}}$  onset.

## 2.2. Wunstorf, NW Germany

The Wunstorf section was sampled from drill core from  $52^{\circ} 24.187' \text{N}$ ,  $09^{\circ} 29.398' \text{E}$  and represents the European type section for the CTBI (Fig. 2.1; Voigt et al., 2008). The CTBI succession (Hesseltal Formation) at Wunstorf was deposited in the distal Lower Saxony Basin, which was part of the western European shelf sea

(Wilmsen, 2003). The 26.5 m-thick Hesseltal Formation comprises cyclically interbedded couplets of organic-carbon rich shales, marls and limestones interpreted to represent nine short eccentricity cycles based on spectral analytical results (Voigt et al., 2008). Accordingly, OAE 2, as defined by the  $\delta^{13}\text{C}_{\text{carb}}$  curve, includes 4.3 short eccentricity cycles or 21.2 precession cycles, respectively, indicating a duration of 430-445 kyr (Voigt et al., 2008).

The biostratigraphy of the Hesseltal Formation is established by zonation with inoceramids, ammonites, acme occurrences of macrofossils and planktonic foraminifera (Ernst et al., 1984; Lehmann, 1999; Voigt et al., 2008). The ammonite and inoceramid zonation can be compared to that of the GSSP in detail. Although no macrofossils are recorded directly from the Wunstorf core, a series of index taxa can be placed based on a bed-by-bed correlation between the Lower Saxony Basin and the Munsterland Cretaceous Basin (Voigt et al., 2007, 2008). The FO of the ammonite *Metoicoceras geslinianum* is equivalent to the FO of *Sciponoceras gracile* at the GSSP (Gale et al., 2005, 2008), which corresponds to the base of the Hesseltal Formation at Wunstorf (Lehmann, 1999). The FO of *W. devonense*, the index taxon for the CTB (Fig. 2.2; Kennedy et al., 2005), is located in the Wunstorf core at  $37.5 \pm 1$  m (Lehmann, 1999, Voigt et al., 2008).

Previously, the stratigraphic extent of OAE 2 was constrained by  $\delta^{13}\text{C}_{\text{carb}}$  (Voigt et al., 2008). Here we present  $\delta^{13}\text{C}_{\text{org}}$  for the Wunstorf section, which shows frequent oscillations from -25 to -27‰ VPDB prior to OAE 2 (Fig. 2.2; Table 2.1b). A facies change depicts the onset throughout the European shelf (Voigt et al., 2007). This change records an initial positive excursion in the  $\delta^{13}\text{C}_{\text{org}}$ , consistent with the  $\delta^{13}\text{C}_{\text{carb}}$ , followed by a second more distinct increase in the  $\delta^{13}\text{C}_{\text{org}}$ . At Wunstorf,  $\delta^{13}\text{C}_{\text{org}}$  only clearly records the second increase; however OAE 2 initiation

corresponds to the first increase. The duration of OAE 2 at Wunstorf was estimated to be ~435 kyr based on spectral analysis of lithological cyclicity (Voigt et al., 2008), which differs from the astrochronological and radioisotopic derived duration at the GSSP (~600 kyr; applied in this study). Voigt et al. (2008) discussed several options for this discrepancy as the possible lack of strata, different definitions of onset and termination of OAE 2 in the Portland #1 and Wunstorf cores, and incorrect orbital frequency assignment to the dominant cycle length. The new organic  $\delta^{13}\text{C}_{\text{org}}$  curve of this study (Fig. 2.2) shows five distinct cycles close to the short eccentricity filter of Voigt et al. (2008). Such a reinterpretation would reduce the temporal discrepancy and is consistent with the recently documented stronger obliquity control during OAE 2 (Meyers et al., 2012). Further spectral analytical research is needed to fully address this question.

### 2.3. *Vocontian Basin (Pont d'Issole and Vergons), SE France*

The Vocontian Basin was part of the western gulf in the European Alpine region of the NW Tethys Ocean ~30°N (Jarvis et al., 2011; Fig. 2.1). High rates of subsidence throughout the mid-Cretaceous provided accommodation space for thick rhythmically bedded bioturbated limestone-marl successions, where the variable facies are indicative of a fluctuating hemipelagic depositional environment of moderate depth. Different depositional and structural processes dependent on their location in the basin have affected CTB sections within the Vocontian Basin; e.g. the Vergons section is affected by syn-sedimentary slumping in the uppermost Cenomanian, but otherwise exposes a continuous Upper Albian – Lower Turonian succession, while the thinner Pont d'Issole section is complete through the CTBI. A ~20 m thick package of black organic-rich calcareous shales, termed the “Niveau

Thomel” (Takashima et al., 2009; Jarvis et al., 2011), characterise the CTBI. Detailed biostratigraphy has been obtained for the 24 m Pont d’Issole section (Grosheny et al., 2006; Jarvis et al., 2011). The distribution of index taxa *R. cushmani* and *H. helvetica*, coupled with complete  $\delta^{13}\text{C}_{\text{org}}$  and  $\delta^{13}\text{C}_{\text{carb}}$  records (Fig. 2.2; Jarvis et al., 2011), permits bed-scale correlation with the GSSP near Pueblo. Above the onset of OAE 2, samples were taken from Pont d’Issole, whereas below the onset some of the samples (n=4) came from Vergons (Table 2.2d), which is correlated with Pont d’Issole based on litho-, bio-, and stable-isotope stratigraphy and is undisturbed by faulting in the pre-OAE 2 interval.

The OAE 2 in the Pont d’Issole section includes a distinct facies change to finely laminated black shales (total organic carbon, TOC 0.3 – 3.5 wt.%) that occurs about a metre below the distinctive positive  $\delta^{13}\text{C}_{\text{org}}$  excursion (3‰) that marks the base of OAE 2 (Fig. 2.2; Table 2.1d; Jarvis et al., 2011). High-frequency fluctuations in the  $\delta^{13}\text{C}_{\text{org}}$  record, up to 1‰ in magnitude, occur throughout OAE 2, associated with the alternation of lithological units. The termination of OAE 2 is recorded by a gradual return to ~ -26‰.

#### 2.4. DSDP Site 530, Hole 530A, South Atlantic

Palaeotectonic reconstruction situates Site 530 at 37 °S, 38 °W (Forster et al., 2008; Fig. 2.1). Site 530 is located on the abyssal floor of the Angola Basin, 4645 metres below sea level (mbsl) and approximately 150 km west of the base of the continental slope of SW Africa with a 3-4 degree incline. Drilling penetrated to a final depth of 1121 metres below sea floor (mbsf) after encountering durable basalt at 1103 mbsf (Forster et al., 2008). The  $\delta^{13}\text{C}_{\text{org}}$  excursion marking OAE 2 occurs within a 49 m section of the CTBI. Low sample resolution due to poor core recovery,

and thus limited nannofossil data, only provide an approximate stratigraphic identification of the CTB.

Lithology in the CTBI includes interbedded shales, clays and mudstones, some of which are pyritiferous. The organic matter in the black shales is of marine origin, but includes a significant fraction of terrigenous material (Forster et al., 2008). The black shales are highly laminated and relatively undisturbed by bioturbation. The  $\delta^{13}\text{C}_{\text{org}}$  record is incomplete due to poor core recovery and low sample yield, but an excursion signifying OAE 2 is recorded: a 0.5‰ VPDB negative shift immediately precedes the 4‰ positive excursion, from -27.7 to -23.7‰ (Fig. 2.2; Table 2.1f; Forster et al., 2008). The characteristic excursion spans ~2 m of finely interbedded shales and mudstones. Throughout OAE 2, the  $\delta^{13}\text{C}_{\text{org}}$  values fluctuate between ~ -23.5‰ to -27.5‰. The maximum enrichment in the  $\delta^{13}\text{C}_{\text{org}}$  is at 1035.75 mbsf, ~3.52 m into OAE 2 (Forster et al., 2008).

### 2.5. ODP Site 1260, Hole 1260B, Demerara Rise and Furlo, Italy

In an effort to augment the understanding of seawater chemistry prior to OAE 2 provided by Turgeon and Creaser (2008), additional samples (n = 12 [ODP] and n = 6 [Furlo]; Fig. 2.1) were analysed and the resolution of the  $\text{Os}_i$  profiles was increased.

The facies at Site 1260 include a mixture of terrigenous detritus and carbonates, with high organic contents up to ~23 wt.%. The  $\delta^{13}\text{C}_{\text{org}}$  positive excursion reaches a maximum enrichment of -22.1‰ VPDB and the entire excursion is 1.2 m thick (Fig. 2.2; Table 2.1c; Forster et al., 2007).

In the Furlo section the CTBI lies within the Scaglia Bianca Formation, which includes abundant biosiliceous limestone. The Livello Bonarelli is a 1m thick

condensed interval of millimetre-laminated black shale and brown radiolarian sand that represents the sedimentary expression of part of OAE 2 (Arthur and Premoli Silva, 1982). Up to 20 m beneath the Bonarelli level there are numerous centimetre scale organic-rich shale layers (Jenkyns et al., 2007). The  $\delta^{13}\text{C}_{\text{org}}$  record has a narrow variation in background values prior to OAE 2,  $\sim -25.9$  to  $-26.5\%$ . The characteristic positive excursion in  $\delta^{13}\text{C}_{\text{org}}$  is a  $4\%$  shift, from  $-27.2$  to  $-23.1\%$ , occurring within  $<0.5$  m (Fig. 2.2; Table 2.1e).

### **3. Methods**

In this study we have applied  $\delta^{13}\text{C}_{\text{org}}$  and Re-Os methodologies to determine the geochemical signatures of OAE 2 related strata. We have used published analytical protocols (e.g., Selby and Creaser, 2003; Jarvis et al., 2011), which are described in detail in the following sub-sections, together with our sampling protocol from core and outcrop.

#### *3.1. Sampling Protocol*

The collection of samples at outcrop was undertaken with care in order to avoid areas of high surface weathering. Where erosion and weathering was obvious the samples were dug out from 10-20 cm beneath the exposure surface. Fresh samples would prevent sample exposure to isotopic alteration through chemical and physical weathering and/ or diagenesis. At each section samples were collected at 10 – 50 cm intervals; with the highest resolution through periods of most interest, e.g., 1 – 2 m prior to the onset of organic-rich laminated facies and throughout the first 2 – 3 m of these facies (which commonly mark the OAE intervals).

Core samples, each of ~50 g, were collected from the cores for Re-Os isotope analysis. Portland #1 core samples were collected from within every shale interval, approximately every 30-50 cm, with the exception of ~1 m below the marker bed 63, where the sample interval was 10 cm to yield a higher resolution Re-Os data over the onset interval of the OAE 2. For the Wunstorf core, samples were collected at 50 cm intervals. Above the onset of the OAE 2 samples were taken every 30 cm over ~2 m. From the Vocontian Basin samples were collected every 20-50 cm and from the Site 530 core, samples were taken at ~50 cm intervals. Sampling intensity was designed within each shale interval with Os residence time in mind (<10 kyr; Oxburgh, 2001).

In order to establish a better understanding of the ocean-climate system prior to the onset of the OAE 2, additional samples from Site 1260 and Furlo were analysed (see Table 2.2c and 2.2e) to enhance the resolution of the existing record by Turgeon and Creaser (2008).

### 3.2. *Re – Os Isotope analysis of organic-rich sediment (ORS)*

Prior to being powdered, all the samples were polished to remove any minor drill marks and weathered material. Samples were powdered in a Zr dish. A dried sample weight of  $\geq 30$  g was powdered in order to homogenise the Re and Os within the sample (Kendall et al., 2009). The Re-Os analysis ORS was conducted using Carius tube digestion in a 0.25 g/g  $\text{CrO}_3$  4N  $\text{H}_2\text{SO}_4$  reagent at 220°C for 48 hrs, with the Re and Os isolated from the acid medium using solvent extraction, micro-distillation and anion chromatography methodology (Selby and Creaser, 2003). In brief, 0.5 to 1 g of sample powder was loaded in a Carius tube with a known amount of mixed tracer solution,  $^{190}\text{Os} + ^{185}\text{Re}$ , with 8 ml of  $\text{CrO}_3$ - $\text{H}_2\text{SO}_4$  solution. The sealed Carius tubes are then placed in an oven at 220 °C for 48 hrs. Osmium is

isolated and purified using solvent extraction ( $\text{CHCl}_3$ ) and microdistillation methods. Anion chromatography is used to purify the Re from 1 ml of the  $\text{CrO}_3\text{-H}_2\text{SO}_4$  solution (Selby and Creaser, 2003). The purified Re and Os fractions were loaded onto Ni and Pt filaments, respectively (Selby and Creaser, 2003) with the addition of  $\sim 0.5$   $\mu\text{l}$   $\text{BaNO}_3$  and  $\text{BaOH}$  activator solutions, respectively. Isotope compositions were measured using negative thermal ion mass spectrometry (NTIMS; Creaser et al., 1991; Volkening et al., 1991) via faraday cups for Re and electron multiplier (SEM) in peak hopping mode for Os. Osmium isotopic ratios were calculated relative to  $^{188}\text{Os}$  and corrected for mass fractionation using a  $^{192}\text{Os}/^{188}\text{Os}$  value of 3.08261 (Nier, 1937). The oxide corrected  $^{185}\text{Re}/^{187}\text{Re}$  was normalised using a  $^{185}\text{Re}/^{187}\text{Re}$  value of 0.59738 (Gramlich et al., 1973). Total procedural blanks for Re and Os during this study are  $13.3 \pm 1.8$  ppt and  $0.32 \pm 0.17$  ppt, respectively, with  $^{187}\text{Os}/^{188}\text{Os}$  value of  $0.19 \pm 0.12$  (1 SD,  $n = 2$ ). Uncertainties for  $^{187}\text{Re}/^{188}\text{Os}$  and  $^{187}\text{Os}/^{188}\text{Os}$  are determined through full propagation of uncertainties in Re and Os mass spectrometer measurements, blank abundances and isotopic compositions, spike calibrations and reproducibility of standard Re and Os isotopic values (Table 2.2). In-house standard solutions (DROsS and Re Std) were run repeatedly throughout each batch of samples to monitor mass spectrometer reproducibility. The Re standard yields an average  $^{187}\text{Re}/^{188}\text{Re}$  of  $0.59795 \pm 0.0016$  (1 SD,  $n = 20$ ). The Os standards (AB-2 and DROsS) yields an  $^{187}\text{Os}/^{188}\text{Os}$  average of  $0.10682 \pm 0.00012$  (1 SD,  $n = 26$ ) and  $0.16094 \pm 0.00015$  (1 SD,  $n = 22$ ). The isotope compositions of these Re and Os solutions are consistent within uncertainty to those published by Selby et al. (2009) and Nowell et al. (2008).

A black shale reference sample, SDO-1, was used continuously throughout geochemical analysis, in order to determine analytical reproducibility. SDO-1 is a

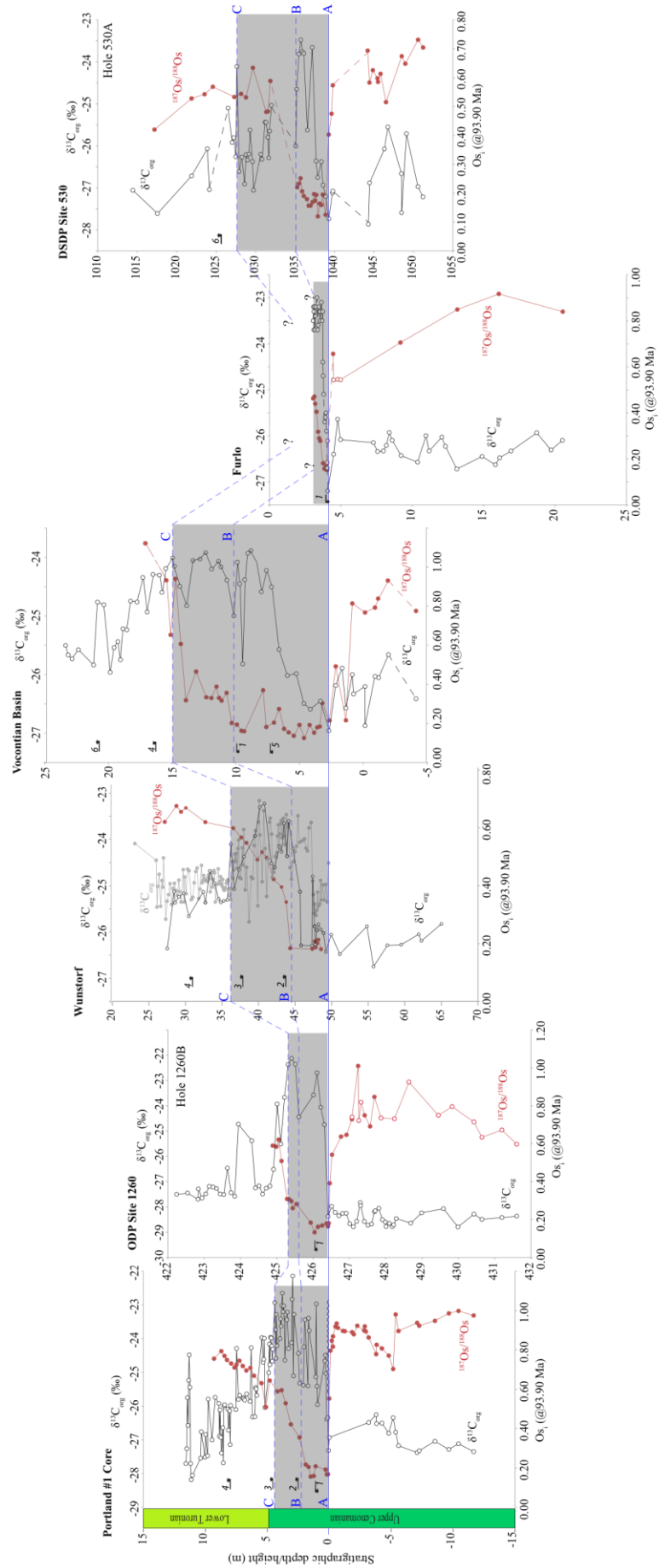
reference sample used by the USGS principally for trace element analysis of black shale units. It is Devonian-Mississippian, collected from the Huron Member of the Ohio Shale near Morehead, Kentucky (Kane et al., 1990). In this study 12 analysis of SDO-1 yielded an average  $^{187}\text{Re}/^{188}\text{Os}$  of  $1166.0 \pm 88.1$  (2 SD) and  $^{187}\text{Os}/^{188}\text{Os}$  of  $7.831 \pm 0.568$  (2 SD). The average Re and Os abundance for SDO-1 is  $75.5 \text{ ppb} \pm 11.3$  (2 SD) and  $626.1 \text{ ppt} \pm 101.8$  (2 SD). The average  $\text{Os}_i$  (calculated at 366 Ma) is  $0.70 \pm 0.04$  (2 SD; Table 2.3). Based on the reproducibility of the calculated  $\text{Os}_i$  for SDO-1, we only consider variations in  $\text{Os}_i$  to be of geological significance when the difference between samples is  $>0.04$ . For samples analysed from the Portland, Wunstorf and Site 530 cores and the Vocontian Basin initial  $^{187}\text{Os}/^{188}\text{Os}$  ( $\text{Os}_i$ ) were calculated using 93.90 Ma with the  $^{187}\text{Re}$  decay constant of Smoliar et al. (1996). The  $\text{Os}_i$  values of Turgeon and Creaser (2008) were recalculated with the new date (93.90 Ma) to allow a direct comparison.

### 3.3. Organic $\delta^{13}\text{C}$ analytical protocol

The organic carbon  $\delta^{13}\text{C}$  analysis (Table 2.1) was conducted at Durham University (UK) and in the Federal Institute for Geosciences and Natural Resources, Hannover (Germany) using similar methodologies in both laboratories on the Wunstorf samples. The Hannover  $\delta^{13}\text{C}_{\text{org}}$  record is of higher resolution and includes the isotopic composition of limestones in the OAE 2 succession. The Durham  $\delta^{13}\text{C}_{\text{org}}$  record, instead, covers a longer stratigraphic interval. Here, we combine both records to obtain the best definition of the datum levels ‘A’, ‘B’ and ‘C’ (Fig. 2.2; black – Hannover; grey – Durham). At Durham, aliquots of the powdered samples used for Re- Os isotope analysis were used for  $\delta^{13}\text{C}_{\text{org}}$  determination. Prior to analysis samples were decalcified: ~1 g of powder was mixed with 3 M HCl and left for 24

hrs. Samples were then thoroughly washed using Milli-Q water until acid was neutralised before being dried down in an oven at 60°C for 48 hrs. The samples were ground down to homogenise the decalcified residue and finally loaded into tin caps. Carbon isotope data was obtained using a Costech EA coupled to a ThermoFinnigan Delta V Advantage. At Hanover, the decalcified samples were measured with an elemental analyzer (Thermo-Electron Flash EA 1112) coupled to an isotope-ratio mass-spectrometer (Finnigan DeltaPlus). Ratios are corrected for  $^{17}\text{O}$  contribution (Craig, 1957) and stated in standard delta ( $\delta$ ) notation in per mil (‰) comparative to the VPDB scale.  $\delta^{13}\text{C}_{\text{org}}$  data is calibrated against a range of in-house standards, which are stringently calibrated against international standards (e.g., USGS 40, USGS 24, IAEA 600, IAEA N1, IAEA N2). Typically, analytical uncertainty for  $\delta^{13}\text{C}_{\text{org}}$  is better than  $\pm 0.1\text{‰}$  for replicate analyses of the international standards and typically  $<0.2\text{‰}$  on replicate sample analysis in both laboratories.

**Figure 2.2 (next page 50)  $\delta^{13}\text{C}_{\text{org}}$  (black) and  $\text{Os}_i$  (red) vs. stratigraphic height/depth.** Initial  $^{187}\text{Os}/^{188}\text{Os}$  calculated at 93.90 Ma.  $\delta^{13}\text{C}_{\text{org}}$  data from: Portland #1 Core, Sageman et al. (2006); Site 1260, Forster et al. (2007); Wunstorff (this study); Vocontian Basin, Jarvis et al. (2011); Furlo, Jenkyns et al. (2007); Site 530, Forster et al. (2008). Sites correlated using datum levels on the carbon isotope profiles (A, B, C; see text for details); where ‘A’ is the positive  $\delta^{13}\text{C}_{\text{org}}$  excursion marks the onset of the OAE 2 (Pratt et al., 1985), ‘B’ is the trough of relatively depleted values following the initial positive excursion in  $\delta^{13}\text{C}_{\text{org}}$ , and ‘C’ is the last relatively enriched  $\delta^{13}\text{C}_{\text{org}}$  value before the trend back to pre-excursion values (Tsikos et al., 2004). The positioning of the datum levels is determined for each site based on: Sageman et al., 2006 (Portland #1 Core); Forster et al., 2007 (Site 1260); this study (Wunstorff); Jarvis et al., 2011 (Vocontian Basin); Jenkyns et al., 2007 (Furlo); Forster et al., 2008 (Site 530). Biostratigraphic horizons are labelled: FO - first occurrence, LO – last occurrence; 1 – LO *R. cushmani*; 2 – FO *N. juddii*; 3 – FO *W. devonense*; 4 – FO *H. helvetica*; 5 – LO *T. greenhornensis*; 6 – FO *Q. gartneri*. The biozones illustrate low-resolution and inconsistent global distribution, which restricts correlation. Dashed red lines represent intervals of pore core recovery. Note that symbol size is greater than the measured uncertainty. Carbon and osmium isotope data are reported in Tables 2.1 and 2.2.



### 3.4. OAE 2 correlation

To date, the CTBI has been correlated ‘globally’ using biostratigraphy and carbon isotope chemostratigraphy. Typically, characteristic peaks and troughs in the  $\delta^{13}\text{C}$  record are combined with key bioevents to establish correlation. The six sections presented here (Fig. 2.2) are correlated according to this method using points ‘A’, ‘B’ and ‘C’ of the  $\delta^{13}\text{C}_{\text{org}}$  curve that are similar to those first defined by Pratt et al., (1985) in the Western Interior and used later by Tsikos et al. (2004). For this correlation method, ‘A’ represents the last value of relatively depleted  $\delta^{13}\text{C}_{\text{org}}$  before the first major shift to positive values (typically -24 to -22‰). This shift marks the base of  $\delta^{13}\text{C}_{\text{org}}$  excursion defined as OAE 2 (reference respective of location). ‘B’ defines a trough of depleted values following the initial positive excursion that occurs prior to the second positive shift (Pratt et al., 1985). ‘C’ is the last relatively enriched  $\delta^{13}\text{C}_{\text{org}}$  value before the trend back toward pre-excursion values, or the end of the so-called “plateau” (Tsikos et al., 2004).

In order to establish a common chronostratigraphic framework for comparing  $\text{Os}_i$  data from distant localities, the chemostratigraphic method described above, confirmed by available biostratigraphic data, is used to extend the Pueblo GSSP timescale from the Portland #1 core (Meyers et al., 2012a) to the other sites. The Portland core record has the highest resolution CTB timescale based on integration of new radioisotope dates (Ar-Ar and U-Pb) and astrochronology (Meyers et al., 2012a), and new work (Ma et al., 2014) has extended this timescale further down section into the Cenomanian. As a result, our new  $\text{Os}_i$  data and  $\text{Os}_i$  results from a previous study (Turgeon and Creaser, 2008), can be plotted relative to individual timescales created for each section by exporting temporal information from the

Portland #1 core (Fig. 2.3). Timescale development is based on the following steps (see Table 2.4):

- i. The new geochronology for the CTBI (Meyers et al., 2012a) employs a short eccentricity band pass to more accurately interpolate the age datum levels between dated tuff horizons. Based on this method, the stage boundary is constrained to  $93.90 \pm 0.15$  Ma
- ii. The ages of the ‘A’, ‘B’ and ‘C’ markers defined by the  $\delta^{13}\text{C}_{\text{org}}$  record of the Portland core are also precisely determined using this approach (Fig. 2.2; Table 2.4).
- iii. Nominal ages for the ‘A’, ‘B’, and ‘C’ markers are exported to the ‘A’, ‘B’ and ‘C’ datum levels of the  $\delta^{13}\text{C}_{\text{org}}$  curve in the other sections (Fig. 2.2), allowing calculation of local linear sedimentation rate values between the datum levels (Table 2.4). A variable sedimentation rate is more realistic over such time frames, i.e., ~100 kyr. In some sections there is a distinct decrease in rate in the B-C interval, which likely reflects condensation related to global sea-level highstand. Thus, the linear sedimentation rate calculated for A-B is applied to develop a timescale below the ‘B’ datum, and a linear sedimentation rate for B-C is used for the sections above the ‘B’ datum (Table 2.4).
- iv. Each timescale is developed using the onset of ‘A’ as the temporal datum set to 0 kyr (Fig. 2.3). This creates a coherent global framework using the onset of  $\delta^{13}\text{C}_{\text{org}}$  excursion as the key datum level.

Although our methodology increases resolution and reduces uncertainty in the time scales for each section, it cannot eliminate uncertainty (e.g., constant sedimentation rates are still assumed for time scale segments). For the purpose of

comparing  $\delta^{13}\text{C}_{\text{org}}$  and  $\text{Os}_i$  records between different localities, however, we believe the chronostratigraphic framework is sufficient to recognise differences in the timing of key events.

**Table 2.4**

Age of datum A, B and C to calculate the LSR to derive the Integrated timescale

$\delta^{13}\text{C}_{\text{org}}$ datum levels <sup>a</sup>	Age (Ma) <sup>b</sup>	kyr	
<b>Portland #1 Core, Colorado, USA</b>			
Datum A	94.38	0	
Datum B	94.23	150	
Datum C	93.95	430	
CTB	93.90	480	
End of OAE2	93.78	600	
Interval A-B		150	
Interval B-C		280	
Interval C-CTB		50	
Interval A-CTB		480	
	<b>Depth (m)</b>	<b>Datum interval</b>	<b>LSR <sup>c</sup></b>
<b>ODP Site1260, Hole 1260B, Demerara Rise</b>			
Datum A	426.41		
Datum B	425.61	A to B	0.53
Datum C	425.31	B to C	0.11
<b>Wunstorf, NW Germany</b>			
Datum A	49.6		
Datum B	44.5	A to B	3.40
Datum C	36.2	B to C	2.96
<b>Vocontian Basin, SE France</b>			
Datum A	1.8		
Datum B	10.3	A to B	5.67
Datum C	15.1	B to C	1.71
<b>Furlo, Italy</b>			
Datum A	4.07		
Datum B	d		
CTB	3.05	A to CTB	0.21
<b>DSDP Site 530, Hole 530A, South Atlantic</b>			
Datum A	1039.27		
Datum B	1035.08	A to B	2.79
Datum C	1027.62	B to C	2.66

a - determined from the  $\delta^{13}\text{C}_{\text{org}}$  Portland #1 Core by Sageman et al. (2006); see Fig. 2.2

b - derived from geochronology and astrochronology of GSSP section (Meyers et al., 2012a)

c - units cm/kyr

d - datum B in Furlo section is undetermined

### 3.5. Initial $^{187}\text{Os}/^{188}\text{Os}$ ( $\text{Os}_i$ )

The  $\text{Os}_i$  values in this study were determined from Re-Os data and the  $^{187}\text{Re}$  decay constant ( $1.666\text{e}^{-11}\text{a}^{-1}$ ; Smoliar et al., 1996; Table 2.2a-f) using the CTB age of  $93.90 \pm 0.15$  Ma that was determined from astrochronologic interpolation between volcanic ash ages (based on both  $^{40}\text{Ar}/^{39}\text{Ar}$  and  $^{206}\text{Pb}/^{238}\text{U}$  determinations; Gradstein et al., 2012; Meyers et al., 2012a). Analytical uncertainty for individual calculated  $\text{Os}_i$  is  $\leq 0.01$ . The reproducibility of calculated  $\text{Os}_i$ , based on 12 analyses of the USGS rock reference material SDO-1 (Devonian Ohio Shale), was  $\sim 0.04$  (2 SD; Table 2.3). This uncertainty was used to account for the maximum uncertainty in the sample set for the calculated  $\text{Os}_i$ . Calculated  $\text{Os}_i$  ratios assume closed system behaviour after deposition with respect to both rhenium and osmium. Furthermore, the  $^{187}\text{Os}/^{188}\text{Os}$  ratios reflect the isotope composition of the local seawater and are unaffected by mineral detritus.

## 4. Results

### 4.1. Re-Os Abundance

Across the onset of OAE 2 there is a dramatic shift to very high values in Os isotope concentration. At Portland Os concentration increases by  $\sim 1000$  ppt within  $\sim 10$  cm; at Wunstorf an increase of  $\sim 1000$  ppt within  $\sim 30$  cm; Site 1260 increases by  $\sim 1000$  ppt in  $< 60$  cm; in the Vocontian Basin there is an increase of  $\sim 3500$  ppt within 50 cm. In both Furlo and Site 530 there are very considerable changes in the Os concentration;  $> 10000$  ppt within 10 cm and 40 cm, respectively. Conversely, Re abundance is relatively constant at each section, therefore the dramatic difference between the Re and Os abundance produce a similar profile in  $^{187}\text{Re}/^{188}\text{Os}$  to the  $\text{Os}_i$

profile, with an abrupt decrease in the  $^{187}\text{Re}/^{188}\text{Os}$  directly associated with the abrupt increase in Os.

#### 4.2. $^{187}\text{Os}/^{188}\text{Os}$ isotope stratigraphy

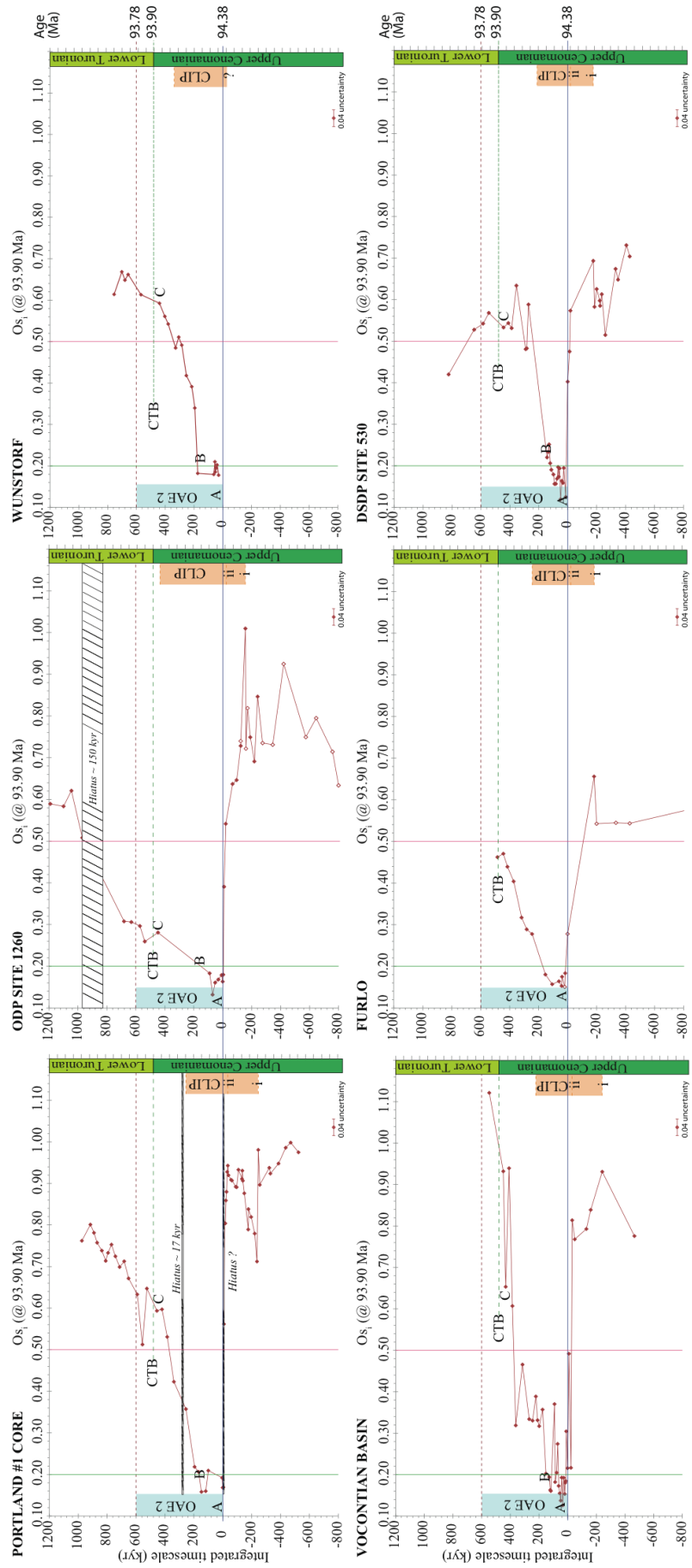
The  $\text{Os}_i$  profiles for all six sections show a similar trend; highly radiogenic values that suddenly become unradiogenic, before gradually returning to radiogenic values (Figs 2.2, 2.3; all  $\text{Os}_i$  data presented in full in Table 2.2). At Portland the  $\text{Os}_i$  values show some distinct fluctuations prior to the onset of OAE 2 (point ‘A’ on the  $\delta^{13}\text{C}_{\text{org}}$  curve). The Os trend from  $\sim 1.0$  to  $0.9$ , briefly return to  $\sim 1.0$ , and then drop abruptly to  $\sim 0.7$  at  $\sim -237$  kyr (below ‘A’). The trend toward unradiogenic values then reverses back toward the radiogenic end member up until the major shift to unradiogenic  $\text{Os}_i$  at ‘A’.

In the Site 1260 record, a trend from  $\sim 0.6$  to  $1.0$  in the lowest samples is followed by a shift in the opposite direction, toward the unradiogenic end-member, but the values are variable and some spikes to  $>1$  (radiogenic) persist. From  $-157$  kyr there is a consistent trend toward unradiogenic  $\text{Os}_i$  reaching a minimum value of  $\sim 0.2$  at the ‘A’ datum. At Wunstorf the rock units prior to ‘A’ are bereft of Re and Os. The Vocontian Basin record shifts to radiogenic  $\text{Os}_i$  values ( $>0.9$ ), before a gradual decrease to  $\sim 0.76$  followed by a brief increase to  $\sim 0.82$ . A few metres below the positive excursion a major shift to  $<0.3$  occurs. The  $\text{Os}_i$  values at Furlo remain stable at  $\sim 0.55$  then shift suddenly to  $\sim 0.65$ . Above this horizon there are no samples until ‘A’ when the  $\text{Os}_i$  is unradiogenic  $<0.3$ . Site 530 has  $\text{Os}_i$  values of  $\sim 0.70$  before showing a  $0.2$  decrease. The trend reverses to  $\sim 0.7$ , then the major unradiogenic shift to  $<0.2$  at ‘A’. Importantly, the  $\text{Os}_i$  record in the Portland core (Fig. 2.3) is

significantly different between  $\sim -230$  kyr and  $\sim -50$  kyr relative to the other 4 sites (no data for Wunstorf).

From 'A' through to the lower Turonian, the  $\text{Os}_i$  profiles and values are very similar across Portland, Furlo, Site 530 and Wunstorf, progressively trending from unradiogenic ( $\sim 0.2$ ) to radiogenic values ( $\sim 0.6$  to  $0.7$ ; Fig. 2.3) within  $\sim 350$  kyr. The  $\text{Os}_i$  values from point 'A' remain unradiogenic for  $\sim 200$ - $250$  kyr before becoming progressively more radiogenic (Fig. 2.3). The majority of the  $\text{Os}_i$  data from the Vocontian Basin, from slightly before the onset of the positive  $\delta^{13}\text{C}_{\text{org}}$  excursion through the initial  $\sim 200$  kyr are unradiogenic at  $\sim 0.2$ , with some fluctuation to  $\sim 0.4$ . In contrast to other sites that show a progressive return to radiogenic  $\text{Os}_i$  values, the Vocontian Basin remains at values of  $\sim 0.4$  for an additional  $200$  kyr and then becomes radiogenic ( $0.94$ ) very rapidly (within  $\sim 80$  kyr; Fig. 2.3). This abrupt change could indicate a minor hiatus during the latter part of OAE 2. The  $\text{Os}_i$  values at Site 530 remain unradiogenic ( $0.12 - 0.25$ ) for  $\sim 145$  kyr, returning to radiogenic values after  $\sim 270$  kyr. However, due to poor core recovery there is a  $\sim 125$  kyr gap in the  $\text{Os}_i$  record (Fig. 2.3).

**Figure 2.3 (next page 57)  $\text{Os}_i$  data calculated at 93.90 Ma relative to chemostratigraphically integrated timescale (kyr).** 0 kyr marks the onset of OAE 2 ( $\sim 94.38$  Ma) that is equal to the onset of the positive  $\delta^{13}\text{C}_{\text{org}}$  excursion and defined as datum 'A'. The  $\delta^{13}\text{C}_{\text{org}}$  profile also includes markers 'B' and 'C'. These datum levels provide the basis for chemostratigraphic correlation within the OAE 2 interval. The green dashed line shows the CTB. The blue shaded area from 0 to 600 kyr illustrates the duration of OAE 2 (Sageman et al., 2006), and the red dashed line represents the upper limit of the event. The initial onset of CLIP volcanism 'i' is at  $\sim 94.58$  Ma, with the major pulse 'ii' at  $\sim 94.41$  Ma and main cessation at  $\sim 94.13$  Ma (CLIP – Caribbean LIP). Uncertainty on all ages is nominally  $< \pm 0.2$  Ma (Meyers et al. 2012a). The open red squares are the additional samples analysed for Site 1260B and Furlo in this study, the remainder of the data for these localities are from Turgeon and Creaser (2008). The grey hatched sections represent hiatuses: Portland hiatus just prior to the onset of OAE 2 is minor and has an un-quantified duration (Ma et al., 2014). The hiatus at Site 1260 is based on core images and the  $\delta^{13}\text{C}_{\text{org}}$  profile (this study, see section 5.3. for discussion). Vertical lines at  $\text{Os}_i$  values 0.2 (green) and 0.5 (pink) facilitate comparison of absolute values between profiles;  $\text{Os}_i$  values  $< 0.2$  represent a predominantly hydrothermal source,  $> 0.5$  represent a predominance of continental weathering. Note that individual  $\text{Os}_i$  uncertainty is  $< 0.01$  and thus symbol size is greater than the measured uncertainty. Uncertainty is shown based on 2 SD of 12 analyses of SDO-1 is  $< 0.04$ .



## 5. Discussion

### 5.1. Heterogeneous seawater $^{187}\text{Os}/^{188}\text{Os}$ prior to OAE 2

Overall the  $\text{Os}_i$  profiles from each section show similar variability in  $\text{Os}_i$  values and in the  $^{187}\text{Re}/^{188}\text{Os}$  composition before and during OAE 2. Combined with previous Os isotope stratigraphy (Turgeon and Creaser, 2008) and detailed litho-, bio-, and chemostratigraphy, the sections are interpreted to be reliable records of the CTBI.

The  $\text{Os}_i$  values for all sites in the WIS, western Tethys and proto-North Atlantic from -800 kyr to -210 kyr are radiogenic, and range from ~0.5 to ~1.0, illustrating that the seawater  $^{187}\text{Os}/^{188}\text{Os}$  ratio during this time was not homogeneous, but was controlled by the  $^{187}\text{Os}/^{188}\text{Os}$  composition of the fluxes entering the individual basins (Figs 2.1, 2.3). The radiogenic heterogeneity and high  $\text{Os}_i$  values at Portland are attributed to the influence of weathered crustal components from the Sevier Orogenic Belt and the Canadian Shield, the major sources of weathered material to the basin. Recent seawater Os isotope studies during glacial episodes in the last 200 kyr demonstrate how regional variation is correlated to the heterogeneous flux of material into proximal basins (Paquay and Ravizza, 2012). This hypothesis is supported by the observed radiogenic  $\text{Os}_i$  values for >500 kyr prior to 'A' at Portland and elsewhere (Fig. 2.3). We therefore infer that water masses were reasonably well connected until ~ -210 kyr, but the  $^{187}\text{Os}/^{188}\text{Os}$  composition of the seawater in the individual basins was strongly influenced by regional factors (Figs 2.1, 2.3). In addition, the heterogeneity of the  $^{187}\text{Os}/^{188}\text{Os}$  data may provide information on vertical mixing as a function of depth and circulation; the variations may indicate that seawater was not always well mixed.

### *5.1.1. Implications of basin connectivity*

Between  $\sim -300$  and  $-200$  kyr,  $\text{Os}_i$  values at Portland in the WIS reverse toward more radiogenic values. A similar pattern is observed at Site 1260, Vocontian Basin, Furlo and Site 530, although in each of these sites the radiogenic  $\text{Os}_i$  inflection is brief (only a single data point) before the decline in  $\text{Os}_i$  values (Fig. 2.3). There are two possible mechanisms that could contribute to produce an  $\text{Os}_i$  signal of this type within a shallow epeiric seaway: increased input of weathered material and restriction of the connection to the open ocean, which would allow a radiogenic (weathering input) signal to dominate (e.g., Portland and the Vocontian Basin). In contrast, it is assumed that deep water sites preserve a signal more consistently representative of the open ocean (e.g., Site 1260 and 530).

The shallow epeiric setting at Portland would certainly have become restricted from the global ocean during sea-level lowstands. However, the degree of sea level fall necessary to produce restriction is difficult to know. There is evidence of a small hiatus and a bone bed within the uppermost Hartland Shale, and two seaward stepping parasequences in the Dakota Formation of SW Utah correlate basinward to a level just below this hiatus (Elder et al., 1994), suggesting that a minor relative sea-level fall may have occurred (Gale et al., 2008). Subsequently, the lowermost beds of the Bridge Creek Limestone contain a diverse marine fauna with many Tethyan taxa (Kauffman, 1984), and there is strong evidence for transgression during the deposition of the basal limestone bed (Arthur and Sageman, 2005). Thus, the onset may have been immediately preceded by a relative fall in sea level that could have briefly reduced or shut down exchange of water masses with the global ocean, followed by a rapid sea-level rise.

Basin restriction may also provide an explanation for the delayed return to pre-OAE 2  $\text{Os}_i$  values in the Vocontian Basin.  $\text{Os}_i$  values return to  $\sim 0.3$  at 'B' comparable to other sections (Fig. 2.3). Yet between 'B' and 'C' the  $\text{Os}_i$  values fluctuate around  $\sim 0.4$  for an additional  $\sim 200$  kyr relative to other sites, which suggests that mixing with the rest of the proto-North Atlantic was temporarily limited.

### *5.1.2. Implications of enhanced weathering rates*

To explain the radiogenic pre-OAE 2  $\text{Os}_i$  values, a continuous radiogenic continental input into the ocean is required (Peucker-Ehrenbrink and Ravizza, 2000). Hence, the other mechanism resulting in radiogenic  $\text{Os}_i$  values is a significant increase in the flux of weathered material to a basin. Interpreted increases in temperature before 'A' indicate a period of significant warming (Clarke and Jenkyns, 1999; Forster et al., 2007; Jenkyns et al., 2004; Barclay et al., 2010), an intensification of the hydrological cycle, and more extensive flooding in continental interiors, which led to the build-up of terrestrially derived nutrients and organic-rich sediments in shallow basin water masses immediately prior to 'A'. The radiogenic  $\text{Os}_i$  prior to 'A' reflects sequestration of hydrogenous Os derived from the continent as a result of high weathering rates. If, in fact, the WIS did become briefly restricted, the influence of local weathering inputs and changes in mixing between basins would be amplified in the seawater chemistry.

Additionally, there is evidence that increased input of weathered material influenced the Os chemistry of the shallow bathyal Site 1260 and the abyssal Site 530 before 'A'. Continental turbiditic sediments deposited on the continental slope at Site 1260 produce an oscillating  $\text{Os}_i$  profile before the onset. At Site 530,

comparatively less radiogenic  $\text{Os}_i$  values prior to 'A' (Fig 2.3) suggest that juvenile turbidites were sourced from juvenile detritus from the Walvis Ridge.

The high rates of weathering produced waters enriched in micro-nutrients that led to an increase in productivity coincident with OAE 2, which is supported by bulk rock enrichments of Si, P, Ba, Cu, Mo, Ni and Zn in black shales at Demerara Rise ODP sites (Jimenez Berrocoso et al., 2008). In addition, enhanced weathering is inferred from Sr isotope trends, which despite possessing a longer residence time (1 - 4 Ma) have been interpreted to reflect global warming prior to, and during OAE 2 (Frijia and Parente, 2008).

### 5.2. *Caribbean Large Igneous Province and OAE 2*

In contrast to the elevated radiogenic  $\text{Os}_i$  values just before 'A' at Portland, the  $\text{Os}_i$  values of Site 1260, Vocontian Basin, Furlo and Site 530 show a progressive trend to unradiogenic  $\text{Os}_i$  values (0.75 to 0.55) over ~155 kyr (Fig. 2.3) suggesting that hydrothermal input dominated Os chemistry in the open oceans. Within the WIS the stratigraphic evidence for sea-level rise is coincident with an abrupt shift of radiogenic  $\text{Os}_i$  values to very unradiogenic values at Portland ~50 kyr prior to 'A'. Therefore the trend to almost homogeneous unradiogenic  $\text{Os}_i$  recorded in all sites at 'A' requires a sustained source of unradiogenic Os input to the ocean.

Basaltic igneous provinces release unradiogenic Os, close to chondritic values (~0.13; Cohen and Coe, 2002). There are two potential sources of volcanism: the Caribbean LIP and the High Arctic LIP. The eruption history from the High Arctic remains poorly constrained (Tegner et al., 2011) and trends interpreted at this stage are relatively ambiguous (Zheng et al., 2013). Consequently, the abrupt unradiogenic trend is interpreted to reflect an episode of submarine mafic volcanism

from the Caribbean LIP (Fig. 2.3), sufficient to influence the global Os isotope budget (Turgeon and Creaser, 2008).

The high-resolution of the  $\text{Os}_i$  data presented here make an important contribution to the discussion of Caribbean LIP onset and cessation. Evidence supports the hypothesis that an influx of unradiogenic Os in the marine Os record is a direct consequence of volcanism (Ravizza and Peucker-Ehrenbrink, 2003). From ~ -50 kyr all sites show a synchronous abrupt trend towards unradiogenic  $\text{Os}_i$  values (Fig. 2.3). Based on the trend to unradiogenic  $\text{Os}_i$  values at Site 1260, Vocontian Basin, Furlo and Site 530 we suggest that the initiation of volcanism was at least ~200 kyr prior to 'A' (~94.58 Ma; Fig. 2.3, CLIP i), with the major pulse of submarine volcanism happening at ~ -30 kyr (94.41 Ma; Fig. 2.3, CLIP ii), where all locations possess near mantle-like  $\text{Os}_i$  values. The timing of Caribbean LIP ii is supported by the rapid change in Os concentration (section 4.2; Table 2.2) in all sections with the exception of Wunstorf where there is no record (Fig. 2.3). The sudden and high increase in Os concentrations occurs within 1 metre of deposition, which equates to <20 kyr at Furlo and Site 530, and <10 kyr at Portland, Site 1260 and Vocontian Basin. The increase in concentration is directly synchronous with the abrupt decrease to very low seawater  $\text{Os}_i$  values and is contemporaneous with 'A' within <20 kyr.

The trend recorded in the new sections studied here is consistent with the pattern observed in the previous work by Turgeon and Creaser (2008), where there was a clear and large increase in Os concentration at the onset of OAE 2. As discussed, high weathering rates across the CTB released large amounts of organic-rich material to the oceans, which sequester hydrogenous Os (Peucker-Ehrenbrink and Ravizza, 2000). The trend therefore implies that within <20 kyr the amount of

unradiogenic dissolved Os to seawater significantly reduced the influence of radiogenic Os (Cohen and Coe, 2002, 2007; Ravizza and Peucker-Ehrenbrink, 2003). Therefore, the observed regional variations in the data support the short residence time of Os in seawater and confirm the capability of Os to detect short-term forcing mechanisms, such as activity from LIPs.

The interaction of both volcanism and enhanced global weathering on  $\text{Os}_i$  means that quantifying the magnitude and isolating the extent of the two signals is problematic, since the putative weathering influence on seawater chemistry is attenuated by the inputs from the Caribbean LIP to the global ocean. We can only estimate the Os contribution to seawater chemistry using a mixing model and assumed abundances. If we assume that the average seawater  $^{187}\text{Os}/^{188}\text{Os}$  prior to the LIP onset was  $\sim 0.8$ , and use an average Os abundance in seawater of 10 ppq (based on the present-day average; Peucker-Ehrenbrink & Ravizza, 2000), a basalt  $^{187}\text{Os}/^{188}\text{Os}$  of 0.13 (Meisel et al., 2001) and an average Os abundance, we can evaluate the approximate Os contribution from the Caribbean LIP to the global ocean using a progressive mixing model (Faure, 1986, eqs. 9.2 and 9.10). The progressive mixing model assumes the starting  $\text{Os}_i$  was 0.93 (pre-OAE 2 seawater composition) with an average seawater abundance of 10 ppq (based on present day average; Peucker-Ehrenbrink and Ravizza, 2000), mixing with mantle derived  $^{187}\text{Os}/^{188}\text{Os}$  ( $\sim 0.13$ ; Meisel et al., 2001) and Os abundance of basalts and in volcanic gases. We note that there are no published Os data for the Caribbean LIP and therefore we use typical mantle  $^{187}\text{Os}/^{188}\text{Os}$  data (Meisel et al., 2001). Basalts can have variable Os abundances (1 to 600 ppt; Martin, 1991, Crocket and Paul, 2008); typical values range from 1 to 30 ppt (e.g., Shirey and Walker, 1998; Allégre et al., 1999; Dale et al., 2008; Yudovskya et al., 2008). Using an Os abundance for a basalt of 30 ppt

would require 75% Os contribution from the LIP to yield the least radiogenic  $\text{Os}_i$  observed at all locations. Considerably less Os input from the LIP (25%) is needed if the LIP basalts possess higher Os abundances (100 ppt) and if the Os contribution to seawater also occurred through the addition of gas known to be enriched 20 times that of the basalt (e.g., Yudovskaya et al., 2008).

If we assume the emplacement and weathering of the LIP are direct indicators of volcanic activity (Cohen and Coe, 2002, 2007), we can estimate the duration of volcanism at the Caribbean LIP based on the marine  $^{187}\text{Os}/^{188}\text{Os}$  record. During the emplacement of the LIP we assume that growth of the plateau does not continue to affect the Os isotope composition (Robinson et al., 2009), since the  $\text{Os}_i$  values are homogeneous ( $\sim 0.2$ ; Fig. 2.3). The subsequent trend to radiogenic  $\text{Os}_i$  values  $\sim 200$  kyr after 'A' potentially represents the cessation of volcanism. If we consider that the predominant  $^{187}\text{Os}/^{188}\text{Os}$  of the ocean prior to the Caribbean LIP was 0.8, the influence of Os abundance and isotopic composition from the Caribbean LIP was less than 5% once the seawater  $^{187}\text{Os}/^{188}\text{Os}$  had reached  $\sim 0.50$ , which occurred  $\sim 450$  kyr after the onset (until  $\sim 94.13 \pm 0.15$  Ma; Fig. 2.3, vertical pink line).

### 5.3. *Hiatuses identified during the CTBI*

At Portland the  $\sim 17$  kyr hiatus above 'B' was previously identified by Meyers and Sageman (2004), and the hiatus just before 'A', though quantitatively unconstrained, is equally minor based on site comparison (Elder et al., 1994; Ma et al., 2014). This study has identified one hiatus in the higher part of the OAE 2 at Site 1260. At Site 1260 Erbacher et al. (2005) suggested that  $\sim 150$  kyr is missing from Site 1258, yet present at Site 1260. However, distinct lithological breaks in the core images at 425.19 m and the  $\delta^{13}\text{C}_{\text{org}}$  record indicate that the hiatus may also be present

in the latter section. A 150 kyr hiatus is inferred here from the Os isotope profile (Fig. 2.3).

#### 5.4. *Palaeocirculation across OAE 2*

A model of quasi-estuarine circulation that was proposed for the WIS, which includes surface outflows causing deeper Atlantic/Tethyan water masses to be advected into the basin (Slingerland et al. 1996), is also suggested as a means to import Caribbean LIP influenced proto-Pacific waters into the proto-Atlantic and Tethys (Trabucho-Alexandre et al., 2010). The similar shape of the  $\text{Os}_i$  profiles (from  $\sim -50$  kyr until  $\sim 200$  kyr into OAE 2) suggest that unradiogenic Os-bearing water was rapidly transported from the proto-Pacific into and across the proto-North Atlantic/Tethys, and into the WIS (Fig. 2.4). This model is consistent with the hypothesis that palaeocirculation was not sluggish, as also indicated by climate models (Trabucho-Alexandre et al., 2010) and data from Nd isotopes. The latter suggest a dynamic deep/bottom-water circulation (MacLeod et al., 2008; Martin et al., 2012); the synchronous  $\epsilon_{\text{Nd}}$  positive excursion at Eastbourne and Site 1260 is consistent with a volcanic influx that is interpreted to reflect the relationship between bottom-water sources, climate, ocean anoxia, and circulation (Martin et al., 2012; Zheng et al., 2013).

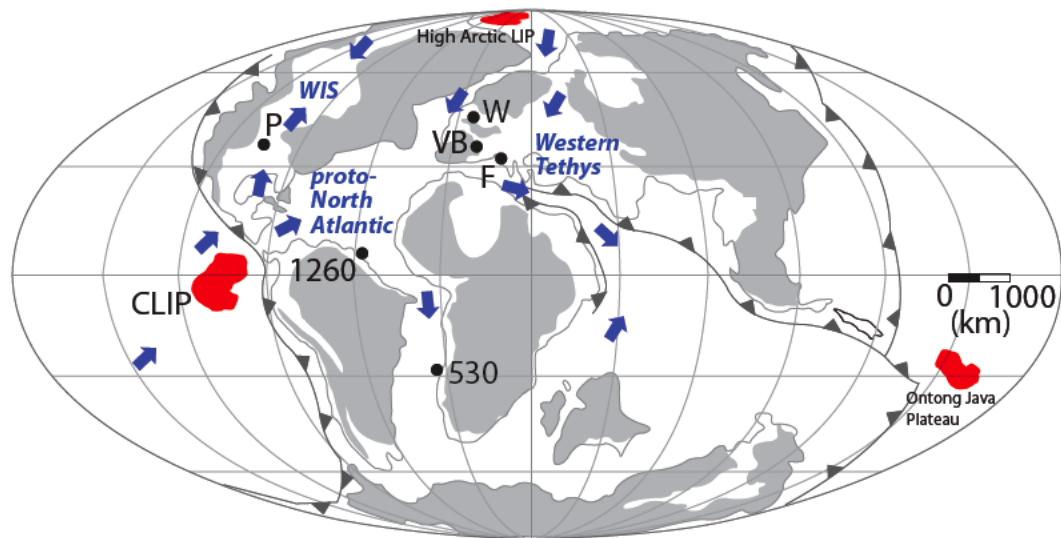


**Figure 2.4** Palaeocirculation pattern during the Cenomanian-Turonian boundary interval. Blue arrows represent the direction of palaeocirculation interpreted based on this study, Slingerland et al. (1996) and Trabucho-Alexandre et al. (2010).

## 6. Conclusions

Submarine volcanism alone cannot be the sole driving mechanism for OAEs, especially OAE 2.  $\text{Os}_i$  data from 6 transatlantic and epeiric sections demonstrate that OAE 2 resulted from a combination of interacting factors. An influx of nutrients from the continents preconditioned the oceans and helped to trigger OAE 2 through increased productivity and, similarly to Jones and Jenkyns (2001), we infer that rising sea level may have been the tipping point for the development of widespread anoxia. The  $\text{Os}_i$  profile at Portland suggests that the restriction of the epeiric WIS during the pre-OAE 2 interval amplified the effects of high weathering rates as abundant organic-rich sediments sequestered radiogenic Os derived from the ancient continental crust. The close similarity of  $\text{Os}_i$  profiles from ~50 kyr prior to the OAE 2 and throughout the syn-OAE 2 interval indicates that transgression progressed to a point where a homogeneous global seawater signal was delivered to multiple proto-transatlantic basins by active ocean circulation. Furthermore, the synchronicity of the unradiogenic  $\text{Os}_i$  pattern suggests that the magnitude of Caribbean LIP volcanism

was sufficient to simultaneously influence the seawater chemistry of each basin; the abundance of organic-rich sediments added to the water column as a result of enhanced continental weathering permitted sequestration of hydrogenous unradiogenic Os from the contemporaneous Caribbean LIP. The temporal coincidence provides empirical evidence for the duration of the Caribbean LIP of ~450 kyr.

## REFERENCES

- Allegre, C. J., Birck, J. L., Capmas, F., Courtillot, V., 1999. Age of the Deccan traps using  $^{187}\text{Re} - ^{187}\text{Os}$  systematic. *Earth Planet. Sci. Lett.* 170, 197-204.
- Arthur, M. A., Sageman, B.B., 1994. Marine black shales: Depositional mechanisms and environments of ancient deposits. *Annu. Rev. Earth Planet. Sci. Lett.* 22, 499-551.
- Arthur, M. A., Schlanger, S. O., Jenkyns, H. C., 1987. The Cenomanian/Turonian Oceanic Anoxic Event, II: Palaeoceanographic controls on organic matter production and preservation, in *Marine Petroleum Source Rocks*, edited by J. Brooks and A. J. Fleet, *Geol. Soc. London Spec. Publ.* 26, 401-420.
- Arthur, M.A., Premoli Silva, I., 1982. Development of widespread organic carbon-rich strata in the Mediterranean Tethys, in *Nature and Origin of Cretaceous Carbon-Rich Facies*, edited by S. O. Schlanger and M. B. Cita, pp. 7 -54, Academic, London.
- Arthur, M.A., Sageman, B.B., 2005. Sea level control on source rock development: Perspectives from the Holocene Black Sea, the mid-Cretaceous Western Interior Basin of North America, and the Late Devonian Appalachian Basin, In Harris, N.B. (ed.), *The Deposition of Organic Carbon-rich Sediments: Models, Mechanisms and Consequences*, *SEPM Spec. Publ.* 82, 35-59.
- Barclay, R. S., McElwain, J. C., Sageman, B. B., 2010. Carbon sequestration activated by a volcanic  $\text{CO}_2$  pulse during Oceanic Anoxic Event 2. *Nature Geoscience* 3, DOI: 10.1038/NGEO757.
- Blättler, C. L., Jenkyns, H. C., Reynard, L. M., Henderson, G. M., 2011. Significant increases in global weathering during Oceanic Anoxic Events 1a and 2 indicated by calcium isotopes. *Earth Planet. Sci. Lett.* 309, 77-88.
- Clarke, L. J., Jenkyns, H. C., 1999. New oxygen isotope evidence for long-term Cretaceous climatic change in the Southern Hemisphere. *Geology* 27, 8; 699-702.

- Cobban, W., Walaszczyk, I., Obradovich, J.D., McKinney, K.C., 2006. A USGS zonal table for the Upper Cretaceous Middle Cenomanian - Maastrichtian of the Western Interior of the United States based on ammonites, inoceramids, and radiometric ages. USGS Open-File Report 2006–1250.
- Cobban, W.A., Scott, G. R., 1972. Stratigraphy and ammonite fauna of the Graneros Shale and Greenhorn Limestone near Pueblo, Colorado. U.S. Govt. Print. Off. (Washington), 101-368-424.
- Cohen, A. S., 2004. The rhenium-osmium isotope system: Applications to geochronological and palaeoenvironmental problems. *J. Geol. Soc. London* 161, 729-734.
- Cohen, A., Coe, A., 2002. New geochemical evidence for the onset of volcanism in the Central Atlantic magmatic province and the environmental change at the Triassic–Jurassic boundary. *Geology* 30, 267–270.
- Cohen, A., Coe, A., 2007. The impact of the Central Atlantic Magmatic Province on climate and on the Sr- and Os-isotope evolution of seawater. *Palaeogeog. Palaeoclimatol. Paleoecol.* 244, 374–390.
- Craig, H. 1957. Isotopic standards for carbon and oxygen and correction factors for mass-spectrometric analysis of carbon dioxide. *Geochim. Cosmochim. Acta* 12, 133-149.
- Creaser, R.A., Papanastassiou, D.A., Wasserburg, G.J., 1991. Negative thermal ion mass spectrometry of osmium, rhenium and iridium. *Geochim. Cosmochim. Acta* 55, 397-401.
- Crocket, J. H., Paul, D. K., 2008. Platinum-group elements in igneous rocks of the Kutch rift basin, NW India: implications for relationships with the Deccan volcanic province. *Chem. Geol.* 248, 239-255.
- Dale, C. W., Luguet, A., Macpherson, C. G., Pearson, D.G., Hickey-Vargas, R., 2008. Extreme platinum-group element fractionation and variable Os isotope compositions in Philippine Sea Plate basalts: Tracing mantle source heterogeneity. *Chem. Geol.* 248, 213-238.
- Dean, W.E., Arthur, M.A., 1998. Geochemical expression of cyclicity in Cretaceous pelagic limestone sequences: Niobrara Formation, Western Interior Seaway in: Dean, W.E., and Arthur, M.A., eds., *Stratigraphy and Paleoenvironments of the Cretaceous Western Interior Seaway, U.S.A.* SEPM, Concepts Sedimentology, Paleontology 6, 227- 255.
- Eicher, D.L., Worstell, P., 1970. Cenomanian and Turonian foraminifera from the Great Plains, United States. *Micropaleontology* 16, 269-324.
- Elder, W. P., 1988. Geometry of Upper Cretaceous bentonite beds: implications about volcanic source areas and paleowind patterns, western interior, United States. *Geology* 16, 835-838.

- Elder, W.P., Gustason, E.R., Sageman, B.B., 1994. Correlation of basinal carbonate cycles to nearshore parasequences in the Late Cretaceous Greenhorn Seaway, Western Interior, U.S. *Geol. Soc. Am. Bull.* 106, 892-902.
- Erbacher, J., Friedrich, O., Wilson, P. A., Birch, H., Mutterlose, J., 2005. Stable organic carbon isotope stratigraphy across Oceanic Anoxic Event 2 of Demerara Rise, western tropical Atlantic. *Geochem. Geophys. Geosyst.* 6, Q06010, doi:10.1029/2004GC000850.
- Ernst, G., Wood, C. J., Hilbrecht, H., 1984. The Cenomanian-Turonian boundary problem in NW-Germany with comments on the north-south correlation to the Regensburg area. *Bull. Geol. Soc. Denmark* 33, 103–113.
- Faure, G., 1986. *Principles of Isotope Geology*. Second edition. John Wiley & Sons, Inc., ISBN 0-471-86412-9.
- Forster, A., Kuypers, M. M. M., Turgeon, S. C., Brumsack, H-J., Petrizzo, M. R., Sinninghe Damste, J. S., 2008. The Cenomanian/Turonian oceanic anoxic event in the South Atlantic: New insights from a geochemical study of DSDP 530A. *Palaeogeog. Palaeoclimatol. Palaeoecol.* 267, 256 – 283.
- Forster, A., Schouten, S., Moriya, K., Wilson, P.A., Sinninghe Damsté, J.S., 2007. Tropical warming and intermittent cooling during the Cenomanian/Turonian oceanic anoxic event 2: Sea surface temperature records from the equatorial Atlantic. *Paleoceanography* 22, PA1219. doi:10.1029/2006PA001349.
- Frijia, G., Parente, M., 2008. Strontium isotope stratigraphy in the upper Cenomanian shallow-water carbonates of the southern Apennines: Short-term perturbations of marine  $^{87}\text{Sr}/^{86}\text{Sr}$  during the oceanic anoxic event 2. *Palaeogeog. Palaeoclimatol. Palaeoecol.* 261, 15-29.
- Gale, A. S., Jenkyns, H. C., Kennedy, W. J., Corfield, R. M., 1993. Chemostratigraphy versus biostratigraphy: Data from around the Cenomanian-Turonian boundary. *J. Geol. Soc.* 150, 29–32.
- Gale, A. S., Voigt, S., Sageman, B. B., Kennedy, W. J. 2008. Eustatic sea-level record for the Cenomanian (Late Cretaceous) – Extension to the Western Interior Basin, USA. *Geology* 36, 859-862.
- Gale, A.S., Kennedy, W.J., Voigt, S., Walaszczyk, I., 2005. Stratigraphy of the Upper Cenomanian-Lower Turonian Chalk succession at Eastbourne, Sussex, UK: ammonites, inoceramid bivalves and stable carbon isotopes. *Cretaceous Research* 26, 460 – 487.
- Gradstein, F.M., Ogg, J.G., Schmitz, M., eds., 2012. *The Geologic Time Scale 2012*, 2-volume set. Elsevier.

- Gramlich, J.W., Murphy, T.J., Garner, E.L., Shields, W.R., 1973. Absolute isotopic abundance ratio and atomic weight of a reference sample of rhenium. *J. Res. Natl. Bur. Stand.* 77A, 691–698.
- Grosheny, D., Beaudoin, B., Morel, L., Desmares, D., 2006. High-resolution biostratigraphy and chemostratigraphy of the Cenomanian/Turonian boundary event in the Vocontian Basin, southeast France. *Cretaceous Research* 27, 629-640.
- Hattin, D. E., 1971. Widespread, synchronously deposited, burrow-mottled limestone beds in Greenhorn Limestone (Upper Cretaceous) of Kansas and central Colorado. *Am. Assoc. Petroleum Geologists Bull.* 55, 412-431.
- Jarvis, I., Lignum, J. S., Grocke, D. R., Jenkyns, H. C., Pearce, M. A., 2011. Black shale deposition, atmospheric  $\text{CO}_2$  drawdown, and cooling during the Cenomanian-Turonian Oceanic Anoxic Event. *Paleoceanography* 26, PA3201, doi:10.1029/2010PA002081.
- Jenkyns, H. C., Matthews, A., Tsikos, H., Erel, Y., 2007. Nitrate reduction, sulfate reduction, and sedimentary iron isotope evolution during the Cenomanian-Turonian oceanic anoxic event. *Paleoceanography* 22, PA3208, doi:10.1029/2006PA001355.
- Jenkyns, H.C., 1980. Cretaceous anoxic events: from continents to oceans. *J. Geol. Soc. London* 137, 171–188.
- Jenkyns, H.C., Forster, A., Schouten, S., Sinninghe Damste, J.S., 2004. High temperatures in the Late Cretaceous Arctic Ocean. *Nature* 432, 888 -892.
- Jimenez Berrosoco, A., MacLeod, K. G., Calvert, S. E., Elorza, J., 2008. Bottom water anoxia, inoceramid colonization, and benthopelagic coupling during black shale deposition on Demerara Rise. *Paleoceanography* 23, PA3212, doi:10.1029/2007PA001545.
- Jones, C. E., Jenkyns, H. C., 2001. Seawater strontium isotopes, oceanic anoxic events, and seafloor hydrothermal activity in the Jurassic and Cretaceous. *Am. J. Sci.* 301, 112 – 149.
- Kane, J.S., Arbogast, B.F., and Leventhal, J.S., 1990. Characterization of Devonian Ohio Shale SDO-1 as a USGS geochemical reference sample: *Geostandards Newsletter* 14, 169-196.
- Kauffman, E.G., 1984. Paleobiogeography and evolutionary response dynamic in the Cretaceous Western Interior Seaway of North America, in *Jurassic-Cretaceous Biochronology and Paleogeography of North America*, G. E. G. Westermann, ed., *Geol. Assoc. Canada Spec. Paper* 27, 273 – 306.
- Keller, G., Berner, Z., Adatte, T., Stueben, D., 2004. Cenomanian–Turonian and  $\delta^{13}\text{C}$ , and  $\delta^{18}\text{O}$ , sea level and salinity variations at Pueblo, Colorado. *Palaeogeog. Palaeoclimatol. Palaeoecol.* 211, 19–43.

- Keller, G., Pardo, A., 2004. Age and paleoenvironment of the Cenomanian/Turonian global stratotype section and point at Pueblo, Colorado. *Mar. Micropaleontol.* 51, 95–128.
- Kendall, B., Creaser, R. A., and Selby, D., 2009,  $^{187}\text{Re}$ - $^{187}\text{Os}$  geochronology of Precambrian organic-rich sedimentary rocks. *Geol. Soc. London Spec. Pub.* 326, 85-107.
- Kennedy, W.J., Walaszczyk, I., Cobban, W.A., 2005. The Global Boundary Stratotype Section and Point for the base of the Turonian Stage of the Cretaceous: Pueblo, Colorado, USA. *Episodes* 28, 93–104.
- Kennedy, W.J., Walaszczyk, I., Cobban, W.A., 2000, Pueblo, Colorado, USA, candidate Global Boundary Stratotype Section and Point for the base of the Turonian Stage of the Cretaceous and for the base of the middle Turonian Substage, with a revision of the Inoceramidae (Bivalvia). *Acta Geologica Polonica* 50, 295–334.
- Lehmann, J., 1999. Integrated stratigraphy and palaeoenvironment of the Cenomanian-Lower Turonian (Upper Cretaceous) of Northern Westphalia, North Germany. *Facies* 40, 25–70.
- Ma, Chao, Meyers, S.R., Sageman, B.B., Singer, B.S., Jicha, B.R., 2014. Testing the astronomical time scale for Oceanic Anoxic Event 2, and its extension into Cenomanian strata of the Western Interior Basin. *Geol. Soc. Am. Bull.* doi: 10.1130/B30922.1
- MacLeod, K. G., Marin, E. E., Blair, S. W., 2008. Nd excursions across the Cretaceous oceanic anoxia event 2 (Cenomanian-Turonian) in the tropical North Atlantic. *Geology* 36, 811-814.
- Martin, C. E., 1991. Osmium isotopic characteristics of mantle-derived rocks. *Geochim. Cosmochim. Acta* 55, 1421 – 1434.
- Martin, E. E., MacLeod, K. G., Jimenez Berroco, A., Bourbon, E., 2012. Water mass circulation on Demerara Rise during the Late Cretaceous based on Nd isotopes. *Earth Planet. Sci. Lett.* 327-328, 111-120.
- McArthur, J.M., Howarth, R.J., Bailey, T., 2004. Strontium isotope stratigraphy. In: Gradstein, F., Ogg, J., Smith, A., (Eds.) *A Geological Time Scale 2004*. Cambridge University Press, Cambridge, U.K., pp. 96–105.
- Meisel, T., Walker, R. J., Irving, A. J., Lorand, J., 2001. Osmium isotopic compositions of mantle xenoliths: A global perspective. *Geochim. Cosmochim. Acta* 65, 1311-1323.
- Meyers, S.R, Sageman, B.B., Arthur, M.A., 2012b. Obliquity forcing and the amplification of high-latitude climate processes during Oceanic Anoxic Event 2. *Paleoceanography* 27, PA3212, doi:10.1029/2012PA002286.
- Meyers, S.R., Sageman, B.B., 2004. Detection, quantification, and significance of hiatuses in pelagic and hemipelagic strata. *Earth Planet. Sci. Lett.* 224, 55 – 72.

- Meyers, S.R., Sageman, B.B., Hinnov, L.A., 2001. Integrated quantitative stratigraphy of the Cenomanian-Turonian Bridge Creek Limestone member using Evolutive Harmonic Analysis and stratigraphic modelling. *J. Sed. Res.* 71, 628-644.
- Meyers, S.R., Siewert, S.E., Singer, B.S., Sageman, B.B., Condon, D.J., Obradovich, J.D., Jicha, B.R., Sawyer, D.A., 2012a. Intercalibration of radioisotopic and astrochronologic time scales for the Cenomanian-Turonian boundary interval, Western Interior Basin, USA. *Geology* 40, 7-10.
- Montoya-Pino, C., Weyer, S., Anbar, A.D., Pross, J., Oschmann, W., van de Schootbrugge, B., Arz, H.W., 2010. Global enhancement of ocean anoxia during Oceanic Anoxic Event 2: A quantitative approach using U isotopes. *Geology*, 38, 315-318.
- Mort, H., Jacquat, O., Adatte, T., Steinmann, P., Follmi, K., Matera, V., Berner, Z., Stuben, D., 2007. The Cenomanian/Turonian anoxic event at the Bonarelli Level in Italy and Spain: enhanced productivity and/or better preservation? *Cretaceous Research* 28, 597 - 612.
- Nier, A. O., 1937. The isotopic constitution of osmium. *Physics Reviews* 52, 885.
- Nowell, G. M., Luguët, A., Pearson, D. G., Horstwood, M. S. A., 2008. Precise and accurate  $^{186}\text{Os}/^{188}\text{Os}$  and  $^{187}\text{Os}/^{188}\text{Os}$  measurements by multi-collector plasma ionisation mass spectrometry (MC-ICP-MS) part I: Solution analyses. *Chem. Geol.* 248, 363-393.
- Oxburgh, R., 2001, Residence time of osmium in the oceans. *Geochem. Geophys. Geosyst.* 2, 2000GC000104.
- Paquay, F. S., Ravizza, G., 2012. Heterogeneous seawater  $^{187}\text{Os}/^{188}\text{Os}$  during the Late Pleistocene glaciations. *Earth Planet. Sci. Lett.* 349 – 350, 126 – 138.
- Peucker-Ehrenbrink, B. and Ravizza, G. 2000. The marine osmium isotope record. *Terra Nova* 12, 205-219.
- Pogge von Strandmann, P.A.E., Jenkyns, H.C., Woodfine, R.G., 2013. Lithium isotope evidence for enhanced weathering during Oceanic Anoxic Event 2. *Nature Geoscience*, doi:10.1083/NGE01875
- Pratt, L.M., Kauffman, E.G., Zelt, F.B., 1985. Fine-grained deposits and biofacies of the Cretaceous Western Interior Seaway: evidence for cyclic sedimentary processes. *Soc. Econ. Paleont. Miner. Field Trip Guidebook* 4, 1985 Midyear Meeting, Golden, Colorado.
- Ravizza, G., Peucker-Ehrenbrink, B., 2003. Chemostratigraphic evidence of Deccan volcanism from the marine osmium isotope record. *Science* 302, 1392–1395.
- Robinson, N., Ravizza, G., Coccioni, R., Peucker-Ehrenbrink, B, Norris, R., 2009. A high-resolution marine  $^{187}\text{Os}/^{188}\text{Os}$  record for the late Maastrichtian: Distinguishing the chemical fingerprints of Deccan volcanism and the KP impact event. *Earth Planet Sci. Lett.* 281, 159–168.

- Sageman, B.B., Meyers, S.R., Arthur, M.A., 2006. Orbital time scale and new C-isotope record for Cenomanian–Turonian boundary stratotype. *Geology* 34, 125–128.
- Schlanger, S.O., Arthur, M.A., Jenkyns, H.C., Scholle, P.A. 1987. The Cenomanian/Turonian Oceanic Anoxic Event, I. Stratigraphy and distribution of organic carbon-rich beds and the marine  $\delta^{13}\text{C}$  excursion. In: Brooks, J. & Fleet, A.J. (eds) *Marine Petroleum Source Rocks*. Geol. Soc. London, Spec. Publ. 26, 371–399.
- Selby, D., Creaser, R.A., 2003. Re–Os geochronology of organic rich sediments: an evaluation of organic matter analysis methods. *Chem. Geol.* 200, 225–240.
- Selby, D., Mutterlose, J., Condon, D.J., 2009. U–Pb and Re–Os geochronology of the Aptian/Albian and Cenomanian/Turonian stage boundaries: Implications for timescale calibration, osmium isotope seawater composition and Re–Os systematics in organic-rich sediments. *Chem. Geol.* 265, 394 – 409.
- Shirey, S.B., Walker, R.J., 1998. The Re–Os isotope system in cosmochemistry and high-temperature geochemistry. *Annual Review Earth Planet. Sci. Lett.* 26, 423–500.
- Slingerland, R., Kump, L. R., Arthur, M. A., Fawcett, P. J., Sageman, B. B., Barron, E. J., 1996. Estuarine circulation in the Turonian Western Interior seaway of North America. *Geol. Soc. Am. Bull.* 108, 941–952.
- Smoliar, M.I., Walker, R.J., Morgan, J.W., 1996. Re–Os ages of group IIA, IIIA, IVA, and IVB iron meteorites. *Science* 23, 1099 – 1102.
- Snow, L. J., Duncan, R. A., Bralower, T. J., 2005. Trace element abundances in the Rock Canyon Anticline, Pueblo, Colorado, marine sedimentary section and their relationship to Caribbean plateau construction and oxygen anoxic event 2. *Paleoceanography* 20, PA3005, doi:10.1029/2004PA001093.
- Takashima, R., Nishi, H., Hayashi, K., Okada, H., Kawahata, H., Yamanaka, T., Fernando, A. G., Mampuku, M., 2009. Litho-, bio- and chemostratigraphy across the Cenomanian/Turonian boundary (OAE 2) in the Vocontian Basin of southeast France. *Palaeogeog. Palaeoclimatol. Palaeoecol.* 273, 61–74.
- Tegner, C., Storey, M., Holm, P.M., Thorarinsson, S.B., Zhao, X., Lo, C.-H., Knudsen, M.F., 2011. Magmatism and Eureka deformation in the High Arctic Large Igneous Province:  $^{40}\text{Ar} - ^{39}\text{Ar}$  age of Kap Washington Group volcanics, North Greenland. *Earth Planet. Sci. Lett.* 303, 203–214.
- Trabucho-Alexandre, J., Tuenter, E., Henstra, G.A., van der Zwan, K.J., van de Wal, R.S.W., Dijkstra, H.A., de Boer, P.L., 2010. The mid-Cretaceous North Atlantic nutrient trap: Black shales and OAEs. *Paleoceanography* 25, PA4201, doi:10.1029/2010PA001925.
- Tsikos, H., Jenkyns, H.C., Walsworth-Bell, B., Petrizzo, M.R., Forster, A., Kolonic, S., Erba, E., Premoli-Silva, I.P., Baas, M., Wagner, T., Sinninghe Damsté, J.S., 2004. Carbon-isotope stratigraphy recorded by the Cenomanian - Turonian Oceanic Anoxic

- Event: correlation and implications based on three key localities. *J. Geol. Soc. London* 161, 711-719.
- Turgeon, S.C., Creaser, R.A., 2008. Cretaceous anoxic event 2 triggered by a massive magmatic episode. *Nature* 454, 323–326.
- Voigt, S., Aurag, A., Leis, F., Kaplan, U., 2007. Late Cenomanian to Middle Turonian high-resolution carbon isotope stratigraphy: New data from the Munsterland Cretaceous Basin, Germany. *Earth Planet. Sci. Lett.* 253, 196–210.
- Voigt, S., Erbacher, J., Mutterlose, J., Weiss, W., Westerhold, T., Wiese, F., Wilmsen, M., Wonik, T., 2008. The Cenomanian-Turonian of the Wunstorf section (North Germany): global stratigraphic reference section and new orbital time scale for Oceanic Anoxic Event 2. *Newsl. Stratigr.* 43, 65-89.
- Volkening, J., T. Walczyk, et al., 1991. Osmium isotope ratio determinations by negative thermal ion mass spectrometry. *International Journal of Mass Spectrometry Ion Processes* 105, 147-159.
- Wilmsen, M., 2003. Sequence stratigraphy and palaeoceanography of the Cenomanian stage in northern Germany. *Cretaceous Research* 24, 525–568.
- Yudovskaya, M. A., Tessalina, S. G., Distler, V.V., Chaplygin, I.V., Chugaev, A.V., Dikov, Y.P. 2008. Behaviour of highly-siderophile elements during magma degassing: A case study at the Kudryavy volcano. *Chem. Geol.* 248, 318-341.
- Zheng X-Y., Jenkyns, H.C., Gale, A.S., Ward, D.J., Henderson, G.M., 2013. Changing ocean circulation and hydrothermal inputs during Oceanic Anoxic Event 2 (Cenomanian-Turonian): Evidence from Nd-isotopes in the European shelf sea. *Earth Planet. Sci. Lett.* <http://dx.doi.org/10.1016/j.epsl.2013.05.053i>

## Data Tables

Table 2.1a

 $\delta^{13}\text{C}_{\text{org}}$  data for Portland #1 Core, Colorado, USA (Sageman et al., 2006)

Depth (m)	$\delta^{13}\text{C}_{\text{org}}$ [‰]*						
11.58	-27.70	7.48	-24.29	3.93	-23.41	0.06	-27.31
11.50	-27.26	7.33	-25.80	3.88	-23.63	0.00	-26.93
11.45	-25.75	7.23	-25.68	3.83	-23.02	-3.18	-26.49
11.40	-26.57	6.95	-25.75	3.78	-22.65	-3.79	-26.25
11.35	-25.23	6.91	-25.78	3.73	-23.20	-3.82	-26.52
11.30	-24.48	6.82	-25.82	3.67	-23.03	-4.25	-26.50
11.25	-25.44	6.67	-25.64	3.58	-24.64	-4.80	-26.80
11.19	-27.70	6.39	-25.86	3.48	-23.39	-5.16	-26.34
11.14	-28.18	6.30	-24.27	3.43	-23.44	-5.36	-26.77
11.04	-28.05	6.20	-26.32	3.38	-23.21	-5.59	-27.17
10.38	-27.54	6.00	-26.31	3.29	-24.29	-7.09	-27.38
10.33	-26.76	5.95	-25.45	3.05	-24.12	-7.26	-27.32
10.03	-27.51	5.90	-25.49	3.00	-22.83	-8.53	-27.04
9.98	-26.84	5.85	-25.68	2.95	-22.14	-9.65	-27.28
9.82	-27.47	5.44	-23.97	2.89	-25.10	-10.43	-27.11
9.77	-25.79	5.34	-24.70	2.85	-23.28	-11.65	-27.35
9.46	-27.00	5.29	-24.61	2.49	-24.43		
9.21	-25.74	5.24	-23.99	2.39	-25.32		
8.91	-25.92	5.19	-26.04	2.09	-25.38		
8.86	-26.89	4.89	-25.01	2.04	-24.24		
8.81	-26.11	4.84	-24.16	1.96	-23.44		
8.75	-26.93	4.79	-24.77	1.72	-25.40		
8.70	-27.39	4.74	-23.96	1.67	-23.39		
8.60	-26.64	4.69	-23.98	1.62	-23.76		
8.55	-27.68	4.64	-24.22	1.09	-25.13		
8.50	-25.99	4.60	-24.67	1.04	-22.97		
8.45	-25.96	4.56	-24.31	0.99	-25.41		
8.19	-26.09	4.40	-22.93	0.95	-25.95		
8.14	-26.71	4.35	-23.73	0.36	-24.66		
8.04	-26.14	4.30	-24.58	0.31	-24.49		
8.00	-27.14	4.27	-23.28	0.26	-25.03		
7.96	-25.98	4.22	-24.21	0.21	-26.39		
7.54	-26.10	3.97	-24.00	0.11	-26.34		

\* values reported permil (‰) relative to the VPDB standard

Table 2.1b

<sup>δ<sup>13</sup>C<sub>org</sub></sup> data for Wunstorf, NW Germany (this study)

Sample ID	Depth (m)	<sup>δ<sup>13</sup>C<sub>org</sub></sup> [‰]*	Sample ID	Depth (m)	<sup>δ<sup>13</sup>C<sub>org</sub></sup> [‰]*	Sample ID	Depth (m)	<sup>δ<sup>13</sup>C<sub>org</sub></sup> [‰]*	Sample ID	Depth (m)	<sup>δ<sup>13</sup>C<sub>org</sub></sup> [‰]*
WK_23.4	23.08	-23.95	WK_32.3	31.99	-25.12	WK_36.1	35.78	-24.88	WK_40.8	40.50	-24.93
WK_26.3	26.00	-24.38	WK_32.5	32.19	-24.51	WK_36.2	35.88	-24.90	WK_41	40.70	-23.11
WK_26.4	26.10	-25.58	WK_32.6	32.29	-24.96	WK_36.3	35.98	-25.29	WK_41.2	40.90	-24.08
WK_26.5	26.20	-25.05	WK_32.7	32.39	-24.90	WK_36.4	36.08	-25.11	WK_41.4	41.10	-25.31
WK_26.7	26.40	-24.74	WK_32.8	32.49	-24.77	WK_36.5	36.18	-25.39	WK_41.6	41.30	-24.35
WK_26.9	26.60	-25.56	WK_32.9	32.59	-24.86	WK_36.6	36.28	-25.11	WK_41.8	41.50	-23.40
WK_27.1	26.80	-24.90	WK_33.1	32.78	-24.90	WK_36.7	36.38	-24.84	WK_41.9	41.60	-23.30
WK_27.2	26.90	-25.07	WK_33.2	32.88	-24.92	WK_36.8	36.48	-24.41	WK_42.1	41.79	-23.71
WK_27.3	27.00	-24.32	WK_33.3	32.98	-24.92	WK_36.9	36.58	-24.63	WK_42.2	41.89	-24.81
WK_27.6	27.30	-25.89	WK_33.4	33.08	-24.82	WK_37	36.68	-24.40	WK_42.3	41.99	-24.60
WK_27.8	27.50	-25.43	WK_33.5	33.18	-24.75	WK_37.1	36.78	-24.22	WK_42.4	42.09	-24.69
WK_28	27.70	-25.26	WK_33.6	33.28	-24.85	WK_37.2	36.88	-24.41	WK_42.5	42.19	-24.57
WK_28.2	27.90	-24.98	WK_33.7	33.38	-25.19	WK_37.3	36.98	-24.20	WK_42.6	42.29	-24.28
WK_28.4	28.10	-25.51	WK_33.9	33.58	-24.69	WK_37.4	37.08	-24.58	WK_42.7	42.39	-24.30
WK_28.6	28.30	-25.10	WK_34	33.69	-25.07	WK_37.5	37.18	-24.08	WK_42.8	42.49	-24.19
WK_28.8	28.50	-24.97	WK_34.1	33.79	-24.87	WK_37.6	37.28	-23.86	WK_42.9	42.59	-23.76
WK_29	28.70	-25.16	WK_34.2	33.89	-24.64	WK_37.7	37.38	-24.82	WK_43	42.71	-23.47
WK_29.2	28.90	-25.28	WK_34.3	33.99	-24.70	WK_37.9	37.58	-24.85	WK_43.1	42.81	-24.00
WK_29.4	29.10	-24.89	WK_34.4	34.09	-25.45	WK_38.1	37.77	-24.06	WK_43.2	42.91	-23.71
WK_29.5	29.20	-25.18	WK_34.6	34.29	-25.00	WK_38.2	37.87	-24.50	WK_43.3	43.01	-23.45
WK_29.7	29.40	-25.45	WK_34.8	34.49	-24.60	WK_38.3	37.97	-23.59	WK_43.4	43.11	-23.36
WK_30	29.70	-24.62	WK_34.9	34.59	-24.98	WK_38.5	38.17	-25.14	WK_43.5	43.21	-23.80
WK_30.1	29.80	-25.45	WK_35	34.70	-24.92	WK_38.7	38.37	-24.56	WK_43.6	43.31	-23.38
WK_30.2	29.90	-24.81	WK_35.1	34.80	-24.80	WK_39	38.69	-25.96	WK_43.7	43.41	-23.30
WK_30.4	30.10	-25.24	WK_35.2	34.90	-24.99	WK_39.3	38.99	-24.81	WK_43.8	43.51	-23.76
WK_30.7	30.30	-24.61	WK_35.3	35.00	-25.04	WK_39.5	39.19	-24.85	WK_43.9	43.61	-23.98
WK_30.8	30.50	-24.65	WK_35.4	35.10	-24.87	WK_39.7	39.39	-24.00	WK_44.1	43.80	-23.21
WK_31.1	30.80	-25.39	WK_35.5	35.20	-25.11	WK_39.8	39.49	-23.76	WK_44.2	43.90	-24.27
WK_31.3	31.00	-25.33	WK_35.6	35.30	-25.15	WK_39.9	39.59	-23.62	WK_44.3	44.00	-23.53
WK_31.5	31.20	-24.96	WK_35.7	35.40	-25.08	WK_40.2	39.90	-25.55	WK_44.4	44.10	-23.44
WK_31.7	31.40	-24.67	WK_35.8	35.50	-25.12	WK_40.3	40.00	-23.40	WK_44.6	44.30	-24.57
WK_31.9	31.60	-24.58	WK_35.9	35.60	-24.97	WK_40.4	40.10	-22.85	WK_44.8	44.50	-24.87
WK_32.1	31.79	-25.36	WK_36	35.68	-24.91	WK_40.5	40.20	-23.73	WK_45.1	44.79	-24.41

\* values reported permil (‰) relative to the VPDB standard; 'WK' samples analysed by Voigt at Hanover; 'AD' samples analysed by Grocke at Durham

Table 2.1b

<sup>δ<sup>13</sup>C<sub>org</sub></sup> data for Wunstorf, NW Germany (this study)

Sample ID	Depth (m)	<sup>δ<sup>13</sup>C<sub>org</sub></sup> [‰]*	Sample ID	Depth (m)	<sup>δ<sup>13</sup>C<sub>org</sub></sup> [‰]*	Sample ID	Depth (m)	<sup>δ<sup>13</sup>C<sub>org</sub></sup> [‰]*
WK_45.3	44.99	-24.16	AD43-09	27.51	-26.64	AD11-09	47.66	-26.08
WK_45.5	45.19	-24.02	AD42-09	28.46	-25.18	AD10-09	47.77	-26.54
WK_45.7	45.39	-23.24	AD46-09	28.57	-25.47	AD09-09	47.99	-26.18
WK_45.9	45.59	-23.92	AD41-09	29.10	-25.32	AD08-09	48.17	-26.02
WK_46.3	45.99	-23.88	AD40-09	29.76	-25.23	AD07-09	48.53	-26.16
WK_46.6	46.29	-23.83	AD39-09	30.45	-25.82	AD06-09	48.88	-26.25
WK_46.8	46.49	-24.07	AD38-09	32.44	-25.19	AD05-09	49.20	-26.73
WK_47.0	46.69	-24.14	AD37-09	32.73	-25.47	AD04-09	49.93	-26.29
WK_47.2	46.89	-23.55	AD36-09	33.33	-24.65	AD02-09	51.10	-26.79
WK_47.5	47.19	-23.41	AD35-09	33.94	-24.98	AD118-09	54.82	-26.08
WK_47.7	47.39	-24.91	AD34-09	34.54	-25.37	AD03-09	55.72	-27.11
WK_47.8	47.49	-25.26	AD33-09	34.85	-25.46	AD119-09	57.61	-26.56
WK_47.9	47.59	-25.74	AD32-09	35.22	-25.42	AD120-09	59.50	-26.55
WK_48	47.67	-25.50	AD31-09	35.73	-25.40	AD121-09	61.89	-26.28
WK_48.1	47.77	-25.73	AD30-09	36.21	-23.97	AD122-09	62.27	-26.45
WK_48.2	47.87	-25.80	AD29-09	36.68	-25.12	AD01-09	65.00	-26.01
WK_48.3	47.97	-25.66	AD28-09	37.31	-24.62			
WK_48.4	48.07	-25.20	AD27-09	38.01	-24.29			
WK_48.5	48.17	-25.56	AD26-09	39.53	-23.75			
WK_48.7	48.37	-25.50	AD25-09	40.17	-23.02			
WK_48.8	48.47	-24.90	AD24-09	40.80	-22.92			
WK_48.9	48.57	-25.40	AD23-09	41.74	-24.46			
WK_49.1	48.78	-25.01	AD22-09	42.21	-24.56			
WK_49.3	48.98	-25.40	AD21-09	42.86	-24.03			
WK_49.5	49.18	-25.00	AD20-09	43.15	-24.16			
WK_49.7	49.38	-25.45	AD19-09	43.49	-23.43			
WK_49.9	49.58	-24.45	AD18-09	43.89	-24.28			
			AD17-09	44.09	-23.37			
			AD16-09	44.69	-24.08			
			AD15-09	45.66	-25.19			
			AD14-09	45.81	-26.56			
			AD13-09	47.30	-26.57			
			AD12-09	47.39	-24.79			

\* values reported permil (‰) relative to the VPDB standard; 'WK' samples analysed by Voigt at Hanover; 'AD' samples analysed by Grocke at Durham

**Table 2.1c** $\delta^{13}\text{C}_{\text{org}}$  data for ODP Site 1260, Hole 1260B, Demerara Rise (Forster et al., 2007)

Depth (mcd) <sup>^</sup>	$\delta^{13}\text{C}_{\text{org}}$ [‰] <sup>*</sup>	Depth (mcd) <sup>^</sup>	$\delta^{13}\text{C}_{\text{org}}$ [‰] <sup>*</sup>
422.24	-27.51	426.41	-28.38
422.54	-27.46	426.51	-27.98
422.83	-27.70	426.61	-28.22
422.84	-27.30	426.71	-28.36
422.94	-27.65	426.81	-28.26
423.04	-27.49	426.91	-28.26
423.14	-27.19	427.01	-28.67
423.24	-27.22	427.11	-28.79
423.34	-27.28	427.20	-28.58
423.44	-27.49	427.30	-27.84
423.54	-27.52	427.31	-27.95
423.64	-26.47	427.41	-28.58
423.74	-27.45	427.51	-28.73
423.84	-27.58	427.61	-28.68
423.94	-24.73	427.69	-28.19
424.31	-25.38	427.71	-28.16
424.41	-27.25	427.81	-28.06
424.51	-27.17	427.91	-28.51
424.61	-27.50	427.99	-28.61
424.71	-27.26	428.01	-28.78
424.81	-27.18	428.10	-28.66
424.91	-26.52	428.18	-28.78
425.01	-23.93	428.22	-28.71
425.11	-25.51	428.29	-28.47
425.21	-23.67	428.69	-28.65
425.31	-22.37	428.99	-28.24
425.41	-22.13	429.59	-28.07
425.51	-22.35	429.99	-28.80
425.61	-24.45	430.43	-28.29
426.01	-23.58	430.65	-28.50
426.11	-22.70	431.20	-28.42
426.21	-24.06	431.61	-28.37
426.31	-24.75		

<sup>\*</sup> values reported permil (‰) relative to the VPDB standard<sup>^</sup> meters in core depth

**Table 2.1d** $\delta^{13}\text{C}_{org}$  data from Vocontian Basin (Pont d'Issole (ADx-10 & ISLx) and Vergons (VGN) sections), SE France (Jarvis et al., 2011)

Height (m)	$\delta^{13}\text{C}_{org}$ [‰]*	Height (m)	$\delta^{13}\text{C}_{org}$ [‰]*
23.50	-25.5	10.00	-24.1
23.30	-25.7	9.80	-24.5
23.00	-25.7	9.60	-25.8
22.50	-25.6	9.40	-24.4
21.30	-25.8	9.20	-23.9
21.00	-24.8	9.00	-23.9
20.50	-24.8	8.50	-24.1
20.00	-26.0	8.10	-24.6
19.70	-25.5	7.70	-24.2
19.40	-25.4	7.30	-24.5
19.20	-25.7	6.75	-25.6
19.00	-25.2	6.10	-26.0
18.70	-25.2	5.40	-26.0
18.40	-24.7	4.80	-26.5
17.90	-24.8	4.30	-26.6
17.40	-24.3	3.50	-26.5
17.10	-24.9	2.80	-27.0
16.60	-24.3	2.30	-26.2
16.10	-24.3	1.80	-25.9
15.90	-24.6	1.50	-26.57
15.60	-24.2	1.00	-26
15.10	-24.0	0.90	-26.3
15.00	-24.2	0.00	-26.2
14.50	-24.5	0.00	-26.87
14.00	-24.8	-0.78	-26.03
13.50	-24.1	-1.07	-26.05
13.00	-24.0	-1.84	-25.66
12.50	-23.9	-4.00	-26.41
12.00	-24.2		
11.50	-24.1		
11.30	-24.2		
10.80	-24.4		
10.30	-25.0		

\* values reported permil (‰) relative to the VPDB standard

**Table 2.1e** $\delta^{13}\text{C}_{org}$  data for Furlo, Italy (Jenkyns et al., 2007)

Depth (m)	$\delta^{13}\text{C}_{org}$ [‰]*	Depth (m)	$\delta^{13}\text{C}_{org}$ [‰]*
101.9	-23.50	-390.0	-26.33
98.9	-23.20	-411.0	-26.21
96.7	-23.70	-432.0	-25.93
95.9	-23.30	-452.0	-26.10
91.9	-23.20	-515.0	-26.43
89.7	-23.70	-630.0	-26.57
86.2	-23.40	-689.0	-26.00
83.5	-23.20	-711.0	-26.33
75.2	-23.00	-800.0	-26.03
70.5	-23.70	-825.0	-26.23
65.6	-23.60	-905.0	-26.72
61.8	-23.20	-1082.0	-26.45
58.3	-23.30	-1175.0	-26.63
55.8	-23.30	-1205.0	-26.48
55.1	-23.30	-1285.0	-26.33
53.3	-23.50	-1465.0	-25.94
44.1	-23.10	-1565.0	-26.31
37.8	-23.50	-1645.0	-26.10
34.4	-23.30		
34.0	-24.40		
31.8	-24.70		
27.8	-25.10		
20.9	-25.70		
15.6	-25.60		
11.2	-25.50		
8.1	-25.90		
3.6	-26.70		
0.0	-27.20		
-42.0	-26.40		
-70.0	-25.64		
-90.0	-26.08		
-320.0	-26.15		
-350.0	-26.34		

\* values reported permil (‰) relative to the VPDB standard

**Table 2.1f** $\delta^{13}\text{C}_{org}$  data for DSDP Site 530, Hole 530A, South Atlantic (Forster et al., 2008)

Depth (mbsf) <sup>^</sup>	$\delta^{13}\text{C}_{org}$ [‰] <sup>*</sup>	Depth (mbsf) <sup>^</sup>	$\delta^{13}\text{C}_{org}$ [‰] <sup>*</sup>
1014.44	-27.06	1036.56	-25.63
1017.56	-27.61	1037.18	-23.66
1021.88	-26.72	1037.66	-26.36
1023.88	-26.07	1037.86	-26.75
1024.14	-27.04	1038.33	-26.38
1026.51	-25.10	1038.53	-26.94
1027.03	-25.92	1038.90	-27.21
1027.23	-25.81	1039.27	-27.73
1027.48	-26.26	1039.73	-27.12
1027.62	-24.11	1039.78	-27.08
1027.91	-26.61	1044.29	-27.87
1028.25	-26.27	1044.44	-26.88
1028.60	-26.91	1046.32	-26.07
1028.78	-26.21	1046.76	-25.55
1028.97	-26.34	1048.48	-26.66
1029.16	-26.20	1048.50	-27.59
1029.29	-25.63	1049.11	-25.71
1029.61	-26.38	1050.57	-26.97
1029.73	-27.06	1051.21	-27.22
1030.65	-26.20		
1030.81	-26.32		
1031.19	-25.44		
1031.33	-25.44		
1031.55	-25.80		
1031.66	-26.29		
1031.77	-25.65		
1032.00	-25.04		
1035.08	-26.00		
1035.21	-24.65		
1035.49	-23.82		
1035.73	-23.48		
1035.94	-23.76		
1036.10	-23.80		

\* values reported permil (‰) relative to the VPDB standard

<sup>^</sup> meters below sea floor



**Table 2.2b**  
Re - Os data for samples for the CTB, from Wunstorf, NW Germany

WUNSTORF	Depth (m)	kyr	Re (ppb)	±	Os (ppt)	±	$^{187}\text{Re}/^{188}\text{Os}$	±	$^{187}\text{Os}/^{188}\text{Os}$	±	$^{182}\text{Os}$ (ppt)	$^{182}\text{Os}$ (@93.9 Ma)	±
AD44-09	26.9	757.66	2.6	0.01	70.7	0.46	194.9	2.0	0.919	0.012	26.5	0.614	0.010
AD42-09	28.5	703.94	1.0	0.01	53.6	0.36	95.6	1.2	0.818	0.011	20.3	0.669	0.012
AD41-09	29.1	682.32	1.6	0.01	44.2	0.32	191.9	2.3	0.949	0.013	16.5	0.648	0.012
AD40-09	29.8	660.02	14.9	0.05	505.8	1.43	156.3	0.6	0.907	0.003	189.5	0.662	0.003
AD38-09	32.4	570.49	1.1	0.01	118.7	0.68	48.1	0.5	0.688	0.008	45.7	0.613	0.010
AD30-09	36.2	442.11	38.8	0.13	398.1	0.97	551.6	1.9	1.456	0.003	140.1	0.593	0.002
AD28-09	37.3	404.95	0.5	0.01	88.2	0.34	30.4	0.4	0.608	0.004	34.3	0.561	0.008
AD27-09	38.0	381.30	1.7	0.01	253.9	0.81	34.4	0.2	0.596	0.003	98.8	0.542	0.004
AD26-09	39.5	329.95	5.2	0.02	288.0	0.78	93.2	0.4	0.631	0.002	111.6	0.485	0.003
AD25-09	40.2	308.33	9.9	0.03	270.7	0.64	192.4	0.7	0.812	0.002	102.6	0.511	0.002
AD24-09	40.8	287.05	12.4	0.04	296.7	0.65	220.6	0.8	0.837	0.002	112.1	0.491	0.002
AD23-09	41.7	255.29	1.2	0.01	133.1	0.69	46.1	0.5	0.490	0.006	52.5	0.418	0.007
AD21-09	42.9	217.45	6.9	0.02	737.4	2.20	47.2	0.2	0.465	0.002	291.6	0.391	0.003
AD19-09	43.5	196.17	16.8	0.05	485.0	1.00	177.1	0.7	0.617	0.001	188.2	0.340	0.002
AD17-09	44.1	175.90	5.0	0.02	2247.3	4.86	10.8	0.1	0.199	0.001	919.2	0.182	0.001
AD12-09	47.4	64.41	3.4	0.01	1375.3	5.03	12.1	0.1	0.198	0.002	562.6	0.179	0.002
AD11-09	47.7	56.47	0.7	0.01	223.7	2.13	14.5	0.3	0.232	0.007	91.1	0.210	0.008
AD10-09	47.8	53.24	8.5	0.03	801.8	1.58	52.1	0.2	0.267	0.001	325.1	0.185	0.001
AD9-09	48.0	46.76	3.7	0.01	551.0	1.69	32.9	0.2	0.246	0.002	224.0	0.195	0.002
AD8-09	48.2	41.47	0.3	0.01	353.6	12.41	4.6	0.4	0.203	0.023	144.6	0.202	0.015
AD7-09	48.5	30.88	0.7	0.01	950.7	17.04	3.4	0.1	0.183	0.010	389.7	0.177	0.006

Note: individual ratio uncertainties are given at the  $2\sigma$  level.

Os uncertainties are determined through full propagation of uncertainties in Re & Os mass spectrometry, spike, blanks and std Re & Os isotopic values kyr calculated as detailed in chapter 2, section 3.4.

**Table 2.2c**  
 Additional Re - Os data for samples for the CTB, from ODP Site 1260, Hole 1260B, Demerara Rise

ODP Site 1260	Depth (m)	kyr	Re (ppb)	Os (ppt)	$^{187}\text{Re}/^{188}\text{Os}$	$\pm$	$^{187}\text{Os}/^{188}\text{Os}$	$\pm$	$^{187}\text{Os}$ (ppt)	$^{187}\text{Os}$ (@93.9 Ma)	$\pm$
35/05W/125-127	427.07	-124.53	62.9	0.20	572	2.16	642.3	2.8	194.9	0.738	0.002
35/05W/144-147	427.26	-160.38	146.7	0.47	473	2.46	2316.7	11.1	125.9	0.721	0.002
35/06W/01-03	427.32	-171.70	125.2	0.40	411	2.21	2281.4	11.4	109.2	0.818	0.003
35/06W/55-57	427.87	-275.47	35.5	0.12	246	1.49	874.2	6.3	80.8	0.735	0.004
36/01W/14-17	428.24	-345.28	33.7	0.11	112	1.25	2214.0	32.8	30.3	0.730	0.008
36/01W/54-56	428.64	-420.75	186.6	0.60	699	3.00	1925.4	7.8	192.8	0.924	0.002
36/01W/135-138	429.45	-573.58	68.6	0.22	565	2.50	717.6	3.4	190.1	0.749	0.002
36/02W/23-25	429.83	-645.28	111.4	0.36	538	2.49	1360.9	6.1	162.8	0.794	0.002
36/02W/83-85	430.43	-758.49	62.1	0.20	514	2.07	712.1	3.2	173.5	0.714	0.002
36/02W/105-108	430.65	-800.00	629.9	2.03	5127	29.87	717.9	4.3	1745.5	0.633	0.003
36/03W/10-12	431.20	-903.77	65.3	0.21	585	2.38	646.5	3.0	200.9	0.672	0.002
36/03W/51-53	431.61	-981.13	184.8	0.60	760	2.86	1635.5	6.3	224.8	0.597	0.001

Note: individual ratio uncertainties are given at the 2 $\sigma$  level.

Os, uncertainties are determined through full propagation of uncertainties in Re & Os mass spectrometry, spike, blanks and std Re & Os isotopic values kyr calculated as detailed in chapter 2, section 3.4.

Table 2.24  
Re - Os data for samples for the CTB, from Vercorian Basin (Point d'Issole (ADs-10 and ISLx) and Verpasa (VGN) sect)

YUCCONTIAN BASIN	Height (m)	Kyr	Re (ppb)	Os (ppt)	<sup>187</sup> Re/ <sup>188</sup> Os	<sup>187</sup> Os/ <sup>188</sup> Os	<sup>187</sup> Os/ <sup>188</sup> Os	<sup>187</sup> Os/ <sup>188</sup> Os	Os (ppm)	Os (ppm)			
AD41-10	17.22	555.57	0.2	0.02	366.2	1.59	3.8	0.3	1.128	0.609	111.8	1.322	0.050
AD43-10	15.55	467.91	0.1	0.02	226.8	1.47	3.1	0.4	0.937	0.612	85.4	0.952	0.066
AD45-10	15.26	446.95	13.2	0.05	324.4	1.72	217.8	1.7	0.994	0.609	126.3	0.653	0.004
AD47-10	14.86	417.56	0.1	0.02	284.4	1.95	2.1	0.4	0.943	0.613	106.1	0.940	0.080
AD49-10	14.46	394.17	0.3	0.02	6.5	0.45	227.7	41.1	0.963	0.168	2.4	0.607	0.076
AD51-10	14.06	370.78	1.2	0.02	83.8	1.62	69.0	3.1	0.427	0.025	33.3	0.319	0.012
AD55-10	13.26	324.00	0.8	0.02	169.3	3.89	37.0	3.1	0.524	0.660	42.9	0.466	0.033
AD59-10	12.46	277.21	12.5	0.05	340.7	1.71	188.4	1.6	0.629	0.606	132.0	0.334	0.002
AD61-10	12.06	253.82	1.4	0.03	149.1	5.27	47.5	3.9	0.905	0.046	29.4	0.330	0.025
AD63-10	11.66	230.43	12.8	0.05	600.9	2.56	106.5	0.8	0.558	0.605	234.9	0.389	0.002
AD64-10	11.46	218.73	14.0	0.05	461.8	2.64	154.9	1.1	0.574	0.605	180.1	0.331	0.002
AD65-10	11.26	207.04	7.5	0.03	295.4	1.85	129.8	1.3	0.520	0.608	115.2	0.317	0.003
AD67-10	10.86	183.64	10.3	0.04	366.1	2.00	143.9	1.3	0.582	0.607	142.7	0.357	0.003
AD69-10	10.46	166.25	1.5	0.01	671.1	12.09	11.1	0.5	0.220	0.612	273.8	0.203	0.007
AD71-10	10.06	136.86	2.3	0.02	733.7	13.23	15.2	0.6	0.218	0.612	289.4	0.194	0.007
AD73-10	9.66	129.81	2.4	0.01	697.4	12.52	16.8	0.7	0.189	0.611	285.6	0.163	0.006
AD75-10	9.45	126.10	0.4	0.01	1642.1	57.51	1.1	0.1	0.162	0.618	674.9	0.100	0.011
VGN 437	8.00	106.53	7.6	0.03	362.9	6.83	106.5	4.3	0.537	0.600	142.2	0.370	0.013
AD02-10	7.75	96.12	0.4	0.01	461.2	8.27	4.7	0.2	0.189	0.611	188.9	0.182	0.007
AD05-10	7.15	85.54	0.2	0.00	269.8	9.46	3.2	0.3	0.210	0.604	110.2	0.205	0.014
AD07-10	6.75	78.48	14.4	0.05	1294.0	4.82	55.3	0.4	0.361	0.603	518.4	0.274	0.001
AD09-10	6.35	71.43	4.4	0.03	670.8	6.37	31.8	0.7	0.223	0.606	273.5	0.175	0.003
AD11-10	5.95	64.37	5.9	0.02	748.4	3.22	38.2	0.3	0.215	0.602	305.5	0.155	0.001
AD13-10	5.55	57.32	4.0	0.04	651.2	2.75	29.7	0.4	0.184	0.602	266.9	0.137	0.001
AD15-10	5.15	50.26	463.9	1.50	57827.0	42.56	68.3	0.2	0.287	0.600	15297.3	0.195	0.000
AD17-10	4.75	43.21	5.1	0.02	790.9	7.30	31.2	0.6	0.175	0.605	324.5	0.126	0.002
AD19-10	4.35	36.16	11.5	0.04	2853.1	8.39	19.6	0.1	0.223	0.602	1163.4	0.192	0.001
AD21-10	3.95	29.10	5.4	0.02	1675.3	7.66	15.7	0.1	0.178	0.602	687.1	0.153	0.001
AD22-10	3.75	25.57	2.0	0.01	602.4	5.73	16.0	0.3	0.206	0.606	246.2	0.181	0.003
AD23-10	3.55	22.05	1.5	0.01	625.4	11.20	10.3	0.4	0.201	0.611	254.9	0.185	0.006
AD24-10	3.35	18.52	4.4	0.02	275.3	2.90	88.2	1.7	0.430	0.613	106.3	0.305	0.006
ISL8	2.80	8.82	18.5	0.06	4084.2	10.75	22.1	0.1	0.250	0.601	1659.5	0.216	0.001
ISL7	2.50	0.00	0.4	0.01	179.6	3.37	11.7	0.6	0.510	0.629	70.6	0.492	0.019
VGN 436.5	1.50	-14.11	0.9	0.03	167.2	0.85	25.9	0.9	0.257	0.604	67.9	0.217	0.004
VGN 436	1.00	-22.93	0.3	0.01	31.2	0.65	52.2	2.4	0.896	0.602	11.7	0.814	0.030
VGN 435	0.00	-40.56	0.2	0.01	30.2	0.61	36.4	1.8	0.825	0.648	11.4	0.768	0.030
AD27-10	-0.78	-121.81	0.4	0.01	31.1	1.12	66.0	5.5	0.896	0.102	11.7	0.793	0.056
AD29-10	-1.07	-152.02	0.3	0.00	35.7	1.29	40.2	3.3	0.902	0.302	13.4	0.839	0.029
AD33-10	-1.84	-232.23	0.3	0.00	57.0	1.53	28.1	1.6	0.975	0.679	21.2	0.931	0.046
VGN 431	-4.00	-457.23	0.5	0.01	33.8	0.72	74.4	3.8	0.892	0.654	12.7	0.776	0.031

Note: individual ratio uncertainties are given at the 2σ level.  
Os uncertainties are determined through full propagation of uncertainties in Re & Os mass spectrometry, spike, blanks and old Re & Os isotopic values.  
Vergeno sections - correlated with Point d'Issole (Jarvis unpub.)  
Kyr calculated as detailed in chapter 2, 48

**Table 2.2e**  
Additional Re - Os data for samples for the CTB, from Furlo, Italy

<b>FURLO</b>	<b>Depth (m)</b>	<b>kyr</b>	<b>Re (ppb)</b>	<b>Os (ppt)</b>	$^{187}\text{Re}/^{188}\text{Os}$	$^{187}\text{Os}/^{188}\text{Os}$	$^{192}\text{Os}$ (ppt)	$\text{Os}_1$ (@93.9 Ma)	$\pm$				
<b>Furlo 8.1</b>	3.99	38.57	81.1	0.27	10316.0	17.40	38.4	0.2	0.235	0.001	0.4	0.175	0.000
<b>Furlo 3.6</b>	4.03	17.14	130.4	0.43	11355.4	16.46	56.4	0.2	0.272	0.001	0.3	0.184	0.000
<b>Furlo 0</b>	4.07	0.00	0.3	0.01	163.8	2.06	8.1	0.3	0.291	0.011	0.5	0.278	0.007
<b>Furlo -42</b>	4.49	-2.00	3.4	0.02	55.3	0.51	330.0	5.4	1.059	0.020	0.8	0.543	0.007
<b>Furlo -70</b>	4.77	-333.33	1.0	0.01	42.1	0.64	126.9	4.2	0.743	0.031	0.7	0.545	0.014
<b>Furlo -90</b>	4.97	-428.57	1.5	0.01	57.2	0.69	134.7	3.3	0.754	0.023	0.7	0.543	0.011

Note: individual ratio uncertainties are given at the  $2\sigma$  level.

Os<sub>1</sub> uncertainties are determined through full propagation of uncertainties in Re & Os mass spectrometry, spike, blanks and std Re & Os isotopic values kyr calculated as detailed in cha

Table 2.27  
Re - Os data for samples for the CTB, from IODP Site 530, Hole 530A, South Atlantic

IODP Site 530	Depth (m)	kyr	Re(ppb)	Os(ppt)	<sup>187</sup> Re/ <sup>188</sup> Os	<sup>187</sup> Os/ <sup>188</sup> Os							
AD086-10	1017.18	823.49	6.2	0.01	14.3	0.38	70.3	6.0	0.530	0.041	5.6	0.430	0.024
AD086-10	1021.88	646.80	11.6	0.04	682.2	3.65	87.5	0.6	0.665	0.006	265.2	0.528	0.003
AD086-10	1023.53	584.77	10.7	0.04	331.6	1.79	169.9	1.4	0.868	0.008	125.7	0.542	0.004
AD096-10	1024.58	545.29	2.8	0.01	213.5	1.72	66.0	1.0	0.671	0.013	83.1	0.568	0.007
AD922-10	1027.29	443.41	35.4	0.13	1025.7	5.64	181.0	1.3	0.816	0.007	388.5	0.533	0.003
AD946-10	1028.16	410.71	156.2	0.51	2385.9	6.56	355.6	1.4	1.100	0.003	870.1	0.544	0.001
AD955-10	1028.78	387.40	183.4	0.60	1665.0	5.29	627.4	2.5	1.514	0.004	581.4	0.551	0.001
AD975-10	1029.65	354.69	198.2	0.65	1817.4	5.89	627.5	2.5	1.616	0.005	628.3	0.634	0.002
AD995-10	1031.35	290.78	18.8	0.07	455.1	2.32	217.5	1.7	0.821	0.008	172.3	0.481	0.003
AD100-10	1031.56	282.89	34.2	0.13	642.2	4.65	283.1	2.7	0.826	0.011	240.1	0.483	0.004
AD101-10	1031.87	271.25	79.1	0.26	1599.1	6.46	265.5	1.4	1.004	0.006	592.4	0.588	0.002
AD102-10	1033.28	143.64	6.3	0.01	39.8	1.44	39.6	3.6	0.242	0.033	16.1	0.220	0.016
AD103-10	1035.50	134.77	1.7	0.01	206.8	1.97	42.9	0.9	0.361	0.009	81.0	0.213	0.004
AD104-10	1035.69	127.86	1.8	0.02	348.9	4.40	25.5	0.7	0.292	0.011	141.0	0.252	0.006
AD105-10	1035.89	120.79	2.5	0.01	354.7	3.42	34.1	0.7	0.260	0.007	145.9	0.286	0.004
AD106-10	1036.10	113.26	12.4	0.05	1642.3	5.34	58.5	0.6	0.242	0.004	421.8	0.190	0.002
AD106-10	1036.51	98.57	11.4	0.05	1868.2	8.10	29.8	0.3	0.226	0.003	761.5	0.179	0.001
AD109-10	1036.72	91.04	48.1	0.16	6144.1	12.50	38.2	0.2	0.216	0.001	2597.5	0.156	0.000
AD110-10	1036.97	82.08	6.6	0.04	2465.9	16.09	13.0	0.2	0.177	0.005	1011.5	0.157	0.002
AD111-10	1037.21	73.48	13.7	0.05	2195.9	11.35	30.3	0.3	0.216	0.003	896.2	0.169	0.002
AD112-10	1037.41	66.31	51.4	0.17	5239.7	12.02	48.1	0.2	0.272	0.001	2123.1	0.197	0.001
AD113-10	1037.54	61.65	104.6	0.35	4429.2	10.05	117.3	0.5	0.357	0.001	1775.3	0.174	0.001
AD114-10	1037.69	56.27	122.5	0.40	8478.9	17.56	71.2	0.3	0.365	0.001	3420.9	0.184	0.001
AD115-10	1037.89	49.10	122.9	0.40	9101.5	18.69	65.9	0.3	0.223	0.001	3711.4	0.119	0.000
AD116-10	1038.12	40.86	6.5	0.01	571.5	10.23	4.6	0.2	0.171	0.010	234.6	0.164	0.006
AD117-10	1038.35	32.62	177.5	0.58	9451.3	24.13	92.6	0.3	0.364	0.001	2814.2	0.159	0.000
AD118-10	1038.50	27.24	280.3	0.95	14395.4	24.15	96.5	0.4	0.346	0.001	5778.3	0.195	0.000
AD119-10	1038.67	13.98	356.4	1.16	12387.3	16.94	142.6	0.5	0.348	0.001	4970.8	0.125	0.000
AD120-10	1039.26	0.00	77.4	0.26	1713.0	5.29	236.1	1.1	0.772	0.003	652.3	0.403	0.001
AD121-10	1039.62	-12.90	6.4	0.01	45.8	0.87	46.8	2.0	0.548	0.031	17.9	0.475	0.017
AD122-10	1039.78	-18.64	13.9	0.05	394.9	2.22	185.3	1.6	0.864	0.009	148.7	0.573	0.004
AD123-10	1044.20	-177.06	1.0	0.01	105.7	2.07	51.1	2.2	0.773	0.044	40.2	0.693	0.025
AD124-10	1044.43	-185.30	6.9	0.01	36.6	0.58	122.2	4.3	0.774	0.033	13.9	0.583	0.016
AD125-10	1044.86	-200.72	6.4	0.01	38.2	0.79	60.1	3.1	0.720	0.043	14.7	0.626	0.025
AD126-10	1045.44	-221.51	0.8	0.01	88.4	1.71	46.4	2.0	0.670	0.038	34.1	0.598	0.022
AD127-10	1045.51	-224.01	1.1	0.01	125.9	2.42	45.2	1.9	0.656	0.037	48.6	0.585	0.021
AD129-10	1045.83	-235.48	2.3	0.01	112.3	0.86	107.1	1.7	0.781	0.016	42.7	0.613	0.008
AD131-10	1046.52	-240.22	6.3	0.01	56.3	0.80	23.2	1.3	0.551	0.022	22.0	0.515	0.018
AD137-10	1048.51	-331.54	2.4	0.01	111.0	0.97	112.9	1.8	0.851	0.017	41.9	0.674	0.009
AD139-10	1048.97	-348.03	1.4	0.02	73.9	1.51	99.5	4.5	0.804	0.047	28.9	0.648	0.02
AD141-10	1050.59	-466.09	13.2	0.05	456.3	2.16	154.5	1.0	0.973	0.007	169.7	0.731	0.00
AD143-10	1051.25	-429.03	18.4	0.07	576.1	2.97	171.0	1.3	0.972	0.008	214.3	0.704	0.00

Note: individual ratio uncertainties are given at the 2σ level.  
Os uncertainties are determined through full propagation of uncertainties in Re & Os mass spectrometry, spike, blanks and sd Re & Os isotopic values  
kyr calculated as detailed in chapter 2, section 3.4.

**Table 2.3**  
 Re - Os data for USGS Std. SDO-1.

STD SAMPLE	Re (ppb)	±	Os (ppt)	±	$^{187}\text{Re}/^{188}\text{Os}$	±	$^{187}\text{Os}/^{188}\text{Os}$	±	$\text{O}_5$ ( $\bar{n}$ 366 Ma)	±
SDO-1	77.2	0.25	637.8	3.65	1175.5	5.5	7.909	0.029	0.72	0.004
SDO-1	77.7	0.25	641.2	3.62	1177.0	5.4	7.916	0.028	0.72	0.004
SDO-1	76.7	0.25	674.7	3.61	1039.3	4.6	7.012	0.023	0.66	0.004
SDO-1	76.3	0.25	626.2	3.81	1186.2	5.7	7.952	0.032	0.70	0.004
SDO-1	76.8	0.25	631.4	3.65	1186.6	5.5	7.972	0.029	0.71	0.004
SDO-1	75.1	0.24	618.4	3.39	1182.1	5.1	7.954	0.026	0.72	0.004
SDO-1	75.8	0.25	621.9	3.65	1189.7	5.6	7.980	0.030	0.70	0.002
SDO-1	76.3	0.25	638.1	3.63	1145.0	5.3	7.688	0.028	0.69	0.002
SDO-1	72.4	0.23	597.8	3.63	1175.1	5.7	7.896	0.032	0.71	0.002
SDO-1	61.0	0.20	497.8	3.18	1196.3	6.3	7.983	0.036	0.67	0.002
SDO-1	84.9	0.27	701.4	3.80	1172.9	5.2	7.881	0.026	0.71	0.002
SDO-1	85.5	0.28	699.8	3.85	1191.5	5.3	7.975	0.027	0.69	0.002
Average	76.3		632.2		1168.1		7.843		0.70	
2 S.D.	12.2		106.0		85.3		0.548		0.04	
2σ % uncertainty	16.0		16.8		7.3		7.0		6.2	

Note: individual SDO-1 data uncertainties are given at the 2σ level.

$\text{O}_5$  uncertainties are determined through full propagation of uncertainties in Re & Os mass spectrometry, spike, blanks and std Re & Os isotopic values

# 3

## **Pacific $^{187}\text{Os}/^{188}\text{Os}$ isotope chemistry and U-Pb geochronology: Implications for global synchronicity of OAE 2**

A version of this chapter will be submitted to *Earth and Planetary Science Letters*; co-authored by David Selby of Durham University, Dan Condon of NIGL BGS Keyworth, UK, Reishi Takashima and Hiroshi Nishi of Tohoku University, Sendai, Japan.

### **1. Introduction**

Oceanic anoxic events (OAEs) are a consequence of an imbalance to a sensitive global ocean-atmosphere system, which results in episodes of oxygen depletion in the oceans (Schlanger et al., 1987). They are characterised by the accumulation of organic-rich material, often associated with biodiversity and/or extinctions in the biostratigraphic record, and typically identified by a 2 – 4‰ shift in the  $\delta^{13}\text{C}_{\text{org}}$  and  $\delta^{13}\text{C}_{\text{carb}}$  record (Schlanger et al., 1987). Such characteristics are representative of OAE 2, which occurred during the late Cretaceous across the Cenomanian-Turonian boundary (CTB 93.90 Ma) and is hypothesised to have influenced basinal environments on a global scale (Jenkyns, 1980). This theory is based on studies that have predominately focussed on a globally narrow region, e.g., the proto-Atlantic, Tethyan and Western Interior Sea (WIS). To date, analysis of OAE 2 sections recording deposition from basins of the Cretaceous World's largest water mass, the proto-Pacific, are extremely limited and have predominately focussed on  $\delta^{13}\text{C}$  records in comparison to the multi-element/isotope studies of the proto-Atlantic, Tethyan and WIS (Kaiho et al., 1993; Hasegawa and Saito, 1993; Hasegawa, 1995, 1999; Tamaki and Itoh, 2008; Takashima et al., 2004, 2011; Quidelleur et al., 2011). The main reasons for the limited studies are the poor preservation and the uncertainty of stratigraphic location of the OAE 2 record. Two sites that represent a complete record of OAE 2 from deposition in the proto-Pacific are the Yezo Group (YG) section, Hokkaido, Japan and the Great Valley Sequence (GVS), California, USA (Fig. 3.1). Herein we report and discuss the implications of the Os isotope data (YG and GVS) and U-Pb zircon geochronology (YG only) for these sites.

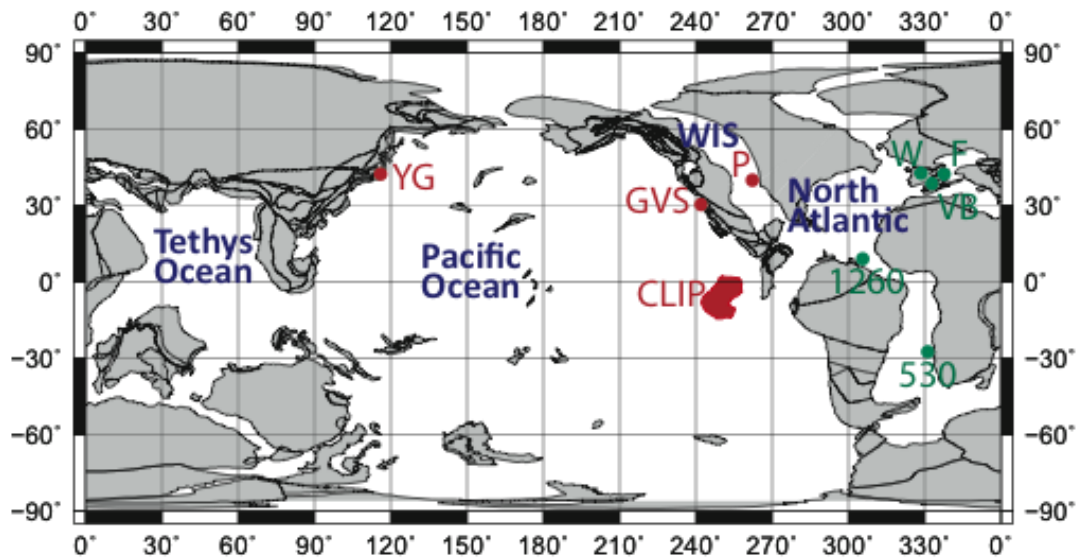


**Figure 3.1 Palaeogeographic map illustrating sample locations.** In RED: YG – Yezo Group, Hokkaido, Japan; GVS – Great Valley Sequence, California, USA; P – Portland #1 core, Colorado, USA; WIS – Western Interior Seaway; CLIP – Caribbean Large Igneous Province. In GREEN previously studied sections (Turgeon and Creaser, 2008; Du Vivier et al., 2014; Chapter 2, this thesis): W – Wunstorf, Germany; VB – Vocontian Basin, SE France; F – Furlo, Italy; 1260 – Site 1260 B, Demerara Rise, North Atlantic; 530 – Site 530, Angola Basin, South Atlantic. Modified from: [www.odsc.de/odsn/services/paleomap/paleomap.html](http://www.odsc.de/odsn/services/paleomap/paleomap.html)

The correlation of OAE 2 is fundamentally based upon the carbon isotope record combined with biostratigraphy and subordinate radio-isotopic dating. Here we apply the traditional  $\delta^{13}\text{C}$  datum levels for correlation to both the YG and the GVS sections, where peaks and troughs in the  $\delta^{13}\text{C}$  record are associated with bioevents and changes in lithology. The sections are correlated according to this method using points ‘A’, ‘B’ and ‘C’ of the  $\delta^{13}\text{C}$  curve that are similar to those first defined by Pratt et al. (1985) in the WIS for the GSSP and refined later by Tsikos et al. (2004); where ‘A’ represents the last value of relatively depleted  $\delta^{13}\text{C}$  before the first major shift to positive values; the base of the excursion marks the onset of OAE 2 (Pratt et al., 1985); ‘B’ marks the trough of depleted values following the positive excursion

in the  $\delta^{13}\text{C}$  record (Pratt et al., 1985); and ‘C’ denotes the end of the ‘plateau’, the last relatively enriched value prior to the  $\delta^{13}\text{C}$  trending back to pre-OAE 2 values (Tsikos et al., 2004). However, since the discovery of OAEs, isotopic analysis has revealed a number of isotopic proxies that are sensitive to the chemical perturbations that occur during these events (e.g. carbon, strontium, osmium, calcium, neodymium, phosphorus, lead, lithium, uranium; Arthur et al., 1987; McArthur et al., 2004; Forster et al., 2007; MacLeod et al., 2008; Turgeon and Creaser, 2008; Voigt et al., 2008; Montoya-Pino et al., 2010; Blättler et al., 2011; Kuroda et al., 2011; Mort et al., 2011; Pogge von Strandmann et al., 2013; Du Vivier et al., 2014; Chapter 2, this thesis), which have improved correlation and facilitated the understanding of the driving mechanisms of oceanic anoxia.

Osmium isotope stratigraphy has shown the potential of global correlation throughout many proto-Atlantic and Tethyan basins (Turgeon and Creaser, 2008; Du Vivier et al., 2014; Chapter 2, this thesis), but work so far has not been extended into the proto-Pacific. Here we apply initial osmium ( $^{187}\text{Os}/^{188}\text{Os} - \text{Os}_i$ ) isotope stratigraphy from the YG section, Japan and the GVS, USA (Fig. 3.1). In addition, existing studies have utilised isotope profiles as time correlation markers (Forster et al., 2007; MacLeod et al., 2008; Turgeon and Creaser, 2008; Voigt et al., 2008; Blättler et al., 2011; Mort et al., 2011; Martin et al., 2012; Du Vivier et al., 2014; Chapter 2, this thesis), but the majority of sites are unsupported by absolute dating. An exception is in the WIS where volcanic tuff horizons from multiple locations throughout the WIS have been integrated to nominally constrain the geochronology of the Portland #1 core (Meyers et al., 2012a). Similarly the YG section is interbedded with tuff horizons, which we utilise for U-Pb zircon geochronology to

support and develop integration of the YG section with other OAE 2 sites, specifically the Portland #1 core. As a result we compare the Os isotope composition of seawater from the proto-Pacific with that of the WIS, proto-Atlantic and the Tethyan realm to evaluate if similar trends observed are correlative, and/or temporally identical, and therefore assess the truly global extent of OAE 2 on ocean chemistry.

Existing U-Pb zircon geochronology of two tuff horizons from the Cenomanian-Turonian boundary interval (CTBI) of the YG produced imprecise ages and dates, which limits their application (Quidelleur et al., 2011). The latter study reported a LA-ICP-MS U-Pb zircon date of  $92.9 \pm 1.3$  Ma ( $n = 16$ ; HKt002) for a tuff located above the last occurrence of *R. cushmani* (Upper Cenomanian), whereas the stratigraphically younger tuff (HKt003) generated a U-Pb multi-grain ID-TIMS age of  $94.3 \pm 0.3$  Ma ( $n = 7$ ; MSWD = 1.5). The accuracy of the existing U-Pb dates for the YG are problematic based on the  $^{40}\text{Ar}/^{39}\text{Ar}$  calibrated age model of the OAE 2 from the WIS, which constrains the CTB to  $93.90 \pm 0.15$  Ma (Meyers et al., 2012a). Therefore given the OAE 2 temporal constraints the dated horizon HKt002 and HKt003 of the YG should be  $> 93.9$  Ma (see discussion).

To permit integration with the OAE 2 section of the Portland #1 core we provide accurate and precise temporal constraints of the OAE 2 of the YG section via U-Pb (zircon) ID-TIMS analysis ages from 5 volcanic tuff horizons. In addition to using the most current analytical protocols (e.g., chemical abrasion-isotope dilution thermal ionisation, CA-IDTIMS: Mattinson, 2005) we also use the EARTHTIME U-Pb tracer solutions (Condon et al., 2007; Condon et al., *in review*; McLean et al., *in review*) to provide absolute temporal constraints for the YG to present a potential

OAE 2 reference section for the proto-Pacific Ocean. We use the U-Pb zircon ages to help constrain the sediment accumulation rate for the YG section OAE 2 interval, which in turn permits a quantitative estimate for the duration of events across the CTBI. Furthermore we use an age-depth model (OxCal; Bronk Ramsey, 2008) to interpolate dates between the dated tuff horizons and additionally integrate the  $^{40}\text{Ar}/^{39}\text{Ar}$ -based ages from the integrated age model of the WIS (Meyers et al., 2012a) on to the YG section in order to objectively compare the  $\text{Os}_i$  and carbon isotope profiles.

The Caribbean LIP is contemporaneous with OAE 2 and regarded as a fundamental mechanism in the development of the event based on evidence from trace metals, oxidation of metals and an influx of biolimiting metals increasing oxygen consumption, radiometric  $^{40}\text{Ar}/^{39}\text{Ar}$  dating, and Os isotope stratigraphy (Sinton and Duncan, 1997; Leckie et al., 2002; Snow et al., 2005; Turgeon and Creaser, 2008; Du Vivier et al., 2014). The  $\text{Os}_i$  profiles across the OAE 2 (Du Vivier et al., 2014; Chapter 2, this thesis) demonstrate the response of seawater chemistry due to submarine volcanism, and infer the significance of water mass exchange in the transfer of nutrients and the development of anoxia in the proto-Atlantic, Tethys and the WIS. Here we combine the U-Pb data with the  $\text{Os}_i$  to provide evidence of water mass exchange and efficient palaeocirculation in the Pacific Ocean during the CTBI.

## ***2. Geological setting and stratigraphy***

### *2.1. Yezo Group (YG), Hokkaido, Japan*

The YG was deposited along an active continental margin in an arc-trench system at  $\sim 45^\circ\text{N}$  along the Eurasian margin during the late Mesozoic (Tamaki and

Itoh, 2008; Fig. 3.1). The 300 km N-S trending trench acted as a depositional basin for the YG and the sediments accumulated at shallow marine-bathyal depths in a continental slope environment (Kaiho et al., 1993; Takashima et al., 2004). Post deposition the YG was compacted and then tilted by the late Tertiary rotation of the Japan Sea back-arc basin (Tamaki and Itoh, 2008).

The YG records a conformable sequence determined through bioevents and sedimentary structures (Kaiho et al., 1993). The OAE 2 section of the YG is part of the Saku Formation and outcrops on the Hakkin River, at Oyubari, on Hokkaido at  $\sim 142^{\circ} 9' 27''$  E,  $43^{\circ} 2' 44''$  N. The 300 m exposed OAE 2 section of the Saku Formation is represented in part by the Hakkin muddy-sandstone member and comprises dark-grey terrigenous sandy siltstone, bedded conglomeritic turbidites and finely laminated pyrite-rich green-grey mudstone (Fig. 3.2; Takashima et al., 2004). In addition, multiple thick and thin (0.02 – 2 m) felsic volcanic tuffs are interbedded throughout the sequence (Fig. 3.2; Takashima et al., 2004; Takashima et al., 2011), which are locally altered to bentonite (Takashima et al., 2004). Bioturbation is inconsistent yet intensifies up sequence and is abundant after the facies change in to the Hakkin muddy-sandstone Member, which demonstrates a change in depositional environment to shallow bathyal slope (Hasegawa and Saito, 1993). Despite the lack of true ‘black shales’, due to siliciclastic dilution, a high sedimentation rate ( $\sim 16$  cm/kyr) and a high voluminous influx of terrigenous detritus, the organic-rich sediments have a higher TOC content,  $\sim 0.5 - 1.2$  wt.% (Takashima et al., 2004), than some European Pelagic Shelf carbonate-rich sections, e.g., Eastbourne and Wunstorf. The sediment accumulation rate of the YG was high relative to other OAE 2

sections, because of the shoreface-inner shelf depositional setting at an active continental margin (Takashima et al., 2004).

The Oyubari YG section contains sufficient stratigraphic indicators for high-resolution global correlation of OAE 2, making it a key regional reference section for the NW Pacific (Hasegawa 1995). Global correlations of planktonic foraminifera illustrate a moderately diversified assemblage (Hasegawa 1999; Takashima et al., 2010): LO (last occurrence) of *R. cushmani* and *R. greenhornensis*, and FO (first occurrence) of *H. helvetica* and *M. schneegansi*, associated with the CTBI in the lower Saku Formation (Fig. 3.2; Hasegawa 1999). The aforementioned species are correlative in Portland, SW England and Poland (Hasegawa 1995), where *H. helvetica* is the datum biozone for the basal Turonian (Hasegawa 1999). Worldwide correlation and the identification of the CTBI in this instance is dependent upon the identification of *W. archaeocretacae*. However, the absence of *W. archaeocretacae* and the rare occurrence of *H. helvetica* means the FO of *M. schneegansi* identifies the base of the Turonian (Fig. 3.2; Takashima et al., 2010). The Hakkin muddy-sandstone member is characterised by radiolarians dominating 90% of the bio-grains within the grey siltstone (Hasegawa and Saito, 1993). Near to the CTB the diversity in faunal assemblages indicate higher dissolved  $\text{O}_2$  than in the Atlantic region (Kaiho et al., 1993). However, the reduction of dissolved  $\text{O}_2$  coincides with the extinction event at the CTB, and is reflected by the decrease in diversity and abundance of species (Kaiho et al., 1993).

This study revises the stratigraphic position of the OAE 2 onset from -39 m to -16.15 m (Fig. 3.3), facilitated by radiolarian stratigraphy, which will be discussed further in this paper based on  $\text{Os}_i$  and U-Pb data. The  $\delta^{13}\text{C}_{\text{wood}}$  is presented as a 5-

point moving average curve to smooth out the highly variable scatter, which may be a result of vital or diagenetic affects (Takashima et al., 2011). By averaging out the scatter, the  $\delta^{13}\text{C}_{\text{wood}}$  record is correlated with the Pont d'Issole section of the Vocontian Basin through 'B' and 'C' (Takashima et al., 2011). The revised stratigraphic position of 'A' demonstrates the characteristic positive excursion associated with the OAE 2 -16.15 m below the facies change to the Hakkin Muddy-Sandstone Member, from -25.3‰ to -19.4‰ VPDB (Fig. 3.3). The ~6‰ positive excursion is identified as the onset of OAE 2 (Fig. 3.3; this study). The  $\delta^{13}\text{C}_{\text{wood}}$  reaches a maximum of -19.3‰ (Fig. 3.3; Takashima et al., 2011) before the decline in  $\delta^{13}\text{C}_{\text{wood}}$  values to 'B'. The  $\delta^{13}\text{C}_{\text{wood}}$  values across the 'plateau' up to 'C' are less enriched in this section compared to other OAE 2 sites (e.g., GVS; Takashima et al., 2011). As such the profile records a continuous gradual trend to pre-OAE 2  $\delta^{13}\text{C}_{\text{wood}}$  values, which could be a reflection of the homogeneous nature of the deposits throughout the duration of OAE 2.

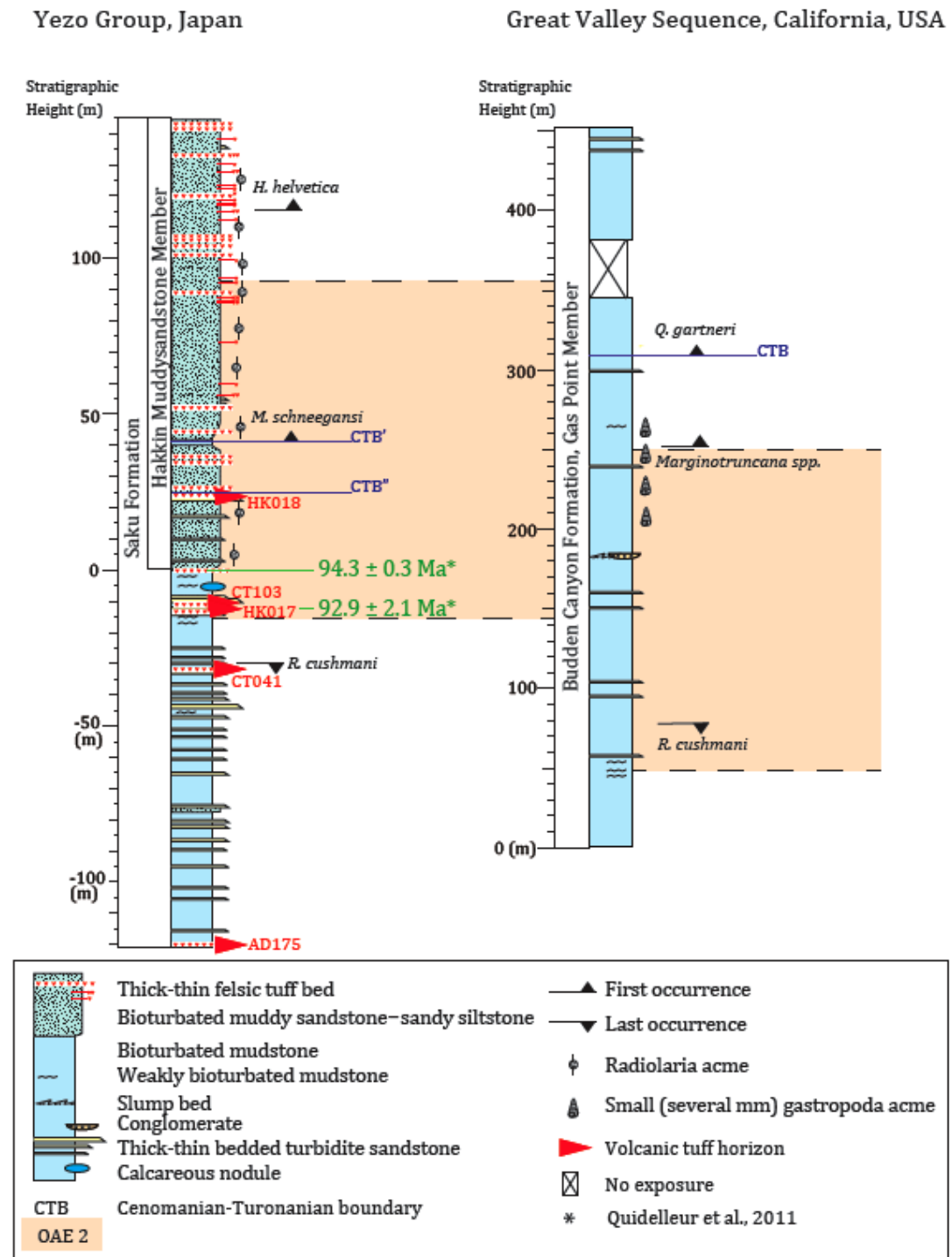


**Figure 3.2 Stratigraphic columns for Yezo Group, Japan and Great Valley Sequence, California, USA.** Cenomanian-Turonian boundary identified based on biozones. CTB' denotes the CTB according to Takashima et al. (2011). CTB'' denotes the CTB according to U-Pb ages (see section 5.1 for discussion). Volcanic tuff horizons for U-Pb zircon dating are marked on the Yezo Group section (red arrows). The OAE 2 interval is shaded in orange.

## 2.2. *Great Valley Sequence (GVS), California, USA*

Similar to the YG, the GVS was deposited along an active continental margin: ~30-40°N on the North American continental fore arc margin in upper bathyal depths (Fernando et al., 2011), along the western border of the Sacramento Valley (Fig. 3.1). The Budden Canyon Formation records sedimentary deposition from the Berriasian to the Turonian and is made up of 7 mappable units throughout road cuttings 122°33'02"W, 40°26'30"N in California (Murphy et al., 1969; Fernando et al., 2011); the youngest and uppermost unit is the Gas Point Member, ~730 m thick, which records the CTB and the OAE 2. Excursions in preliminary TOC results led to the recent identification of the OAE 2 in the GVS (Fernando et al., 2011) with similarly high TOC values as in the YG section. The OAE 2 interval is dominated by dark-grey terrigenous mudstone with some thinly bedded turbidites and minor conglomerate sandstone horizons becoming more frequent up sequence (Murphy et al., 1969; Takashima et al., 2011). The sediment accumulation rate of the GVS is estimated to be faster than at the sections along passive pelagic margins (Takashima et al., 2011). A high rate (from ~20 to 62 cm/kyr) is due to the active bathyal setting and the exceptionally high influx of terrigenous continental run-off (Fernando et al., 2011).

The palaeogeographic location of the GVS in comparison to other OAE 2 sites; i.e., the WIS is an epeiric sea, whereas the GVS is deposited in a fore arc basin (Fernando et al., 2011); results in the absence and/ or variability in abundance, distribution and duration of biozone horizons. The biostratigraphic record facilitates dating and correlation of the sequence; nannofossils are used for trans-basinal correlation and radiolarian zones are correlated to ammonite and foraminifera

bioevents of European age (Fernando et al., 2011). Ammonites and planktic foraminifera are used to estimate the stratigraphic level of the CTB; *P. japonicum* (Cenomanian), *P. californicum* (Turonian); and *R. cushmani* (Cenomanian), *H. helvetica* (Turonian), respectively. The identification of the LO of *L. acutus* nannofossil correlates the Pacific with Tethyan and Boreal Seas. The LO of *R. cushmani* is identified 80 m in to the OAE 2 interval and the FO *Q. gartneri* is the basal Turonian marker and ~315 m above the OAE 2 onset (Fig. 3.2; Takashima et al., 2011).

In this section the  $\delta^{13}\text{C}_{\text{wood}}$  curve is presented like YG as a 5-point moving average (Fig. 3.3). However, the record is less variable than the YG  $\delta^{13}\text{C}_{\text{wood}}$  record and depicts a more typical convex trend despite the subtle 1.2‰ VPDB positive excursion (Fig. 3.3; Takashima et al., 2011). As a result of the lower variability of the  $\delta^{13}\text{C}_{\text{wood}}$  curve, correlation with the Pont d'Issole section through datum levels 'A', 'B' and 'C' is more robust than for the YG section. The excursion marks the onset of OAE 2 at datum level 'A' (49 m; Fig. 3.3) from -24.5‰ to -23.3‰. The trough at 'B' is followed by a gradual enrichment to -20.8‰, where the 'plateau' of enriched  $\delta^{13}\text{C}_{\text{wood}}$  values continues up to 'C'. In the GVS the OAE 2 is recorded throughout an expanded section, ~201 m; after datum level 'C' the  $\delta^{13}\text{C}_{\text{wood}}$  values return to pre-OAE 2 values of ~ -23.5‰ (Fig. 3.3; Takashima et al., 2011).

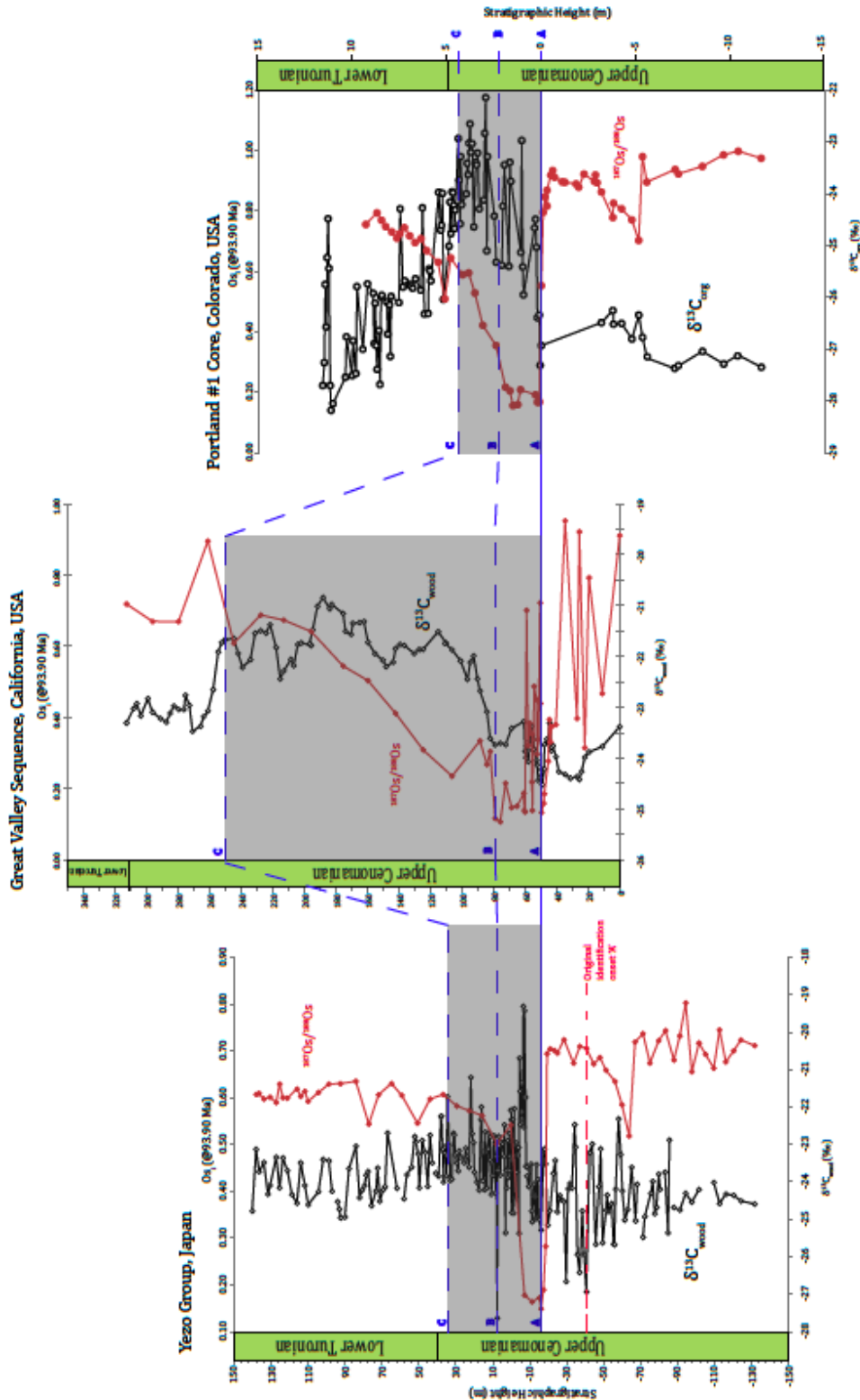


**Figure 3.3  $\delta^{13}\text{C}_{\text{wood}}$  and  $\delta^{13}\text{C}_{\text{org}}$  section correlation.**  $\delta^{13}\text{C}_{\text{wood}}$  (black) from Yezo Group, Japan; Great Valley Sequence, California, USA; and  $\delta^{13}\text{C}_{\text{org}}$  Portland #1 core, Colorado, USA. The  $\delta^{13}\text{C}_{\text{wood}}$  values represent a 5-point moving average. Initial  $^{187}\text{Os}/^{188}\text{Os}$  profiles are in red. The blue lines correlate stratigraphic horizons inferred from a combination of litho-, bio-, and chemostratigraphy (see text for details).

### ***3. Sampling and Analytical methodology***

#### *3.1. Sampling and preparation*

The YG outcrops in a section along the Hakkin River on Hokkaido, Japan. Samples of ~50 g were collected at 2 – 4 m intervals throughout the section. H. Nishi collected samples from the GVS, California, from outcrop approximately every meter. Both sections are considerably expanded and are therefore sampled at a lower spatial resolution relative to the Portland #1 core.

The bulk rock sample was cut and polished to remove any weathered exterior material. A dried sample weight of  $\geq 30$  g was powdered in order to homogenise the Re and Os within the sample (Kendall et al., 2009). A portion of sample, 0.2 – 1 g, was used for Re-Os analysis.

#### *3.2. Re-Os geochemistry*

All Re-Os analysis was conducted at DGC (Durham Geochemistry Centre; previously NIGLT, Northern Centre for Isotope Elemental Tracing) in TLSRG&G (TOTAL Laboratory for Source Rock Geochronology and Geochemistry).

The Re-Os analysis of the organic-rich sediments was conducted using Carius tube digestion in a 0.25 g/g  $\text{CrO}_3$  4N  $\text{H}_2\text{SO}_4$  reagent, with the Re and Os isolated from the acid medium using solvent extraction, micro-distillation and anion chromatography methodology (Selby and Creaser, 2003). In brief, 0.2 to 1 g of sample powder was loaded in a Carius tube with a known amount of mixed tracer solution,  $^{190}\text{Os} + ^{185}\text{Re}$ , with 8 ml of  $\text{CrO}_3\text{-H}_2\text{SO}_4$  solution. The sealed Carius tubes were then placed in an oven at 220°C for 48 hrs. Osmium was isolated and purified using solvent extraction ( $\text{CHCl}_3$ ) and micro distillation methods. To purify the Re

fraction 1 ml of the  $\text{CrO}_3\text{-H}_2\text{SO}_4$  solution was evaporated to dryness, with the Re extracted using solvent extraction methodology of NaOH and acetone (Cumming et al., 2012). The Re fraction was further purified using anion chromatography (Selby and Creaser, 2003). The purified Re and Os fractions were loaded onto Ni and Pt filaments, respectively (Selby and Creaser, 2003) with the addition of  $\sim 0.5\ \mu\text{l}$   $\text{BaNO}_3$  and  $\text{BaOH}$  activator solutions, respectively. Isotope compositions were measured using negative thermal ion mass spectrometry (NTIMS; Creaser et al., 1991; Völkening et al., 1991) via faraday cups for Re and electron multiplier (SEM) in peak hopping mode for Os.

Osmium isotopic ratios were calculated relative to  $^{188}\text{Os}$  and corrected for mass fractionation using a  $^{192}\text{Os}/^{188}\text{Os}$  value of 3.08261 (Nier, 1937). The oxide corrected  $^{185}\text{Re}/^{187}\text{Re}$  was normalised using a  $^{185}\text{Re}/^{187}\text{Re}$  value of 0.59738 (Gramlich et al., 1973). Total procedural blanks for Re and Os during this study are  $13.3 \pm 1.8$  pg/g and  $0.32 \pm 0.17$  pg/g, respectively, with  $^{187}\text{Os}/^{188}\text{Os}$  value of  $0.19 \pm 0.12$  (1 SD,  $n = 2$ ). Uncertainties for  $^{187}\text{Re}/^{188}\text{Os}$  and  $^{187}\text{Os}/^{188}\text{Os}$  are determined through full propagation of uncertainties in Re and Os mass spectrometer measurements, blank abundances and isotopic compositions, spike calibrations and reproducibility of standard Re and Os isotopic values. In-house standard solutions (DROsS and Re Std) are run repeatedly throughout each batch of samples to monitor mass spectrometer reproducibility. The Re standard yields an average  $^{187}\text{Re}/^{188}\text{Re}$  of  $0.59760 \pm 0.0011$  (1 SD,  $n = 37$ ). The Os standard (DROsS) yields an  $^{187}\text{Os}/^{188}\text{Os}$  average of  $0.16091 \pm 0.00020$  (1 SD,  $n = 35$ ). The determined isotope compositions of these Re and Os solutions are consistent within uncertainty to those determined at the Durham

Geochemistry Centre (Nowell et al., 2008; Cumming et al., 2012 and references therein).

### 3.3. Initial $^{187}\text{Os}/^{188}\text{Os}$ ( $O_{Si}$ )

The  $O_{Si}$  values in this study were determined from Re-Os data and the  $^{187}\text{Re}$  decay constant ( $1.666\text{e}^{-11}\text{a}^{-1}$ ; Smoliar et al., 1996) using the CTB age of 93.90 Ma (Meyers et al., 2012a; Gradstein et al., 2012). Analytical uncertainty for individual calculated  $O_{Si}$  is  $\leq 0.02$ . As an in-house standard we use USGS rock reference material SDO-1 (Devonian Ohio Shale; Kane et al., 1990) as recorded by Cumming et al. (2014) and Du Vivier et al. (2014; Chapter 2, this thesis). The reproducibility of calculated  $O_{Si}$  is  $\sim 0.04$  (2 SD; Du Vivier et al., 2014; Chapter 2, this thesis). This uncertainty was used to account for the maximum uncertainty in the sample set for the calculated  $O_{Si}$ . Calculated  $O_{Si}$  ratios assume closed system behaviour after deposition with respect to both rhenium and osmium. Furthermore, the  $^{187}\text{Os}/^{188}\text{Os}$  ratios reflect the isotope composition of the local seawater and are unaffected by mineral detritus (Selby and Creaser, 2003). In this study the SDO-1 Re-Os analysis yield average values (at the 2 SD level,  $n = 4$ ) consistent with accepted values of SDO-1 (Du Vivier et al., 2014; Chapter 2, this thesis; Re of  $79.8 \text{ ppb} \pm 12.9$ ; Os of  $659.3 \text{ ppt} \pm 101.0$ ;  $^{187}\text{Re}/^{188}\text{Os}$  of  $1171.1 \pm 38.6$ ;  $^{187}\text{Os}/^{188}\text{Os}$  of  $7.860 \pm 0.243$ ; and  $O_{Si}$  at 366 Ma of  $0.70 \pm 0.03$  (2 SD); see Table 3.1).

### 3.4. U-Pb zircon geochronology

All U-Pb zircon geochronology preparation, analysis and processing was conducted at NERC Isotope Geosciences Laboratory (NIGL), UK.

### *3.4.1. Zircon Mineral Separation*

For this study, samples have been obtained from 5 tuff horizons throughout the YG succession (Fig. 3.4). To liberate zircons from the soft and porous tuff samples they were submerged in water to completely disaggregate the matrix. This material was then passed through a 355  $\mu\text{m}$  wet sieve. The first density separation was achieved using a Rogers shaking table. The collected heavy fraction was dried at 60°C before magnetic separation using a FRANTZ isodynamic magnetic separator. The non-magnetic fractions of each sample were then density separated using methylene iodide. Cathodoluminescence techniques were used to investigate the zircon morphology. The images were gathered using a Scanning Electron Microscope (SEM); grains with the least cracks and inclusions were handpicked in ethanol for U-Pb zircon CA-ID-TIMS analysis.

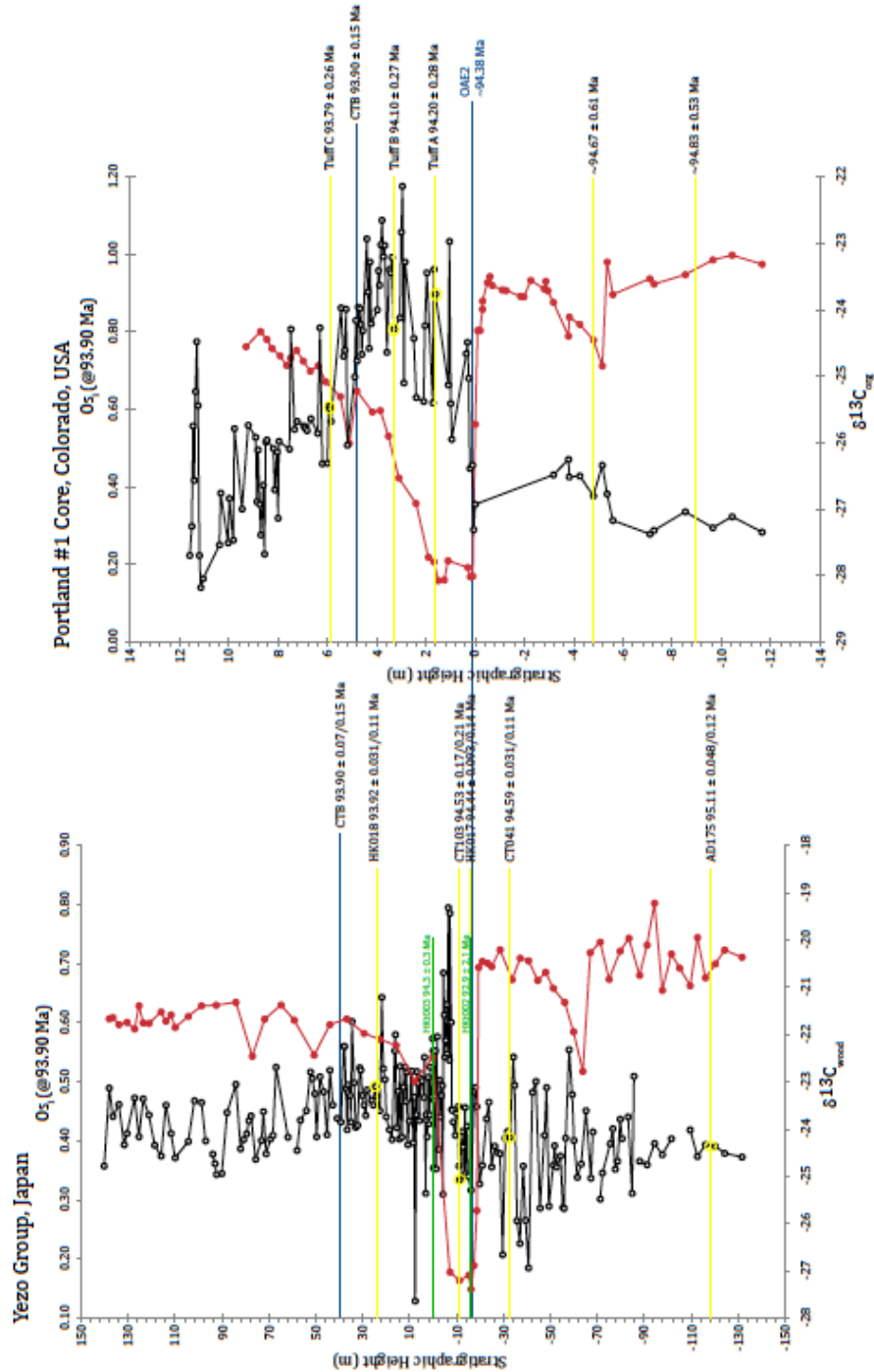


**Figure 3.4** Illustrates the stratigraphic height of the U-Pb dated tuff horizons from the Yezo Group, Japan on the  $\text{Os}_i$  (red) and  $\delta^{13}\text{C}$  (black) profiles.  $^{206}\text{Pb}/^{238}\text{U}$  weighted mean ages are labelled with analytical uncertainties ( $2\sigma$ ) and with total uncertainties ( $2\sigma$ ; analytical+tracer+ $^{238}\text{U}$  decay constant; Jaffey et al., 1971; Condon et al., *in review*). The existing U-Pb ages for the Yezo Group are in green with total uncertainties ( $2\sigma$ ; Quidelleur et al., 2011). The ages on the Portland #1 core are weighted mean  $^{40}\text{Ar}/^{39}\text{Ar}$  ages with total uncertainties ( $2\sigma$ ; Tuff A, B, C; Meyers et al., 2012a) and recalculated  $^{40}\text{Ar}/^{39}\text{Ar}$  ages (D and E; Adams et al., 2010). The correlated datum level ‘A’, the extrapolated age of the onset of OAE 2 (Du Vivier et al., 2014; Chapter 2, this thesis), and the CTB, are shown in blue. See text for discussion.

### 3.4.2. U-Pb Zircon ID-TIMS

In order to eliminate Pb-loss all the analysed zircon crystals were subjected to the chemical abrasion pre-treatment technique: thermal annealing and subsequent leaching (Mattinson, 2005). To anneal the zircons the crystals were put in to quartz beakers that were placed in a muffled furnace at 900°C for ~60 hrs before SEM imaging and/or visual inspection. Selected crystals/fragments were photographed in transmitted light and transferred in to 300 µl Teflon FEP microcapsules and placed in a Parr bomb, and leached in a ~10:1 mix of 29 M HF + 30% HNO<sub>3</sub> for 12 hrs at ~180°C. Subsequent to leaching the acid solution was removed from the zircon fractions which were then rinsed in 30% HNO<sub>3</sub>, then fluxed on a hotplate at ~80°C for >1 hr in 6 M HCl, cleaned for an hour in an ultrasonic bath, then fluxed again for a further 30 minutes. The HCl solution was then removed and crystals were spiked with a mixed  $^{202}\text{Pb}$ - $^{205}\text{Pb}$ - $^{233}\text{U}$ - $^{235}\text{U}$  tracer solution (ET2535; Condon et al., 2007; Condon et al., *in review*; McLean et al., *in review*). The zircon crystals were dissolved in ~120 µl of 29 M HF with a trace amount of HNO<sub>3</sub>, in microcapsules that were placed in Parr bombs at ~220°C for >60 hrs. The samples were then dried down to fluorides, converted to chlorides by adding 3 M HCl at ~180°C in microcapsules in Parr bombs. U and Pb for all zircons were then separated through standard HCl-based anion-exchange chromatographic procedures (Mattinson, 2005).

Isotope ratios were measured using TIMS on a Triton Mass Spectrometer. U and Pb were loaded on a single Re ribbon filament in a silica gel/phosphoric acid mixture. U ratios were made in static Faraday mode. Pb was measured in peak-hopping in a single SEM detector.

All U-Pb dates (ID-TIMS) were calculated using the  $^{238}\text{U}$  and  $^{235}\text{U}$  decay constants of Jaffey et al. (1971). The  $^{238}\text{U}/^{235}\text{U}_{\text{zircon}}$  value of  $137.818 \pm 0.045$  (Hiess et al., 2012) was used in the data reduction calculations for ID-TIMS dates. Data reduction was carried out using U-Pb REDUX (McLean et al., 2011).

## 4. Results

### 4.1. Re-Os Abundance

Across the onset of OAE 2 there is a noticeable shift to an increase Os abundance (Table 3.2). In the YG the Os concentration increases by  $\sim 220$  ppt from 11.45 ppt to 236.71 ppt in  $\sim 1$  m and within 20 m returns to 35.19 ppt. In the GVS the Os concentration is more variable, with the increase in Os abundance occurring simultaneously with unradiogenic  $\text{Os}_i$  values (discussed below). Conversely, Re abundance is relatively constant at both sections, but are typically higher before the onset of OAE 2. The Re abundance ranges from  $\sim 0.20$  -  $\sim 1.60$  ppb at YG and from  $\sim 0.25$  -  $\sim 3.75$  ppb at GVS. The dramatic difference between the Re and Os abundance produce a similar profile in  $^{187}\text{Re}/^{188}\text{Os}$  to the  $\text{Os}_i$  profile, with an abrupt decrease in the  $^{187}\text{Re}/^{188}\text{Os}$  directly associated with the abrupt increase in Os abundance.

### 4.2. Initial osmium ( $\text{Os}_i$ )

The initial osmium isotope data obtained for the two trans-Pacific locations: YG, Japan and the GVS, California are presented in Figure 3.3 and Table 3.2 (3.2a YG; 3.2b GVS).

#### 4.2.1. $\text{Os}_i$ stratigraphy of the Yezo Group, Japan

Prior to 'A', the onset of OAE 2, the  $\text{Os}_i$  values are radiogenic and moderately heterogeneous: 0.66 – 0.80. The  $\text{Os}_i$  show a brief and abrupt trend to a less radiogenic value of 0.52, ~47 m prior to the onset of the event, before returning to radiogenic values (Fig. 3.3). The  $\text{Os}_i$  values remain radiogenic up to ~4 m before the onset of the OAE 2 when the  $\text{Os}_i$  data rapidly become unradiogenic. This dramatic trend from 0.69 to 0.19 coincides with the onset of OAE 2 at 'A' and is characteristic of all  $\text{Os}_i$  profiles for the OAE 2 (Turgeon and Creaser, 2008; Du Vivier et al., 2014; Chapter 2, this thesis). The  $\text{Os}_i$  values remain unradiogenic for ~10 m, before they abruptly return to radiogenic  $\text{Os}_i$  at 'B' (0.50). For the remainder of OAE 2 and after the end of the event, the  $\text{Os}_i$  data are radiogenic and relatively homogeneous, 0.50 – 0.63 (Fig. 3.3).

#### 4.2.2. $\text{Os}_i$ stratigraphy of the Great Valley Sequence, USA

In the GVS the  $\text{Os}_i$  values are highly variable. The radiogenic trend recorded in the YG (and all other OAE 2 sequences) before 'A' is interrupted in the GVS by frequent oscillations to unradiogenic  $\text{Os}_i$  values, 0.95 to 0.32 (Fig. 3.3). The most radiogenic  $\text{Os}_i$  value recorded 15 m before the onset of OAE 2, marks the initiation of the unradiogenic trend in  $\text{Os}_i$  values to 'A'. At 'A' the unradiogenic  $\text{Os}_i$  values, 0.13, are close to chondritic basaltic values (Peucker-Ehrenbrink and Ravizza, 2000). There are two rapid and short-lived trends to radiogenic values (~0.75) within the first 10 m of OAE 2 (Fig. 3.3). The  $\text{Os}_i$  values remain unradiogenic for a further ~20 m, where at 'B' the  $\text{Os}_i$  value is 0.12. The  $\text{Os}_i$  values then exhibit a less sudden return from 0.12 ('B') at ~80 m, to pre-OAE 2 values at 'C', where the  $\text{Os}_i$  is 0.61.

Despite the more variable nature in the  $\text{Os}_i$  data of the GVS the overall trend is akin to the Portland core, the YG (Fig. 3.3) and other sites (Du Vivier et al., 2014; Chapter 2, this thesis; Fig. 3.1). The key difference is that the GVS is characterised by more radiogenic  $\text{Os}_i$  values than the YG section before and after the OAE 2 interval.

#### 4.3. *U-Pb analysis*

For each volcanic tuff sample we identify the population of youngest concordant zircon U-Pb analyses and calculate a  $^{206}\text{Pb}/^{238}\text{U}$  weighted mean age as an approximation for the eruption age of the ash layer (Table 3.3a, 3.3b; Fig. 3.5). The coherence of the youngest population is assessed via the MSWD value, each of which is within the acceptable range for the given number of analyses (Wendt and Carl, 1991). In each case the mean age is based on three to five individual  $^{206}\text{Pb}/^{238}\text{U}$  dates that include the youngest  $^{206}\text{Pb}/^{238}\text{U}$  date in each sample. The assumption made here is that zircon was crystallising in the magma chamber immediately prior to eruption such that the youngest zircons/zircon domains will yield  $^{206}\text{Pb}/^{238}\text{U}$  dates that approximate the eruption age and inferentially the absolute age of the stratigraphic level sampled. As such older zircon  $^{206}\text{Pb}/^{238}\text{U}$  dates are interpreted as reflecting crystallisation in a magmatic system prior to eruption and/or the inclusion of older materials during explosive volcanism and/or ash deposition. Alternative ways to interpret the distribution of  $^{206}\text{Pb}/^{238}\text{U}$  dates from an ash bed are possible, for example, using only the youngest  $^{206}\text{Pb}/^{238}\text{U}$  date as the best approximation of the youngest zircon in the ash bed, and inferentially the eruption age (e.g., Schoene et al., 2010), and our age model using OxCal (Bronk Ramsey, 2008; Fig. 3.6B). This

approach requires that the youngest  $^{206}\text{Pb}/^{238}\text{U}$  date accurately represents the youngest zircon in the ash bed and such an interpretation will be impacted by any minor Pb-loss, and must consider the fact that even if there were a single age population in the ash bed, sampling of this population will result in a normal distribution of  $^{206}\text{Pb}/^{238}\text{U}$  dates around the true age; ad hoc selection of the youngest date could result in an age that is on the young side of the distribution. To counter this effect we chose a ‘youngest coherent’ population of  $^{206}\text{Pb}/^{238}\text{U}$  dates as considered to best approximate the time elapsed since eruption and deposition, having considered the potential for minor Pb-loss and mitigation via pre-treatment methods employed (Mattinson, 2005), inheritance and recycling. We report preferred  $^{206}\text{Pb}/^{238}\text{U}$  weighted mean ages of  $95.114 \pm 0.048/0.12$  Ma (AD175),  $94.591 \pm 0.031/0.11$  Ma (CT041),  $94.436 \pm 0.093/0.14$  Ma (HK017),  $94.530 \pm 0.170/0.21$  Ma (CT103) and  $93.920 \pm 0.031/0.11$  Ma (HK018) with MSWD values ranging between 0.4 to 2.0, values that are acceptable for a single population of the given sample size (Table 3.3b; Fig. 3.5; Wendt and Carl, 1991). The uncertainties reflect the following sources: analytical/analytical + tracer solution + decay constants; the latter value is the total uncertainty in each case which should be used when comparing these dates to other non-U-Pb derived dates (i.e., the age model for the CTB from Meyers et al., 2012a that are largely based upon  $^{40}\text{Ar}/^{39}\text{Ar}$  data), the former is to be used when quantifying differences between dates in this study. Figure 3.5 shows the stratigraphic sequence of tuff horizons in the YG section with the U-Pb zircon dates of this study and those of Quidelleur et al. (2011) are presented on Figure 3.4 for comparison.

Table 3.3a U-Pb zircon CA-ID-TIMS data for tuff horizons throughout the Cenomanian-Turonian boundary interval, Yezo Group, Japan.

Sample	Composition						Isotopic Ratios						Dates (Ma)														
	Fraction	Pb*/(Pb+U)	Pb*/Pb	Th*/(Th+U)	Th*/Pb	Th*/(Th+U)	<sup>206</sup> Pb/ <sup>238</sup> U	<sup>207</sup> Pb/ <sup>235</sup> U	<sup>206</sup> Pb/ <sup>207</sup> Pb	<sup>206</sup> Pb/ <sup>238</sup> U	<sup>207</sup> Pb/ <sup>235</sup> U	<sup>206</sup> Pb/ <sup>207</sup> Pb	<sup>206</sup> Pb/ <sup>238</sup> U	<sup>207</sup> Pb/ <sup>235</sup> U	<sup>206</sup> Pb/ <sup>207</sup> Pb	<sup>206</sup> Pb/ <sup>238</sup> U	<sup>207</sup> Pb/ <sup>235</sup> U	<sup>206</sup> Pb/ <sup>207</sup> Pb	<sup>206</sup> Pb/ <sup>238</sup> U	<sup>207</sup> Pb/ <sup>235</sup> U	<sup>206</sup> Pb/ <sup>207</sup> Pb	<sup>206</sup> Pb/ <sup>238</sup> U	<sup>207</sup> Pb/ <sup>235</sup> U	<sup>206</sup> Pb/ <sup>207</sup> Pb			
	([206]/([206]+[238]))	([206]/([206]+[238]+[232]))	([206]/([206]+[238]))	([207]/([207]+[232]))	([207]/([207]+[232]+[238]))	([207]/([207]+[232]))	([206]/[238])	([207]/[235])	([206]/[207])	([206]/[238])	([207]/[235])	([206]/[207])	([206]/[238])	([207]/[235])	([206]/[207])	([206]/[238])	([207]/[235])	([206]/[207])	([206]/[238])	([207]/[235])	([206]/[207])	([206]/[238])	([207]/[235])	([206]/[207])	([206]/[238])	([207]/[235])	
HK018	1. z1	21.66	24.04	0.90	0.57	1450	0.014690	0.04	0.094877	0.21	0.047895	0.20	0.0418	94.008	0.04	93.889	0.19	93.041	4.76								
	2. z1B	15.17	12.91	1.26	0.57	733	0.014672	0.06	0.096595	0.45	0.047814	0.42	0.0493	93.895	0.05	93.628	0.40	89.021	10.02								
	2. z3	12.66	12.99	1.05	0.64	725	0.014700	0.19	0.096986	0.71	0.047874	0.61	0.024	94.075	0.18	93.917	0.64	91.993	14.54								
	z1	28.66	20.14	1.42	0.66	1188	0.014704	0.08	0.096033	0.32	0.047876	0.28	0.014	94.096	0.07	93.941	0.29	92.084	6.59								
	z2	38.22	33.82	1.16	0.65	1942	0.014700	0.06	0.097137	0.20	0.047990	0.16	0.065	94.071	0.06	94.130	0.18	92.724	3.91								
	z5	40.68	33.81	2.26	0.71	1053	0.014693	0.15	0.097096	0.30	0.047900	0.31	0.065	94.030	0.14	94.092	0.34	97.507	7.28								
	z6A	10.16	33.30	0.30	0.53	2019	0.014688	0.04	0.096752	0.22	0.047842	0.21	0.284	93.994	0.03	93.774	0.19	90.397	4.95								
	z8B	20.37	37.78	0.54	0.56	2270	0.014680	0.04	0.096592	0.38	0.047787	0.36	0.479	93.945	0.04	93.626	0.16	87.678	3.94								
	z7B	24.03	51.56	0.47	0.63	3037	0.014710	0.04	0.097140	0.34	0.047960	0.32	0.448	94.133	0.04	94.138	0.12	96.240	2.94								
	z8	33.31	63.79	0.52	0.58	3806	0.014664	0.13	0.096881	0.37	0.047986	0.30	0.792	93.846	0.12	93.902	0.15	97.507	2.89								
z9	9.68	18.84	0.51	0.77	1084	0.014756	0.04	0.097283	0.32	0.047878	0.31	0.273	94.126	0.04	94.285	0.29	92.177	7.42									
CT103	z1	116.61	191.44	0.61	0.07	12326	0.0207141	0.07	3.227135	0.13	0.113053	0.68	0.771	34.344	1213.566	0.76	1463.709	0.99	1848.242	1.57							
	z2	1.25	2.23	0.56	0.65	147	0.014757	0.05	0.095685	4.66	0.047088	4.57	0.253	94.437	0.43	92.786	4.13	52.623	109.04								
	z4	1.85	4.15	0.33	0.77	252	0.014769	0.26	0.094181	2.78	0.046271	2.73	0.233	94.510	0.24	91.317	2.43	30.663	65.67								
	z5	1.11	1.41	0.79	0.64	100	0.014736	0.69	0.092917	7.66	0.043792	7.35	0.203	94.303	0.64	90.217	6.61	14.410	102.41								
	z6	0.99	2.60	0.38	0.66	169	0.014793	0.44	0.090174	3.86	0.049178	3.80	0.177	94.665	0.41	96.937	3.57	155.253	89.05								
	z8	0.61	1.64	0.57	0.66	113	0.014800	0.60	0.097716	6.37	0.047948	6.28	0.196	94.709	0.56	94.666	5.76	95.639	148.64								
HK017	z1	5.28	7.70	0.69	0.47	487	0.014836	0.13	0.092947	1.51	0.045562	1.49	0.204	418.367	94.936	0.13	90.245	1.30	20.792	36.05							
	z2	1.44	1.36	1.06	0.60	98	0.014884	0.73	0.097087	7.60	0.047372	7.30	0.185	42.091	93.242	0.69	94.084	6.25	66.969	176.61							
	z3	4.76	2.07	2.29	0.52	142	0.014759	0.05	0.098241	4.65	0.048382	4.59	0.167	17.948	94.449	0.42	95.151	4.22	115.002	108.35							
	z7	4.41	7.26	0.61	0.70	434	0.014743	0.15	0.097486	1.48	0.047982	1.46	0.212	3.156	94.343	0.14	94.379	1.33	97.334	34.45							
	z8	3.56	7.52	0.47	0.61	459	0.014771	0.16	0.096433	1.47	0.047413	1.43	0.296	36.837	94.524	0.15	93.478	1.31	69.016	34.09							
	z9	3.99	2.16	1.85	0.58	145	0.014761	0.08	0.098325	4.52	0.048378	4.46	0.177	19.170	94.457	0.45	95.229	4.11	116.753	105.23							
CT041	z10	7.44	4.70	1.58	0.62	292	0.014828	0.21	0.098615	2.13	0.048380	2.10	0.199	16.080	94.884	0.20	95.497	1.94	112.938	49.51							
	z11	9.26	2.84	3.26	0.82	176	0.014761	0.36	0.097193	3.71	0.047816	3.67	0.179	-5.927	94.459	0.34	94.182	3.34	89.101	86.91							
	z12	2.46	9.24	0.27	1.09	503	0.014868	0.11	0.097522	1.81	0.047626	1.76	0.568	-39.361	95.141	0.10	94.486	0.92	79.653	22.70							
	z12A	15.65	49.38	0.32	0.61	2925	0.014818	0.04	0.097927	0.36	0.047995	0.35	0.391	3.300	94.322	0.04	94.861	0.14	97.971	3.50							
	z13B	6.95	10.96	0.69	0.86	575	0.014785	0.10	0.097697	0.56	0.047984	0.51	0.583	2.937	94.614	0.09	94.648	0.51	97.399	12.15							
	z13A	20.27	54.64	0.37	0.71	3159	0.014782	0.04	0.097667	0.13	0.047982	0.11	0.452	2.071	94.594	0.03	94.620	0.11	97.307	2.69							
AD175	z14	5.83	8.51	0.45	0.80	497	0.014766	0.14	0.097369	0.70	0.047857	0.65	0.446	-3.598	94.491	0.13	94.289	0.63	91.135	15.35							
	z15	5.64	15.14	0.37	0.56	921	0.014914	0.06	0.098879	0.38	0.047955	0.35	0.484	0.691	95.432	0.05	95.372	0.35	93.859	8.42							
	z16	13.06	18.92	0.72	0.75	1044	0.014882	0.36	0.097749	0.55	0.047699	0.40	0.674	-14.249	95.229	0.34	94.696	0.49	81.300	9.58							
	z15A	61.28	29.56	2.07	0.42	1849	0.014879	0.17	0.098374	0.25	0.048020	0.17	0.704	4.097	95.210	0.16	95.275	0.23	96.891	4.19							
	z15C	18.08	30.05	0.69	0.40	1889	0.014863	0.06	0.098327	0.20	0.048049	0.18	0.476	5.582	95.108	0.05	95.231	0.18	90.322	4.26							
	z17	57.30	16.98	3.56	0.41	1018	0.014831	0.25	0.097969	0.41	0.047979	0.29	0.701	2.417	94.902	0.23	94.900	0.37	94.846	6.95							
z22	44.75	42.96	1.06	0.38	2648	0.014881	0.27	0.098346	0.32	0.0484081	0.24	0.902	3.189	95.221	0.26	95.248	0.29	95.937	3.29								
z3	5.42	5.29	1.02	0.92	307	0.015084	1.19	0.098845	1.78	0.047583	1.24	0.722	-24.436	96.514	1.14	95.710	1.63	75.597	29.42								
z4a	8.28	7.11	1.16	0.87	411	0.014972	0.40	0.098264	1.11	0.047660	1.00	0.433	-17.647	95.798	0.38	95.172	1.01	79.517	23.83								

(a) Total mass of radiogenic Pb.  
 (b) Ratio of radiogenic Pb (including 208Pb) to common Pb.  
 (c) Total mass of common Pb.  
 (d) Th contents calculated from radiogenic 208Pb and the 207Pb/206Pb date of the sample, assuming concordance between U-Th and Pb systems.  
 (e) Measured ratio corrected for fractionation and spike contribution only.  
 (f) Measured ratios corrected for fractionation, tracer and blank.  
 (g) Corrected for initial Th/U disequilibrium using radiogenic 208Pb and Th/U (magmas) = 2.80008.  
 (h) % discordance = 100 - (100 \* (206Pb/238U date) / (207Pb/235U date)).  
 (i) Isotopic dates calculated using the decay constants λ238 = 1.55125E-10 and λ235 = 9.8485E-10 (Jaffey et al. 1971).

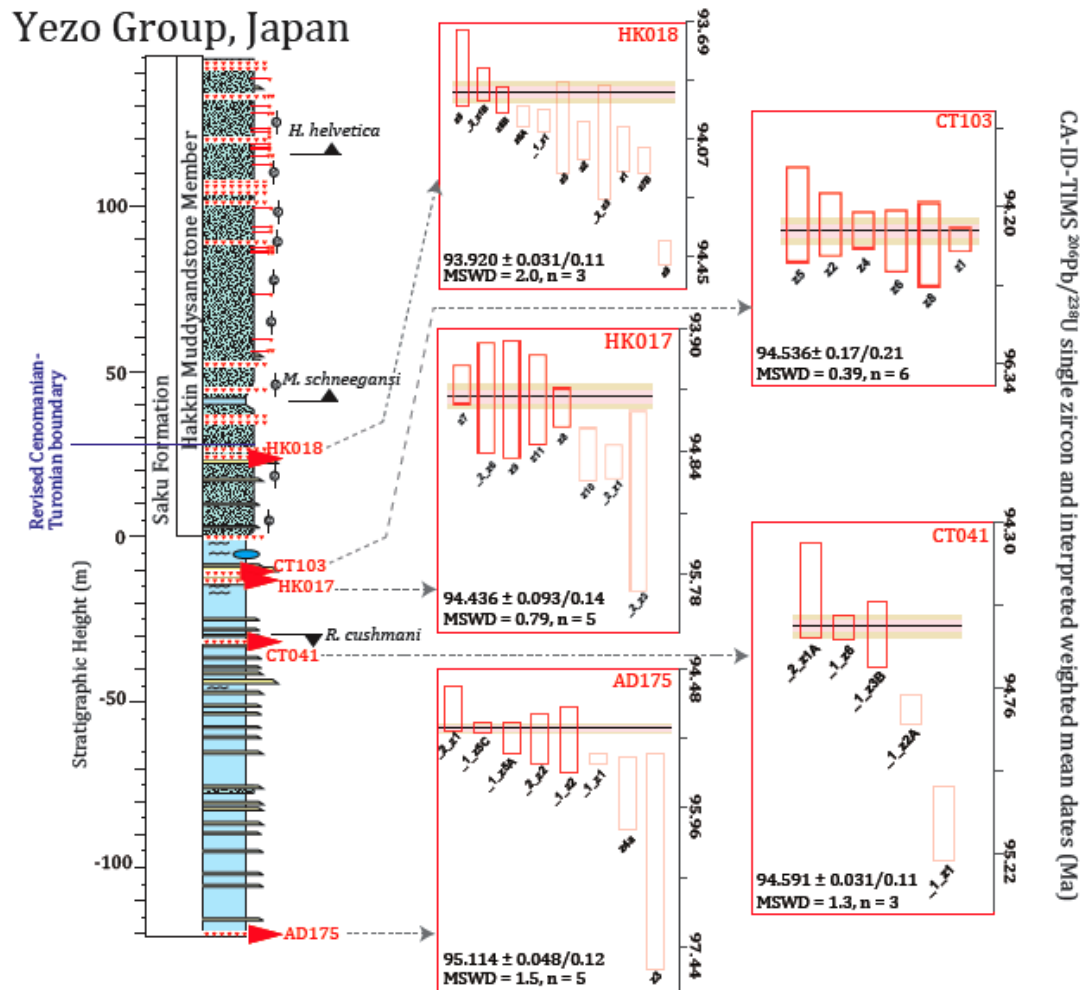


**Figure 3.5** Lithostratigraphy and biostratigraphy of the Yezo Group section, Japan with CA-ID-TIMS  $^{206}\text{Pb}/^{238}\text{U}$  single zircon and interpreted weighted mean ages.  $^{206}\text{Pb}/^{238}\text{U}$  weighted mean ages, bold red squares, are plotted with analytical uncertainties ( $2\sigma$ ) and with total uncertainties ( $2\sigma$ ; analytical+tracer+ $^{238}\text{U}$  decay constant; Jaffey et al., 1971; Condon et al., *in review*). Analyses excluded from weighted mean calculation for  $^{206}\text{Pb}/^{238}\text{U}$  (i.e., Pb loss; inheritance) are indicated by opaque red squares (see text for discussion). The MSWD and the number of single zircon analyses included for each sample are also shown (see text for discussion, Wendt and Carl, 1991).

**Table 3.3b** U-Pb Zircon CA-ID-TIMS summary data for volcanic tuff horizons throughout the CTBI, Yezo Group, Japan

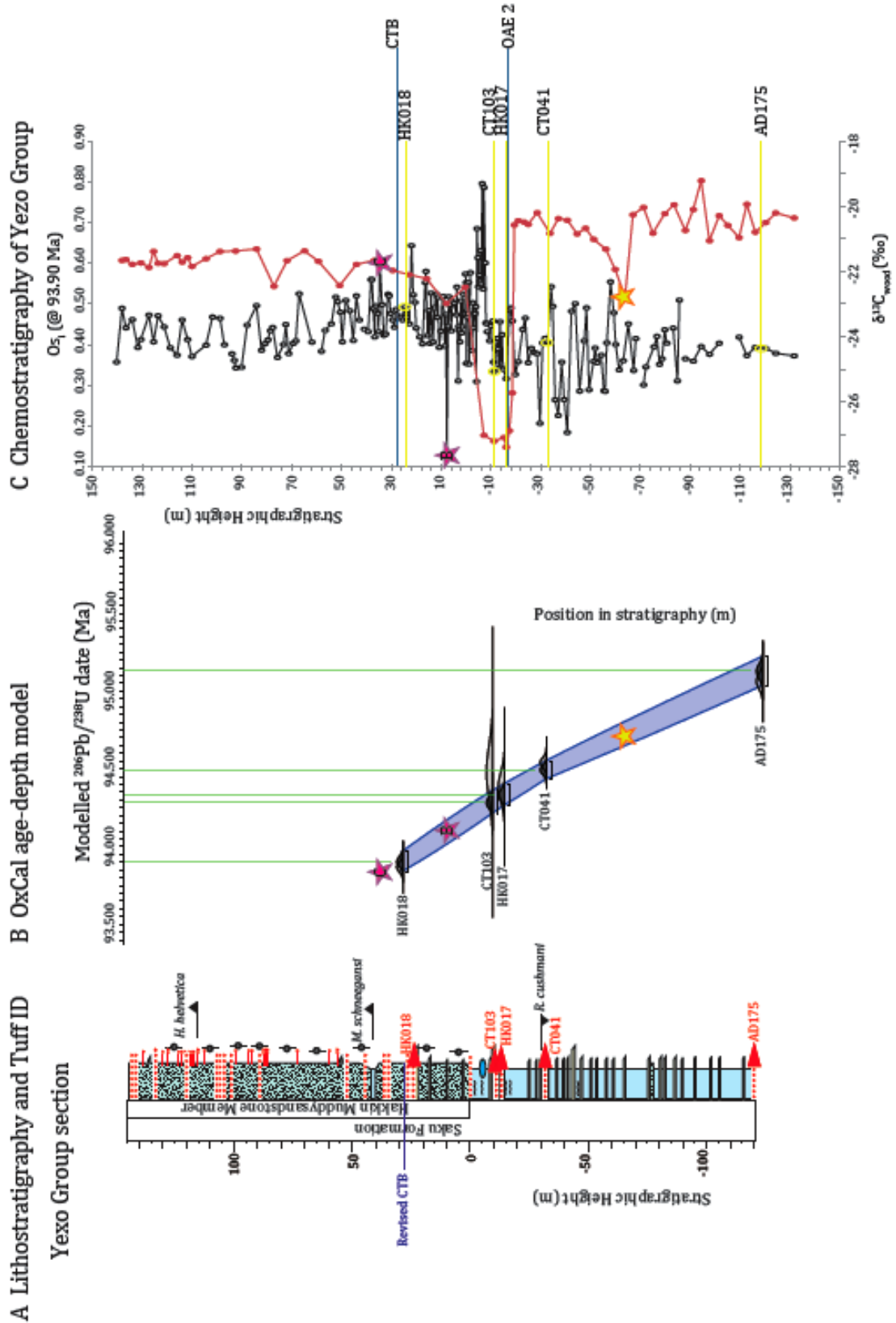
Sample ID	$^{206}\text{Pb}/^{238}\text{U}$ date (Ma)	$\pm(a)$	$\pm(b)$	MSWD	dates used
HK018	93.920	0.031	0.11	2.0	youngest 3 (of 13)
CT103	94.536	0.170	0.21	0.4	youngest 6 (of 6)
HK017	94.436	0.093	0.14	0.8	youngest 5 (of 8)
CT041	94.591	0.031	0.11	1.3	youngest 3 (of 5)
AD175	95.114	0.048	0.12	1.5	youngest 5 (of 8)

(a) analytical

(b) analytical + tracer +  $^{238}\text{U}$  decay constant

The age-depth model (Fig. 3.6B) graphically illustrates the temporal relationships of the tuff horizons relative to depth. The model demonstrates that the  $^{206}\text{Pb}/^{238}\text{U}$  ages obey superposition; with the exception of CT103 the tuff horizons get stratigraphically younger within uncertainty (Fig. 3.5, 3.6B). The model therefore graphically demonstrates the uncertainty of the CT103 age (Fig. 3.6B; see discussion section 5.1).

**Figure 3.6 (next page 114) Lithostratigraphy and Tuff ID of the Yezo Group section (A) vs. OxCal age-depth model (B) vs. Chemostratigraphy of the Yezo Group section (C).** OxCal age-model (Bronk Ramsey, 2008) authenticates the weighted mean  $^{206}\text{Pb}/^{238}\text{U}$  zircon ages in the stratigraphy. The light grey areas represent the distribution for single calibrated dates. The dark grey areas demonstrate the marginal posterior distribution (Bronk Ramsey, 2008; see text for discussion, section 5.1; Table 3.6). The Yezo Group section  $\delta^{13}\text{C}_{\text{wood}}$  (black) and  $\text{Os}_i$  (red) profiles are plotted against stratigraphic height.  $^{206}\text{Pb}/^{238}\text{U}$  weighted mean ages are given with total uncertainties ( $2\sigma$ ; analytical+tracer+ $^{238}\text{U}$  decay constant): HK018 =  $93.92 \pm 0.031/0.11$  Ma; CT103 =  $94.53 \pm 0.17/0.21$  Ma; HK017 =  $94.44 \pm 0.093/0.14$  Ma; CT041 =  $94.59 \pm 0.031/0.11$  Ma; AD175 =  $95.11 \pm 0.048/0.12$  Ma. The Bayesian age of the CTB  $93.90 \pm 0.07/0.15$  Ma is from Meyers et al. (2012a). Ages between dated tuff horizons can be interpolated from both the WIS and the Yezo Group, which can be projected on to the isotope profiles of the Portland core and the Yezo Group section, respectively. Equally, stratigraphic datum levels (pink stars ‘B’ and ‘C’) or isotope values (yellow star) can be projected from 3.6C on to the age model to clarify trans-basin integration (see text for discussion, section 5.3.1 and 5.3.2, respectively).



## 5. Discussion

### 5.1. OAE 2 correlation

Traditionally the onset of OAE 2 is identified by a positive excursion in the  $\delta^{13}\text{C}$  record ('A', Pratt et al., 1985; Schlanger et al., 1987; Jenkyns, 1980). The development of  $\text{Os}_i$  profiles for Atlantic, WIS and Tethyan OAE 2 sections exhibit an abrupt shift from radiogenic ( $\sim 0.7$  to  $1.0$ ) to unradiogenic values ( $\sim 0.20$  to  $0.30$ )  $\sim 50$  kyr prior to the onset of OAE 2 (Fig. 3.7; Turgeon and Creaser, 2008; Du Vivier et al., 2014; Chapter 2, this thesis). The change in Os isotope composition relates directly to a major pulse of volcanic activity that was associated with the Caribbean LIP that was contemporaneous with the onset of OAE 2 (Fig. 3.7; Snow et al., 2005; Turgeon and Creaser, 2008; Du Vivier et al., 2014; Chapter 2, this thesis).

Previously, the onset of the OAE 2 in the two Pacific sections was tentatively identified by Takashima et al. (2011) based on the  $\delta^{13}\text{C}_{\text{wood}}$ ; however, it was uncertain due to a lack of definitive biostratigraphic and in particular additional chemostratigraphic data, which would facilitate with the identification of the onset horizon from the variable  $\delta^{13}\text{C}_{\text{wood}}$ . Figure 3.3 shows the height of the original interpretation of the onset of OAE 2 in the YG section, 'red line' (Takashima et al., 2011). This position of the OAE 2 is  $\sim 24$  m below the unradiogenic trend in  $\text{Os}_i$ , which contrasts to the similarity between  $\delta^{13}\text{C}$  and  $\text{Os}_i$  from all other OAE 2 sites (Du Vivier et al., 2014; Chapter 2, this thesis). The unradiogenic trend at the onset of OAE 2 coincides with the simultaneous increase ( $\sim 220$  ppt) in Os concentration, an increase that is observed in the  $\text{Os}_i$  record from all other sections. In addition, despite the lack of additional isotopic analyses (i.e., Nd, Pb, Sr, P, U) compared to sites such as Portland and the Vocontian Basin, if we integrate on going research on  $\delta^{13}\text{C}_{\text{wood}}$ ,

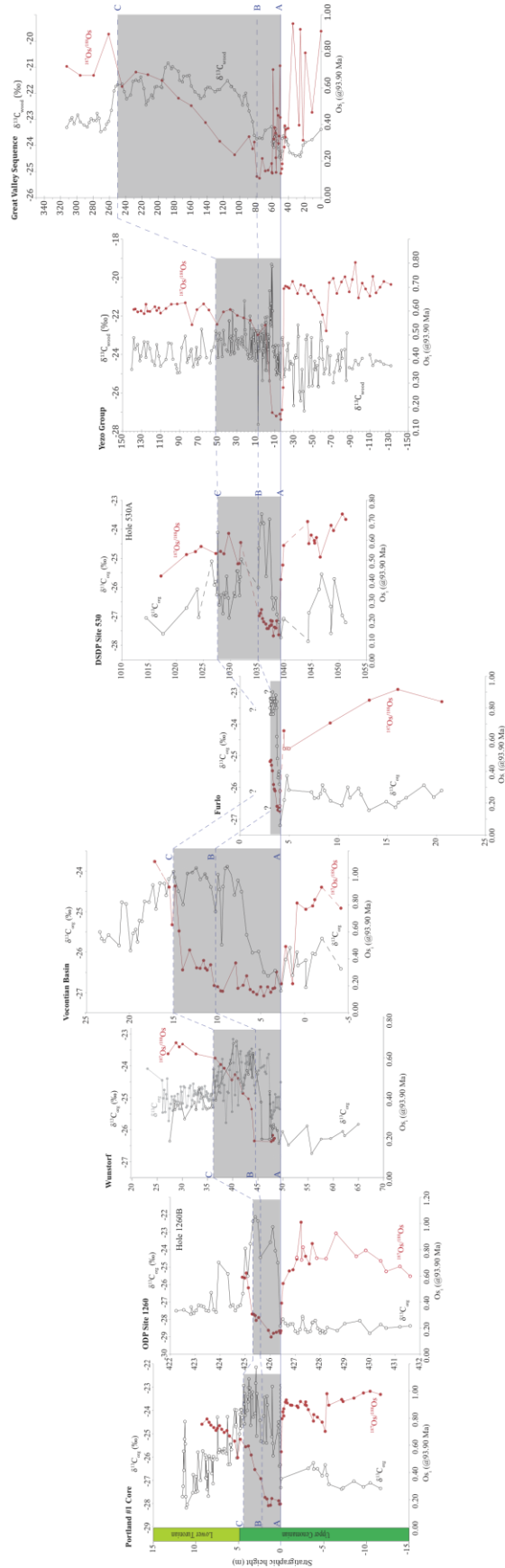
litho-, bio-, and chemostratigraphy (Takashima, *pers comm.*) with the interpretation of the  $\text{Os}_i$  trend from other global sites (Fig. 3.7; Du Vivier et al., 2014; Chapter 2, this thesis), the onset of OAE 2 occurs at -16.15 m (Fig. 3.3) in the YG section.

Absolute evidence to support the correlation of the onset of OAE 2 comes from U-Pb ages in the YG section (Table 3.3b; Fig. 3.5) relative to  $^{40}\text{Ar}/^{39}\text{Ar}$  and U-Pb and cyclostratigraphy based age-model from the Portland #1 core (Fig. 3.4; Meyers et al., 2012a). The WIS temporal framework is based on an integrated approach, which combines U-Pb (zircon) and  $^{40}\text{Ar}/^{39}\text{Ar}$  (sanidine) radio-isotopic data with astrochronology using Markov Chain Monte Carlo simulations (Meyers et al., 2012a). In this approach a high-resolution floating astrochronology based timescale is based upon orbitally influenced rhythmic strata, which is constrained in an absolute temporal sense by a dataset of  $^{40}\text{Ar}/^{39}\text{Ar}$  (sanidine) and subordinate U-Pb (zircon) dating. The accuracy of these radio-isotopic dates are based upon their respective calibrations, the age of the Fish Canyon sanidine (FCs) at 28.201 Ma for the  $^{40}\text{Ar}/^{39}\text{Ar}$  dates, and the gravimetric calibration of the EARTHTIME mixed U-Pb tracer for the zircon U-Pb dates. Although there is potential for bias between the geochronological systems, particularly related to the choice of an age of 28.201 Ma for FCs, a suite of new U-Pb (zircon) and  $^{40}\text{Ar}/^{39}\text{Ar}$  (sanidine) data for the Cretaceous Niobara Formation in the WIS suggest no resolvable bias (Sageman et al., 2014). We therefore apply the WIS integrated age-model (Meyers et al., 2012a), which is based upon  $^{40}\text{Ar}/^{39}\text{Ar}$  and subordinate U-Pb dates for comparison with the age-model we have developed for YG (Fig. 3.6B). However, it is worth noting that the WIS age-model is based upon a number of radio-isotopic dates from across the WIS that are then correlated into the Portland #1 core stratigraphy (Meyers et al.,

2012a) and uncertainty in biostratigraphy correlation is not included (see Sageman et al., 2014 for further discussion). Consequently, the integrated chronostratigraphy of the CTBI utilises the derived age model for the Portland core (Meyers et al., 2012a) and determines the age of the onset of OAE 2 at  $\sim 94.38 \pm 0.15$  Ma (Du Vivier et al., 2014; Chapter 2, this thesis).

Utilising the integrated age model justifies the revised stratigraphic correlation based on the modification of stratigraphic horizons. Hence the tuff unit HK017 in the YG section occurs at -16.10 m, adjacent to the first least radiogenic  $\text{Os}_i$  value, which is 0.05 m above the onset of the excursion in the  $\delta^{13}\text{C}_{\text{wood}}$  record. The HK017 U-Pb (zircon) systematics yield a date that is nominally equal (and overlaps within uncertainty;  $94.44 \pm 0.14$  Ma) to the date of the onset of OAE 2 established from the WIS ( $\sim 94.38 \pm 0.15$  Ma). As a result, these dates justify the revision of the OAE 2 onset in the YG, and confirm the trend in the  $\text{Os}_i$  profiles to unradiogenic  $\text{Os}$  values as globally contemporaneous (Fig. 3.7), as proposed by Du Vivier et al. (2014; Chapter 2, this thesis). Furthermore, the age of HK018,  $93.92 \pm 0.031/0.11$  Ma, implies that the CTB (dated at  $93.90 \pm 0.15$  Ma, Meyers et al., 2012a) is present in the horizon directly above or below the tuff since the date for HK018 is statistically indistinguishable from the date of the CTB. As such we amend the stratigraphic height of the CTB, previously determined by the FO of *M. schneegansi* (Hasegawa, 1995; Takashima et al., 2011; see Fig. 3.2, CTB<sup>?</sup>; Fig. 3.5).

**Figure 3.7 (next page 118) Global correlation of  $\delta^{13}\text{C}_{\text{org}}$  and  $\delta^{13}\text{C}_{\text{wood}}$  (black) and  $\text{Os}_i$  (red) vs. stratigraphic height (m). Initial  $^{187}\text{Os}/^{188}\text{Os}$  calculated at  $93.90 \pm 0.15$  Ma.  $\delta^{13}\text{C}$  data from: Portland #1 Core, Sageman et al. (2006); Site 1260, Forster et al. (2007); Wunstorf (Chapter 2, this thesis); Vocontian Basin, Jarvis et al. (2011); Furlo, Jenkyns et al. (2007); Site 530, Forster et al. (2008); Yezo Group, Takashima et al. (2010); Great Valley Sequence, Takashima et al. (2010). Sites correlated using datum levels on the  $\delta^{13}\text{C}$  record (A, B, C; see text for details), ‘A’ denotes the onset of the OAE 2. Dashed lines represent intervals of pore core recovery. Note that symbol size is greater than the measured uncertainty. Osmium isotope data are reported for YG and GVS in Table 3.2 and for the other sites in Chapter 2 (this thesis; Du Vivier et al., 2014).**



The age-depth model (Fig. 3.6B) is generated using OxCal (Bronk Ramsey, 2008) in order to graphically illustrate the  $^{206}\text{Pb}/^{238}\text{U}$  zircon dates and justify interbasinal integration. The model permits the interpolation of ages between the dated tuff horizons for the YG section and thus allows objective comparison of the YG and WIS sections based on the stratigraphy,  $\delta^{13}\text{C}$  and the  $\text{Os}_i$  profiles they contain (Bronk Ramsey, 2008). On Figure 3.6B the light grey areas represent the distribution for single calibrated dates, i.e., the likelihood of distribution derived from the actual dated values, and the dark grey areas demonstrate the marginal posterior distribution, which considers the depth model (Bronk Ramsey, 2008). The U-Pb zircon dates, with the exception of CT103 (Fig. 3.4;  $94.53 \pm 0.21$  Ma), conform to stratigraphic order (Fig. 3.5). The model therefore demonstrates the uncertainty of the CT103 age (Fig. 3.6B – light grey area of sample) but forces superposition to be upheld (Fig. 3.6B – dark grey area of sample). The high uncertainty ( $\pm 0.17/0.21$  Ma) enables CT103 to be manipulated in the model since it takes more of its weight from the other more precise zircon  $^{206}\text{Pb}/^{238}\text{U}$  dates from above and below, such that the date of CT103 has no weight in the resultant age-model (section 5.2; Fig. 3.9). For CT103 it is likely that the zircons either record inheritance and/or crystallisation in the magmatic chamber a period of time prior to eruption since the sample yields a date older than zircons from tuff units below CT103, e.g., HK017 ( $94.44 \pm 0.093$  Ma). Nonetheless, Figure 3.6B shows that the age-depth model fits the remaining  $^{206}\text{Pb}/^{238}\text{U}$  ages within uncertainty. The projection of Tuff A, B and C from the WIS on to the YG stratigraphy illustrates the integration of the YG and WIS records and supports the interpretation of HK018 revising the CTB, and HK017 revising the onset of OAE 2. As such we optimise the integrated chronostratigraphy of the YG

Pacific data with the high-resolution initial osmium isotope profile of the Portland #1 core (Du Vivier et al., 2014; Chapter 2, this thesis) and the age-model from the WIS (Tuff A, B and C; Meyers et al., 2012a) in order to provide integration between the two sites, and the first understanding of Pacific Ocean chemistry during OAE 2.

The pre-existing dates from 2 dated tuff horizons (Quidelleur et al., 2011) are indicated on Figure 3.4 in green. The sample HKt002 is at the same stratigraphic height as the onset of the OAE 2 (-16.15 m) but the LA-ICP-MS analysis produced a  $^{206}\text{Pb}/^{238}\text{U}$  date of  $92.9 \pm 2.1$  Ma, which is nominally  $>1.5$  Myr younger than the onset of OAE 2 defined in the WIS (94.38 Ma) and the age of HK017;  $94.44 \pm 0.14$  Ma. In addition to the stratigraphic disparity with the dated tuffs (Meyers et al., 2012a; and this study) and the  $\text{Os}_i$  profile, HKt002 has a significant uncertainty ( $\pm 2.1$  Ma). The uncertainty is intrinsic to the analytical method therefore we discount the utility of the HKt002 date for integration at the sub 0.5 Ma level.

Furthermore, analysis of the degree of pyritization (DOP) in addition to Os isotope stratigraphy records a sudden increase synchronous with the first unradiogenic  $\text{Os}_i$  value just after the onset of OAE 2 in the YG section (DOP peak 1; Fig. 3.8A; Table 3.4; Takashima et al., 2011). The isochronous onset of OAE 2 throughout the proto-Pacific is supported by a similarly synchronous increase in DOP in the GVS (DOP peak 1; Fig. 3.8B), which supports the revised position of the onset of OAE 2 in the YG section (Fig. 3.7). A high DOP is indicative of dysoxic to euxinic conditions, such as during the syn-OAE 2 interval (Takashima et al., 2011). For the application of DOP to be a useful tool it ought to be applied to multiple sections to establish the enrichment of sulphides and hence the development of

euxinia. As a result a global application could determine the level of anoxia in different basinal settings.

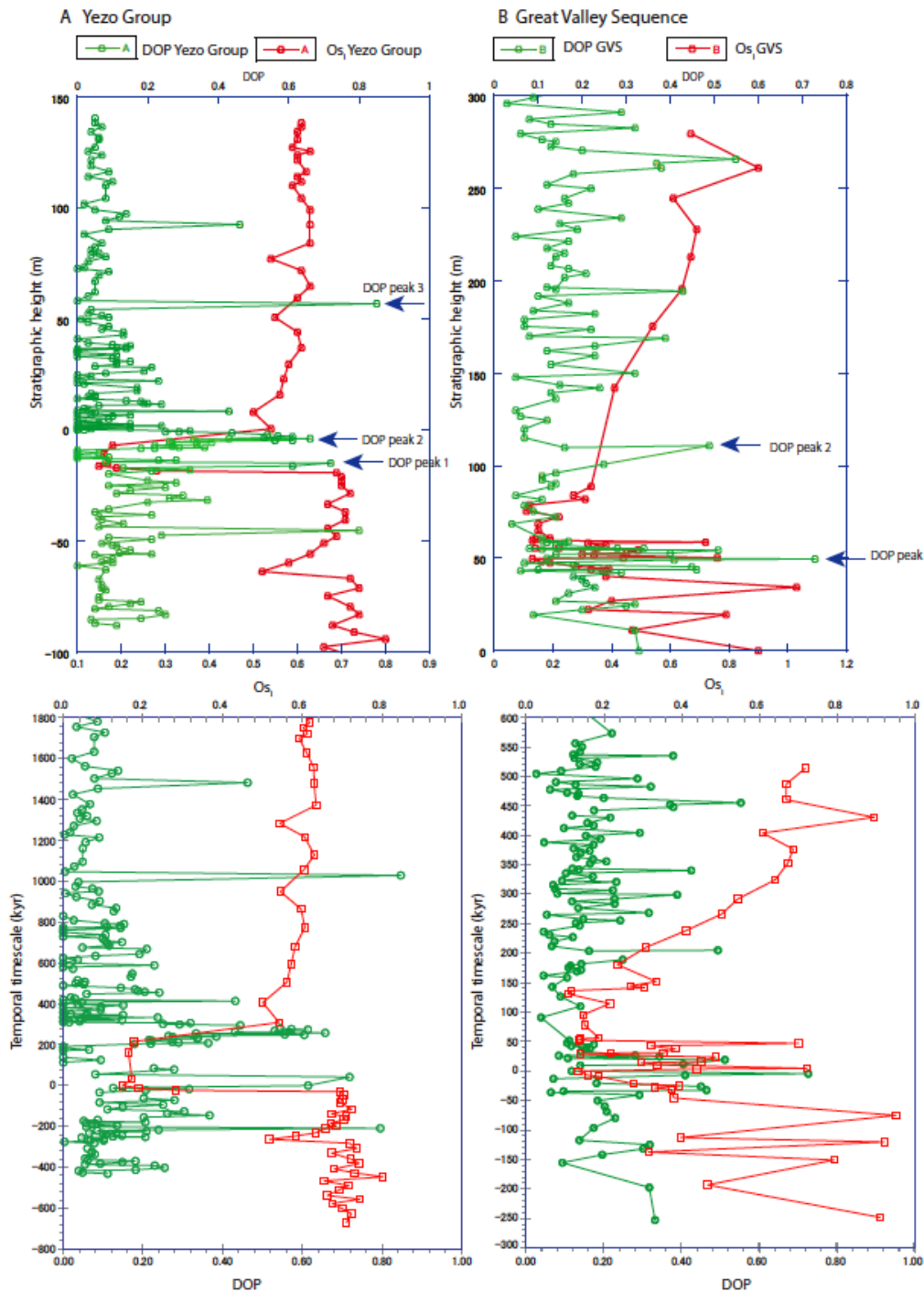


**Figure 3.8 Degree of Pyritization (DOP) vs.  $\text{Os}_i$  in Yezo Group, Japan and Great Valley Sequence, California, USA.** Figure 3.8A shows YG DOP (green) and  $\text{Os}_i$  (red) vs. stratigraphic height (m) in the top figure and below vs. temporal timescale (kyr). Figure 3.8B shows GVS DOP (green) and  $\text{Os}_i$  (red) vs. stratigraphic height (m) in the top figure and below vs. temporal timescale (kyr). The peaks in the DOP profile are indicated by blue arrows, labelled ‘DOP’.

## 5.2. Temporal framework

The U-Pb dates for the YG provide an absolute timescale for the CTB. We therefore use these dates to constrain sedimentation rates (cm/kyr) for each section (Table 3.5) and calculate a temporal model (Table 3.2) in order to quantitatively assess the duration of events occurring across the CTBI based on the  $\text{Os}_i$  profile, and potentially reduce the discrepancy observed in stratigraphic correlations based solely on  $\delta^{13}\text{C}$  records. Du Vivier et al. (2014; Chapter 2, this thesis) established a common chronostratigraphic framework relative to individual timescales created for each section by exporting temporal information, based on the integration of radio-isotope dates (Ar-Ar and U-Pb) and astrochronology (Meyers et al., 2012a) and new work (Ma et al., 2014), from the Portland #1 core (Du Vivier et al., 2014; Chapter 2, this thesis).

We apply the timescale model from Du Vivier et al. (2014; Chapter 2, this thesis) to the GVS based on the integrated information from the GSSP section (Meyers et al., 2012a), whereby the sections without radio-isotopic dates are correlated according to the characteristic peaks and troughs in the  $\delta^{13}\text{C}$  record, combined with key bioevents to establish datum levels 'A', 'B' and 'C' of the  $\delta^{13}\text{C}_{\text{org}}$  curve that are the same as those first defined by Pratt et al., (1985) in the Western Interior and revised by Tsikos et al. (2004). The age of the 'A', 'B' and 'C' datum levels of the  $\delta^{13}\text{C}_{\text{org}}$  curve are derived from the nominal ages for the 'A', 'B' and 'C' markers from the GSSP (Fig. 3.3), allowing calculation of linear sedimentation rate values between the datum levels (Table 3.5). Thus, the linear sedimentation rate calculated for A-B is applied to develop a timescale below the 'B' datum, and a linear sedimentation rate for B-C is used for the section above the 'B' datum (Table

3.5). Conversely, the YG section  $\delta^{13}\text{C}$  excursions are not well defined and the U-Pb zircon dates from this study constrain the stratigraphy through the CTBI, as discussed in section 5.1. Therefore the dates are utilised to derive the YG temporal framework using the same methodology as facilitated for the GSSP framework (Du Vivier et al., 2014; Chapter 2, this thesis). A linear sediment accumulation rate (cm/kyr) is calculated between each  $^{206}\text{Pb}/^{238}\text{U}$  age for each tuff interval; HK018-HK017, HK017-CT041, and CT041-AD175 (Table 3.5), and utilised to develop a thousand year timescale (kyr; Table 3.2). However, a variable linear sediment accumulation rate is more realistic over such time frames, i.e., hundreds of thousands of years. The established global framework utilises the onset of OAE 2 as the temporal datum 'A', which is set to 0 kyr (Fig. 3.3). The revised onset of OAE 2 in the  $\delta^{13}\text{C}_{\text{wood}}$  excursion for the YG section is applied, based on  $\text{Os}_i$  profile (this study).

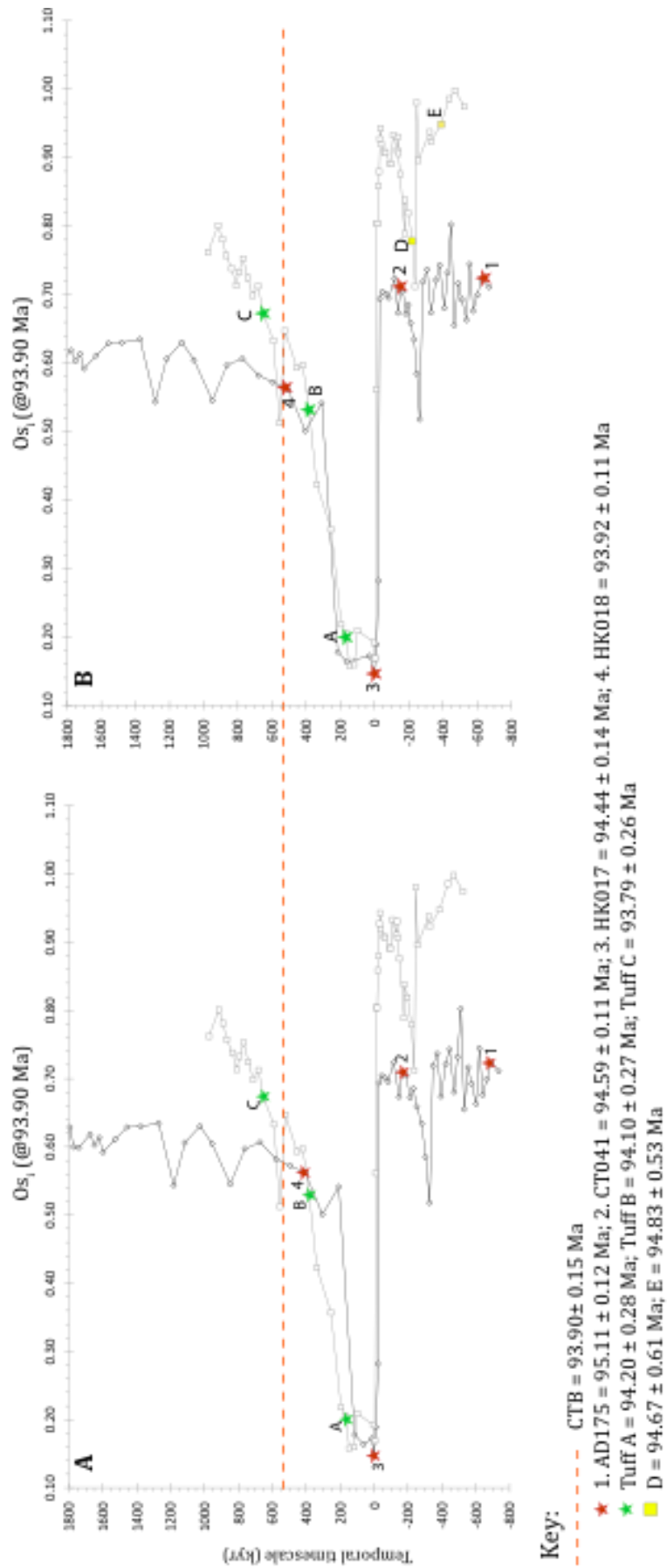
Our temporal constraints, based upon U-Pb zircon dates from ash beds in the YG section permit integration of YG data with data from the Portland #1 core and objective comparison of the  $\text{Os}_i$  profiles from both sections (see section 5.3.1).

**Table 3.5** Calculation of Linear Sedimentation Rate to derive the Temporal framework

<b>Yezo Group, Japan</b>						
Sample	AGE (Ma) <sup>1</sup>	Depth (m)	kyrs	Tuff interval	LSR <sup>4</sup>	
HK018	93.92	24.70				
HK017	94.44	-16.10	516	HK018 to HK017	7.91	
CT041	94.59	-32.75	157	HK017 to CT041	10.61	
AD175	95.11	-119.40	520	CT041 to AD175	16.66	
<b>Great Valley Sequence, California</b>						
$\delta^{13}\text{C}_{\text{org}}$ datum levels <sup>2</sup>	AGE (Ma) <sup>3</sup>	Depth (m)	kyrs	Datum interval	LSR <sup>4</sup>	
A	94.38	49.00				
B	94.23	78.90	150	A to B	19.93	
C	93.95	252.20	280	B to C	61.89	

<sup>1</sup>  $^{206}\text{Pb}/^{238}\text{U}$  zircon ages from YG (this study)<sup>2</sup> determined from the  $\delta^{13}\text{C}_{\text{org}}$  datum levels Portland #1 core by Sageman et al. (2006); see Fig.3.3<sup>3</sup> derive from geochronology and astrochronology of GSSP section (Meyers et al., 2012a)<sup>4</sup> units cm/kyr

**Figure 3.9 (next page 125)  $\text{Os}_i$  profiles from Yezo Group (black) and Portland #1 Core (grey) vs. temporal timescale (kyr).** Red stars mark the U-Pb dated tuff horizons from this study in the Yezo Group section. Green stars mark the weighted mean  $^{40}\text{Ar}/^{39}\text{Ar}$  ages in the WIS, Meyers et al. (2012a). CTB based on the Portland timescale. Figure 3.9B shows the  $\text{Os}_i$  profile having applied a varied sedimentation rate to the stratigraphy between HK018 (see text for discussion), inferred from integration based on U-Pb dated tuffs. The yellow markers (D and E) on the Portland  $\text{Os}_i$  profile in Figure 3.9B are recalculated  $^{40}\text{Ar}/^{39}\text{Ar}$  ages (Adams et al., 2010).



### 5.3. *Interpreted $\text{Os}_i$ correlation based on the temporal framework and age model*

#### 5.3.1. *Correlation of OAE 2 interval*

Figure 3.9 shows the  $\text{Os}_i$  profiles of the YG section and the Portland #1 core versus the temporal timescale (kyr), determined using the linear interpolated sediment accumulation rate. The tuff horizons are marked on; red stars for YG and green stars for Portland. The position of the CTB (Fig. 3.9) is based on the well-constrained astrochronological timescale of the Portland core (Meyers et al., 2012a). Figure 3.9A illustrates the discrepancy in age integration. The age of HK018 ( $93.92 \pm 0.11$  Ma) is nominally analogous with the age of the CTB ( $93.90 \pm 0.15$  Ma) as shown by the age-depth model (Fig. 3.6B). However, based on the temporal timescale for the YG, the HK018 tuff horizon is concomitant with Tuff B in the WIS age-model, which is  $\sim 200$  kyr older ( $94.10 \pm 0.27$  Ma; Fig. 3.9A).

The sedimentation rates for the integrated timescale of the Portland core are supported by astrochronology. Therefore we propose that the discrepancy in correlation of the Portland core and YG is a function of the linear sedimentation rate, which is a key parameter of the temporal model presented. As explained in section 5.2, the linear sedimentation rate is derived from the ages of the tuff horizons, as such a constant sedimentation rate is assumed between the tuff horizons. The similar analytical dates, including uncertainty, of tuff horizons of the WIS and the YG suggest that the sedimentation rate between tuff horizons of the YG was considerably more variable than is assumed (Fig. 3.9A, Table 3.5).

The onset of OAE 2 in Portland and the YG agree within  $\sim 150$  kyr supported by the integration of  $^{40}\text{Ar}/^{39}\text{Ar}$  and U-Pb dates, respectively, which is also supported by the age-depth model (Fig. 3.6B; as discussed in section 5.1). Subsequently, the

unradiogenic interval at Portland and elsewhere (Fig. 3.7) lasts for ~180 kyr (based on the integrated timescale Du Vivier et al. (2014); Chapter 2, this thesis; and also in agreement with the short eccentricity cycles in Meyers et al. (2012b)); however, in the YG section the  $\text{Os}_i$  values abruptly return to radiogenic values ~100 kyr after ‘A’ based on the timescale using a linear interpolated sediment accumulation rates (Fig. 3.9A). As such we propose that the sedimentation rate between HK017 and HK018 was not constant, which is consistent with the facies change from mudstone to muddy-sandstone between the two horizons, respectively. We use the age-depth model to support the proposed variation of the sedimentation rate. Where the first least unradiogenic  $\text{Os}_i$  is immediately adjacent to HK017 and dated  $94.44 \pm 0.093$  Ma, subsequently the return to radiogenic  $\text{Os}_i$  is interpolated from the age-depth model at  $\sim 94.25 \pm 0.10$  Ma (Fig. 3.6B). The difference is ~180 kyr, thus the duration of the unradiogenic interval concurs with the global trend of ~180 kyr (Du Vivier et al., 2014; Chapter 2, this thesis). As a result we apply a slower sedimentation rate at the onset of OAE 2, ~3 cm/kyr, before it increased to the calculated rate of ~7 cm/kyr (Table 3.5), which expands the section (Fig. 3.9B). Therefore the unradiogenic interval after the onset of OAE 2 is analogous to the globally correlated duration (Fig. 3.7), and the dated tuff horizon HK018 is integrated with the CTB (Fig. 3.9B), which is quantified by the age-depth model (Fig. 3.6B).

Furthermore the age-depth model ascertains the age of the datum levels ‘B’ and ‘C’ in the YG section (Fig. 3.3). Figure 3.6B illustrates two pink stars labelled ‘B’ and ‘C’ on the age model, interpolated from 3.6C, that yield ages of ‘B’  $\sim 94.15 \pm 0.11$  Ma and ‘C’  $\sim 93.90 \pm 0.11$  Ma. Both dates concur within uncertainty with the integrated ages for the ‘B’ ( $\sim 94.23 \pm 0.20$  Ma) and ‘C’ ( $\sim 93.95 \pm 0.20$  Ma) datum

levels in the Portland core (derived from Meyers et al., 2012a; Table 3.5; Du Vivier et al., 2014; Chapter 2, this thesis). Consequently we further verify the correlation of the YG section with the WIS facilitated by the integration of the temporal framework.

### *5.3.2. Pre-OAE 2 Yezo Group section, western Pacific*

The heterogeneous  $\text{Os}_i$  profile prior to the onset of OAE 2 in the YG is directly comparable to the profile recorded in the WIS at Portland (Fig. 3.4, 3.8). The  $\text{Os}_i$  values are interpreted to reflect weathering of the radiogenic continental crust (Peucker-Ehrenbrink and Ravizza, 2000; Cohen, 2004). For the YG section the  $\text{Os}_i$  are marginally less radiogenic than at Portland, indicative that the isotopic composition of the weathered material from which the hydrogenous Os was derived; i.e., the western Pacific interior was less isotopically evolved (Mesozoic forearc; Tamaki and Itoh, 2008) than the continental mass of the Archean Canadian Shield weathering into the WIS.

The brief trend to less radiogenic  $\text{Os}_i$  values ~330 kyr before the onset of OAE 2 in the YG section (Fig. 3.9A) is identical to the trend recorded at Portland; where the short-lived perturbation is indicative of the initial pulse of volcanism from the Caribbean LIP (Sinton and Duncan, 1997; Snow et al., 2005; Turgeon and Creaser, 2008; Du Vivier et al., 2014; Chapter 2, this thesis). However, the timing of the trend is not directly synchronous; at Portland it occurs at ~240 kyr before OAE 2, but records the same amount of change (~0.2). Therefore, it is probable that the unradiogenic source and its portion controlling the  $\text{Os}_i$  in the YG section was similar to that for Portland (i.e. the Caribbean LIP).

Prior to the onset of OAE 2 in the Portland core there are two  $^{40}\text{Ar}/^{39}\text{Ar}$  ages from the WIS that yield recalculated dates of  $94.67 \pm 0.61$  Ma and  $94.83 \pm 0.53$  Ma (using the 28.201 Ma age for the FCs; Fig. 3.4: D and E; Obradovich, 1993; recalculated in Adams et al., 2010), and a recently dated bentonite ~27 m below Tuff A in the Lincoln limestone, which yields an  $^{40}\text{Ar}/^{39}\text{Ar}$  date of  $95.39 \pm 0.18$  Ma (Ma et al., 2014). These  $^{40}\text{Ar}/^{39}\text{Ar}$  dates provide time markers that can be used to nominally correlate the  $\text{Os}_i$  profiles. Further utilising these ages generates an identical temporal model to that determined by the stratigraphy (Ma et al., 2014).

In the WIS the  $^{40}\text{Ar}/^{39}\text{Ar}$  date constrains the non-radiogenic inflection to  $\sim 94.68 \pm 0.61$  Ma (Fig. 3.9B marker 'D'; Adams et al., 2010). An identical age within uncertainty is determined for the same point in the  $\text{Os}_i$  profile for the YG section from the age-depth model ( $\sim 94.70 \pm 0.11$  Ma; Fig. 3.6B, 3.6C, yellow star). Consequently, based on the inference that the source of the non-radiogenic inflection is contemporaneous, the  $\text{Os}_i$  record infers that the sedimentation rate was faster than calculated (Table 3.5) in the YG section before the onset of OAE 2. As a result the application of a varied sedimentation rate facilitates the correlation of the non-radiogenic trend at ~250 kyr prior to the onset of OAE 2 by condensing the  $\text{Os}_i$  profile (Fig. 3.9B). As discussed in section 5.2, the temporal model is established using a constant sedimentation rate between tuff horizons. Accordingly, a constant sedimentation rate over 600 kyr between AD175 and CT041 is derived from the model. Therefore it is reasonable to suggest the timing of the non-radiogenic perturbation may be affected by variable sedimentation rates.

Moreover, despite the long-term transgression to highstand in the early Turonian, sea level was frequently oscillating short-term (Haq et al., 1988; Leckie et

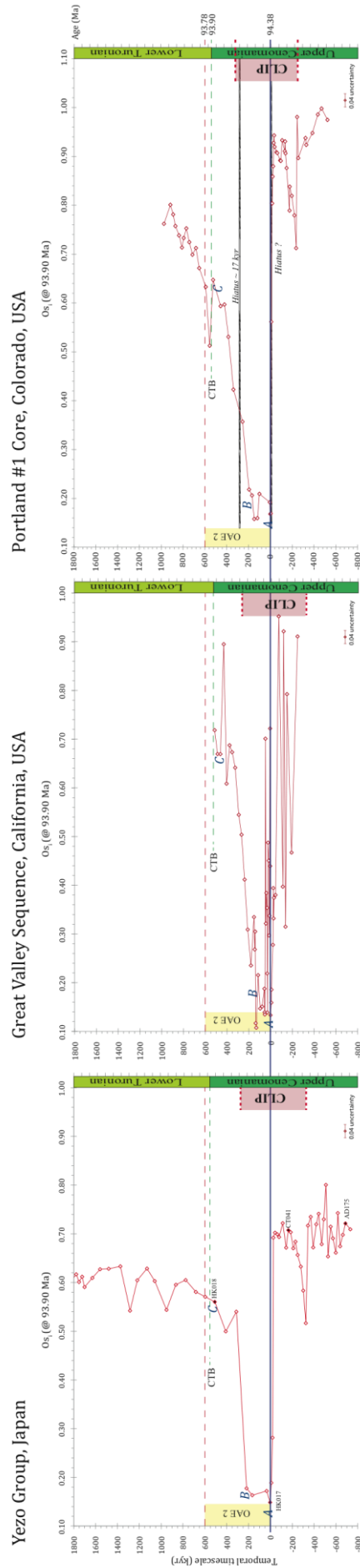
al., 2002; Takashima et al., 2010). As a result, the interval prior to anoxia implies that brief basin restriction permitted the radiogenic continental flux of Os to dominate the composition of organic-rich deposits (Du Vivier et al., 2014; Chapter 2, this thesis) during the short-term regression (Haq et al., 1988). The maximum atmospheric and sea surface temperatures during this interval meant that weathering rates were also at a maximum (Forster et al., 2007), which led to an abundance of nutrients that boosted productivity and ultimately primed the ocean system for the development of anoxia as rising sea levels facilitated the distribution of the build up in nutrients. As nutrients became prolific,  $\text{CO}_2$  drawdown increased and expanded the oxygen minimum zones throughout the global basins (Erbacher et al., 1996; Jones and Jenkyns, 2001; Du Vivier et al., 2014; Chapter 2, this thesis). Sea level transgression, which started immediately prior to the OAE 2 and continued up to the lower Turonian highstand, permitted the distribution of unradiogenic Os and elevated Os concentrations derived from activity at the Caribbean LIP, in to the basin. Consequently the  $\text{Os}_i$  profiles from all sections infer that the trend to unradiogenic  $\text{Os}_i$  values was penecontemporaneous (Fig. 3.7, 3.9) and interpreted to reflect the major onset of volcanic activity at the Caribbean LIP.

#### *5.4. Great Valley Sequence, eastern Pacific*

The  $\text{Os}_i$  data for the GVS do not record the same pre-OAE 2 trend as Portland and Japan (Fig. 3.10). Instead the rapidly oscillating radiogenic to unradiogenic  $\text{Os}_i$  values recorded in the GVS are indicative to a highly sensitive ocean basin during the ~220 kyr interval before the onset of OAE 2. The frequency of the perturbations in the  $\text{Os}_i$  record every 20 – 30 kyr supports the short residence time of Os in

seawater (Oxburgh, 2001; Du Vivier et al., 2014; Chapter 2, this thesis), and suggests that the Os isotope composition was sensitive to unradiogenic Os from hydrothermal inputs at the Caribbean LIP (Turgeon and Creaser, 2008; Du Vivier et al., 2014; Chapter 2, this thesis) in addition to radiogenic Os from continental weathering inputs. The sporadic variability in the Os concentration is consistent with the rapidly changeable  $\text{Os}_i$  profile of the GVS. The data show that there is a correlation between unradiogenic Os isotope composition and high Os concentration, which may be indicative to the high frequency of changing seawater chemistry in the basin as a result of alternating sea level and accelerated weathering rates. The high terrigenous component of the GVS lithology coupled with the radiogenic  $\text{Os}_i$  suggests that the main flux of material is derived from the continent. This may have been the result of an increase in marginal and intercontinental weathering driven by the aforementioned peak in global temperatures and fluctuating sea level in the lead up to OAE 2 (Jones and Jenkyns, 2001).

**Figure 3.10 (next page 132)  $\text{Os}_i$  vs. temporal timescale (kyr).** ‘A’, ‘B’ and ‘C’ represent the  $\delta^{13}\text{C}$  correlative datum levels. The onset (‘A’) of OAE 2 is in blue and the Cenomanian-Turonian boundary (CTB) is in green. The duration of the OAE 2 is in yellow (~600 kyr; Meyers et al., 2012b). The tuff horizons in the Yezo Group are labelled and the adjacent  $\text{Os}_i$  data point filled in black. The duration of the Caribbean LIP is in shaded pink (~450 kyr), derived from Chapter 2 and this study (see text for discussion). The 2 minor hiatuses in the Portland #1 core are marked on as black hashes. The uncertainty of each analysis is <0.04.



While the GVS record is indicative to regional basin factors controlling  $\text{Os}_i$  prior to the OAE 2, the more open ocean  $\text{Os}_i$  signal becomes more unradiogenic, e.g., Site 1260, Site 530, Furlo, Vocontian Basin (Fig. 3.7), as the water column is more sufficiently mixed. By the onset of OAE 2 rising sea levels to the approaching highstand (in the Turonian, Haq et al., 1988; Leckie et al., 2002; Forster et al., 2007) facilitated the growth of the oxygen minimum zone (Erbacher et al., 1996). As water mass exchange became more efficient the contemporaneous unradiogenic  $\text{Os}$  derived from the Caribbean LIP was readily transferred to the GVS basin and influenced the isotopic composition of seawater prior to and in the first ~50 kyr of OAE 2 (Fig. 3.10). Overall the variability of the  $\text{Os}$  isotope composition throughout the CTBI is indicative of a dynamic palaeocirculation and highlights the sensitivity of the seawater chemistry in the GVS as a function of proximity to the Caribbean LIP.

Neodymium isotopes also assess water mass exchange and ocean circulation, whereby the  $\epsilon_{\text{Nd}}$  record exhibits a positive excursion at the onset of OAE 2 at Demerara Rise (Macleod et al., 2008), which implies a change in the source of circulation and input to the ocean (i.e., hydrothermal processes associated with the Caribbean LIP: Macleod et al., 2008; Martin et al., 2012). Evidence from the  $\epsilon_{\text{Nd}}$  record at Eastbourne exhibits a synchronous positive excursion with Demerara Rise (Zheng et al., 2013). Therefore, a vigorous deep ocean circulation throughout the late Cretaceous combined with transgression permitted the exchange of Pacific seawater into the Atlantic and European Pelagic Shelf basins across the CTB (Trabucho-Alexander et al., 2011; Martin et al., 2012), which reflects the concurrent emplacement of the Caribbean LIP with the global  $\text{Os}_i$  record (Fig. 3.7; Du Vivier et al., 2014; Chapter 2, this thesis).

### 5.5. *Longevity of the Caribbean Large Igneous Province*

The  $\text{Os}_i$  isotope stratigraphy records an unradiogenic influence associated with submarine volcanism at the Caribbean LIP (Sinton and Duncan, 1997; Snow et al., 2005; Turgeon and Creaser, 2008; Du Vivier et al., 2014; Chapter 2, this thesis). The period of formation of the Caribbean LIP is estimated to be ~450 kyr (Du Vivier et al., 2014; Chapter 2, this thesis). At ~240 kyr prior to the onset of anoxia the trend in  $\text{Os}_i$  values represents an initial pulse, followed by a major pulse ~50 kyr prior to the onset. Subsequently, the return to radiogenic  $\text{Os}_i$  values ( $>0.5$ ) ~210 kyr after the OAE 2 onset indicates the cessation of activity at the Caribbean LIP, and as a result the re-equilibrium of seawater chemistry. The time frame recorded in the YG is identical to the  $\text{Os}_i$  record from the Atlantic, Tethyan and WIS regions (Fig. 3.10; Du Vivier et al., 2014; Chapter 2, this thesis).

As discussed in section 5.4, the continual variability of the Os isotope composition throughout the CTBI highlights the sensitivity of the seawater chemistry in the deposits at the GVS, which could be associated with the high TOC levels and the process of sequestration; following the build-up of Os from pulses of volcanic activity, the drawdown of Os was rapid as a result of the abundance of organic-rich material from pre-OAE 2 weathering and  $\text{CO}_2$  drawdown. As a result the section could be used to improve the nominal constraint on the duration of activity at the Caribbean LIP, given the basin proximity to the oceanic plateau (Fig. 3.1). From the start of the  $\text{Os}_i$  record in the GVS the  $\text{Os}_i$  oscillates dramatically from radiogenic (~0.9) to unradiogenic (~0.4; Fig. 3.3, 3.9) within  $\leq 30$  kyr until the early part of OAE 2. The  $\text{Os}_i$  values remain unradiogenic up to datum level 'B' when at ~180 kyr the  $\text{Os}_i$  values become more radiogenic (Fig. 3.10) as the influence of volcanically

derived Os decreased. The trend to more radiogenic values reveal a more abrupt cessation of the Caribbean LIP, yet the timing is concurrent within uncertainty with Atlantic, Tethyan and WIS sites and supports the same interpretation of duration as Du Vivier et al. (2014; Chapter 2, this thesis; ~450 kyr). Therefore circulation was not stagnant and was sufficient to re-equilibrate seawater chemistry of palaeobasins adjacent to the Caribbean LIP and at the peripheral margins of the oceans worldwide (Trabucho-Alexander et al., 2011; Du Vivier et al., 2014; Chapter 2, this thesis).

## 6. *Summary*

The high-resolution  $\text{Os}_i$  profiles for two proto-Pacific sections demonstrate the changes in global ocean chemistry across the OAE 2. The  $\text{Os}_i$  stratigraphy facilitates the traditional method of correlation and integration of stratigraphic successions using  $\delta^{13}\text{C}$  isotopes, and we use the  $^{206}\text{Pb}/^{238}\text{U}$  zircon ages to show the synchronous onset of OAE 2 and assess the contemporaneity of the Caribbean LIP.

The use of U-Pb ages (Fig. 3.5) has permitted the application of a temporal model to both Pacific sections (Fig. 3.9), which has revised the definition of the onset of OAE 2 and the position of the CTB in the YG section, and quantitatively constrained the onset of OAE 2 and the duration of the Caribbean LIP. Furthermore, the age-depth model (Fig. 3.6B) supports the objective integration of the  $\text{Os}_i$  profiles (Fig. 3.6C) and synchronicity of changes in the seawater Os isotope composition. The improved correlation and integration of the proto-Pacific with the WIS across the CTB has created a nominal correlation to the GSSP in the WIS.

The YG and GVS sections are at the western and eastern periphery of the proto-Pacific ocean, respectively. The discrepancy between the  $\text{Os}_i$  profiles

illustrates the extent of regional variability of inputs to basinal environments (Paquay and Ravizza, 2012) and basin restriction comparable to the WIS, as well as the proximity to the source of the Caribbean LIP combined with sea-level change continually influencing local water masses at the GVS. Despite the variability of the  $\text{Os}_i$  values the overall trend of the  $\text{Os}_i$  profiles; radiogenic – unradiogenic – return to radiogenic  $\text{Os}_i$ , are characteristic of the OAE 2 with respect to the correlation of Os isotope stratigraphy throughout the proto-Atlantic, Tethys and WIS (Du Vivier et al., 2014; Chapter 2, this thesis). Therefore, with the addition of the high-resolution Os isotope stratigraphy from both proto-Pacific sections and U-Pb dates from the YG section, we conclude that the OAE 2 was an isochronous event with worldwide basinal dispersion and penecontemporaneous with the major pulse of volcanism at the Caribbean LIP.

## REFERENCES

- Adams, D. D., Hurtgen, M. T., Sageman, B. B., 2010. Volcanic triggering of biochemical cascade during Oceanic Anoxic Event 2. *Nature Geoscience* 3, DOI: 10.1038/NGEO743.
- Arthur, M. A., Sageman, B.B., 1994. Marine black shales: Depositional mechanisms and environments of ancient deposits. *Annu. Rev. Earth Planet. Sci.* 22, 499-551.
- Arthur, M. A., Schlanger, S. O., Jenkyns, H. C., 1987. The Cenomanian/Turonian Oceanic Anoxic Event, II: Palaeoceanographic controls on organic matter production and preservation, in *Marine Petroleum Source Rocks*, edited by J. Brooks and A. J. Fleet, *Geol. Soc. London Spec. Publ.*, 26, 401–420.
- Blättler, C. L., Jenkyns, H. C., Reynard, L. M., Henderson, G. M., 2011. Significant increases in global weathering during Oceanic Anoxic Events 1a and 2 indicated by calcium isotopes. *Earth Planet. Sci. Letts.* 309, 77-88.
- Bronk Ramsey, C., 2008. Deposition models for chronological records. *Quaternary Science Reviews* 27, 42-60.

- Cohen, A. S., 2004. The rhenium-osmium isotope system: Applications to geochronological and palaeoenvironmental problems. *Journal of the Geological Society London* 161, 729-734.
- Condon, D., Schoene, B., Bowring, S.A., Parrish, R., McLean, N., Noble, S., Crowley, Q., 2007. EARTHTIME: Isotopic tracers and optimized solutions for high-precision U-Pb ID-TIMS geochronology. *Eos (Transactions, American Geophysical Union)*, 88, 52. Abstract no. V41E-06.
- Condon, D.J., others, a., in-review. Metrology and Traceability of U-Pb Isotope Dilution Geochronology (EARTHTIME Tracer Calibration Part I). *Geochim Cosmochim. Acta*.
- Creaser, R.A., Papanastassiou, D.A., Wasserburg, G.J., 1991. Negative thermal ion mass spectrometry of osmium, rhenium and iridium. *Geochim. Cosmochim. Acta* 55, 397-401.
- Cumming, V.M., Selby, D., Lillis, P.G., 2012. Re–Os geochronology of the lacustrine Green River Formation: Insights into direct depositional dating of lacustrine successions, Re–Os systematics and paleocontinental weathering. *Earth Planet. Sci. Lett.* 359-360, 194-205.
- Du Vivier, A.D.C., Selby, D., Sageman, B.B., Jarvis, I., Grocke, D.R., Voigt, S., 2014. Marine  $^{187}\text{Os}/^{188}\text{Os}$  isotope stratigraphy reveals the interaction of volcanism and ocean circulation during Oceanic Anoxic Event 2. *Earth Planet. Sci. Lett.* 389, 23-33.
- Erbacher, J., Thurow, J., Littke, R., 1996. Evolution patterns of radiolaria and organic matter variations: A new approach to identify sea-level changes in mid-Cretaceous pelagic environments. *Geology*, 24, 499-502.
- Fernando, A.G.S., Nishi, H., Tanabe, K., Moriya, K., Iba, Y., Kodama, K., Murphy, M.A., Okada, H., 2011. Calcareous nannofossil biostratigraphic study of forearc basin sediments: Lower to Upper Cretaceous Budden Canyon Formation (Great Valley Group), northern California, USA. *Island Arc* 20, 346-370.
- Forster, A., Schouten, S., Moriya, K., Wilson, P.A., Sinninghe Damsté, J.S., 2007. Tropical warming and intermittent cooling during the Cenomanian/Turonian oceanic anoxic event 2: Sea surface temperature records from the equatorial Atlantic. *Paleoceanography*, 22, PA1219. doi:10.1029/2006PA001349.
- Forster, A., Kuypers, M. M. M., Turgeon, S. C., Brumsack, H-J., Petrizzo, M. R., Sinninghe Damsté, J. S., 2008. The Cenomanian/Turonian oceanic anoxic event in the South Atlantic: New insights from a geochemical study of DSDP 530A. *Palaeogeog. Palaeoclimatol., Palaeoecol.* 267, 256 – 283.

- Gradstein, F.M., Ogg, J.G., Schmitz, M., eds., 2012. The Geologic Time Scale 2012, 2-volume set. Elsevier.
- Gramlich, J.W., Murphy, T.J., Garner, E.L., Shields, W.R., 1973. Absolute isotopic abundance ratio and atomic weight of a reference sample of rhenium. *J. Res. Natl. Bur. Stand.* 77A, 691–698.
- Haq, B.U., Hardenbol, J., Vail, P.A., 1988. Mesozoic and Cenozoic chronostratigraphy and cycles of sea-level change, in *Sea-Level Changes: An Integrated Approach*, edited by C.K. Wilgus et al., *Spec. Publ. Soc. Econ. Plaeontol. Mineral.* 42, 71-108.
- Hasegawa, T., 1995. Correlation of the Cenomanian/Turonian boundary between Japan and Western Interior of the United States. *J. Geol. Soc. Japan* 101, 2-12.
- Hasegawa, T., 1999. Planktonic foraminifera and biochronology of the Cenomanian-Turonian (Cretaceous) sequence in the Oyubari area, Hokkaido, Japan. *Paleontol. Res.* 3, 173-192.
- Hasegawa, T., Saito, T., 1993. Global synchronicity of a positive carbon isotope excursion at the Cenomanian/Turonian boundary: validation by calcareous microfossil biostratigraphy of the Yezo Group, Hokkaido, Japan. *The Island Arc* 2, 181-191.
- Hiess, J., Condon, D.J., McLean, N., Noble, S.R., 2012.  $^{238}\text{U}/^{235}\text{U}$  systematics in terrestrial uranium-bearing minerals. *Science* 335, 1610-1614.
- Jaffey, A.H., Flynn, K.F., Glendenin, L.E., Bentley, W.C., Essling, A.M., 1971. Precision measurement of half-lives and specific activities of  $^{235}\text{U}$  and  $^{238}\text{U}$ . *Physical Review C* 4, 1889-1906.
- Jarvis, I., Lignum, J. S., Grocke, D. R., Jenkyns, H. C., Pearce, M. A., 2011. Black shale deposition, atmospheric  $\text{CO}_2$  drawdown, and cooling during the Cenomanian-Turonian Oceanic Anoxic Event. *Paleoceanography* 26, PA3201.
- Jenkyns, H.C., 1980. Cretaceous anoxic events: from continents to oceans. *J. Geol. Soc. London* 137, 171–188.
- Jenkyns, H. C., Matthews, A., Tsikos, H., Erel, Y., 2007. Nitrate reduction, sulfate reduction, and sedimentary iron isotope evolution during the Cenomanian-Turonian oceanic anoxic event. *Paleoceanography*, 22, doi:10.1029/2006PA001355.
- Jones, C. E., Jenkyns, H. C., 2001. Seawater strontium isotopes, oceanic anoxic events, and seafloor hydrothermal activity in the Jurassic and Cretaceous. *Am. J. Sci.*, 301, 112 – 149.
- Kaiho, K., Fujiwara, O., Motoyama, I., 1993. Mid-Cretaceous faunal turnover of intermediate-water benthic foraminifera in the northwestern Pacific Ocean margin. *Mar. Micropaleontol.* 23, 13-49.

- Kane, J.S., Arbogast, B.F., and Leventhal, J.S., 1990. Characterization of Devonian Ohio Shale SDO-1 as a USGS geochemical reference sample: *Geostandards Newsletter* 14, 169-196.
- Kendall, B., Creaser, R. A., Selby, D., 2009.  $^{187}\text{Re}$ - $^{187}\text{Os}$  geochronology of Precambrian organic-rich sedimentary rocks. *Geol. Soc. London Spec. Pub.* 326, 85-107.
- Kuroda, J., Tanimizu, M., Hori, R.S., Suzuki, K., Ogawa, N.O., Tejada, M.L., Ohkouchi, N., 2011. Lead isotopic record of Barremian–Aptian marine sediments: Implications for large igneous provinces and the Aptian climatic crisis. *Earth Planet. Sci. Lett.* 307, 126-134.
- Leckie, R. M., Bralower, T. J., Cashman, R., 2002. Oceanic anoxic events and plankton evolution: Biotic response to tectonic forcing during the mid-Cretaceous. *Paleocean.* 17, 3.
- Ma, Chao, Meyers, S.R., Sageman, B.B., Singer, B.S., Jicha, B.R., 2014. Testing the astronomical time scale for Oceanic Anoxic Event 2, and its extension into Cenomanian strata of the Western Interior Basin. *Geol. Soc. Am. Bull.* doi: 10.1130/B30922.1
- MacLeod, K. G., Marin, E. E., Blair, S. W., 2008. Nd excursions across the Cretaceous oceanic anoxia event 2 (Cenomanian-Turonian) in the tropical North Atlantic. *Geology* 36, 811-814.
- Martin, E. E., MacLeod, K. G., Jimenez Berroco, A., Bourbon, E., 2012. Water mass circulation on Demerara Rise during the Late Cretaceous based on Nd isotopes. *Earth Planet. Sci. Lett.*, 327-328, 111-120.
- Mattinson, J.M., 2005. Zircon U-Pb chemical abrasion (“CA-TIMS”) method: combined annealing and multi-step partial dissolution analysis for improved precision and accuracy of zircon ages. *Chem. Geol.* 220, 47–66.
- McArthur, J.M., Howarth, R.J., Bailey, T., 2004. Strontium isotope stratigraphy. In: Gradstein, F., Ogg, J., Smith, A., (Eds.) *A Geological Time Scale 2004*. Cambridge University Press, Cambridge, U.K., pp. 96–105.
- McLean, N., Bowring, J., Bowring, S., 2011. An Algorithm for U-Pb Isotope Dilution Data Reduction and Uncertainty Propagation. *Geochemistry Geophysics Geosystems*.
- McLean, N., Others, in-review. Evaluating Uncertainties in the Calibration of Isotopic Reference Materials and Multi-Element Isotopic Tracers (EARTHTIME Tracer Calibration Part II). *Geochim. Cosmochim. Acta*.
- Meyers, S.R., Siewert, S.E., Singer, B.S., Sageman, B.B., Condon, D.J., Obradovich, J.D., Jicha, B.R., Sawyer, D.A., 2012a. Intercalibration of radioisotopic and

- astrochronologic time scales for the Cenomanian-Turonian boundary interval, Western Interior Basin, USA. *Geology* 40, 7-10.
- Meyers, S.R, Sageman, B.B., Arthur, M.A., 2012b. Obliquity forcing and the amplification of high-latitude climate processes during Oceanic Anoxic Event 2. *Paleoceanography* 27, PA3212, doi:10.1029/2012PA002286.
- Montoya-Pino, C., Weyer, S., Anbar, A.D., Pross, J., Oschmann, W., van de Schootbrugge, B., Arz, H.W., 2010. Global enhancement of ocean anoxia during Oceanic Anoxic vent 2: A quantitative approach using U isotopes. *Geology* 38, 315-318.
- Mort, H. P., Adatte, T., Follmi, K. B., Keller, G., Steinmann, P., Matera, V., Berner, Z., Stüben, D., 2011. Phosphorus and the roles of productivity and nutrient recycling during Oceanic Anoxic Event 2. *Geology*, 35, 6; 483-486.
- Murphy, M. A., Rodda, P. U., Morton, D. M., 1969. Geology of the Ono Quadrangle, Shasta and Tehama Counties, California. California Division of Mines and Geology, San Francisco, CA. Bulletin 192.
- Nier, A. O., 1937. The isotopic constitution of osmium. *Physics Reviews*, 52: 885.
- Nowell, G.M., Luguet, A., Pearson, D.G., Horstwood, M.S.A., 2008. Precise and accurate  $^{186}\text{Os}/^{188}\text{Os}$  and  $^{187}\text{Os}/^{188}\text{Os}$  measurements by multi-collector plasma ionisation mass spectrometry (MC-ICP-MS) part I: Solution analyses. *Chem. Geo.* 248, 363-393.
- Obradovich, J. 1993. The Evolution of the Western Interior Basin, Geological Association of Canada, Special Paper 39, 379-396.
- Oxburgh, R., 2001, Residence time of osmium in the oceans. *Geochemistry, Geophysics, Geosystems* 2, 2000GC000104.
- Paquay, F. S., Ravizza, G., 2012. Heterogeneous seawater  $^{187}\text{Os}/^{188}\text{Os}$  during the Late Pleistocene glaciations. *Earth Planet. Sci. Lett.* 349 – 350, 126 – 138.
- Peucker-Ehrenbrink, B., Ravizza, G., 2000. The marine osmium isotope record. *Terra Nova* 12, 205-219.
- Pogge von Strandmann, P.A.P., Jenkyns, H.C., Woodfine, R.G., 2013. Lithium isotope evidence for enhanced weathering during Oceanic Anoxic Event 2. *Nature Geoscience*, 6, 668-672.
- Pratt, L.M., Kauffman, E.G., Zelt, F.B., 1985. Fine-grained deposits and biofacies of the Cretaceous Western Interior Seaway: evidence for cyclic sedimentary processes. *Soc. Econ. Paleont. Miner. Field Trip Guidebook* 4, 1985 Midyear Meeting, Golden, Colorado.
- Quidelleur, X., Paquette, J.L., Fiet, N., Takashima, R., Tiepolo, M., Desmares, D., Nishi, H., Grosheny, D., 2011. New U-Pb (ID-TIMS and LA-ICPMS) and  $^{40}\text{Ar}/^{39}\text{Ar}$

- geochronological constraints of the Cretaceous geologic time scale calibration from Hokkaido (Japan). *Chem. Geol.* 286, 72-83.
- Sageman, B.B., Meyers, S.R., Arthur, M.A., 2006. Orbital time scale and new C-isotope record for Cenomanian–Turonian boundary stratotype. *Geology* 34, 125–128.
- Sageman, B.B., Singer, B.S., Meyers, S.R., Siewert, S.E., Walaszczyk, I., Condon, D.J., Sawyer, D.A., 2014. Integrating  $^{40}\text{Ar}/^{39}\text{Ar}$ , U-Pb, and astronomical clocks in the Cretaceous Niobrara Formation, Western Interior Basin, USA. *Geol. Soc. Am. Bull.* B30929-1.
- Schlanger, S.O., Arthur, M.A., Jenkyns, H.C., Scholle, P.A. 1987. The Cenomanian/Turonian Oceanic Anoxic Event, I. Stratigraphy and distribution of organic carbon-rich beds and the marine  $\delta^{13}\text{C}$  excursion. In: Brooks, J. & Fleet, A.J. (eds) *Marine Petroleum Source Rocks*. Geological Society London, Spec. Publ., 26, 371–399.
- Schoene, B., Guex, J., Bartolini, A., Schaltegger, U., Blackburn, T., 2010. Correlating the end-Triassic mass extinction and flood basalt volcanism at the 100 ka level. *Geology* 38, 387-390.
- Selby, D., Creaser, R.A., 2003. Re-Os geochronology of organic rich sediments: an evaluation of organic matter analysis methods. *Chem. Geol.* 200, 225–240.
- Sinton, C. W., Duncan, R. A., 1997. Potential links between ocean plateau volcanism and global ocean anoxia and the Cenomanian-Turonian boundary. *Econ. Geol.*, 92, 836-842.
- Smoliar, M.I., Walker, R.J., Morgan, J.W., 1996. Re-Os ages of group IIA, IIIA, IVA, and IVB iron meteorites. *Science* 23, 1099 – 1102.
- Snow, L. J., Duncan, R. A., Bralower, T. J., 2005. Trace element abundances in the Rock Canyon Anticline, Pueblo, Colorado, marine sedimentary section and their relationship to Caribbean plateau construction and oxygen anoxic event 2. *Paleoceanography* 20, doi:10.1029/2004PA001093.
- Takashima, R., Kawabe, F., Nishi, H., Moriya, K., Wani, R., Ando, H., 2004. Geology and stratigraphy of forearc basin sediments in Hokkaido, Japan: Cretaceous environmental events on the northwest Pacific margin. *Cret. Res.* 25, 365-390.
- Takashima, R., Nishi, H., Yamanaka, T., Hayashi, K., Waseda, A., Obuse, A., Tomosugi, T., Deguchi, N., Mochizuki, S., 2010. High-resolution terrestrial carbon isotope and planktic foraminiferal records of the Upper Cenomanian to the Lower Campanian in the Northwest Pacific. *Earth Planet. Sci. Lett.* 289, 570-582.

- Takashima, R., Nishi, H., Yamanaka, T., Tomosugi, T., Fernando, A.G., Tanabe, K., Moriya, K., Kawabe, F., Hayashi, K., 2011. Prevailing oxic environments in the Pacific Ocean during the mid-Cretaceous Oceanic Anoxic Event 2. *Nature Comms.* 2:234 DOI:10.1038/ncomms1233.
- Tamaki, M., Itoh, Y., 2008. Tectonic implications of paleomagnetic data from upper Cretaceous sediments in the Oyubari area, central Hokkaido, Japan. *Island Arc* 17, 270-284.
- Trabucho-Alexandre, J., Tüenter, E., Henstra, G.A., van der Zwan, K.J., van de Wal, R.S.W., Dijkstra, H.A., de Boer, P.L., 2010. The mid-Cretaceous North Atlantic nutrient trap: Black shales and OAEs. *Paleoceanography* 25, doi:10.1029/2010PA001925.
- Tsikos, H., Jenkyns, H.C., Walsworth-Bell, B., Petrizzo, M.R., Forster, A., Kolonic, S., Erba, E., Premoli-Silva, I.P., Baas, M., Wagner, T., Sinninghe Damsté, J.S., 2004. Carbon-isotope stratigraphy recorded by the Cenomanian - Turonian Oceanic Anoxic Event: correlation and implications based on three key localities. *J. Geol. Soc. London* 161, 711-719.
- Turgeon, S.C., Creaser, R.A., 2008. Cretaceous Anoxic Event 2 triggered by a massive magmatic episode. *Nature* 454, 323–326.
- Voigt, S., Erbacher, J., Mutterlose, J., Weiss, W., Westerhold, T., Wiese, F., Wilmsen, M., Wonik, T., 2008. The Cenomanian-Turonian of the Wunstorf section (North Germany): global stratigraphic reference section and new orbital time scale for Oceanic Anoxic Event 2. *Newsl. Stratigr.* 43, 65-89.
- Völkening, J., T. Walczyk, et al., 1991. Osmium isotope ratio determinations by negative thermal ion mass spectrometry. *International Journal of Mass Spectrometry Ion Processes*, 105, 147-159.
- Wendt, I., Carl, C., 1991. The statistical distribution of the mean squared weighted deviation. *Chemical Geology: Isotope Geoscience section* 86, 275-285.
- Zheng X-Y., Jenkyns, H.C., Gale, A.S., Ward, D.J., Henderson, G.M., 2013. Changing ocean circulation and hydrothermal inputs during Oceanic Anoxic Event 2 (Cenomanian-Turonian): Evidence from Nd-isotopes in the European shelf sea. *Earth Planet. Sci. Lett.* <http://dx.doi.org/10.1016/j.epsl.2013.05.053i>

Data tables

Table 3.1 Re - Os data for USGS Std. SDO-1.

Std Sample	Re(ppb)	±	Os(ppt)	±	<sup>187</sup> Re/ <sup>188</sup> Os	±	<sup>187</sup> Os/ <sup>188</sup> Os	±	Os <sub>i</sub> (@366Ma)	±
SDO-1	76.3	0.25	638.1	3.63	1145.0	5.3	7.688	0.028	0.69	0.002
SDO-1	72.4	0.23	597.8	3.63	1175.1	5.7	7.896	0.032	0.71	0.002
SDO-1	84.9	0.27	701.4	3.80	1172.9	5.2	7.881	0.026	0.71	0.002
SDO-1	85.5	0.28	699.8	3.85	1191.5	5.3	7.975	0.027	0.69	0.002
Average	79.8		659.3		1171.1		7.860		0.70	
2 S.D.	12.9		101.0		38.6		0.243		0.03	
2σ % uncertainty	16.2		15.3		3.3		3.097		3.66	

Note: individual SDO-1 data uncertainties are given at the 2σ level.

Os<sub>i</sub> uncertainties are determined through full propagation of uncertainties in Re & Os mass spectrometry, spike, blanks and std Re & Os isotopic values

Table 3.2a Re/Os data for geochemical analysis of Yucca Group stratigraphy, Texas

Sample ID	Depth (m)	kyr	Re (ppb)	±	Os (ppt)	±	<sup>187</sup> Re/ <sup>188</sup> Os	±	<sup>187</sup> Os/ <sup>188</sup> Os	±	Os <sub>i</sub> (ppb)	Os <sub>i</sub> (@85.9 Ma)	±
TT40A	138.10	2058.80	0.30	0.006	39.27	0.531	59.80	1.507	0.67	0.826	13.14	0.81	0.016
TT36A	138.53	2036.90	0.34	0.006	45.86	0.513	58.38	1.808	0.67	0.828	13.72	0.81	0.012
TT35A	133.96	2084.32	0.34	0.006	48.85	0.604	56.83	1.108	0.63	0.825	18.56	0.80	0.015
TT33A	138.55	1981.00	0.33	0.006	51.32	0.504	53.37	1.103	0.63	0.825	18.75	0.80	0.015
TT30A	127.23	1919.25	0.42	0.006	41.85	0.471	51.86	1.548	0.67	0.828	16.13	0.79	0.012
TT28A	125.40	1885.80	0.35	0.006	52.55	0.727	54.44	1.123	0.68	0.826	28.22	0.83	0.016
TT26A	123.60	1872.98	0.32	0.006	46.37	0.648	56.32	1.207	0.66	0.825	17.83	0.80	0.015
TT24A	121.20	1842.55	0.43	0.006	41.82	0.444	54.23	1.484	0.68	0.828	15.79	0.80	0.012
TT19A	118.00	1776.03	0.40	0.006	47.87	0.683	42.87	1.357	0.69	0.826	18.34	0.82	0.015
TT17A	113.96	1750.76	0.25	0.006	37.26	0.726	34.87	1.661	0.66	0.830	14.39	0.80	0.023
TT15A	111.75	1722.74	0.29	0.006	39.82	0.545	38.22	1.341	0.67	0.826	14.86	0.81	0.016
TT13A	110.00	1706.56	0.32	0.006	41.11	0.575	48.43	1.264	0.66	0.826	15.88	0.79	0.015
TT10A	104.36	1629.05	0.30	0.006	35.53	0.503	43.53	1.514	0.68	0.827	13.68	0.81	0.026
AD60-11	88.75	1557.50	0.23	0.006	27.86	0.553	42.80	2.888	0.69	0.830	18.71	0.83	0.024
AD62-11	82.50	1478.69	0.32	0.006	47.22	0.816	34.71	1.565	0.68	0.830	18.17	0.83	0.023
AD64-11	84.18	1372.18	0.28	0.006	41.37	0.806	35.24	1.616	0.69	0.830	15.91	0.83	0.023
AD66-11	77.18	1283.45	0.45	0.006	42.20	0.816	54.83	2.368	0.63	0.836	16.35	0.54	0.026
AD68-11	71.85	1236.89	0.23	0.006	33.33	0.853	35.48	1.748	0.66	0.838	12.86	0.81	0.021
AD68-11	64.85	1128.14	0.25	0.006	42.66	0.828	36.38	1.433	0.68	0.838	16.43	0.83	0.023
AD60-11	59.25	1057.14	0.29	0.006	46.54	0.788	37.51	1.721	0.66	0.838	15.84	0.80	0.022
AD64-11	59.75	949.38	0.28	0.006	46.28	0.777	35.88	1.616	0.66	0.835	15.67	0.55	0.026
AD66-11	44.00	861.89	0.36	0.006	29.35	0.578	27.39	1.566	0.64	0.838	11.28	0.80	0.025
AD68-11	36.89	773.79	0.17	0.006	34.34	0.672	25.38	1.378	0.65	0.837	13.78	0.84	0.024
AD118-11	29.50	679.87	0.32	0.006	46.30	0.782	46.37	1.828	0.65	0.837	15.58	0.58	0.021
AD112-11	22.75	584.39	0.20	0.006	28.27	0.557	36.37	1.878	0.63	0.837	18.85	0.57	0.022
AD114-11	35.80	396.28	0.36	0.006	36.29	0.592	27.86	1.532	0.61	0.835	11.77	0.56	0.023
AD116-11	7.80	486.32	0.26	0.006	32.89	0.838	59.38	1.887	0.56	0.833	12.89	0.80	0.019
AD118-11	6.25	389.35	0.32	0.006	35.39	0.883	46.42	2.108	0.61	0.835	13.86	0.54	0.020
AD128-11	-7.35	214.31	1.30	0.012	187.68	3.548	17.42	0.728	0.21	0.812	125.71	0.18	0.006
AD123-11	-11.25	183.35	1.37	0.012	580.82	30.410	9.78	0.409	0.18	0.810	258.38	0.16	0.006
AD123-11	-15.28	53.87	1.40	0.013	738.64	33.248	9.21	0.378	0.19	0.811	302.80	0.17	0.006
CT818	-16.15	0.08	1.43	0.013	238.73	7.244	29.27	0.847	0.19	0.808	96.87	0.15	0.003
CT815	-17.48	-11.72	0.73	0.012	11.45	0.332	331.13	23.308	0.71	0.809	4.39	0.19	0.010
CT813	-18.68	-22.96	0.55	0.012	8.88	0.323	322.53	27.407	0.79	0.808	5.43	0.28	0.018
AD123-11	-19.35	-28.99	1.24	0.012	81.82	1.247	185.83	4.543	0.66	0.809	23.33	0.89	0.025
AD124-11	-21.80	-45.46	1.39	0.012	57.71	1.368	189.08	4.705	0.87	0.801	23.71	0.70	0.023
AD125-11	-23.25	-68.55	1.81	0.012	78.24	0.823	136.33	8.196	0.91	0.805	14.89	0.70	0.026
AD128-11	-24.65	-82.48	1.84	0.009	46.22	1.097	98.86	3.609	0.84	0.846	22.75	0.70	0.025
AD128-11	-28.55	-118.23	1.80	0.013	87.85	1.288	125.48	3.533	0.92	0.833	23.82	0.72	0.026
AD138-11	-33.78	-157.89	1.84	0.012	58.82	1.384	93.89	4.847	0.82	0.846	22.31	0.87	0.024
AD132-11	-37.18	-151.85	0.82	0.009	58.35	1.154	83.37	3.511	0.84	0.846	23.96	0.71	0.023
AD134-11	-40.65	-186.84	1.30	0.012	64.79	1.298	89.21	3.842	0.84	0.848	24.46	0.71	0.025
AD136-11	-44.60	-183.30	1.21	0.013	49.34	1.806	130.68	5.694	0.88	0.851	18.40	0.67	0.025
AD138-11	-47.85	-197.86	0.80	0.010	56.33	1.136	82.81	3.562	0.82	0.847	21.49	0.69	0.025
AD148-11	-51.25	-210.81	1.63	0.016	76.38	1.423	122.43	5.279	0.85	0.849	26.55	0.66	0.024
AD143-11	-56.18	-251.82	0.83	0.013	65.26	1.291	65.79	2.807	0.74	0.843	24.86	0.63	0.023
AD144-11	-59.85	-246.68	1.30	0.013	87.86	1.228	64.83	1.846	0.69	0.827	33.83	0.58	0.014
AD146-11	-63.80	-263.30	1.88	0.012	181.45	1.386	54.59	1.628	0.60	0.823	38.44	0.52	0.013
AD148-11	-67.80	-282.31	0.72	0.012	56.78	1.832	74.48	3.408	0.84	0.849	18.19	0.72	0.027
AD158-11	-71.25	-307.81	0.80	0.012	56.47	1.816	83.56	3.765	0.87	0.851	18.80	0.74	0.027
AD153-11	-75.80	-336.31	0.89	0.012	44.57	0.694	72.88	1.537	0.79	0.817	24.55	0.67	0.010
AD154-11	-79.75	-358.82	0.55	0.012	46.34	0.838	71.55	3.408	0.83	0.850	15.25	0.72	0.026
AD156-11	-83.45	-381.82	1.35	0.012	64.88	0.856	94.45	2.896	0.89	0.835	24.28	0.74	0.019
AD158-11	-88.00	-408.33	0.82	0.012	45.48	0.833	94.34	4.293	0.83	0.849	17.20	0.68	0.025
AD168-11	-91.28	-427.53	0.58	0.012	47.51	0.873	64.30	3.855	0.83	0.849	17.86	0.73	0.028
AD163-11	-94.48	-446.34	0.59	0.012	44.56	0.824	76.79	3.365	0.91	0.854	16.88	0.80	0.030
AD164-11	-97.78	-466.58	0.83	0.012	47.82	0.878	181.67	4.532	0.81	0.848	18.16	0.66	0.024
AD164-11	-104.68	-489.85	0.72	0.012	46.59	0.855	81.56	3.758	0.84	0.850	17.59	0.72	0.027
AD168-11	-105.16	-510.85	0.67	0.012	43.54	0.877	83.30	3.896	0.82	0.849	16.10	0.69	0.026
AD178-11	-109.68	-537.85	0.75	0.012	46.35	0.848	83.87	3.884	0.80	0.847	17.80	0.66	0.023
AD172-11	-112.78	-556.56	0.83	0.012	57.31	1.158	76.49	3.597	0.86	0.850	23.58	0.74	0.027
AD174-11	-116.18	-576.86	0.87	0.012	46.82	0.848	83.85	4.834	0.81	0.848	15.40	0.68	0.026
AD178-11	-120.38	-602.37	0.76	0.012	44.80	0.823	89.75	4.118	0.84	0.850	16.86	0.70	0.026
AD178-11	-124.34	-626.37	0.76	0.012	54.88	1.113	72.55	3.278	0.84	0.849	28.77	0.72	0.027
AD188-11	-131.78	-676.86	0.73	0.012	36.36	1.077	57.68	3.203	0.80	0.854	11.40	0.71	0.033

Note: individual ratio uncertainties are given at the 2σ level.

Os<sub>i</sub> uncertainties are determined through full propagation of uncertainties in Re & Os mass spectrometry, spike, blanks and std Re & Os isotopic values by calculated as detailed in chapter 3, section 5.2.

CHAPTER 3. TRANS-PACIFIC OAE 2

Table 3.2b Re-Os data for geochemical analysis of the Great Valley Sequence, California, USA

Sample ID	Depth (m)	kyr	Re (ppb)	+	Os (ppt)	+	<sup>187</sup> Re/ <sup>188</sup> Os	+	<sup>187</sup> Os/ <sup>188</sup> Os	+	<sup>187</sup> Os (ppm)	Os <sub>c</sub> (±93.9 Ma)	+
US 908	312.50	515.75	1.03	0.012	85.03	1.681	63.54	2.713	0.82	0.047	52.20	0.72	0.026
US 903	296.00	487.07	0.76	0.012	65.38	1.297	61.03	2.714	0.77	0.044	24.92	0.67	0.024
US 089	279.50	460.41	0.87	0.012	78.25	1.474	60.94	2.654	0.76	0.046	28.34	0.67	0.025
US 613	261.00	430.52	0.32	0.006	24.10	0.376	71.93	2.561	1.01	0.041	8.92	0.80	0.024
US 621	244.50	403.86	0.48	0.006	53.99	0.746	45.89	1.390	0.68	0.026	20.79	0.61	0.015
US 626	227.50	376.39	0.38	0.006	40.95	0.805	48.66	2.142	0.76	0.044	15.61	0.69	0.025
US 612	212.80	352.64	0.45	0.006	49.77	0.698	46.59	1.438	0.75	0.029	19.01	0.67	0.017
US 637	195.50	324.69	0.61	0.012	56.59	1.128	56.25	2.622	0.75	0.045	21.66	0.64	0.024
US 648	175.20	291.89	0.29	0.006	54.13	1.034	27.72	1.263	0.59	0.034	21.08	0.54	0.020
US 653	159.50	266.52	1.05	0.012	82.73	1.596	65.19	2.782	0.61	0.035	32.13	0.50	0.018
US 084	142.00	238.25	0.89	0.012	140.46	2.654	31.99	1.377	0.46	0.027	55.56	0.41	0.015
US 662	124.50	209.97	0.48	0.006	156.16	1.978	15.11	0.450	0.33	0.013	62.78	0.31	0.007
US 666	106.20	180.40	0.62	0.012	179.10	3.264	16.91	0.758	0.26	0.015	72.66	0.24	0.009
US 674	88.50	151.80	1.05	0.012	154.62	2.853	34.00	1.429	0.59	0.022	61.50	0.33	0.012
US 675	84.10	144.69	0.86	0.012	223.71	4.085	18.91	0.807	0.30	0.017	90.35	0.27	0.010
US 061	82.00	141.30	0.92	0.012	176.47	3.247	25.93	1.101	0.35	0.020	70.84	0.31	0.011
US 676	78.90	136.29	0.80	0.012	32.30	0.654	122.66	5.794	0.31	0.020	13.03	0.12	0.005
US 677	75.60	130.96	0.81	0.012	30.52	0.624	130.24	6.202	0.31	0.020	12.30	0.11	0.004
US 062	72.30	114.40	1.28	0.015	424.53	5.269	14.72	0.420	0.24	0.009	172.75	0.22	0.005
US 678	68.50	95.33	1.58	0.015	108.22	1.077	71.68	1.607	0.26	0.008	43.92	0.15	0.003
US 679	65.00	77.37	0.59	0.012	67.24	1.248	43.08	1.983	0.22	0.013	27.43	0.15	0.006
US 680	60.70	56.20	1.34	0.015	88.28	0.905	74.96	1.743	0.31	0.009	55.62	0.19	0.004
US 681	60.40	54.69	0.92	0.012	39.94	0.783	113.31	5.121	0.32	0.019	16.09	0.14	0.004
US 682	59.90	52.18	1.94	0.014	36.54	0.475	270.27	7.392	0.56	0.019	14.28	0.13	0.003
US 684	58.90	47.17	1.31	0.015	121.25	1.367	56.68	1.289	0.79	0.023	46.07	0.70	0.013
US 063	58.00	42.65	1.49	0.015	28.23	0.420	274.93	8.667	0.75	0.028	10.78	0.32	0.008
US 687	57.00	37.63	1.24	0.015	20.34	0.365	122.08	12.564	0.89	0.039	7.64	0.38	0.011
US 688	55.71	31.16	1.30	0.015	28.38	0.419	237.81	7.531	0.73	0.027	10.87	0.35	0.009
US 064	55.60	30.61	1.07	0.012	14.23	0.393	396.34	24.693	0.84	0.063	5.38	0.22	0.011
US 065	55.30	29.10	2.34	0.014	30.70	0.404	397.10	10.669	0.76	0.024	11.71	0.14	0.003
US 066	54.20	23.58	0.88	0.012	40.23	0.433	126.35	3.961	0.69	0.018	15.48	0.49	0.009
US 690	52.70	16.06	0.56	0.012	12.30	0.365	240.60	16.766	0.83	0.066	4.65	0.45	0.024
US 067	52.30	14.05	0.97	0.012	9.93	0.316	534.72	39.357	1.13	0.090	3.62	0.30	0.016
US 691	51.60	10.54	0.75	0.012	17.71	0.439	218.85	12.433	0.68	0.048	6.82	0.34	0.015
US 692	50.40	4.52	0.99	0.012	92.01	1.310	56.35	1.716	0.81	0.031	34.88	0.72	0.018
US 068	50.20	3.51	0.67	0.012	17.58	0.449	199.46	11.507	0.75	0.052	6.71	0.44	0.020
US 069	49.50	0.00	1.17	0.015	13.93	0.340	443.10	24.241	0.83	0.052	5.27	0.13	0.006
US 694	48.10	-7.02	1.10	0.015	12.77	0.332	457.20	26.856	0.87	0.058	4.80	0.16	0.007
US 070	47.70	-9.05	1.22	0.015	21.53	0.403	280.33	11.955	0.64	0.032	8.33	0.19	0.006
US 071	45.20	-21.58	0.57	0.012	17.82	0.434	160.81	9.288	0.53	0.037	6.99	0.28	0.013
US 072	44.50	-23.09	3.74	0.017	61.54	0.619	321.96	5.731	0.90	0.022	25.08	0.39	0.006
US 698	43.90	-24.16	2.21	0.014	36.81	0.423	316.08	7.229	0.83	0.022	13.93	0.33	0.006
US 1002	43.20	-31.61	0.69	0.012	15.18	0.404	235.76	14.465	0.74	0.055	5.80	0.37	0.018
US 1003	40.40	-45.66	1.45	0.015	31.97	0.451	236.64	7.032	0.75	0.027	12.21	0.38	0.009
US 1007	34.50	-75.26	0.63	0.012	32.40	0.716	106.63	5.270	1.12	0.068	11.85	0.95	0.037
US 1009	27.00	-112.90	1.57	0.015	22.33	0.386	377.44	13.700	0.99	0.042	8.29	0.40	0.011
US 075	25.50	-120.42	1.12	0.015	36.12	0.610	170.08	5.903	1.19	0.051	13.10	0.92	0.023
US 1011	22.10	-137.48	1.11	0.012	14.97	0.352	396.42	20.826	0.94	0.056	5.59	0.32	0.013
US 1012	19.40	-151.03	1.35	0.015	72.41	1.461	99.57	4.214	0.95	0.055	27.00	0.79	0.028
US 076	11.00	-193.18	0.82	0.012	20.56	0.400	208.74	9.169	0.79	0.040	7.81	0.47	0.016
US 077	0.00	-248.37	2.74	0.015	78.35	0.613	192.16	2.488	1.21	0.018	28.34	0.91	0.009

Note: individual ratio uncertainties are given at the 2 $\sigma$  level.

Os<sub>c</sub> uncertainties are determined through full propagation of uncertainties in Re & Os mass spectrometry, spikes, blanks and old Re & Os isotopic values kyr calculated as detailed in chapter 3, section 5.2.

CHAPTER 3. TRANS-PACIFIC OAE 2

Table 3.4 ODP and  $\delta^{18}O_{carb}$  for the West Pacific Ocean, Sites 803

Sample No.	Stratigraphic Level (m)	$\delta^{18}O_{carb}$ (‰)	Age (ka)	Depth (m)	Core No.	Stratigraphic Level (m)	$\delta^{18}O_{carb}$ (‰)	Age (ka)	Depth (m)	Core No.	Stratigraphic Level (m)	$\delta^{18}O_{carb}$ (‰)	Age (ka)	Depth (m)	Core No.
T142a	146.25	-24.78	0.847	2099.23	T995	3.25	-25.36	0.879	311.36	T0707	467.8	-23.58	198.33	05855	148.8
T142b	136.10	-23.13	0.847	3096.88	T953	3.60	-23.68	0.868	349.16	T0706	425.5	-24.98	71.57	05863	143.5
T142c	123.24	-23.73	0.846	2662.87	T923	2.71	-23.85	0.216	143.98	T0692	413.8	-24.47	696.43	05884	142.8
T142d	121.94	-23.48	0.833	2609.49	T984	3.41	-24.14	0.856	312.18	T0704	408.8	-24.21	472.37	05858	139.2
T142e	111.75	-24.33	0.863	1985.47	T958	3.30	-22.88	0.880	337.75	T0693	382.5	-23.76	668.8	05879	136.5
T142f	106.01	-24.89	0.865	1996.26	T951	3.75	-23.89	0.827	333.25	T0692	388.5	-23.31	622.1	05788	136.2
T142g	121.25	-23.34	0.849	1954.42	T983	3.81	-23.79	0.868	318.24	T0691	328.8	-23.81	612.7	05843	127.8
T142h	121.40	-24.16	0.834	1998.96	T982	3.31	-22.69	0.841	326.87	T0692	324.3	-24.23	614.4	05846	124.5
T142i	121.60	-23.38	0.873	1878.14	T981	6.70	-23.52	0.848	320.88	T0694	314.8	-24.23	613.9	05845	120.8
T142j	121.20	-23.79	0.845	1887.72	T982	6.40	-23.80	0.860	314.23	T0693	314.2	-23.93	612.2	05844	115.8
T142k	118.70	-24.34	0.836	1816.82	T988	6.23	-22.88	0.841	314.28	T0693	313.9	-24.87	617.9	05833	111.8
T142l	136.80	-24.57	0.886	1785.79	809	6.60	-22.94	0.888	311.13	T0698	312.3	-22.33	612.9	05868	111.7
T142m	113.94	-23.89	0.833	1755.93	T9711	6.38	-24.82	0.813	309.28	T0697	308.8	-24.68	618.3	05822	109.6
T142n	111.73	-24.89	0.834	1727.81	T9786	6.40	-23.09	0.879	306.85	T0696	308.8	-21.77	618.8	05849	108.8
T142o	116.80	-24.61	0.878	1710.72	T9783	6.79	-23.88	0.828	301.42	T0695	303.5	-22.31	618.8	05849	96.4
T142p	104.36	-24.28	0.878	1614.22	T9712	6.93	-22.94	0.822	299.28	T0694	299.8	-23.68	609.5	05818	96.4
T142q	101.37	-23.48	0.822	1596.13	T9784	6.40	-23.84	0.844	295.18	T0693	296.8	-23.14	607.7	05833	92.5
T142r	98.75	-23.44	0.855	1543.89	T9783	6.75	-22.84	0.844	289.94	T0698	296.8	-22.96	610.7	05825	90.1
T142s	97.88	-24.25	0.838	1548.98	T9781	6.28	-23.84	0.844	286.58	T0693	287.3	-23.38	607.7	05814	88.5
T142t	96.88	-24.73	0.845	1488.23	T9782	6.40	-23.84	0.844	286.58	T0692	286.8	-23.14	612.7	05825	88.5
T142u	96.38	-24.73	0.845	1488.23	T9782	6.40	-23.84	0.844	286.58	T0692	286.8	-23.14	612.7	05825	88.5
T142v	96.38	-24.73	0.845	1488.23	T9782	6.40	-23.84	0.844	286.58	T0692	286.8	-23.14	612.7	05825	88.5
T142w	96.38	-24.73	0.845	1488.23	T9782	6.40	-23.84	0.844	286.58	T0692	286.8	-23.14	612.7	05825	88.5
T142x	87.81	-23.65	0.824	1424.98	T9786	6.81	-23.88	0.833	282.52	T0697	272.7	-23.36	613.2	05848	88.5
T142y	81.36	-23.65	0.824	1352.28	T9786	6.81	-23.88	0.833	282.52	T0697	272.7	-23.36	613.2	05848	88.5
T142z	82.38	-24.42	0.847	1352.28	T9789	6.40	-23.88	0.833	282.52	T0697	272.7	-23.36	613.2	05848	88.5
T142aa	86.75	-24.22	0.833	1334.89	T9788	6.80	-23.88	0.833	282.52	T0697	272.7	-23.36	613.2	05848	88.5
T142ab	79.78	-24.18	0.880	1314.84	T9785	6.80	-22.87	0.880	247.74	T0693	264.3	-22.95	607.9	05848	88.5
T142ac	79.33	-24.18	0.880	1314.84	T9785	6.80	-22.87	0.880	247.74	T0693	264.3	-22.95	607.9	05848	88.5
T142ad	77.62	-23.72	0.884	1296.28	T9787	6.40	-22.88	0.884	239.89	T0697	264.4	-22.82	607.3	05866	87.9
T142ae	79.78	-24.64	0.827	1278.88	T9787	6.80	-21.86	0.879	237.88	T0698	264.8	-23.22	613.3	05819	87.9
T142af	71.28	-24.24	0.817	1229.57	T9788	6.80	-22.88	0.879	235.88	T0698	264.8	-23.22	613.3	05819	87.9
T142ag	72.33	-23.83	0.853	1228.89	T9784	6.98	-21.85	0.837	232.72	T0692	264.5	-22.84	613.8	05822	86.9
T142ah	71.22	-24.52	0.898	1214.88	T9783	6.98	-22.84	0.838	232.80	T0692	264.8	-23.91	617.9	05868	86.9
T142ai	68.48	-24.23	0.896	1198.89	T9783	6.73	-21.84	0.822	232.88	T0692	264.8	-23.91	617.9	05868	86.9
T142aj	68.32	-24.42	0.847	1177.38	T9786	6.76	-21.74	0.874	231.58	T0694	264.8	-22.11	617.9	05828	86.9
T142ak	66.99	-22.65	0.849	1168.43	T9786	6.80	-23.58	0.826	230.78	T0695	266.8	-22.41	615.4	05838	86.9
T142al	63.85	-24.57	0.849	1095.27	T9786	6.80	-23.58	0.826	230.78	T0695	266.8	-22.41	615.4	05838	86.9
T142am	64.85	-24.57	0.849	1095.27	T9786	6.80	-23.58	0.826	230.78	T0695	266.8	-22.41	615.4	05838	86.9
T142an	58.85	-24.45	0.884	1047.89	T9781	6.45	-23.85	0.878	230.36	T0695	265.9	-22.55	617.4	05835	86.9
T142ao	56.48	-23.81	0.848	1028.71	T9789	6.45	-24.13	0.888	214.32	T0698	263.7	-23.88	612.3	05781	86.9
T142ap	54.85	-23.81	0.838	998.38	T9788	6.45	-23.87	0.888	216.88	T0698	263.5	-23.88	612.3	05781	86.9
T142aq	52.38	-22.74	0.831	974.19	T9788	6.85	-23.82	0.887	218.84	T0692	262.8	-23.84	614.8	05838	86.9
T142ar	51.38	-22.83	0.873	944.85	T9787	6.80	-23.78	0.888	211.47	T0693	263.3	-23.29	612.3	05833	86.9
T142as	48.41	-23.25	0.849	918.74	T9783	6.25	-23.87	0.888	212.25	T0692	263.5	-23.87	612.3	05833	86.9
T142at	49.78	-24.16	0.885	940.23	T9782	6.80	-23.84	0.888	218.83	T0693	264.8	-21.87	620.7	05822	86.9
T142au	48.23	-22.89	0.833	922.81	T9784	6.24	-24.85	0.894	218.88	T0696	266.8	-22.23	614.8	05822	86.9
T142av	46.45	-23.23	0.891	902.58	T9785	6.70	-23.88	0.888	213.83	T0697	265.2	-21.45	613.8	05874	86.9
T142aw	45.23	-24.12	0.872	884.81	T9781	6.23	-23.88	0.888	212.88	T0698	264.8	-22.23	612.8	05838	86.9
T142ax	44.88	-22.79	0.833	868.96	T9783	6.24	-23.84	0.828	212.88	T0698	264.8	-21.13	612.3	05838	86.9
T142ay	42.79	-22.49	0.827	853.22	T9783	6.80	-23.80	0.878	203.88	T0698	264.8	-21.68	613.3	05838	86.9
T142az	41.88	-22.49	0.827	853.22	T9783	6.80	-23.80	0.878	203.88	T0698	264.8	-21.68	613.3	05838	86.9
T142ba	41.43	-22.49	0.827	853.22	T9783	6.80	-23.80	0.878	203.88	T0698	264.8	-21.68	613.3	05838	86.9
T142bb	40.98	-23.77	0.888	828.88	T9786	6.33	-23.29	0.833	209.88	T0694	262.3	-23.88	612.3	05838	86.9
T142bc	41.25	-23.88	0.849	828.88	T9783	6.45	-23.28	0.823	212.88	T0698	264.8	-21.68	613.3	05838	86.9
T142bd	38.11	-22.25	0.834	794.29	T9784	6.80	-23.12	0.836	211.34	T0698	264.8	-22.23	612.3	05838	86.9
T142be	37.88	-22.25	0.834	794.29	T9784	6.80	-23.12	0.836	211.34	T0698	264.8	-22.23	612.3	05838	86.9
T142bf	37.88	-22.25	0.834	794.29	T9784	6.80	-23.12	0.836	211.34	T0698	264.8	-22.23	612.3	05838	86.9
T142bg	37.88	-22.25	0.834	794.29	T9784	6.80	-23.12	0.836	211.34	T0698	264.8	-22.23	612.3	05838	86.9
T142bh	36.48	-23.22	0.888	772.81	T9786	6.25	-23.78	0.888	206.88	T0698	264.8	-21.68	613.3	05838	86.9
T142bi	36.25	-23.86	0.844	778.71	T9789	6.75	-23.83	0.878	211.34	T0692	262.8	-21.13	611.3	05822	86.9
T142bj	35.48	-23.29	0.888	768.88	T9784	6.80	-23.84	0.888	206.88	T0698	264.8	-21.68	613.3	05838	86.9
T142bk	35.68	-23.85	0.888	758.88	T9747	26.21	-24.88	0.821	194.47	T0692	262.8	-21.68	613.3	05838	86.9
T142bl	34.68	-23.72	0.888	748.78	T9746	27.48	-24.89	0.849	195.45	T0692	262.8	-21.68	613.3	05838	86.9
T142bm	33.68	-23.82	0.845	738.88	T9745	28.55	-24.52	0.811	181.13	T0692	262.8	-21.68	613.3	05838	86.9
T142bn	33.05	-23.94	0.888	738.14	T9744	29.65	-24.84	0.884	182.48	T0692	262.8	-21.68	613.3	05838	86.9
T142bo	32.25	-23.92	0.899	728.88	T9743	30.75	-24.19	0.821	168.85	T0692	262.8	-21.68	613.3	05838	86.9
T142bp	31.38	-22.78	0.895	702.95	T9741	31.76	-24.95	0.867	165.75	T0692	262.8	-21.68	613.3	05838	86.9
T142bq	30.81	-22.78	0.848	688.28	T9741	32.75	-24.17	0.862	162.88	T0692	262.8	-21.68	613.3	05838	86.9
T142br	30.28	-23.28	0.833	684.81	T9740	34.28	-22.87	0.844	161.44	T0692	262.8	-21.68	613.3	05838	86.9
T142bs	29.38	-23.49	0.831	680.13	T9740	34.70	-23.87	0.844	161.44	T0692	262.8	-21.68	613.3	05838	86.9
T142bt	28.78	-23.71	0.848	675.42	T9740	35.78	-23.84	0.888	160.88	T0692	262.8	-21.68	613.3	05838	86.9
T142bu	28.28	-23.17	0.836	668.85	T9740	36.82	-24.81	0.811	157.30	T0692	262.8	-21.68	613.3	05838	86.9
T142bv	26.23	-23.39	0.891	663.93	T9740	38.40	-24.78	0.866	156.78	T0692	262.8				



# 4

## **Calcium isotope stratigraphy across the Cenomanian-Turonian OAE 2: Implications on the controls of marine Ca isotope composition**

A version of this chapter will be submitted *Geochimica et Cosmochimica Acta*; co-authored by Andrew Jacobson and Gregory Lehn and Brad Sageman of Northwestern University, and David Selby of Durham University.

### **1. Introduction**

Calcium is highly abundant in the Earth's crust and has the ability to move as an element ( $\text{Ca}^{2+}$ ) between the lithosphere, biosphere, hydrosphere and atmosphere reservoirs as part of the Ca cycle. The mobility through the Ca cycle influences the Ca isotope composition of geochemical reservoirs, which provides an important link between tectonics, climate and the carbon cycle, and has the potential to simulate the evolution of Ca isotope composition in seawater (DePaolo, 2004; Fantle and DePaolo, 2005; Fantle, 2010). This study presents and discusses the marine  $\delta^{44/40}\text{Ca}$  ( $\delta^{44}\text{Ca}$ ) values across the Oceanic Anoxic Event (OAE) 2.

The OAE 2 brackets the Cenomanian-Turonian boundary (CTB) ~93.90 Ma (Meyers et al., 2012a), for ~600 kyr (Meyers et al., 2012b). OAEs are episodes of disequilibrium between the ocean and atmosphere systems. During this interval the oceans become sub-oxic to anoxic and an abundance of organic-rich material accumulated in ocean basins. The onset of OAEs are characterised by the enhanced burial of organic material and the drawdown of  $\text{CO}_2$ , which produce a positive excursion in the  $\delta^{13}\text{C}$  record (Jenkyns, 1980). More recently the onset of OAE 2 is characterised by an abrupt trend to unradiogenic  $\text{Os}_i$ , which is synchronous worldwide (Du Vivier et al., 2014; Chapter 2, 3, this thesis). There have been many studies that have utilised numerous isotope proxies (e.g., carbon, strontium, lead, lithium, neodymium, osmium, phosphorus; Schlanger et al., 1987; Clarke and Jenkyns 1999; McArthur et al., 2004; MacLeod et al., 2008; Turgeon and Creaser, 2008; Kuroda et al., 2011; Mort et al., 2011; Martin et al., 2012; Pogge von Standmann et al., 2013; Zheng et al., 2013; Du Vivier et al., 2014) in order to assess the factors driving changes in seawater chemistry across the OAE 2. The catalogue

of data have facilitated in determining the driving mechanisms of anoxia and the causes of variable climatic conditions across the CTB.

Calcium is a key element involved in the long-term carbon cycle. Many studies have addressed the factors controlling the  $\delta^{44}\text{Ca}$  evolution of seawater (De La Rocha and DePaolo, 2000; Gussone et al., 2003, 2005, 2006; DePaolo, 2004; Böhm et al., 2006, 2009; Farkaš et al., 2007a, 2007b; Griffith et al., 2008; Fantle, 2010; Blättler et al., 2012; Holmden et al., 2012; Fantle and Tipper, 2013). Calcium isotope values are typically stable throughout the modern and historical oceans, and marine calcium isotope ratios are reported relative to a normalised standard as  $\delta^{44/40}\text{Ca} = [({}^{44}\text{Ca}/{}^{40}\text{Ca})_{\text{sample}}/({}^{44}\text{Ca}/{}^{40}\text{Ca})_{\text{std}} - 1] * 1000$ . The oceanic mass balance of the marine budget largely reflects the mass flux and isotopic evolution of inputs from rivers and mid-ocean ridges, and outputs through the precipitation of calcium carbonate (De La Rocha and DePaolo, 2000; Schmitt et al., 2003; DePaolo, 2004; Fantle and DePaolo, 2005; Sime et al., 2007; Blättler et al., 2012; Fantle and Tipper, 2013). In order to maintain a steady-state isotopic composition in the ocean, i.e., a net mass balance of zero, the influx and removal of elements occurs at the same rate. The evaluation of inputs and outputs has shown that overall the output flux of Ca into carbonate sediments exceeds the flux of Ca from riverine or hydrothermal inputs (Holmden et al., 2012).

The inputs and outputs are influenced by a number of physical and biological controls, such as, rainfall, temperature, salinity, lithology/ $\text{CaCO}_3$  mineralogy, and growth rate (De La Rocha and DePaolo, 2000; Farkaš et al., 2007b; Fantle, 2010; Blättler et al., 2011; Kisakurek et al., 2011; Pretet et al., 2013). Examination to date suggests that seawater  $\delta^{44}\text{Ca}$  values are often influenced by the fractionation of Ca isotopes during precipitation of  $\text{CaCO}_3$  as a consequence of solution chemistry and

the mineralogy of the sediment flux (DePaolo, 2004; Fantle and DePaolo, 2005; Fantle, 2010; Fantle and Tipper, 2013; Ockert et al., 2013). Therefore unlike the other isotopic and elemental studies (Os, Sr, Nd), where the isotopic composition varies from the mixing of predetermined end-members as a function of the source (e.g., Os; Peucker-Ehrenbrink and Ravizza, 2000), the evaluation of variability for Ca isotope studies is made more complicated due to the additional effect of mass dependent fractionation from source to sink (Gussone et al., 2003; Fantle, 2010; Fantle and Tipper, 2013). In addition, simple end-member mixing cannot differentiate the factor influencing the  $\delta^{44}\text{Ca}$  values since the isotopic values of input fluxes are very similar ( $-0.95\text{‰}$  for hydrothermal and  $-1.03\text{‰}$  for riverine; Amini et al., 2008; Holmden et al., 2012). The long residence time of Ca  $\sim 0.5 - 1$  Ma (Schmitt et al., 2003; Farkaš et al., 2007a; Holmden et al., 2012; Fantle and Tipper, 2013) permits the examination of weathering and climate and facilitates the correlation of events over long time scales of a million years (Fantle, 2010); however, geologically instantaneous events can be recorded if the magnitude of the event is sufficiently large, i.e., OAE 2 (Blättler et al., 2011). To date, studies assessing the variability of marine  $\delta^{44}\text{Ca}$  values do not resolve the absolute causes of  $\delta^{44}\text{Ca}$  variability (De La Rocha and DePaolo, 2000; DePaolo, 2004, Fantle and DePaolo, 2005).

A number of the aforementioned isotope proxies suggest that an accelerated hydrological cycle prior to the onset of OAE 2 was responsible for delivering an abundance of nutrient-rich material to the ocean from the continent, which boosts the abundance of organic-rich material and increased productivity in seawater. As a result the deposition of organic-rich material sequestered carbon from  $\text{CO}_2$ , which subsequently led to the development of oceanic anoxia (Jones and Jenkyns, 2001). In addition, a number of proxies imply that hydrothermal input influenced seawater

chemistry contemporaneously with the onset of OAE 2 (Jones and Jenkyns, 2001; Erba, 2004; Frijia and Parente, 2008; Turgeon and Creaser, 2008; Jenkyns, 2010; Du Vivier et al., 2014; Chapter 2, 3, this thesis). However, the extent to which the input from hydrothermalism influences the Ca budget of seawater is poorly understood. We endeavour to evaluate if the dramatic unradiogenic trend in  $Os_i$  associated with volcanism at the Caribbean LIP is recorded by  $\delta^{44}Ca$  values, or if we can quantify the increase in flux of riverine Ca due to weathering as previously proposed (Blättler et al., 2011) that begins prior to the onset of OAE 2, and if this continues for the duration of OAE 2.

In order to differentiate between the increase in input fluxes and determine the dominant factor driving  $\delta^{44}Ca$  variation we utilise a seawater mixing model. The model is derived from modern parameters calculated under a non-steady-state; where the mass and residence time of Ca in seawater is allowed to vary in order to maintain a mass-balance and return to steady-state over time. In order to establish the conditions that best simulate the  $\delta^{44}Ca$  values recorded in nature the input and output fluxes are changed, thus constraining the principal factor that is influencing the evolution of seawater chemistry across the OAE 2.

Our understanding of OAE 2 predominately comes from sites throughout the Atlantic, Tethys and Western Interior basins, which is now supported by two sites in the palaeo-Pacific (Chapter 3, this thesis). This study adds to the proxy data repository of research intending to constrain the parameters controlling the marine Ca isotope cycle, through the evaluation of sections from three globally representative OAE 2 sites: Portland #1 core, USA (WIS), the Yezo Group section, Japan (proto-Pacific Ocean), and the Pont d'Issole section, SE France (Western Tethys Ocean; Fig. 4.1). The Portland #1 core is the representative core for the lower

Turonian GSSP Pueblo Rock Canyon, Colorado, which was ratified through bed-by-bed correlation of chemo-, bio-, and litho- stratigraphy, and age constrained by radio-isotopic dating of tuff horizons (Fig. 4.2; Sageman et al., 2006; Meyers et al., 2012a, 2012b). The Yezo Group is integrated with the WIS timescale using new  $^{206}\text{Pb}/^{238}\text{U}$  ages from tuff horizons (Fig. 4.2; Chapter 3, this thesis) and the Pont d'Issole section has a complete record of correlative bio- and litho- stratigraphy (Fig. 4.2; Grosheny et al., 2006; Jarvis et al., 2011). Site selection was based on stratigraphic features with respect to each site, but also based on the synchronicity of the  $\text{Os}_i$  profiles. This study employed a new high-precision MC-TIMS method (Lehn et al., 2013) to measure  $\delta^{44}\text{Ca}$  values in the Portland #1 core, Pont d'Issole and YG section. We also analysed a subset of samples from the Eastbourne section previously analysed by Blättler et al. (2011).

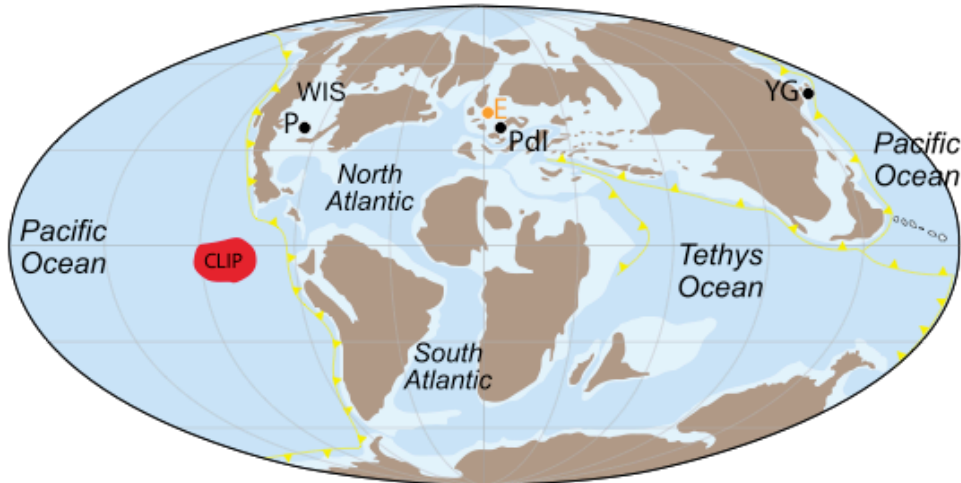


**Figure 4.1 Palaeogeographic map of the late Cretaceous.** Three study sections are representative of global palaeo-basins. P - Portland #1 Core, Colorado, USA (Western Interior Seaway); Pdl - Pont d'Issole, SE France (Western Tethys); YG - Yezo Group, Japan (Pacific Ocean). E - Eastbourne, UK (North Atlantic; samples from Blättler et al., 2011); CLIP is the location of the Caribbean Large Igneous Province.

*1.1. Previous marine  $\delta^{44}\text{Ca}$  isotope OAE 2 study*

A previous study used a MC-ICP-MS method to measure  $\delta^{44/42}\text{Ca}$  values in two OAE 2 sections: Eastbourne, UK and South Ferriby, UK (Blättler et al., 2011), are reported as  $\delta^{44/42}\text{Ca} = [({}^{44}\text{Ca}/{}^{42}\text{Ca})_{\text{sample}}/({}^{44}\text{Ca}/{}^{42}\text{Ca})_{\text{std}} - 1] * 1000$ . The sections are dominated by chalk-limestone lithologies; Eastbourne is an expanded and complete sequence through the CTBI, whereas South Ferriby has a significant undetermined stratigraphic gap that eliminates the onset and much of the initial OAE 2 interval (Blättler et al., 2011).

Blättler et al. (2011) used a simple seawater mixing model to illustrate and interpret the  $\delta^{44/42}\text{Ca}$  data. However, it is important to note the large uncertainty ( $\pm 0.07\text{‰}$ ) on the measurements from Eastbourne and that the data varies on the same order as external reproducibility, which makes the trend and excursion subtle. It is difficult to draw firm conclusions from the South Ferriby dataset because the stratigraphic gap obscures the interval of interest, and the trends in the Eastbourne dataset are extremely subtle. Nevertheless, the authors infer the data to record a negative excursion (Eastbourne  $\sim 0.04 \pm 0.07\text{‰}$ , South Ferriby  $\sim 0.14 \pm 0.06\text{‰}$ ) at the onset of OAE 2 (Fig. 4.5A), which they attribute to enhanced chemical weathering and delivery of terrestrial Ca to the oceans. The hypothesis is inconsistent with the interpretation of other isotopes at the correlative interval of the onset of OAE 2; e.g., unradiogenic Nd and Os, which suggests that the seawater was dominated by mantle-like Nd and Os derived from the Caribbean LIP (Turgeon and Creaser, 2008; Martin et al., 2012; Du Vivier et al., 2014; Chapter 2, 3, this thesis). Blättler et al. (2011) eliminate volcanism as a factor controlling the Ca isotope evolution of seawater because model evidence reveals that unreasonably large volcanic input fluxes are required to significantly shift marine  $\delta^{44}\text{Ca}$  values. However, there are additional

factors that influence the marine Ca isotope cycle, including residence time, isotopic ratios of input fluxes, the initial Ca isotope ratio of seawater, the calcium carbonate fractionation factor, and abundance of Ca in seawater, which are discussed here (section 5) and need to be understood further before interpretation of the apparently complex marine  $\delta^{44}\text{Ca}$  isotope system can be made.

## **2. Location and Geological background**

The following provides detail on litho-, bio- and chemostratigraphy for the 4 sections analysed in this study (Fig. 4.2).

### *2.1. Portland #1 Core, Colorado, USA*

The USGS Portland #1 core was taken from ~40 km west of the Global Stratotype Section and Point (GSSP) for the Cenomanian-Turonian boundary, near Pueblo, CO (32°22.6`N, 105°01.3`W; Dean and Arthur, 1998; Meyers et al., 2001; Fig. 4.1), which can be correlated, bed for bed, to the GSSP section (Hattin, 1971; Elder et al., 1994). The Portland core contains the Cenomanian-Turonian Boundary Interval (CTBI) within a 17.7 m-thick section of the Bridge Creek Limestone (~12 m) and Hartland Shale (~12.6 m) Members of the Greenhorn Formation (Cobban and Scott, 1972). Both units include organic-rich calcareous and rhythmically interbedded shale and fossiliferous biomicritic limestone couplets (Fig. 4.2). In addition the stratigraphy is characterised by four regionally correlative bentonite units of 1 to 20 cm. Recent sanidine  $^{40}\text{Ar}/^{39}\text{Ar}$  and zircon  $^{206}\text{Pb}/^{238}\text{U}$  geochronology integrated with Bayesian astrochronology constrains the CTB at  $93.90 \pm 0.15$  Ma (Meyers et al., 2012a) and is used to correlate sections worldwide (e.g. Yezo Group, Japan; Du Vivier et al., 2014; Chapter 2, 3, this thesis).

The CTBI contains a variety of foraminifera species useful for biostratigraphy, e.g., *Rotalipora cushmani*, *Whiteinella archaeocretacea* and *Helvetoglobotruncana helvetica* (Fig. 4.2; Eicher and Worstell, 1970; Kennedy et al., 2000, 2005; Keller and Pardo, 2004; Keller et al., 2004; Cobban et al., 2006). The FO (first occurrence) of the ammonite *Watinoceras devonense* (Kennedy et al., 2000) is indicative to the basal Turonian recorded at the base of bed 86 of the Bridge Creek Limestone (Fig. 4.2; Meyers et al., 2001; bed numbers are based on Cobban and Scott, 1972). A number of taxa have intercontinental distributions; however, their transcontinental synchronicity is limited.

The onset of OAE 2 is identified by an abrupt positive  $\delta^{13}\text{C}_{\text{org}}$  shift of 2-3‰ (VPDB), 4.3 m below the CT boundary (Fig. 4.3; Sageman et al., 2006). The end of OAE 2 is expressed by a gradual change in  $\delta^{13}\text{C}_{\text{org}}$  back to  $\sim -27\text{‰}$  (Sageman et al., 2006). In addition, the onset of OAE 2 coincides with the abrupt change in  $\text{Os}_i$  from  $\sim 0.75$  to  $\sim 0.20$  (Du Vivier et al., 2014; Chapter 2, this thesis). The abundance of  $\text{CaCO}_3$  is  $\sim 20\text{-}60$  wt.% throughout the sequence; however before and after the OAE 2 interval there are horizons with  $>70$  wt.%  $\text{CaCO}_3$  (Sageman et al., 2006).

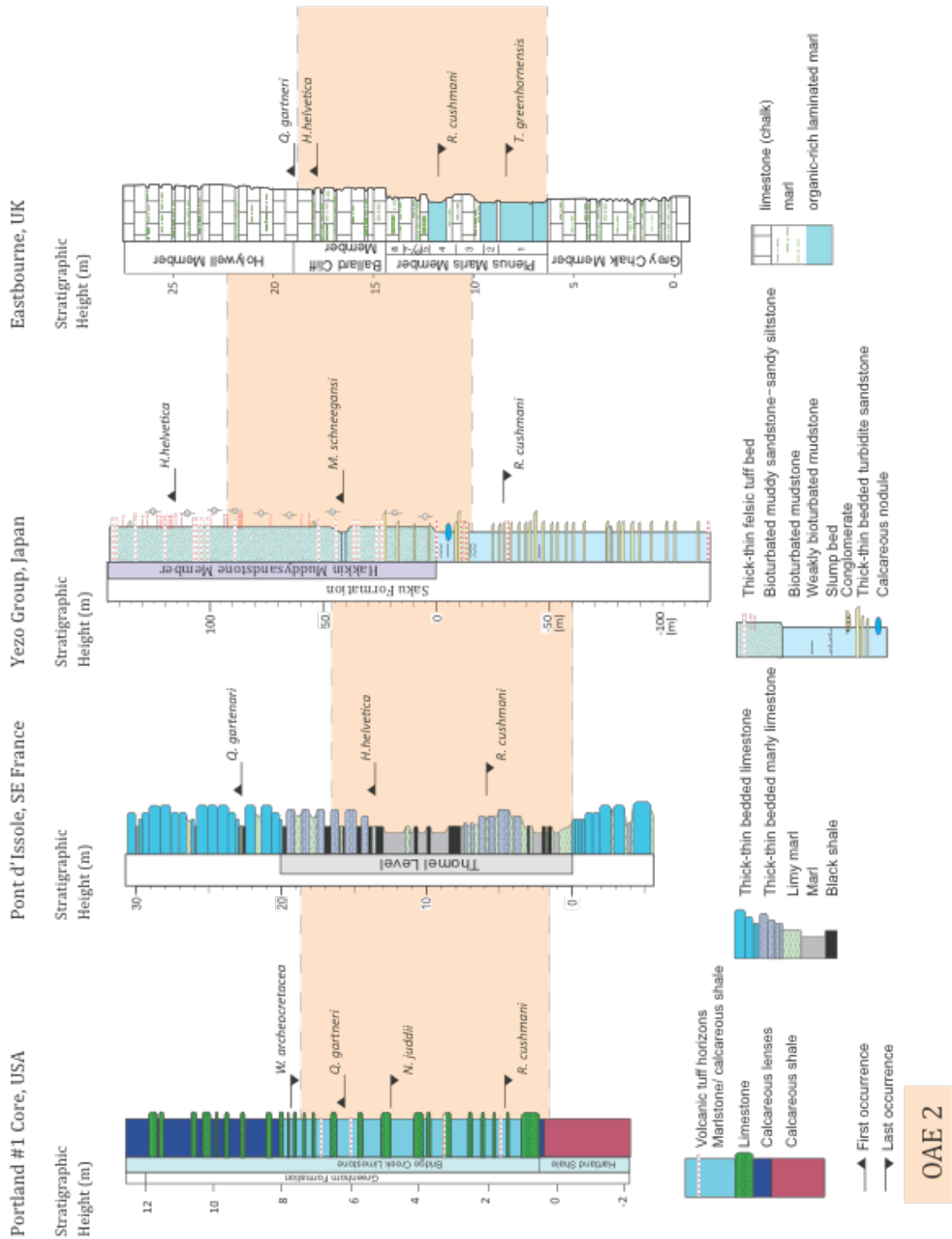


**Figure 4.2 Section stratigraphy.** Representative stratigraphy for each section: Portland #1 Core, Colorado, USA (modified from Sageman et al., 2006); Pont d'Issole, SE France (modified from Jarvis et al., 2011); Yezo Group, Japan (modified from Takashima et al., 2011); Eastbourne, UK (modified from Blättler et al., 2011). The first and last occurrences of correlative and well-known biozones are marked. The stratigraphic thickness of the OAE 2 interval is shaded in yellow across each section.

## 2.2. Pont d'Issole, SE France

The Vocontian Basin was part of the NW Tethys Ocean  $\sim 30^\circ\text{N}$  in the European Alpine region (Jarvis et al., 2011; Fig. 4.1). The 24 m Pont d'Issole section is complete through the CTBI and a  $\sim 20$  m thick package of black organic-rich calcareous shales, termed the "Niveau Thomel" (Takashima et al., 2009; Jarvis et al., 2011), characterise the interval (Fig. 4.2). The rest of the section includes thick rhythmically bedded bioturbated limestone-marl successions (Fig. 4.2), where the variable facies are indicative of a fluctuating hemipelagic depositional environment of moderate depth. Detailed biostratigraphy permits bed-scale correlation with the GSSP near Pueblo (Grosheny et al., 2006; Jarvis et al., 2011); where the distribution of foraminifera index taxa *R. cushmani* and *H. helvetica*, is coupled with complete  $\delta^{13}\text{C}_{\text{org}}$  and  $\delta^{13}\text{C}_{\text{carb}}$  records (Jarvis et al., 2011).

In the Pont d'Issole section a distinct facies change to finely laminated black shales of the Niveau Thomel (total organic carbon, TOC 0.3 – 3.5 wt.%) is indicative to the onset of OAE 2 that occurs about 1 metre below the distinctive positive  $\delta^{13}\text{C}_{\text{org}}$  excursion (3‰; Fig. 4.3; Jarvis et al., 2011). The facies change coincides with the abrupt radiogenic to unradiogenic trend in  $\text{Os}_i$  ( $\sim 0.80$  to  $\sim 0.20$ ), which is indicative to the onset of OAE 2 (Du Vivier et al., 2014; Chapter 2, this thesis). High-frequency fluctuations in the  $\delta^{13}\text{C}_{\text{org}}$ , up to 1‰ in magnitude, occur throughout the OAE 2 interval, which is also associated with the alternation of lithologic units. The  $\delta^{13}\text{C}_{\text{org}}$  record gradually returns to  $\sim -26$ ‰ at the end of OAE 2 (Fig. 4.3). The  $\text{CaCO}_3$  content of the sequence is comparable to Portland,  $\sim 20$ -60 wt.%, with higher values of  $>70$  wt.% before and after the OAE 2 interval (Jarvis et al., 2011).

### 2.3. Yezo Group section, Hokkaido, Japan

The Yezo Group (YG) accumulated at shallow marine-bathyal depths in a continental slope environment (Kaiho et al., 1993; Takashima et al., 2004; Tamaki and Itoh, 2008; Fig. 4.1). The OAE 2 section of the YG is recorded by the Saku Formation and outcrops on the Hakkin River, at Oyubari, on Hokkaido at  $\sim 142^{\circ}135'$  E,  $43^{\circ}054'$  N (Fig. 4.1). The Saku Formation is a 300 m exposed section, which contains the Hakkin muddy-sandstone member. The unit comprises dark-grey terrigenous sandy siltstone and finely laminated pyrite-rich green-grey mudstone, and multiple thick and thin-bedded conglomeritic turbidites that are interbedded with volcanic felsic tuffs (Fig. 4.2; Takashima et al., 2004; Takashima et al., 2011).

The YG section is a key regional reference section for the NW Pacific and contains sufficient biostratigraphic (Hasegawa, 1995) and radio-isotopic (Chapter 3, this thesis) indicators for high precision global correlation of OAE 2. International correlations with Portland, SW England and Poland (Hasegawa, 1995) from planktonic foraminifera illustrate a moderately diversified assemblage (Hasegawa, 1999): LO (last occurrence) of *R. greenhornensis* and *R. cushmani*, and the FO *H. helvetica* and *M. schneegansi* near to the C-T boundary. The basal Turonian was previously identified by the FO of *M. schneegansi* (at  $\sim 40$  m; Fig. 4.2), however recent U-Pb zircon geochronology of volcanic tuff horizons has modified the height of the CTB to  $\sim 25$  m (Fig. 4.3; Chapter 3, this thesis).

The onset of OAE 2, datum level 'A', is identified by a  $\sim 6\%$  positive excursion in the  $\delta^{13}\text{C}_{\text{wood}}$  record,  $-16.15$  m below the facies change to the Hakkin muddy-sandstone member (Fig. 4.3; Du Vivier et al., 2014; Chapter 2, 3, this thesis). In addition, evidence from the YG  $\text{Os}_i$  record illustrates the abrupt trend from  $\sim 0.75$  -  $\sim 0.20$ , characteristic of the OAE 2 (Du Vivier et al., 2014; Chapter 2, 3, this thesis).

The OAE 2 spans ~68 m of stratigraphy and has a maximum enrichment of -19.3‰ (Takashima et al., 2011). From datum level ‘C’ the return to pre-OAE 2  $\delta^{13}\text{C}_{\text{wood}}$  values is gradual (Fig. 4.3), which is a reflection of the homogeneous nature of the deposits throughout the duration of OAE 2. The organic-rich sediments contain a high voluminous influx of terrigenous detritus and have a higher TOC content than some European Pelagic Shelf and Atlantic sections, ~0.5 – 1.2 wt.% (Takashima et al., 2004). The section yields a low  $\text{CaCO}_3$  abundance, <1 wt.%.

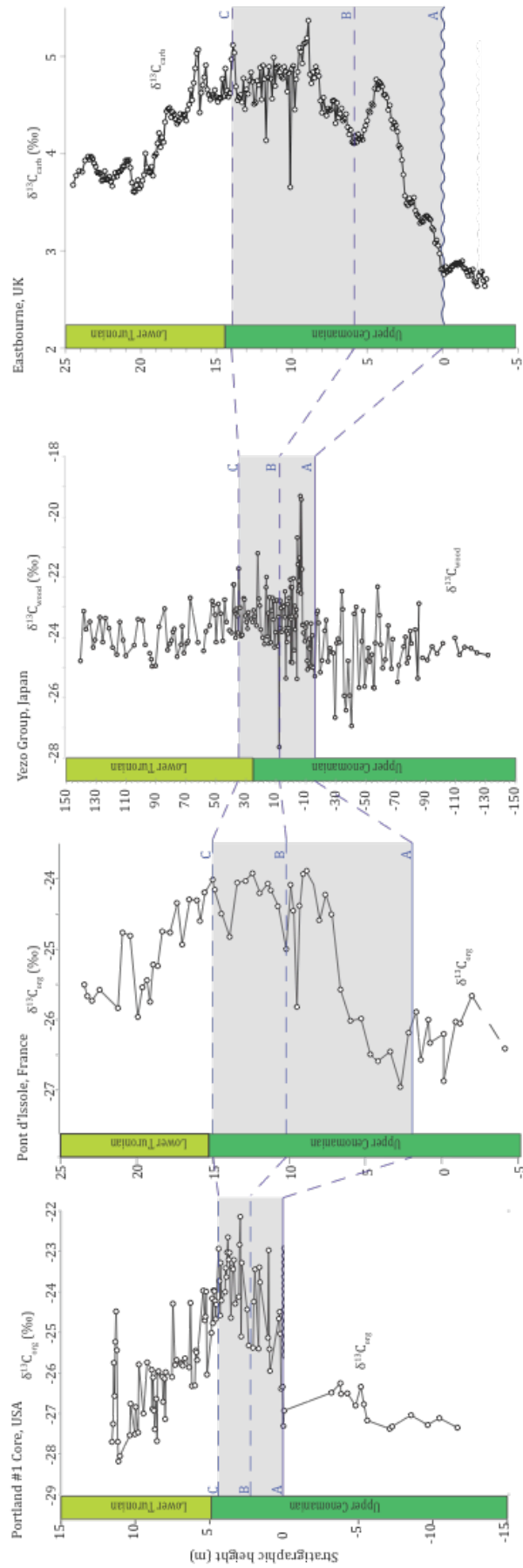
#### *2.4. Eastbourne, UK*

We measure  $\delta^{44/40}\text{Ca}$  values for 11 samples previously analysed by Blättler et al. (2011; by Nu Instruments MC-ICP-MS). The geology of the Eastbourne section is fully described by Gale et al. (2005). In brief, the Eastbourne section is a carbonate-rich sequence dominated by chalk comprising marly (10-20% clay) carbonates of the Plenus Marls, which are overlain by nodular limestones of the White Chalk that contain an abundance of coccoliths and calcispheres (Fig. 4.2; Paul et al., 1999; Gale et al., 2005). The section was deposited in the shallow epicontinental sea that submerged NW Europe, a pelagic shelf-sea environment, and is regarded as the most expanded CTBI section in the Anglo-Paris basin (Jarvis et al., 2006). The section which has exemplary bio-, litho- and chemostratigraphy is well constrained (Tsikos et al., 2004; Gale et al., 2005; Jarvis et al., 2006), inferred to be stratigraphically complete, and affected by minimal diagenesis; consequently it is proposed as a reference locality for the CTBI.

As a result of the dominant chalk lithology and consequently the high abundance of carbonate, it is challenging to obtain a high-resolution  $\delta^{13}\text{C}_{\text{org}}$  record throughout the Eastbourne section. Therefore the highest resolution curves are based

on  $\delta^{13}\text{C}_{\text{carb}}$  (Tsikos et al., 2004; Jarvis et al., 2006, 2011). Figure 4.3 correlates the high-resolution  $\delta^{13}\text{C}_{\text{carb}}$  record (Jarvis et al., 2006) through datum levels ‘A’, ‘B’ and ‘C’. The onset of OAE 2 is identified by positive shift in  $\delta^{13}\text{C}_{\text{carb}}$  that starts at ‘A’,  $\sim 2.7$  to  $\sim 4.5\%$ . ‘B’ identifies the trough in the  $\delta^{13}\text{C}_{\text{carb}}$  data after the first build-up phase and ‘C’ denotes the end of the plateau (Fig. 4.3), both characteristics of the OAE 2  $\delta^{13}\text{C}$  curves. The abundance of  $\text{CaCO}_3$  throughout the sampled section is  $>75$  wt.%.

**Figure 4.3 (next page 161) Stratigraphic correlation of  $\delta^{13}\text{C}$  vs. stratigraphic height.** The blue lines correlate stratigraphic horizons through ‘A’, ‘B’ and ‘C’ inferred from a combination of litho-, bio-, and chemostratigraphy (see text for details). Portland #1 core  $\delta^{13}\text{C}_{\text{org}}$  data from Sageman et al. (2006), Pont d’Issole  $\delta^{13}\text{C}_{\text{org}}$  data from Jarvis et al. (2011), Yezo Group  $\delta^{13}\text{C}_{\text{wood}}$  data from Takashima et al. (2011), and Eastbourne  $\delta^{13}\text{C}_{\text{carb}}$  data from Jarvis et al. (2006).



### 3. *Methods*

#### 3.1. *Sample preparation*

Aliquots of powdered samples from the Portland #1 core, Pont d'Issole and YG sections are taken from the previous Os isotope studies (Du Vivier et al., 2014; Chapter 2, 3, this thesis), conducted at Durham Geochemistry Centre (Durham University). All samples prior to crushing were collected from core or outcrop and cleaned to remove any core drill marks or weathered material. Samples were dried overnight, and  $\geq 30$  g of bulk rock was crushed and homogenised in a Zr dish (Kendall et al., 2009). Powdered aliquots of the previously analysed samples from Eastbourne were obtained from H. Jenkyns (Blättler et al., 2011).

#### 3.2. *Analytical protocol*

Calcium isotope ratios ( $^{44}\text{Ca}/^{40}\text{Ca}$ ; Table 4.1) were measured using an optimised  $^{43}\text{Ca}$ - $^{42}\text{Ca}$  double-spike MC-TIMS technique recently introduced by Lehn et al. (2013). All analyses were made in the Radiogenic Isotope Clean Laboratory at Northwestern University using a Thermo Fisher Triton MC-TIMS. Approximately 5 mg of powdered sample was loaded into acid-cleaned Teflon vials and dissolved in 10 mL 5%  $\text{HNO}_3$  overnight at room temperature. Solutions were passed through acid-cleaned 0.45  $\mu\text{m}$  polypropylene filters to remove insoluble residue. Calcium concentrations in the filtered samples were measured by ICP-OES, and aliquots containing 50  $\mu\text{g}$  of Ca were weighed into acid-cleaned Teflon vials and spiked. The vials were capped and gently heated at  $\sim 60^\circ\text{C}$  overnight to ensure complete sample-spike equilibration. The mixtures were eluted through Teflon columns packed with Bio-Rad AG MP-50 cation exchange resin to isolate Ca from matrix elements. After drying the purified fractions, two drops of 35%  $\text{H}_2\text{O}_2$  were added to oxidise organic

compounds, and two drops of concentrated 16N HNO<sub>3</sub> were added to convert Ca to nitrate form. Approximately 10 – 16 µg of Ca was loaded onto single filaments assemblies containing degassed Ta ribbon, and 0.5 µg of 10% H<sub>3</sub>PO<sub>4</sub> was added before drying at 3.5 amps. Ultrapure reagents were used for all steps and procedural blanks were negligible. Sample to blank ratios were ~500:1 or better. In the mass spectrometer, a 20V <sup>40</sup>Ca ion beam was attained after a 0.5 hr warm-up, and <sup>40</sup>Ca/<sup>42</sup>Ca, <sup>43</sup>Ca/<sup>42</sup>Ca, and <sup>43</sup>Ca/<sup>44</sup>Ca ratios were measured with a three-hop collector cup configuration for a total of 90 duty cycles requiring an additional 2.5 hr. The <sup>41</sup>K beam was monitored during the first hop to ensure that <sup>40</sup>K did not isobarically interfere with <sup>40</sup>Ca. No corrections were required. The internal precision of the measurements is ± 0.02‰ (2 SEM). At Northwestern University, OSIL Atlantic Seawater (SW) is employed as the normalizing standard for the delta equation. Long-term accuracy for the method is continuously monitored by repeated analyses of the following standards (Table 4.2), which are interspersed among samples during an analytical session: OSIL SW [ $\delta^{44}\text{Ca} = 0.000 \pm 0.003\text{‰}$  (2 SEM), n = 159], NIST SRM 915a [ $\delta^{44}\text{Ca} = -1.862 \pm 0.006\text{‰}$  (2 SEM), n = 55], and NIST SRM 915b [ $\delta^{44}\text{Ca} = -1.132 \pm 0.004\text{‰}$  (2 SEM), n = 104]. These data correspond to a global long-term, external reproducibility of ± 0.04‰ (2 SD; Lehn et al., 2013), which is the uncertainty adopted for the present study.

### 3.3. Section correlation

The correlation of the three sections analysed is based on traditionally identified trends of the  $\delta^{13}\text{C}$  isotope curves combined with the interpretation of Os<sub>i</sub> profiles (Fig. 4.3; Du Vivier et al., 2014; Chapters 2, 3, this thesis), which have improved global correlation. The 3 datum horizons are typically defined: ‘A’ the

onset of OAE 2 as construed by Pratt et al. (1985) through work at the GSSP section and facilitated by Takashima et al. (2011) and Chapter 3 (this thesis) at the Yezo Group section, ‘B’ the trough in the  $\delta^{13}\text{C}$  record following the initial positive excursion, and ‘C’ the last most enriched value in the  $\delta^{13}\text{C}$  record, the end of the ‘plateau’ as defined by Pratt et al. (1985) and refined by Tsikos et al. (2004) (see Fig. 4.3). The correlation of sections based on  $\delta^{13}\text{C}$  records coupled with Ar-Ar and U-Pb geochronology, from Portland and Japan respectively, quantitatively constrains the CTBI (Chapter 3, this thesis)

#### **4. Results**

Table 4.1 presents the  $\delta^{44}\text{Ca}$  values (a. Portland,  $n = 52$ ; b. Pont d’Issole,  $n = 13$ ; c. Yezo Group,  $n = 25$ ; d. Eastbourne,  $n = 11$ ). Overall the  $\delta^{44}\text{Ca}$  data for each site have different values and profiles, however some similarities and relationships are observed at the onset of OAE 2 (as discussed below).

##### *4.1. Portland $\delta^{44}\text{Ca}$ values*

The main feature of the  $\delta^{44}\text{Ca}$  values is the positive excursion from  $-1.58$  to  $-1.38\text{‰}$ , which is synchronous with the onset of OAE 2, datum level ‘A’ (Table 4.1a; Fig. 4.4). The excursion is brief,  $\sim 2.20$  m and between ‘A’ and ‘B’, three samples known to contain diagenetic carbonate (Kennedy et al., 2005), display higher  $\delta^{44}\text{Ca}$  values around  $-1.30\text{‰}$ . Subsequently,  $\delta^{44}\text{Ca}$  values return to relatively low  $\delta^{44}\text{Ca}$  values contemporaneous with datum level ‘B’, which are similar to or slightly lower than the pre-excursion values,  $\sim -1.60\text{‰}$ . One sample above datum level ‘C’ is also known to contain diagenetic carbonate (Kennedy et al., 2005) and displays an anomalously high  $\delta^{44}\text{Ca}$  value (Table 4.1a; Fig. 4.4).

#### 4.2. Pont d'Issole $\delta^{44}\text{Ca}$ values

Compared to the Portland core,  $\delta^{44}\text{Ca}$  values for Pont d'Issole are lower resolution. However, the data display a similar magnitude positive shift at the onset of OAE 2,  $-1.45$  to  $-1.40\text{‰}$  (Table 4.1b; Fig. 4.4). The  $\delta^{44}\text{Ca}$  values after 'A' trend to a high of  $-1.37\text{‰}$ , at which point the  $\delta^{44}\text{Ca}$  values trend to lower  $\delta^{44}\text{Ca}$  values consistent with the pattern displayed by the Portland data. The trend continues to datum level 'B', where the  $\delta^{44}\text{Ca}$  values are lower than pre-OAE 2 values  $\sim -1.50\text{‰}$  (Fig. 4.4). A single data point before datum level 'C' reverts to a higher  $\delta^{44}\text{Ca}$  value, similar to pre-OAE 2 values  $-1.45\text{‰}$  (Table 4.1b; Fig. 4.4).

#### 4.3. Yezo Group $\delta^{44}\text{Ca}$ values

The  $\delta^{44}\text{Ca}$  values for the YG are considerably more heterogeneous than Portland and Pont d'Issole (Table 4.1c). Before and after 'A', the variability in the  $\delta^{44}\text{Ca}$  data oscillates within the 2 SD uncertainty of the  $\delta^{44}\text{Ca}$  data ( $\pm 0.04\text{‰}$ ) with no appreciable trend (Table 4.1c; Fig. 4.4). Coincident with the sudden trend to unradiogenic  $\text{Os}_i$  values at the onset of OAE 2 there is nominal excursion from  $-1.26$  to  $-1.13\text{‰}$  (Fig. 4.4). After horizon 'A' the  $\delta^{44}\text{Ca}$  values remain more positive than the pre-OAE 2 values, and oscillate about a mean of  $\sim -1.15\text{‰}$ . The  $\delta^{44}\text{Ca}$  values do not trend back to lower  $\delta^{44}\text{Ca}$  values like at Portland and Pont d'Issole (Table 4.1c; Fig. 4.4).

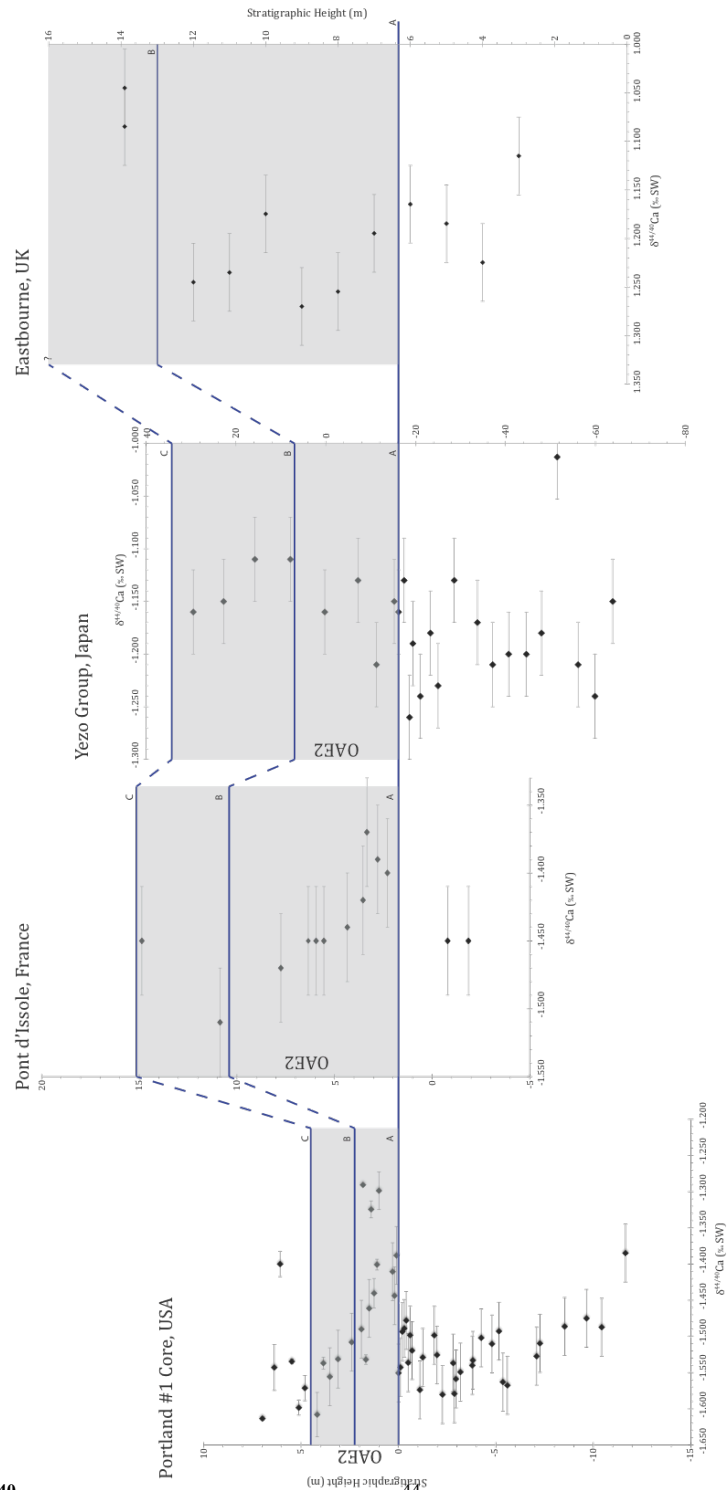


**Figure 4.4**  $\delta^{44/40}\text{Ca}$  vs. stratigraphic height.  $\delta^{44}\text{Ca}$  values from Portland #1 core, Pont d'Issole, Yezo Group and Eastbourne presented are calculated relative to OSIL SW, normalising standard utilised by the Radiogenic Isotope Clean Laboratory at Northwestern University. The error bars correspond to a global long-term, external reproducibility of  $\pm 0.04\text{‰}$  (2 SD; Lehn et al., 2013), which is the uncertainty adopted for the present study. The blue lines illustrate the correlative stratigraphic datum levels from Figure 4.3, where A denotes the onset of OAE 2.

#### 4.4. Eastbourne $\delta^{44}\text{Ca}$ values

The  $\delta^{44}\text{Ca}$  values for the Eastbourne section are relatively low resolution, 1 sample per metre, compared to the Portland and Pont d'Issole data (Table 4.1d). The  $\delta^{44}\text{Ca}$  data produce a variable record (Fig. 4.4). At the onset of OAE 2, 'A', a negative shift is identified from  $-1.16$  to  $-1.19\text{‰}$ ; the same trend described by Blättler et al. (2011). The  $\delta^{44}\text{Ca}$  ratios decrease over  $\sim 3$  m to  $-1.27\text{‰}$  and then return to  $-1.17\text{‰}$  within 1 m (Table 4.1d; Fig. 4.4). After which the  $\delta^{44}\text{Ca}$  values trend to more negative values ( $-1.24\text{‰}$ ) and return to less negative values than prior to the onset of OAE 2 ( $-1.08\text{‰}$ ). A transient negative trend is exhibited by the  $\delta^{44}\text{Ca}$  values.

## 5. Discussion

### 5.1. Analytical comparison and justification

As discussed in section 2.4 and presented in section 4.4 we re-analysed samples from Blättler et al. (2011) using a MC-TIMS method. Blättler et al. (2011) used a Nu Instruments MC-ICP-MS to measure  $\delta^{44/42}\text{Ca}$  values relative to 915a (Fig. 4.5). While it is possible to calculate  $\delta^{44/40}\text{Ca}$  values assuming all isotopic variation is mass dependent, the authors did not report results for other commonly analysed standards, such as OSIL SW and 915b, so it is not possible to account for measurement biases that naturally occur for different instruments. Thus, to compare the two datasets, we first converted our  $\delta^{44/40}\text{Ca}$  values to the 915a scale by subtracting  $-1.86\text{‰}$ , which is the value the Northwestern Laboratory obtains for 915a relative to OSIL SW. Next we multiplied these data by 0.488 to calculate  $\delta^{44/42}\text{Ca}$  values (Fig. 4.5B). This assumes that Ca isotope fractionation in nature and the mass spectrometer follows a kinetic, as opposed to equilibrium, mass

fractionation law (e.g., Holmden et al, 2012; Schiller et al., 2012). Note that converting  $\delta^{44/40}\text{Ca}$  values to  $\delta^{44/42}\text{Ca}$  reduces the uncertainty by a factor of 0.488 to 0.02‰ (2 SD). Figure 4.5 shows the results. On average, the  $\delta^{44/42}\text{Ca}$  values reported in Blättler et al. (2011) are  $\sim 0.20\%$  lower than the values we obtained for the same samples. This cannot be explained by the assumption of kinetic mass fractionation. Even if an equilibrium law is assumed, the conversion factor is only 0.476 (Young et al., 2002). While the origin of the discrepancy is unclear, several potential explanations exist. First, following established convention (Hippler et al., 2003), the Northwestern Laboratory has adopted the standard deviation (SD) of repeated standard analyses as the measure of external reproducibility, whereas Blättler et al. (2011) employed the standard error of the mean (SEM). A recent review paper (Fantle and Tipper, 2013) has argued that the latter, based on duplicate or triplicate analyses, is more appropriate because standards often have simple matrices that obviate the need for column chemistry and that the more complex matrices presented by real samples can translate into outlier measurements. We process OSIL SW (a matrix-rich standard) through column chemistry and have observed no outlier data, which shows that the column chemistry does not fractionate and appreciably affect the Ca isotope composition. The duplicate analyses reported in Table 4.2 similarly reveal no cause for concern. The SEM reveals how well a given delta value is known, but in our view, it incorrectly portrays analytical reproducibility because the magnitude decreases as the number of measurements increases. Clearly, we do not think the repeatability of our OSIL SW analyses is 0.003‰. Blättler et al. (2011) reported a 2 SEM of 0.06‰, presumably for five replicates. This translates into a 2 SD of 0.13‰, or effectively half of the observed difference between the datasets. (It is worth noting that uncertainty, whether SD or SEM, increases by a factor of 2.05

(1/0.488) when  $\delta^{44/42}\text{Ca}$  data are converted to  $\delta^{44/40}\text{Ca}$ , so the difference between directly measuring  $\delta^{44/40}\text{Ca}$  values by TIMS versus calculating them from ICP-MS measurements is rather significant). Second, there is issue of inter laboratory biases as mentioned above. A recent compilation in Holmden et al. (2012) shows that  $\delta^{44/42}\text{Ca}$  differences between seawater and 915a range up to 0.10‰, also half of the difference. Third and finally, 915a appears to be isotopically heterogeneous and may contain a mixture of Ca fractionated by kinetic and equilibrium processes (Simon and DePaolo, 2010; Schiller et al, 2012). Using 915a as the normalizing standard likely introduces discrepancies when inter-converting  $\delta^{44/40}\text{Ca}$  values measured by TIMS and  $\delta^{44/42}\text{Ca}$  values measured by ICP-MS. In general, we agree with the assertion that 915a should be abandoned in favour of 915b (Schiller et al, 2012).

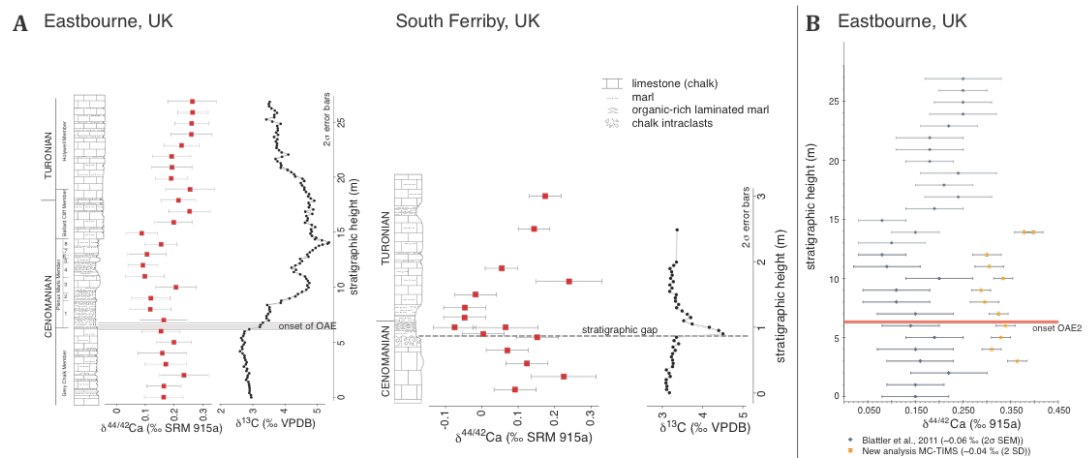


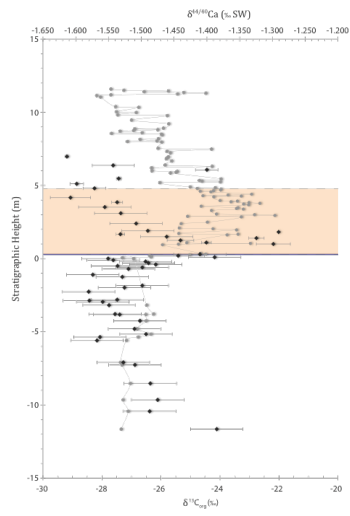
**Figure 4.5  $\delta^{44/42}\text{Ca}$  from Eastbourne and South Ferriby, UK and conversion of  $\delta^{44/40}\text{Ca}$  to  $\delta^{44/42}\text{Ca}$  (this study).** Fig. 4.5A presents the  $\delta^{44/42}\text{Ca}$  data from Blättler et al. (2011) vs.  $\delta^{13}\text{C}$  Eastbourne (Tsikos et al., 2004) and South Ferriby (Blättler et al., 2011). Fig. 4.5B presents the  $\delta^{44/42}\text{Ca}$  analysis from this study; samples across the OAE 2 onset interval were selected (obtained from H. Jenkyns) and re-analysed for  $\delta^{44/40}\text{Ca}$  using MC-TIMS. The  $\delta^{44/40}\text{Ca}$  values were converted to  $\delta^{44/42}\text{Ca}$  (yellow squares) to directly compare to  $\delta^{44/42}\text{Ca}$  (Blättler et al., 2011; blue diamonds). We convert our data relative to OSIL to the 915a scale and then multiply by 0.488 to arrive at  $\delta^{44/42}\text{Ca}$  ratios. Furthermore we improve the external reproducibility of the  $\delta^{44}\text{Ca}$  data record (by  $\sim 0.02\text{‰}$ ), as a result of the different measurement techniques. See text for discussion.

### 5.2. Relationship between marine $\delta^{44}\text{Ca}$ and other isotope proxies

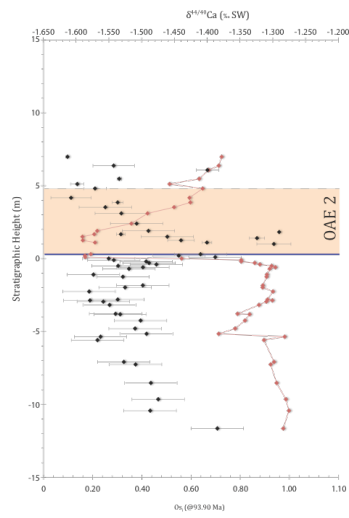
The marine  $\delta^{44}\text{Ca}$  values obtained in this study from Portland and Pont d'Issole show that at the onset of OAE 2 the positive shift is directly synchronous with the unradiogenic trend in the  $\text{Os}_i$  record, hence synchronous with the onset of OAE 2 (Fig. 4.6). The  $\delta^{44}\text{Ca}$  values obtained for the YG section show a negligible variation as a result of minimal abundance in  $\text{CaCO}_3$ , which is discussed in section 5.4.2, therefore the YG section is not discussed in this section. Qualitative observations suggest that there is a temporal agreement of Nd, Os, Pb, U,  $\delta^{13}\text{C}$  and trace metals with Ca (Snow et al., 2005; Sageman et al., 2006; MacLeod et al., 2008; Montoya-Pino et al., 2010; Kuroda et al., 2011; Martin et al., 2012; Pogge von Standmann; Zheng et al., 2013; Du Vivier et al., 2014; Chapter 2, 3, this thesis), which may infer that  $\delta^{44}\text{Ca}$  values are driven by volcanic activity associated with the Cretaceous LIPs. Here we associate volcanism with the Caribbean LIP since the temporal constraints for the High Arctic LIP are not well defined (Tegner et al., 2011) unlike the Caribbean LIP (Snow et al., 2005; Du Vivier et al., 2014; Chapter 2, 3, this thesis). Similarly marine  $^{87}\text{Sr}/^{86}\text{Sr}$  isotope ratios are sensitive to volcanism contemporaneous to OAE 2; however, they do not temporally correlate. The  $^{87}\text{Sr}/^{86}\text{Sr}$  values do become non-radiogenic but the trend to least non-radiogenic values ( $\sim 0.7073$ ) is recorded  $>4\text{Myr}$  after the onset of OAE 2 as a result of the long residence time of Sr ( $\sim 2 - 4\text{Myr}$ ; Frijia and Parente, 2008; Gradstein et al., 2012).

**Figure 4.6 (next page 171)  $\delta^{44}\text{Ca}$  and  $\text{Os}_i$  vs. stratigraphic height.** 4.6A shows  $\delta^{44}\text{Ca}$  (black) and  $\delta^{13}\text{C}$  (grey) vs. stratigraphic height (m). 4.6B shows  $\delta^{44}\text{Ca}$  (black) and  $\text{Os}_i$  (red) vs. stratigraphic height (m).  $\delta^{13}\text{C}$  data is taken from Sageman et al. (2006; Portland), Jarvis et al. (2011; Pont d'Issole) and Takashima et al. (2011; Yezo Group). The  $\text{Os}_i$  data is from Chapter 2, 3 (this thesis; Du Vivier et al., 2014). The error bars on the  $\delta^{44}\text{Ca}$  values show the  $\pm 0.04\%$  2 SD external reproducibility. The uncertainty on the  $\text{Os}_i$  values is  $\leq 0.04$ . The blue line marks the onset of OAE 2. The yellow area denotes the interval of OAE 2, between datum levels 'A' - 'C'.

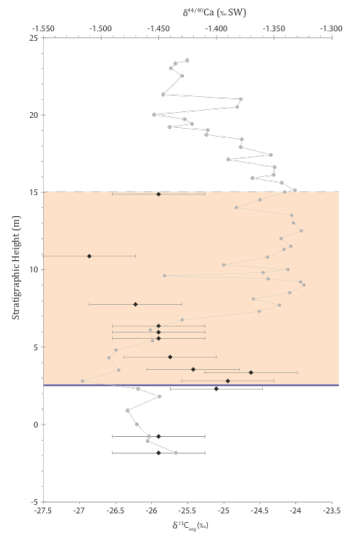
A Portland #1 Core, USA



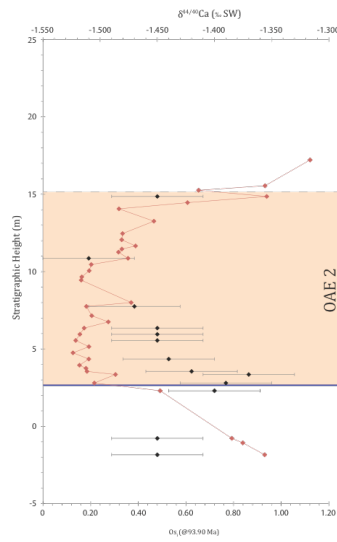
B



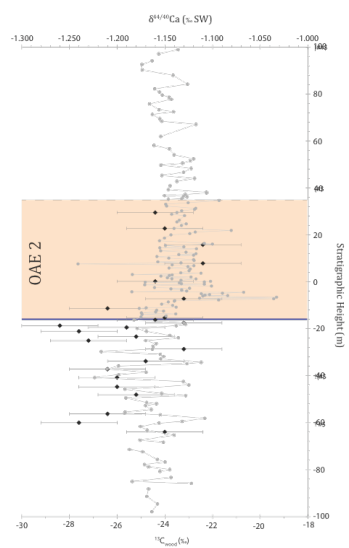
A Pont d'Issole, France



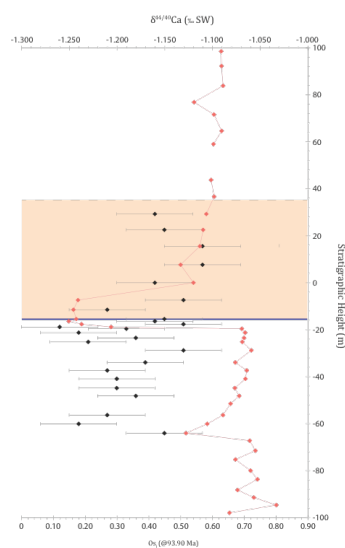
B



A Yezo Group, Japan



B



Multiple OAE 2 sections have been characterised with regard to their  $^{187}\text{Os}/^{188}\text{Os}$  isotope compositions in order to characterise and determine the driving mechanism of OAE 2 (Turgeon and Creaser, 2008; Du Vivier et al., 2014; Chapter 2, 3, this thesis). In general the development of oceanic anoxia is a function of the impact of a period of intensive weathering and submarine volcanism, which are responsible for the input of nutrients to the global ocean basins. In all cases worldwide the initial  $^{187}\text{Os}/^{188}\text{Os}$  ( $\text{Os}_i$ ) profiles from the onset to the end of OAE 2 are broadly homogeneous and show a dramatic trend from radiogenic  $\text{Os}_i$  values ( $>0.7$ ) to unradiogenic  $\text{Os}_i$  values ( $<0.3$ ) within 50 kyr, and after  $\sim 180$ -200 kyr the  $\text{Os}_i$  values gradually return to pre-OAE 2 radiogenic values (as in Fig. 4.6). The perturbation to the  $\text{Os}_i$  isotope profiles indicate that the dominant source of hydrogenous Os was from the continents and the sudden transition to unradiogenic  $\text{Os}_i$  values are indicative of volcanic activity at the Caribbean LIP contemporaneous with OAE 2 (Du Vivier et al., 2014; Chapter 2, 3, this thesis). In addition two sections, Portland #1 core and ODP Site 1260, show distinct  $\text{Os}_i$  profiles prior to the onset of OAE 2, which are indicative of basin restriction and regional variations in seawater chemistry (Du Vivier et al., 2014; Chapter 2, 3, this thesis).

Isotope proxies, namely Nd, Os, Pb, trace metals and even Sr suggest that hydrothermal inputs were influencing seawater chemistry at or just prior to the onset of OAE 2. However, the assessment of marine calcium systematics is relatively limited and recent work presents  $\delta^{44/42}\text{Ca}$  across the OAE 2 that suggest inputs to seawater derived from volcanic activity were not observed in the calcium isotope record (Blättler et al., 2011). From the transient negative trend in the  $\delta^{44/42}\text{Ca}$  profile (Fig. 4.5) and quantitatively from seawater modelling, the study infers that volcanic activity would need to increase by an unrealistic  $\sim 500\%$  to cause a perturbation in

the marine Ca system (Blättler et al., 2011). Conversely in this study the  $\delta^{44/40}\text{Ca}$  values across the CTBI are more negative and trend towards less negative values (e.g., 0.02‰ shift) at the onset of OAE 2 and the positive trend may be the result of either hydrothermal inputs or riverine inputs,  $-0.95\text{‰}$  and  $-1.03\text{‰}$  respectively, to the ocean (Amini et al., 2008; Holmden et al., 2012).

In order to quantitatively constrain the predominant controls on the isotopic evolution of the marine  $\delta^{44}\text{Ca}$  record we derive a seawater model equation to produce a mixing model to illustrate how the isotope composition of seawater evolves as a function of variable inputs and outputs. We can therefore model Ca against realistic variations in the Sr system, given the comparable geochemical systematics of Sr and Ca. The model parameters and discussion are detailed in the following section 5.3.

### 5.3. Evolution of $\delta^{44}\text{Ca}$ isotope composition, seawater mixing model

#### 5.3.1. Model parameters and steady-state simulation

Here, we use a simple box model of the marine Ca isotope cycle to identify mechanisms that caused the temporal variations preserved in the Portland and Pont d'Issole records. The change in the number of moles of calcium in the ocean ( $N_{\text{Ca}}$ ) over time ( $t$ ) is given by the equation:

$$\frac{dN_{\text{Ca}}}{dt} = F_R + F_G + F_H - \frac{N_{\text{Ca}}}{\tau_{\text{Ca}}} \quad (1)$$

where  $F_R$ ,  $F_G$ , and  $F_H$  are input fluxes (moles/yr) from riverine, groundwater, and hydrothermal sources, and  $\tau_{\text{Ca}}$  is the residence time of Ca in seawater (Myr). Collectively, the term  $N_{\text{Ca}}/\tau_{\text{Ca}}$  represents the marine carbonate output flux (moles/yr). The corresponding mass-balance for the isotope composition of Ca in seawater ( $\delta_{\text{SW}}$ ) is given by the equation:

$$\frac{d(N_{Ca}\delta_{SW})}{dt} = F_R\delta_R + F_G\delta_G + F_H\delta_H - \frac{N_{Ca}\delta_C}{\tau_{Ca}}, \quad (2)$$

where  $\delta_R$ ,  $\delta_G$ , and  $\delta_H$  represent the isotope composition of riverine, groundwater, and hydrothermal sources, and  $\delta_C$  is the isotope composition of marine carbonate, which is calculated with the equation:

$$\delta_C = \delta_{SW} + \Delta_C, \quad (3)$$

where  $\Delta_C$  is the carbonate fractionation factor.

At steady-state ( $dN_{Ca}/dt = 0$ ), equation (2) can be analytically solved to yield:

$$\delta_{SW} = (\delta_{in} - \Delta_C) + (\delta_0 - \delta_{in} + \Delta_C) \cdot e^{t/\tau}, \quad (4)$$

where  $\delta_0$  is the initial isotope composition of seawater, and  $\delta_{in}$  is the weighted average of the input fluxes:

$$\delta_{in} = \frac{\sum_i (F_i \delta_i)}{\sum_i (F_i)}. \quad (5)$$

The steady-state assumption implies that  $\tau_{Ca}$  must change to accommodate changes to the input fluxes. Because  $N_{Ca}$  and  $\tau_{Ca}$  have an inverse relationship in equation (1), equivalent results can be obtained by fixing  $\tau_{Ca}$  and allowing  $N_{Ca}$  to vary. The steady-state assumption has no implications for our interpretations. As shown below, numerically solving equations (1) and (2) when  $dN_{Ca}/dt \neq 0$  yields the same results as equation (4), provided  $\tau_{Ca}$  is allowed to vary as  $N_{Ca}$  varies.

Nearly all box models of seawater isotope records are conducted on a relative basis. The ocean is assumed to be in isotopic steady-state prior to the onset of a temporal shift, and key parameters, usually the riverine flux, are estimated by setting all other unknowns equivalent to modern values (Hippler et al., 2003; Schmitt et al., 2003; Tipper et al., 2010; Holmden et al., 2012; Fig. 4.7A). Determining  $\delta_0$  requires

application of  $\Delta_C$ , yet  $\Delta_C$  is variable (Fantle and Tipper, 2013) and may have changed through time (Hippler et al., 2003; Fantle, 2010). Thus, for simplicity, we base our model on the modern Ca isotope cycle, with the assumption that the present provides a reasonable analogue for the past (Table 4.3; Fig. 4.7A). While this approach limits our ability to reproduce the exact delta values of our dataset, we can introduce perturbations to simulate relative variations. Table 4.3 provides the initial conditions, which were taken from Milliman (1993) and Holmden et al. (2012). For the modern  $N_{Ca}$  of  $1.44 \times 10^{19}$  moles (Fantle and Tipper, 2013), the fluxes in Table 4.3 indicate that  $\tau_{Ca}$  equals 450,000 yr. Implementing higher values for  $N_{Ca}$  and  $\tau_{Ca}$ , such as those that likely occurred during the Cretaceous (Blättler et al., 2011), would only delay the response time of the model to a given perturbation. By adopting minimum estimates for  $N_{Ca}$  and  $\tau_{Ca}$ , we maximize the model's sensitivity (Fig. 4.7A). Nonetheless, as we demonstrate below, these parameters are not particularly critical for our interpretation.

**Table 4.3** Symbols and values for parameters used in the seawater mixing model

Symbol	Description	Value	Units
$N_{Ca}$	Mass of Ca in ocean	1.44E+19	mol
$F_R$	Riverine flux	1.3E+13	mol/yr
$F_H$	Hydrothermal flux	3E+12	mol/yr
$F_G$	Groundwater flux	1.6E+13	mol/yr
$\delta_R$	Riverine isotope ratio	-1.03	‰
$\delta_H$	Hydrothermal isotope ratio	-0.95	‰
$\delta_G$	Groundwater isotope ratio	-1.23	‰
$\tau_{Ca}$	Residence time	0.45	Myr
$\delta_{in,o}$	Combined input isotope ratio, weighted by flux	-1.12	‰
$\Delta_C$	Fractionation factor	-1.12	-
$\delta_{sw,o}$	Initial isotope ratio of seawater	0.00	‰

Initial parameter values are from Milliman, 1993, Holmden et al., 2012, Fantle and Tipper, 2013

The timescale applied to the mixing model is based on the integrated timescale for the Portland #1 core (Meyers et al., 2012a; Du Vivier et al., 2014; Chapter 2, this thesis). For the model, 0 kyr equals the onset of OAE 2 (i.e. the onset of the carbon isotope excursion) and runs for the duration of the OAE 2 ~600 kyr (according to Sageman et al., 2006; Meyers et al., 2012b). The time steps increment by 100 kyr for 1 Myr.

### 5.3.2. *Hydrothermal influx model simulation*

To quantitatively simulate the effect of a hydrothermal flux, which is influencing seawater chemistry based on evidence from a number of other isotope proxies (as discussed in section 5.2), the  $F_H$  parameter is adjusted whilst all other parameters remain at steady-state (Fig. 4.7B). The  $F_H$  is based on evidence from the Os progressive seawater mixing model (Du Vivier et al., 2014; Chapter 2, this thesis), which infers a 75% increase at the onset of OAE 2 for 200 kyr, after which the influx decreases to 25% up to 300 kyr, subsequently the influx ceases as activity at the Caribbean LIP terminates. Therefore we apply a  $F_H$  factor of 1.75 from the onset of OAE 2 up to 200 kyr, 1.25 up to 300 kyr and then back to 1 for the remaining 700 kyr. The model shows no appreciable shift to more positive  $\delta^{44}\text{Ca}$  values (0.004‰, Fig. 4.7B). The effect on the Sr values is also negligible (a slight shift to non-radiogenic values of ~0.001). But the shift in Sr occurs ~200 kyr yrs after the OAE 2 onset, which is not recorded in nature. Evidence from the revised short-term Sr isotope curve from the Apennines across the CTB shows that the negative excursion follows a positive shift just after the onset, after which the values start to decrease >400 kyr after the onset of OAE 2 (Frijia and Parente, 2008), which is not supported by other isotope proxies (see section 5.3.3).

Although the model suggests no appreciable shift in the  $\delta^{44}\text{Ca}$  values, submarine hydrothermal activity is recognised as a source for the marine Ca budget (Amini et al., 2008), e.g., the Logatchev Hydrothermal Field suggests that a volcanic flux affects the isotope composition of  $\delta^{44}\text{Ca}$  seawater as Ca is released from the oceanic crust during water-rock interactions (Amini et al., 2008) and possibly from direct volcanic gas injections, as proposed for Os (Du Vivier et al., 2014; Chapter 2, this thesis). Hydrothermal inputs transform seawater to a hydrothermal solution and the Ca concentration increases from 10 mM to 32 mM, as such the seawater adopts a  $\delta^{44/40}\text{Ca}_{\text{HydEnd}}$  of  $-0.95 \pm 0.07\text{‰}$  relative to the  $\delta^{44}\text{Ca}$  initial isotope ratio of seawater  $-0.003\text{‰}$  (Amini et al., 2008). In addition, evidence from hydrothermal vent fluids in both the Mid-Atlantic and the East Pacific Rise result in an average  $\delta^{44/40}\text{Ca}_{\text{HydEnd}}$  of  $-0.96 \pm 0.19\text{‰}$  (Schmitt et al., 2003). Therefore it is inferred that water-rock interactions in hydrothermal systems impact the mass balance of the ocean due to the addition or removal of chemical elements over time (Bernier and Bernier, 1996). Consequently increasing the  $F_H$  by a factor of 3.2 produces a measurable change in the  $\delta^{44}\text{Ca}$  values,  $\sim 0.01\text{‰}$ , but not the change recorded in the sections studied here. However, the analysed sections are not adjacent to submarine activity and as such the influence of volcanism may be diluted in peripheral basins.

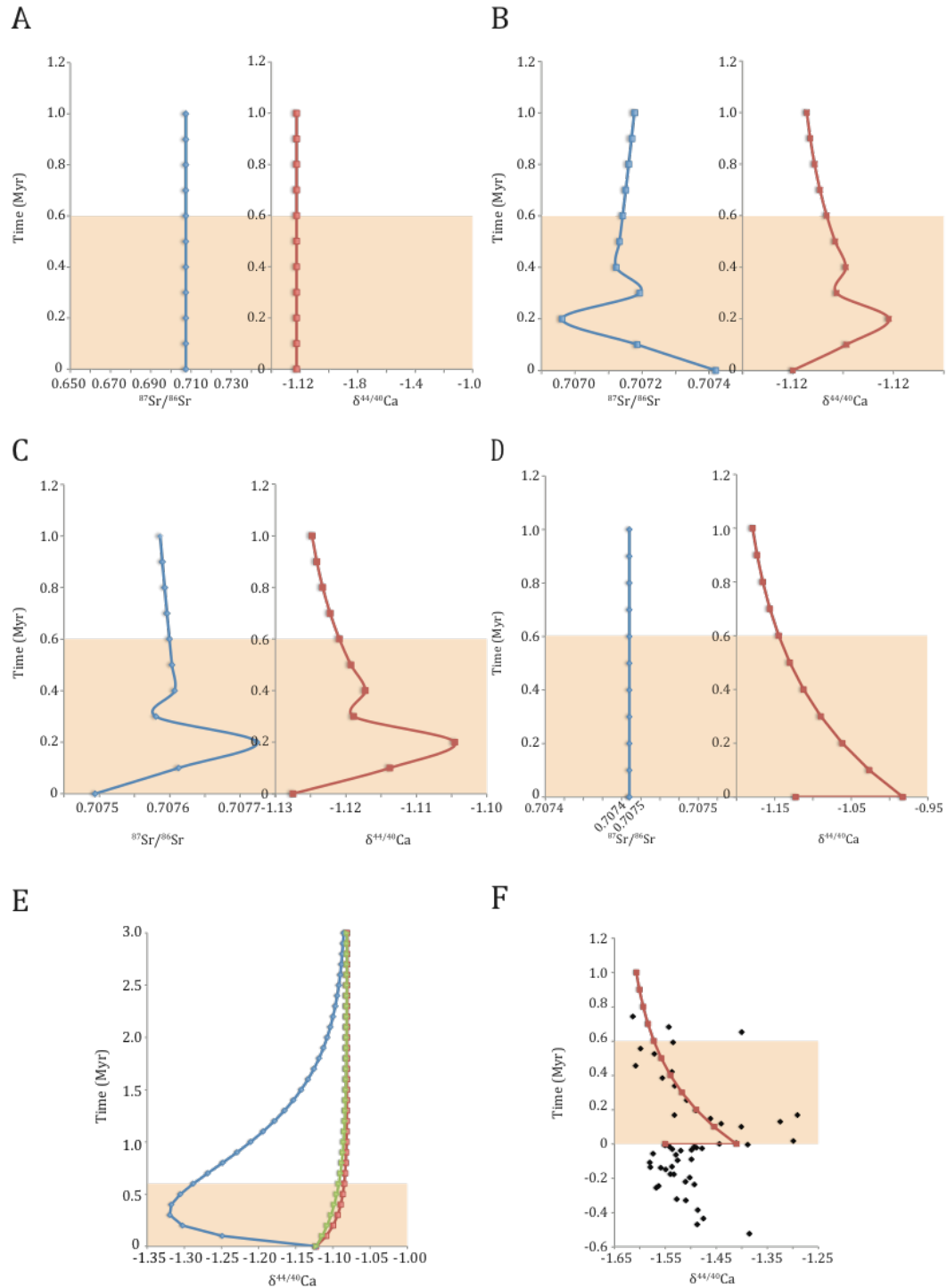


**Figure 4.7 Seawater mixing models.** Simulated  $\delta^{44}\text{Ca}$  (red) and Sr (blue) values vs. Time (Myr). A shows steady-state (section 5.3.1). B shows the effect of increased hydrothermal flux (section 5.3.2). C shows the effect of increased weathering flux (section 5.3.3); D shows the effect of fractionation factor (section 5.3.4). E demonstrates numerically modelled values: red and green curves illustrate how allowing  $\tau_{\text{Ca}}$  to vary as  $N_{\text{Ca}}$  varies produces the discrepancy with the numerical blue curve similar to Blättler et al.'s (2011) model (see section 5.3.3). F illustrates the model data scaled to the Portland data to demonstrate the analogous trend, which implicates fractionation as the driving factor for variable marine  $\delta^{44}\text{Ca}$  isotope composition (section 5.3.4). Orange area denotes the duration of OAE 2.

The Portland and Pont d'Issole records suggest that  $\delta_{SW}$  increased by  $\sim 0.15 - 0.20\%$ . While the direction of change appears consistent with an elevated input of hydrothermal Ca with  $\delta_H = -0.95\%$ , an unreasonably large value for  $F_H$  is required to achieve the observed magnitude. In order to record an equivocal shift, the  $F_H$  flux would need to increase by a factor of 50,  $N_{Ca} = 1.50 \times 10^{14}$  moles in the ocean. As a result, the response in the  $^{87}\text{Sr}/^{86}\text{Sr}$  record is unfeasible as unrealistic unradiogenic values (0.7043) are calculated, as noted by Blättler et al. (2011). Thus the model implies that the scale of input required to impact the  $\delta^{44}\text{Ca}$  record and replicate the Sr record is not achieved from the Caribbean LIP during OAE 2 based on a quantitative seawater mixing model (Fig 4.7B). Conversely, evidence from high-temperature fumarolic condensates suggest that the enrichment of Ca is  $>200$  times that of Sr (Taran et al., 1995). Therefore, it may be possible that Ca and Sr are decoupled as a result of sublimation and so the influence on seawater chemistry may not be ubiquitous under high hydrothermal influx conditions, as inferred by the model (Fig. 4.7B). The quantitative extent of submarine activity at LIPs contemporaneous with the OAE 2 is unverified, but the influence on seawater chemistry is supported by multiple isotopic proxies and trace metals (Kerr, 1998; Snow et al., 2005; Turgeon and Creaser, 2008; MacLeod et al., 2008; Montoya-Pino et al., 2010; Kuroda et al., 2011; Pogge von Strandmann et al., 2013; Zheng et al., 2013; Du Vivier et al., 2014; Chapter 2, 3, this thesis). However, simple end-member mixing cannot detect the change due to lack of isotopic leverage (Holmden et al., 2012). Alternatively, other factors are driving the variability of  $\delta^{44}\text{Ca}$  values in seawater, which we discuss below.

### 5.3.3. Riverine influx model simulation

We agree that enhanced hydrothermal activity cannot fully explain the evolution of seawater  $\delta^{44}\text{Ca}$  record values across OAE 2, but we reach a different conclusion with respect to the riverine flux. To explain the Eastbourne and South Ferriby datasets, Blättler et al. (2011) concluded that the enhanced chemical weathering increased  $F_R$  by a factor of three at the onset of OAE 2. To the extent that the modern marine Ca isotope cycle represents the Cretaceous, we first note that any increase in  $F_R$  should increase, rather than decrease,  $\delta_{SW}$ . Blättler et al. (2011) also found that increasing  $F_R$  by a factor of three produces an initial negative isotope excursion that eventually dampens if the perturbation is maintained longer than  $\tau_{Ca}$ . Equation (4) does not predict this type of behaviour. Equation (4) shows that a sufficiently large perturbation to  $F_R$ , or for that matter,  $\Delta_C$  or any of the variables that affect  $\delta_{in}$ , should permanently shift  $\delta_{SW}$  until the perturbation is relaxed. Our model divides the terrestrial input between riverine runoff and submarine groundwater discharge, whereas Blättler et al. (2011) effectively considered these inputs as one term. To address this point, we added the values for  $F_R$  and  $F_G$  in Table 4.3 and calculated a flux-weighted  $\delta^{44}\text{Ca}$  value. The combined flux of  $2.90 \times 10^{13}$  moles/yr and  $\delta^{44}\text{Ca}$  value of  $-1.14\text{‰}$  are higher and lower, respectively, than the parameters adopted by Blättler et al. (2011;  $2.3 \times 10^{13}$  moles/yr and  $-1.06\text{‰}$ ). The discrepancy arises because Blättler et al. (2011) treated  $\tau_{Ca}$  as a fixed parameter. To illustrate this point, we increased the combined flux by a factor of three and numerically solved equations (1) and (2) while holding  $\tau_{Ca}$  constant. The output shown in Figure 4.7E (blue curve) slightly differs from the model results presented in Blättler et al. (2011) because we adopted different input parameters, but the overall pattern is identical. If we numerically solve the same equations while allowing  $\tau_{Ca}$  to

vary as  $N_{Ca}$  varies (Fig. 4.7E, green curve), then the output matches that obtained with equation (4) (Fig. 4.7E, red curves). Our analytical models show that in a non-steady-state model, instantaneously increasing an input flux must decrease residence time for a given initial reservoir size in order to maintain mass balance. The only real difference between steady-state and non-steady-state approaches to modelling the Ca isotope evolution of seawater is that the former assumes instantaneous shifts in  $\tau_{Ca}$  (or  $N_{Ca}$ ), whereas the latter allows  $\tau_{Ca}$  and  $N_{Ca}$  to change with time until steady-state occurs.

Using the above parameter of increased  $F_R$ , the Sr model (Fig. 4.7C) shows a radiogenic trend  $\sim 200$  kyr after the onset of OAE 2, which Blättler et al. (2011) utilise to support their conclusion. However, the increase in Sr values modelled in Figure 4.7C is concurrent with secular profiles from other isotope proxies (e.g., Nd, Os, Pb, U and trace metals) as discussed in section 5.2 and 5.3.2, which are clearly indicative of hydrothermal flux. Furthermore, evidence suggests that seawater chemistry is affected by enhanced weathering before the onset of OAE 2. It is therefore likely a result of the Sr residence time ( $\sim 2 - 4$  Myr) that the weathering influence is recorded in the OAE 2 interval. Nonetheless, increasing  $F_R$  by a factor of three in our model generates a minimal positive change in  $\delta^{44}\text{Ca}$  values (0.02‰; Fig. 4.7C).

#### 5.3.4. Fractionation factor model simulation

Both hydrothermal and riverine fluxes increased across the OAE 2 yet our  $\delta^{44}\text{Ca}$  data combined with the simulated models derived from the aforementioned parameters illustrate that neither increased to levels sufficient to influence the marine Ca cycle. As a result the variable marine  $\delta^{44}\text{Ca}$  ratios throughout multiple palaeo-

basins across an isochronous event are more tenably explained by other factors (Fantle and Tipper, 2013).

This leaves a change in carbonate fractionation factor ( $\Delta_C$ ) as the principal explanation for the Portland and Pont d'Issole records (Fig. 4.7D, 4.7F). Calcium is extracted from seawater due to the precipitation of calcium carbonate. In short, light calcium isotopes are preferentially removed during uptake into carbonate through the active transport of Ca ions, which leaves seawater depleted and the solid carbonate phase enriched in  $^{40}\text{Ca}$  (DePaolo, 2004; Holmden et al., 2012; Nielsen et al., 2012; Fantle and Tipper, 2013). The extent of isotopic variation is a function of the intensity of inputs and outputs, depending on the source and sink (De La Rocha and DePaolo, 2000; DePaolo, 2004; Fantle, 2010). When the mass flux of inputs is ubiquitous, the variability of  $\delta^{44}\text{Ca}$  values is a function of the fractionation of precipitating carbonate (Fantle, 2010; Fantle and Tipper, 2013). Therefore the abundance of precipitating carbonate from seawater influences the  $\Delta_C$ .

As shown in Figure 4.7D, instantaneously decreasing the magnitude of  $\Delta_C$  by 0.10 – 0.15‰ (i.e., from –1.12 to –1.02 and –0.98‰; Jacobson and Holmden, 2008; Holmden et al., 2012) closely simulates the trend to less negative values observed at the onset of OAE 2. While changing  $\Delta_C$  permanently shifts  $\delta_{SW}$ , the carbonate record shows more complex behaviour (Fantle, 2010). At timescales shorter than  $\tau_{Ca}$ ,  $\delta_C$  is initially offset from seawater by an amount equivalent to  $\Delta_C$ , but at timescales longer than  $\tau_{Ca}$ , seawater adjusts to the change in  $\Delta_C$  such that  $\delta_C$  returns to its starting value (Fantle, 2010). At the onset of OAE 2, decreasing  $\Delta_C$  drives  $\delta_{SW}$  to lower values, while causing a temporary increase in  $\delta_C$ . We note that stratigraphically higher  $\delta^{44}\text{Ca}$  values in the Portland and Pont d'Issole records appear to decrease to levels below the starting values. We think this could represent return of  $\Delta_C$  to the initial value

prior to OAE 2. As shown in Figure 4.7D, instantaneously changing  $\Delta_C$  back to the original value of  $-1.12\text{‰}$  shifts  $\delta_{SW}$  to higher values while causing a temporary decrease in  $\delta_C$ . As such the model (Fig. 4.7D) best replicates the  $\delta^{44}\text{Ca}$  values recorded in this study, which is illustrated in Figure 4.7F. The modelled data scaled to the Portland record implies that the variation in  $\delta^{44}\text{Ca}$  isotope composition is a function of the  $\Delta_C$  (Fig. 4.7F).

Additionally, we observe that the nominal negative trend in the  $\delta^{44}\text{Ca}$  record at Eastbourne and South Ferriby suggests that the  $\Delta_C$  at the onset of OAE 2 is behaving differently (Fig. 4.5). However, at Eastbourne the low resolution of the  $\delta^{44}\text{Ca}$  record could potentially mask the full extent of  $\delta^{44}\text{Ca}$  variability over the onset of OAE 2 (Fig. 4.4, 4.5). In comparison, at Portland and Pont d'Issole the positive shift to less negative  $\delta^{44}\text{Ca}$  values is recorded within  $\sim 1.5$  m of the onset of OAE 2 (Fig. 4.4). After  $\sim 1.5$  m the  $\delta^{44}\text{Ca}$  values are equivalent to those recorded just before the onset of OAE 2. Hence the shift occurs over a condensed interval of stratigraphy, which might not be recorded in the Eastbourne section and the nominal negative trend is an artefact of the low-resolution data, one sample per  $\sim 1$  m. In terms of South Ferriby the undetermined duration of the stratigraphic gap indicates that the onset of OAE 2 is not recorded in this section, therefore the main event is not recorded (Fig. 4.5).

#### *5.4. Further variables of marine $\delta^{44}\text{Ca}$ composition*

The models discussed throughout section 5.3 infer that  $\Delta_C$  is the primary factor controlling the  $\delta^{44}\text{Ca}$  seawater record. However fractionation is a variable sensitive to a number of other factors, e.g., precipitation and ocean acidification

(seawater pH), diagenesis, lithology, and temperature, which may also attenuate the primary seawater signal.

#### *5.4.1. Precipitation and ocean acidification (seawater pH)*

Our analysis combined with the simulated mixing model suggests that a decrease in  $\Delta_C$  proves the best explanation for the patterns preserved in the Portland and Pont d'Issole Ca isotope records (Fig. 4.7D). We suggest that the variability of  $\delta^{44}\text{Ca}$  values across the OAE 2 is a function of ocean acidification potentially driving variation in the  $\Delta_C$ . At an atomic level, a decrease in the  $\Delta_C$  is consistent with decreasing carbonate growth rates, decreasing fluid saturation states, and higher Ca:CO<sub>3</sub> ratios in seawater, all of which drive crystal growth toward isotope equilibrium with aqueous Ca (Nielsen et al., 2012; DePaolo, 2011; Fantle and Tipper, 2013). At chemical equilibrium,  $\Delta_C$  is very close to zero (Fantle and DePaolo, 2007; Jacobson and Holmden, 2008). While the exact mechanism underlying these changes is unclear, we suggest that a decrease in  $\Delta_C$  is consistent with an elevated abundance of dissolved CO<sub>2</sub> and enhanced Ca input associated with submarine volcanism, which decreased the pH of seawater leading to ocean acidification (Payne et al., 2010). As discussed above (section 5.3.2) the injection of Ca from volcanism could have been significant, yet the system appears to be insensitive to reasonable change in volcanic Ca inputs since end-member mixing is nominally equivalent. Only modelling using a factor of >50 produces an appreciable change, without involving fractionation. However the addition of Ca may contribute to the change in  $\Delta_C$  via the Ca:CO<sub>3</sub> ratios.

Previous studies evaluate the development of ocean acidification during oceanic anoxic events and attribute the change in ocean chemistry to excessive

volcanic activity (Marriott et al., 2004; Mort et al., 2007; Robinson et al., 2009; Dias et al., 2010; Erba et al., 2010; Jenkyns, 2010; Keller et al., 2011; Kuroda et al., 2011). Prior to the onset of OAE 2 elevated levels of atmospheric CO<sub>2</sub> led to global warming, which enhanced continental weathering. Consequently the flux of continental material to the ocean increased carbonate deposition (Payne et al., 2010). At the onset of OAE 2 evidence from multiple isotope analyses; for example Li, Mo, Nd, Os, U, and many trace metal proxies, show that seawater was affected by a significant shift in ocean chemistry (Kerr, 1998; Snow et al., 2005; van Bentum et al., 2009; MacLeod et al., 2008; Jenkyns, 2010; Montoya-Pino et al., 2010; Pogge von Strandmann et al., 2013; Zheng et al., 2013; Du Vivier et al., 2014; Chapter 2, 3, this thesis) associated with contemporaneous volcanic activity derived from either the Caribbean LIP or the High Arctic LIP (Sinton and Duncan, 1997; Snow et al., 2005; Tegner et al., 2011; Zheng et al., 2013; Du Vivier et al., 2014; Chapter 2, 3, this thesis). In addition, global transgression facilitated the distribution of nutrients and hydrothermal inputs worldwide. Therefore the injection of CO<sub>2</sub> and SO<sub>2</sub> from submarine volcanism combined with enhanced palaeocirculation increased the concentration of dissolved CO<sub>2</sub> (Erba et al., 2010; Jenkyns et al., 2010), which lowers seawater pH and consumes the abundance of deposited CO<sub>3</sub> and facilitates the chemical and isotopic phenomena noted above. As a result the  $\delta^{44}\text{Ca}$  values and the  $\Delta_{\text{C}}$  decreases as precipitation of CaCO<sub>3</sub> is attenuated due to sufficient mixing of surface waters with carbonate depleted deep waters (Payne et al., 2010). Carbonate dissolution therefore acts to buffer seawater chemistry.

Subsequently, evidence from the aforementioned isotope proxies suggest that the influence from hydrothermal inputs on seawater chemistry progressively decreases as activity from the Caribbean LIP ceases after ~200 kyr (Du Vivier et al.,

2014, and references therein; Fig. 4.4, 4.6). As a result the  $\Delta_C$  returns to the original value and  $\delta^{44}\text{Ca}$  values return to pre-OAE 2 ratios (Fig. 4.4). The positive trend at the onset of OAE 2 and the subsequent transient decrease in  $\delta^{44}\text{Ca}$  isotope composition from both Portland and Pont d'Issole support the proposed hypothesis.

Previous Ca isotope studies focusing on the Permo-Triassic boundary support the relationship between ocean acidification and  $\Delta_C$ , associated with the variation in seawater  $\delta^{44}\text{Ca}$  values. The evaluation of  $\delta^{44}\text{Ca}$  values across the Permo-Triassic boundary proposed that excessive activity from the Siberian Traps acidified seawater to the extent that net carbonate dissolution occurred (Payne et al., 2010). However the impact of the Siberian Traps was much larger than Cretaceous LIPs. Given that the buffering capacity of seawater must be exhausted before the dissolution of carbonate sediment occurs, it is reasonable to expect that different ocean acidification events will manifest in the marine Ca isotope record in different ways.

Furthermore, by analogy with OAE 1a, the implications of ocean acidification may be inferred from the abrupt changes in fossil assemblages, where communities dependent on the abundance of carbonate for biomineralisation became extinct (Erba et al., 2010), coincident with high ion activity ratios in seawater (Nielsen et al., 2012). The excursions in  $\delta^{44/42}\text{Ca}$  data from two sections of OAE 1a (Site 866, Resolution Guyot, Pacific and Coppitella, Gargano, Italy; Blättler et al., 2011) are inferred to be negative, which is interpreted from a single more negative value that coincides with the onset of OAE 1a. The negative excursion could be an artefact of low resolution and lithology, which is similar to Eastbourne: dominated by limestone. Therefore the interval is susceptible to diagenesis (see discussion below, 5.4.3). We suggest that the overall trend across the syn-OAE 1a interval is

positive (see Blättler et al., 2011) and as such support the hypothesis discussed above.

#### 5.4.2. *Diagenesis and lithology*

The effect of diagenesis is not well understood. Chalk-rich stratigraphy has an abundance of pore spaces, which are susceptible to cementation and represent an open system, whereas the marl-rich beds retain the depositional structure and form a closed diagenetic system. The formation of cement modifies the palaeoceanographic isotopic signal and reflects the bulk carbonate  $\delta^{13}\text{C}$  composition, whilst the marls are unaltered (Paul et al., 1999). Evaluation of the lithology of the Eastbourne and South Ferriby sections shows that the stratigraphy is broadly homogeneous; chalk-limestone infrequently interbedded by organic-rich marls, in comparison to the more variable sequence stratigraphy in the Portland core and Pont d'Issole (Fig. 4.2, 4.4, 4.5). However, studies suggest that despite minor modification of carbon-isotope records as a result of carbonate cementation, the geochemical data for Eastbourne and South Ferriby remain undisturbed (Jenkyns et al., 1994; Paul et al., 1999). It is with this reasoning that Blättler et al. (2011) discount the influence of diagenesis.

A recent study by Ockert et al. (2013) discusses the influence of fractionation during Ca exchange on clay minerals in seawater. They find that in marine porewater environments the magnitude of marine  $\delta^{44}\text{Ca}$  fractionation between light  $\text{Ca}^{2+}$  ions preferentially adsorbed in to clay and the  $\text{Ca}^{2+}$  dissolved into seawater, has a wide range. The adsorption of  $\text{Ca}^{2+}$  in varying minerals has a variable  $\Delta_{\text{C}}$  (Ockert et al., 2013). In addition, adsorption is coupled with the velocity of diffusion, which is a function of carbonate deposition. Therefore, fractionation is mineral-specific and dependent on the rate of the depositing mineralogy (Ockert et al., 2013), which may

explain the contrasting data between the sites analysed here. Therefore, the trend recorded in the  $\delta^{44}\text{Ca}$  values of Portland and Pont d'Issole may be an artefact of site-specific fractionation of the depositing sediment as a function of the mineralogical composition; whereas at Eastbourne and South Ferriby the fractionation remains consistent and thus the variation in  $\delta^{44}\text{Ca}$  values is nominal.

The effect of varying lithology is broadly unknown. As shown  $\Delta_C$  is associated with carbonate precipitation; as such there may be potential to interpret a relationship based on isotopic trends that are coincident with the section lithology. The modelled change in  $\Delta_C$ , which produces the positive excursion in the Portland and Pont d'Issole  $\delta^{44}\text{Ca}$  profiles, is consistent with a change in lithology and the site-specific fractionation alluded to above; whereas the nominal change in the  $\delta^{44}\text{Ca}$  profiles at Eastbourne and South Ferriby suggest that the predominately chalk-rich lithology is unaffected by  $\Delta_C$ .

Figure 4.8 illustrates that relationship between the abundance of  $\text{CaCO}_3$  versus  $\delta^{44}\text{Ca}$  isotope composition of seawater. The positive excursion in the  $\delta^{44}\text{Ca}$  values, synchronous with the onset of OAE 2, concurs directly with the change in lithology and an increase in  $\text{CaCO}_3$  abundance (Fig. 4.8). However, overall the trends imply a non-correlative relationship; despite the coincident change in lithology and the positive trend in  $\delta^{44}\text{Ca}$  values, the former is not causing the latter since overall the wt.%  $\text{CaCO}_3$  data remain high, whereas the  $\delta^{44}\text{Ca}$  values show a long-term decrease after the initial positive excursion. It is worth noting that the sharp excursions to the least negative values in Portland and YG (Fig. 4.8) directly correlate with the highest  $\text{CaCO}_3$  values abundance of >70 wt.%, which are horizons known to be affected by diagenetic carbonate (Fig. 4.2, 4.8; Kennedy et al., 2005).

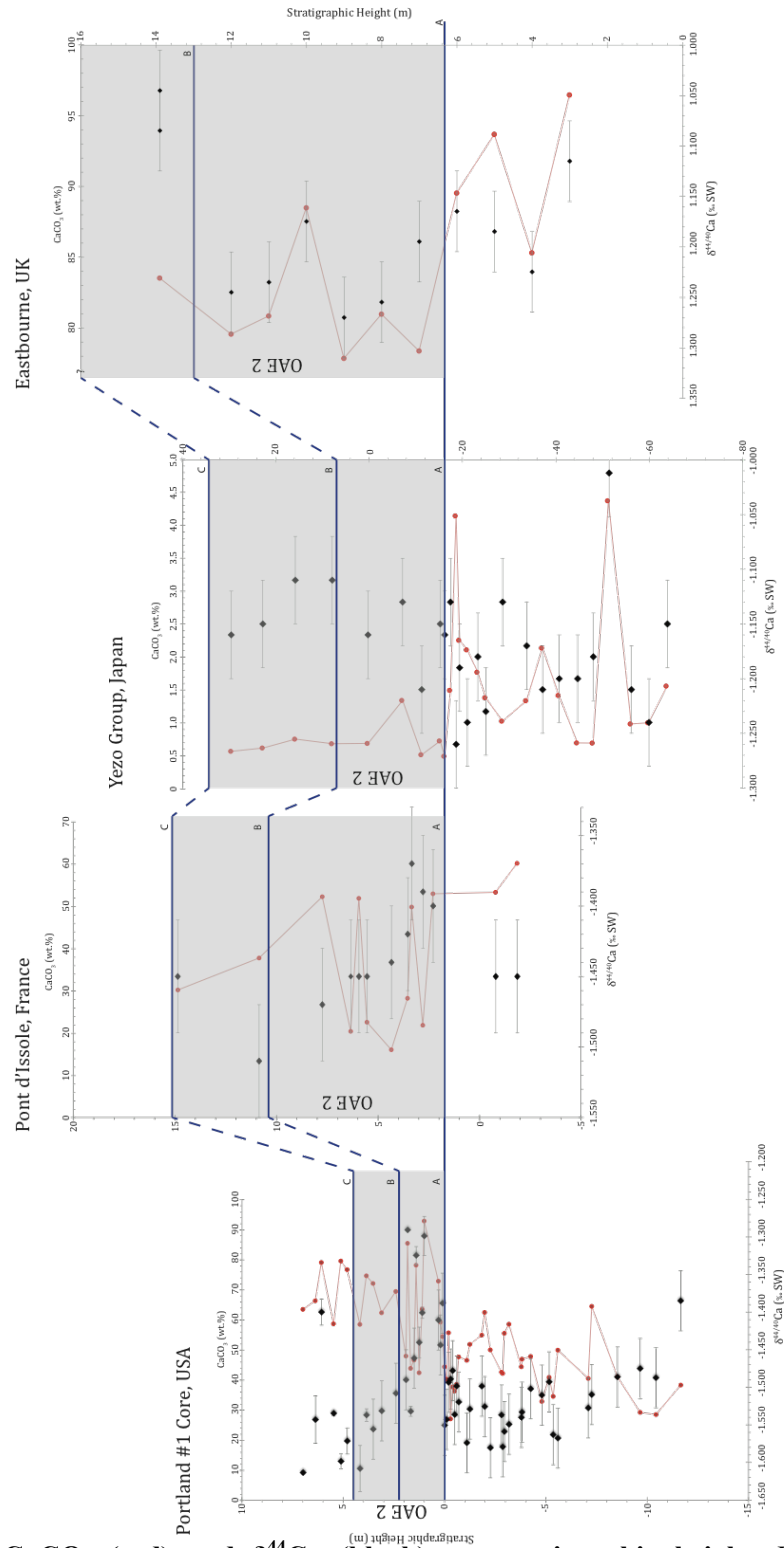


**Figure 4.8** CaCO<sub>3</sub> (red) and δ<sup>44</sup>Ca (black) vs. stratigraphic height. Illustrates the carbonate abundance (wt.%) for Portland #1 core, Pont d'Issole, Yezo Group and Eastbourne. The CaCO<sub>3</sub> abundance shows a non-correlative relationship with the δ<sup>44</sup>Ca values (see section 5.4.2 for discussion).

Global comparisons of other isotope records reveal that minor global discrepancies are indicative to regional variation in seawater geochemistry (Paquay and Ravizza, 2012; Du Vivier et al., 2014; Chapter 2, 3, this thesis); however,  $\delta^{44}\text{Ca}$  values are inferred to record the net change in global reservoirs only. Yet, the global distribution of variable marine  $\delta^{44}\text{Ca}$  excursions is consistent with the heterogeneity of the lithological sequences, respectively. As such by association the  $\Delta_C$  is a function of mineralogy and thus local inputs (Ockert et al., 2013). Therefore contrasting  $\delta^{44}\text{Ca}$  records imply, like many other isotopes (e.g.,  $^{187}\text{Os}/^{188}\text{Os}$ ), that the system is also sensitive to regional variation of local water masses (Schmitt et al., 2003; Paquay and Ravizza, 2012; Owens et al., 2013).

#### *5.4.3. Temperature*

The effect of temperature on seawater  $\delta^{44}\text{Ca}$  values has been discussed at length (De La Rocha and DePaolo, 2000; Nägler et al. 2000; DePaolo, 2004; Marriott et al., 2004; Sime et al., 2005). A small temperature dependence is commonly reported in many analytical studies as a function of species (foraminifera/plankton) that result in an influence of  $\sim 0.02\%$  per  $^{\circ}\text{C}$  (De Paolo, 2004) and vary according to their latitudinal distribution (Blättler et al., 2012). An increase in temperature is recorded by a positive excursion in the  $\delta^{44}\text{Ca}$  record; high temperatures lead to increased weathering and the release of  $^{40}\text{Ca}$  through carbonate and silicate weathering, which in turn leads to increased carbonate sedimentation (Tipper et al., 2006). Therefore  $\Delta_C$  is influenced by temperature, though the effect is small, particularly during small changes in sea surface temperatures (De La Rocha and DePaolo, 2000; Gussone et al., 2003, 2006, 2007; Marriott et al., 2004), such as during the OAE 2 (Forster et al., 2007).

The sections analysed here produce positive excursions in the  $\delta^{44}\text{Ca}$  records,  $\sim 0.20\%$ . However, interpretations based on temperature alone would contradict the interpretation of temperature proxies at the start of the OAE 2; where the onset of anoxia initiated the feedback process, which led to a brief interval of cooling ( $\sim 4^\circ\text{C}$ ) for the first  $\sim 150$  kyr of the OAE 2 (Sinninghe Damsté et al., 2010; Jarvis et al., 2011). Conversely, the  $\sim 0.20\%$  positive excursion is indicative to a  $\sim 10^\circ\text{C}$  temperature increase. The negative excursions in Blättler et al.'s  $\delta^{44}\text{Ca}$  data (2011; Fig. 4.5) are inferred to represent a partial response to the decrease in temperature. However, evidence suggests that atmospheric and sea surface temperatures throughout the palaeo-basins of the CTB were relatively consistent (Forster et al., 2007; Dennis et al., 2013). Furthermore, the analysis of the effect of temperature on fractionation during adsorption is non-correlative (Ockert et al., 2013). Therefore, the effect of temperature can be discounted because of the contradictory trends in the  $\delta^{44}\text{Ca}$  values between sections.

## **6. Summary**

The trends in the marine Ca isotope record have the potential to record the evolution of seawater utilising  $\delta^{44/40}\text{Ca}$  values from carbonate sedimentary successions. A previous study presented  $\delta^{44/42}\text{Ca}$  values against numerical models coupled with Sr isotope curves, which were utilised to interpret the factors influencing the seawater chemistry (Blättler et al., 2011). The study infers that a transient negative excursion in the marine  $\delta^{44/42}\text{Ca}$  composition across the onset of the OAE 2 is indicative to an increase in the weathering influx (Blättler et al., 2011). However, the  $\delta^{44}\text{Ca}$  values from this study reveal a positive excursion that is synchronous with the onset of OAE 2, after which the  $\delta^{44}\text{Ca}$  values gradually return

to pre-OAE 2 values. We evaluate the different analytical methodologies and justify the comparison of samples from Eastbourne re-analysed here and directly compare the two datasets through the conversion of  $\delta^{44/40}\text{Ca}$  to  $\delta^{44/42}\text{Ca}$  based on the standard 915a relative to the value the Northwestern Laboratory obtains for OSIL SW. Thus, we confirm that the discrepancy in Ca isotope trends at the onset of OAE 2 is not an analytical artefact.

Qualitative observations of the positive trend in the  $\delta^{44}\text{Ca}$  values suggest that the  $\delta^{44}\text{Ca}$  values may be sensitive to an increase in hydrothermal flux, which is globally contemporaneous with activity at submarine LIPs based on evidence from Os isotope stratigraphy (Du Vivier et al., 2014; Chapters 2, 3, this thesis) and other isotope proxies (Snow et al., 2005; Turgeon and Creaser, 2008; MacLeod et al., 2008; Montoya-Pino et al., 2010; Kuroda et al., 2011; Pogge von Strandmann et al., 2013; Zheng et al., 2013; Du Vivier et al., 2014). In addition, evidence from hydrothermal condensates may suggest that sublimation significantly enriches Ca in seawater compared to exsolved Sr (Taran et al., 1995). Therefore under non-steady-state conditions Ca and Sr may be decoupled. However, our quantitative analysis is not consistent with such a hypothesis.

In order to quantitatively determine the mechanism controlling changes in marine  $\delta^{44}\text{Ca}$  isotope composition we derive a seawater mixing model based on modern parameters (Milliman, 1993; Holmden et al., 2012; Fantle and Tipper, 2013). The models depict 4 states of the ocean; A – steady-state, B – increased hydrothermal flux, C – increased weathering flux, and D – variable fractionation factor. The models show no appreciable change in  $\delta^{44}\text{Ca}$  values as a result of weathering and/or hydrothermal flux since different behaviour is exhibited by  $\delta^{44}\text{Ca}$  records of the analysed sections compared to the weathering and hydrothermal

models. Therefore despite qualitative observations based on the documented increase in volcanic activity contemporaneous with OAE 2, quantitative evidence suggests that there is no appreciable change in  $\delta^{44}\text{Ca}$  values. The most tenable explanation for the variation in marine  $\delta^{44}\text{Ca}$  values is modelled by a change in  $\Delta_{\text{C}}$ , which varies depending on carbonate precipitation. From this study we infer that increased Ca:CO<sub>3</sub> ratios in seawater are a function of enhanced Ca inputs as well as the increase in dissolved CO<sub>2</sub> associated with isochronous volcanic activity, which leads to ocean acidification, thus the decrease in carbonate precipitation and decrease in  $\Delta_{\text{C}}$ . The contrasting trends in the  $\delta^{44}\text{Ca}$  profiles presented here demonstrate that carbonate and clay-rich samples are subject to varying  $\Delta_{\text{C}}$  as a function of their mineralogy, which may provide an explanation for the global variation in marine  $\delta^{44}\text{Ca}$  values in different depositional settings with varying lithological sequences.

This study and many others show that the marine  $\delta^{44}\text{Ca}$  isotope system has many complexities and there are a number of parameters such as; lithology, diagenesis, temperature and pH, yet to be definitively constrained influencing the fractionation factor itself. Any interpretation of the marine  $\delta^{44}\text{Ca}$  isotope system ought to be considered with a broad appreciation for the complexities of the system and further work will facilitate our understanding of the influence of multiple parameters on the marine records, which appear to be globally site-specific.

## REFERENCES

- Amini, M., Eisenhauer, A., Böhm, F., Fietzke, J., Bach, W., Garbe-Schonberg, D., Rosner, M., Bock, B., Lackschewitz, K.S., Hauff, F., 2008. Calcium isotope ( $\delta^{44/40}\text{Ca}$ ) fractionation along hydrothermal pathways, Logatchev field (Mid-Atlantic Ridge, 14°45'N). *Geochim. Cosmochim. Acta* 72, 4107-4122.
- Berner E.K., Berner R.A., 1996. *Global Environment: Water, Air and Geochemical Cycles*. Englewood Cliffs N.J., Prentice Hall.

- Blättler, C. L., Jenkyns, H. C., Reynard, L. M., Henderson, G. M., 2011. Significant increases in global weathering during Oceanic Anoxic Events 1a and 2 indicated by calcium isotopes. *Earth Planet. Sci. Letts.* 309, 77-88.
- Blättler, C.L., Henderson, G.M., Jenkyns, H.C., 2012. Explaining the Phanerozoic Ca isotope history of seawater. *Geology* 40, 843-846.
- Böhm, F., Gussone, N., Eisenhauer, A., Dullo, W-C., Reynaud, S., Paytan, A., 2006. Ca isotope fractionation in modern corals. *Geochim. Cosmochim. Acta* 70, 4452–4462.
- Böhm, F., Eisenhauer, A., Rausch, S., Bach, W., & Klügel, A., 2009. Calcium isotope systematics of low temperature alteration carbonates in the ocean crust. *Geochim. Cosmochim. Acta* 71, 2524-2546.
- Clarke, L. J., Jenkyns, H. C., 1999. New oxygen isotope evidence for long-term Cretaceous climatic change in the Southern Hemisphere. *Geology* 27, 8; 699-702.
- Cobban, W., Walaszczyk, I., Obradovich, J.D., McKinney, K.C., 2006. A USGS zonal table for the Upper Cretaceous Middle Cenomanian - Maastrichtian of the Western Interior of the United States based on ammonites, inoceramids, and radiometric ages. USGS Open-File Report 2006–1250.
- Cobban, W.A., Scott, G. R., 1972. Stratigraphy and ammonite fauna of the Graneros Shale and Greenhorn Limestone near Pueblo, Colorado. U.S. Govt. Print. Off. (Washington), 101-368-424.
- De La Rocha, C.L., DePaolo, D.J., 2000. Isotopic evidence for variations in the marine calcium cycle over the Cenozoic. *Science* 289, 1176–1178.
- Dean, W.E., Arthur, M.A., 1998. Geochemical expression of cyclicity in Cretaceous pelagic limestone sequences: Niobrara Formation, Western Interior Seaway in: Dean, W.E., and Arthur, M.A., eds., *Stratigraphy and Paleoenvironments of the Cretaceous Western Interior Seaway, U.S.A.* SEPM, Concepts Sedimentology, Paleontology 6, 227- 255.
- Dennis, K.J., Cochran, J.K., Landman, N.H., Schrag, D.P., 2013. The climate of the Late Cretaceous: New insights from the application of the carbonate clumped isotope thermometer to Western Interior Seaway macrofossil. *Earth Planet. Sci. Lett.* 362, 51-65.
- DePaolo, D.J., 2004. Calcium isotopic variations produced by biological, kinetic, radiogenic and nucleosynthetic processes. *Rev. Mineral. Geochem.* 55, 255–288.
- DePaolo, D.J., 2011. Surface kinetic model for isotopic and trace element fractionation during precipitation of calcite from aqueous solutions. *Geochim. Cosmochim. Acta*, 75, 1039-1056.

- Dias, B. B., Hart, M. B., Smart, C. W., Hall-Spencer, J. M., 2010. Modern seawater acidification: the response of foraminifera to high-CO<sub>2</sub> conditions in the Mediterranean Sea. *J. Geol. Soc. Lon.* 167, 843-846.
- Du Vivier, A.D.C., Selby, D., Sageman, B.B., Jarvis, I., Grocke, D.R., Voigt, S., 2014. Marine <sup>187</sup>Os/<sup>188</sup>Os isotope stratigraphy reveals the interaction of volcanism and ocean circulation during Oceanic Anoxic Event 2. *Earth Planet. Sci. Lett.* 389, 23-33.
- Eicher, D.L., Worstell, P., 1970. Cenomanian and Turonian foraminifera from the Great Plains, United States. *Micropaleontology* 16, 269-324.
- Elder, W.P., Gustason, E.R., Sageman, B.B., 1994. Correlation of basinal carbonate cycles to nearshore parasequences in the Late Cretaceous Greenhorn Seaway, Western Interior, U.S. *Geological Society of America Bulletin*, 106, 892-902.
- Erba, E., 2004. Calcareous nannofossils and Mesozoic oceanic anoxic events. *Mar. Micropaleontol.* 52, 85–106.
- Erba, E., Bottini, C., Weissert, J.H., Keller, C.E., 2010. Calcareous nannoplankton response to surface-water acidification around Oceanic Anoxic Event 1a: *Science*, 329, 428–432, doi:10.1126/science.1188886.
- Fantle, M.S., 2010. Evaluating the Ca isotope proxy. *Am. J. Sci.* 310, 194–230.
- Fantle, M.S., DePaolo, D.J., 2005. Variations in the marine Ca cycle over the past 20 million years. *Earth Planet. Sci. Lett.* 237, 102–117.
- Fantle, M.S., DePaolo, D.J., 2007. Ca isotopes in carbonate sediment and pore fluid from ODP Site 807A: The Ca<sup>2+</sup>(aq)–calcite equilibrium fractionation factor and calcite recrystallization rates in Pleistocene sediments. *Geochim. Cosmochim. Acta* 71, 2524–2546.
- Fantle, M.S., Tipper, E.T., 2013. Calcium isotopes in the global biogeochemical Ca cycle: Implications for development of a Ca isotope proxy. *Earth-Science Reviews* doi:10.1016/j.earscirev.2013.10.004
- Farkaš, J., Buhl, D., Blenkinsop, J., Veizer, J., 2007a. Evolution of the oceanic calcium cycle during the late Mesozoic: Evidence from  $\delta^{44/40}\text{Ca}$  of marine skeletal carbonates. *Earth Planet. Sci. Lett.* 253(1), 96-111.
- Farkaš, J., Böhm, F., Wallmann, K., Blenkinsop, J., Eisenhauer, A., Van Geldern, R., Veizer, J., 2007b. Calcium isotope record of Phanerozoic oceans: Implications for chemical evolution of seawater and its causative mechanisms. *Geochim. Cosmochim. Acta* 71(21), 5117-5134.
- Forster, A., Schouten, S., Moriya, K., Wilson, P.A., Sinninghe Damsté, J.S., 2007. Tropical warming and intermittent cooling during the Cenomanian/Turonian oceanic anoxic

- event 2: Sea surface temperature records from the equatorial Atlantic. *Paleoceanography*, 22, PA1219. doi:10.1029/2006PA001349.
- Frijia, G., Parente, M., 2008. Strontium isotope stratigraphy in the upper Cenomanian shallow-water carbonates of the southern Apennines: Short-term perturbations of marine  $^{87}\text{Sr}/^{86}\text{Sr}$  during the oceanic anoxic event 2. *Palaeogeog. Palaeoclimatol. Palaeoecol.* 261, 15-29.
- Gale, A.S., Kennedy, W.J., Voigt, S., Walaszczyk, I., 2005. Stratigraphy of the Upper Cenomanian-Lower Turonian Chalk succession at Eastbourne, Sussex, UK.: ammonites, inoceramid bivalves and stable carbon isotopes. *Cretaceous Research* 26, 3, 460 – 487.
- Gradstein, F.M., Ogg, J.G., Schmitz, M., eds., 2012. *The Geologic Time Scale 2012*, 2-volume set. Elsevier.
- Griffith, E.M., Paytan, A., Caldeira, K., Bullen, T.D., Thomas, E., 2008. A dynamic marine calcium cycle during the past 28 million years. *Science* 322, 1671–1674.
- Grosheny, D., Beaudoin, B., Morel, L., Desmares, D., 2006. High-resolution biostratigraphy and chemostratigraphy of the Cenomanian/Turonian boundary event in the Vocontian Basin, southeast France. *Cretaceous Research* 27, 629-640.
- Gussone, N., Böhm, F., Eisenhauer, A., Dietzel, M., Heuser, A., Teichert, B.M.A., Reitner, J., Worheide, G., Dullo, W-C., 2005. Calcium isotope fractionation in calcite and aragonite. *Geochim. Cosmochim. Acta* 69, 4485-4494.
- Gussone, N., Eisenhauer, A., Heuser, A., Dietzel, M., Bock, B., Böhm, F., Spero, H.J., Lea, D.W., Buma, J., Nägler, T.F., 2003. Model for kinetic effects on calcium isotope fractionation ( $\delta^{44}\text{Ca}$ ) in inorganic aragonite and cultured planktonic foraminifera. *Geochim. Cosmochim. Acta* 67, 1375–1382.
- Gussone, N., Langer, G., Thoms, S., Nehrke, G., Eisenhauer, A., Riebesell, U., Wefer, G., 2006. Cellular calcium pathways and isotope fractionation in *Emiliana huxleyi*. *Geology* 34, 625–628.
- Gussone, N., Langer, G., Geisen, M., Steel, B.A., Riebesell, U., 2007. Calcium isotope fractionation in coccoliths of cultured *Calcidiscus leptoporus*, *Helicosphaera carteri*, *Syracosphaera pulchra* and *Umbilicosphaera foliosa*. *Earth Planet. Sci. Lett.* 260, 505–515.
- Hasegawa, T., 1995. Correlation of the Cenomanian/Turonian boundary between Japan and Western Interior of the United States. *J. Geol. Soc. Japan* 101, 2-12.
- Hasegawa, T., 1999. Planktonic foraminifera and biochronology of the Cenomanian-Turonian (Cretaceous) sequence in the Oyubari area, Hokkaido, Japan. *Paleontol. Res.* 3, 173-192.

- Hattin, D. E., 1971. Widespread, synchronously deposited, burrow-mottled limestone beds in Greenhorn Limestone (Upper Cretaceous) of Kansas and central Colorado. *Am. Assoc. Petroleum Geologists Bull.* 55, 412-431.
- Hippler, D., Schmitt, A.D., Gussone, N., Heuser, A., Stille, P., Eisenhauer, A., Nægler, T.F., 2003. Calcium isotopic composition of various reference materials and seawater. *Geostandards Newsletter*, 27, 13-19.
- Holmden, C., Papanastassiou, D.A., Blanchon, P., Evans, S., 2012.  $\delta^{44/40}\text{Ca}$  variability in shallow water carbonates and the impact of submarine groundwater discharge on Ca-cycling in marine environments. *Geochim. Cosmochim. Acta* 83, 179–194.
- Jacobson A.D., Holmden C., 2008.  $\delta^{44}\text{Ca}$  evolution in a carbonate aquifer and its bearing on the equilibrium isotope fractionation factor for calcite. *Earth Planet. Sci. Lett.* 270, 349–353.
- Jarvis, I., Gale, A. S., Jenkyns, H. C., Pearce, M. A., 2006. Secular variation in Late Cretaceous carbon isotopes: a new  $\delta^{13}\text{C}$  carbonate reference curve for the Cenomanian – Campanian (99.6 – 70.6 Ma). *Geol. Mag.* 143, 561 – 608.
- Jarvis, I., Lignum, J. S., Grocke, D. R., Jenkyns, H. C., Pearce, M. A., 2011. Black shale deposition, atmospheric  $\text{CO}_2$  drawdown, and cooling during the Cenomanian-Turonian Oceanic Anoxic Event. *Paleoceanography* 26, PA3201.
- Jenkyns, H.C., 1980. Cretaceous anoxic events: from continents to oceans. *J. Geol. Soc. London* 137, 171–188.
- Jenkyns, H.C., 2010. Geochemistry of oceanic anoxic events. *Geochem. Geophys. Geosys.* 11.
- Jenkyns, H.C., Gale, A.S., Corfield, R.M., 1994. Carbon- and oxygen-isotope stratigraphy of the English Chalk and Italian Scaglia and its palaeoclimatic significance. *Geol. Mag.* 131, 1–34.
- Jones, C.E., Jenkyns, H.C., 2001. Seawater strontium isotopes, oceanic anoxic events, and seafloor hydrothermal activity in the Jurassic and Cretaceous. *Am. J. Sci.*, 301, 112 – 149.
- Kaiho, K., Fujiwara, O., Motoyama, I., 1993. MidCretaceous faunal turnover of intermediate-water benthic foraminifera in the northwestern Pacific Ocean margin. *Mar. Micropaleontol.* 23, 13-49.
- Keller, G., Berner, Z., Adatte, T., Stueben, D., 2004. Cenomanian–Turonian and  $\delta^{13}\text{C}$ , and  $\delta^{18}\text{O}$ , sea level and salinity variations at Pueblo, Colorado. *Palaeogeog. Palaeoclimatol. Palaeoecol.* 211, 19–43.
- Keller, G., Pardo, A., 2004. Age and paleoenvironment of the Cenomanian/Turonian global stratotype section and point at Pueblo, Colorado. *Mar. Micropaleontol.* 51, 95–128.

- Keller, C.E., Hochuli, P.A., Weissert, H., Bernasconi, S.M., Giorgioni, M., Garcia, T.I., 2011. A volcanically induced climate warming and floral change preceded the onset of OAE1a (Early Cretaceous). *Palaeogeog. Palaeoclimatol. Palaeoecol.* 305, 43-49.
- Kendall, B., Creaser, R. A., and Selby, D., 2009,  $^{187}\text{Re}$ - $^{187}\text{Os}$  geochronology of Precambrian organic-rich sedimentary rocks. *Geol. Soc. London Spec. Pub.* 326, 85-107.
- Kennedy, W.J., Walaszyk, I., Cobban, W.A., 2005. The Global Boundary Stratotype Section and Point for the base of the Turonian Stage of the Cretaceous: Pueblo, Colorado, USA. *Episodes* 28, 93–104.
- Kennedy, W.J., Walaszyk, I., Cobban, W.A., 2000, Pueblo, Colorado, USA, candidate Global Boundary Stratotype Section and Point for the base of the Turonian Stage of the Cretaceous and for the base of the middle Turonian Substage, with a revision of the *Inoceramidae* (Bivalvia). *Acta Geologica Polonica* 50, 295–334.
- Kerr, A.C., 1998. Oceanic plateau formation: a cause of mass extinction and black shale deposition around the Cenomanian–Turonian boundary? *J. Geol. Soc.* 155, 619-626.
- Kisakurek, B., Eisenhauer, A., Böhm, F., Hathorne, E.C., Erez, J., 2011. Controls on calcium isotope fractionation in cultured planktic foraminifera, *Globigerinoides ruber* and *Globigerinella siphonifera*. *Geochim. Cosmochim. Acta* 75 (2), 427-443, DOI [10.1016/j.gca.2010.10.015](https://doi.org/10.1016/j.gca.2010.10.015).
- Kuroda, J., Tanimizu, M., Hori, R.S., Suzuki, K., Ogawa, N.O., Tejada, M.L., Ohkouchi, N., 2011. Lead isotopic record of Barremian–Aptian marine sediments: Implications for large igneous provinces and the Aptian climatic crisis. *Earth Planet. Sci. Lett.* 307, 126-134.
- Lehn, G.O., Jacobson, A.D., Holmden, C., 2013. Precise analysis of Ca isotope ratios ( $\delta^{44/40}\text{Ca}$ ) using an optimized  $^{43}\text{Ca}$ - $^{42}\text{Ca}$  double-spike MC-TIMS method. *International Journal of Mass Spectrometry*, 351, 69-75.
- MacLeod, K. G., Marin, E. E., Blair, S. W., 2008. Nd excursions across the Cretaceous oceanic anoxia event 2 (Cenomanian-Turonian) in the tropical North Atlantic. *Geology* 36, 811-814.
- Marriott, C.S., Henderson, G.M., Belshaw, N.S., Tudhope, A.W., 2004. Temperature dependence of  $\delta^7\text{Li}$ ,  $\delta^{44}\text{Ca}$  and Li/Ca during growth of calcium carbonate. *Earth Planet. Sci. Lett.* 222, 615–624.
- Martin, E. E., MacLeod, K. G., Jimenez Berroco, A., Bourbon, E., 2012. Water mass circulation on Demerara Rise during the Late Cretaceous based on Nd isotopes. *Earth Planet. Sci. Lett.*, 327-328, 111-120.
- McArthur, J.M., Howarth, R.J., Bailey, T., 2004. Strontium isotope stratigraphy. In: Gradstein, F., Ogg, J., Smith, A., (Eds.) *A Geological Time Scale 2004*. Cambridge University Press, Cambridge, U.K., pp. 96–105.

- Meyers, S.R., Sageman, B.B., Hinnov, L.A., 2001. Integrated quantitative stratigraphy of the Cenomanian-Turonian Bridge Creek Limestone member using Evolutive Harmonic Analysis and stratigraphic modelling. *J. Sed. Res.* 71, 628-644.
- Meyers, S.R., Siewert, S.E., Singer, B.S., Sageman, B.B., Condon, D.J., Obradovich, J.D., Jicha, B.R., Sawyer, D.A., 2012a. Intercalibration of radioisotopic and astrochronologic time scales for the Cenomanian-Turonian boundary interval, Western Interior Basin, USA. *Geology* 40, 7-10.
- Meyers, S.R., Sageman, B.B., Arthur, M.A., 2012b. Obliquity forcing and the amplification of high-latitude climate processes during Oceanic Anoxic Event 2. *Paleoceanography* 27, PA3212, doi:10.1029/2012PA002286.
- Milliman J.D., 1993. Production and accumulation of CaCO<sub>3</sub> in the ocean: budget of a non-steady-state. *Global Biogeochem. Cy.* 7, 927-957.
- Mitchell, S.F., Ball, J.D., Crowley, S.F., Marshall, J.D., Paul, C.R., Veltkamp, C.J., Samir, A. 1997. Isotope data from Cretaceous chalks and foraminifera: Environmental or diagenetic signals? *Geology* 25, 691-694.
- Montoya-Pino, C., Weyer, S., Anbar, A.D., Pross, J., Oschmann, W., van de Schootbrugge, B., Arz, H.W., 2010. Global enhancement of ocean anoxia during Oceanic Anoxic Event 2: A quantitative approach using U isotopes. *Geology*, 38, 315-318.
- Mort, H., Jacquat, O., Adatte, T., Steinmann, P., Follmi, K., Matera, V., Berner, Z., Stüben, D., 2007. The Cenomanian/Turonian anoxic event at the Bonarelli Level in Italy and Spain: enhanced productivity and/or better preservation? *Cretaceous Research* 28, 597 - 612.
- Mort, H. P., Adatte, T., Follmi, K. B., Keller, G., Steinmann, P., Matera, V., Berner, Z., Stüben, D., 2011. Phosphorus and the roles of productivity and nutrient recycling during Oceanic Anoxic Event 2. *Geology*, 35, 6; 483-486.
- Nägler, T.F., Eisenhauer, A., Müller, A., Hemleben, C., Kramers, J., 2000. The  $\delta^{44}\text{Ca}$ -temperature calibration on fossil and cultured Globigerinoides sacculifer: New tool for reconstruction of past sea surface temperatures. *Geochem. Geophys. Geosys.* 1, 9.
- Nielsen, L.C., DePaolo, D.J., De Yoreo, J.J., 2012. Self-consistent ion-by-ion growth model for kinetic isotopic fractionation during calcite precipitation. *Geochim. Cosmochim. Acta* 86, 166-181.
- Ockert, C., Gussone, N., Kaufhold, S., Teichert, B.M.A., 2013. Isotope fractionation during Ca exchange on clay minerals in a marine environment. *Geochim. Cosmochim. Acta*, 112, 374-388.

- Owens, J.D., Gill, B.C., Jenkyns, H.C., Bates, S.M., Severmann, S., Kuypers, M.M., Lyons, T.W., 2013. Sulfur isotopes track the global extent and dynamics of euxinia during Cretaceous Oceanic Anoxic Event 2. *Proc. Natl. Acad. Sci.* 110, 18407-18412.
- Paquay, F. S., Ravizza, G., 2012. Heterogeneous seawater  $^{187}\text{Os}/^{188}\text{Os}$  during the Late Pleistocene glaciations. *Earth Planet. Sci. Lett.* 349 – 350, 126 – 138.
- Paul, C.R.C., Lamolda, M.A., Mitchell, S.F., Vaziri, M.R., Gorostidi, A., Marshall, J.D., 1999. The Cenomanian–Turonian boundary at Eastbourne (Sussex, UK): a proposed European reference section. *Palaeogeog. Palaeoclimatol. Palaeoecol.* 150, 83–122.
- Payne, J.L., Turchyn, A.V., Paytan, A., DePaolo, D.J., Lehrmann, D.J., Yu, M., Wei, J., 2010. Calcium isotope constraints on the end-Permian mass extinction. *Proc. Nat. Acad. Sci.* 107, 8543-8548.
- Peucker-Ehrenbrink, B., Ravizza, G., 2000. The marine osmium isotope record. *Terra Nova* 12, 205-219.
- Pogge von Strandmann, P.A.P., Jenkyns, H.C., Woodfine, R.G., 2013. Lithium isotope evidence for enhanced weathering during Oceanic Anoxic Event 2. *Nature Geoscience*, 6, 668-672.
- Pratt, L.M., Kauffman, E.G., Zelt, F.B., 1985. Fine-grained deposits and biofacies of the Cretaceous Western Interior Seaway: evidence for cyclic sedimentary processes. *Soc. Econ. Paleont. Miner. Field Trip Guidebook 4*, 1985 Midyear Meeting, Golden, Colorado.
- Pretet, C., Samankassou, E., Felis, T., Reynaud, S., Böhm, F., Eisenhauer, A., Ferrier-Pagès, C., Gattuso, J-P., Camoin, G., 2013. Constraining calcium isotope fractionation ( $\delta^{44}/^{40}\text{Ca}$ ) in modern and fossil scleractinian coral skeleton *Chemical Geology* 340, 49-58. DOI [10.1016/j.chemgeo.2012.12.006](https://doi.org/10.1016/j.chemgeo.2012.12.006).
- Robinson, N., Ravizza, G., Coccioni, R., Peucker-Ehrenbrink, B., Norris, R., 2009. A high-resolution marine  $^{187}\text{Os}/^{188}\text{Os}$  record for the late Maastrichtian: Distinguishing the chemical fingerprints of Deccan volcanism and the KP impact event. *Earth Planet Sci. Lett.* 281, 159–168.
- Sageman, B.B., Meyers, S.R., Arthur, M.A., 2006. Orbital time scale and new C-isotope record for Cenomanian–Turonian boundary stratotype. *Geology* 34, 125–128.
- Schiller, M., Paton, C., Bizzarro, M., 2012. Calcium isotope measurement by combined HRMC-ICPMS and TIMS. *J. Anal. At. Spectrom.* 27, 38–49.
- Schlanger, S.O., Arthur, M.A., Jenkyns, H.C., Scholle, P.A. 1987. The Cenomanian/Turonian Oceanic Anoxic Event, I. Stratigraphy and distribution of organic carbon-rich beds and the marine  $\delta^{13}\text{C}$  excursion. In: Brooks, J. & Fleet, A.J. (eds) *Marine Petroleum Source Rocks*. Geological Society London, Spec. Publ., 26, 371–399.

- Schmitt, A.-D., Chabaux, F., Stille, P., 2003. The calcium riverine and hydrothermal isotopic fluxes and the oceanic calcium mass balance. *Earth Planet. Sci. Lett.* 6731, 1–16.
- Sime, N.G., De La Rocha, C.L., Galy, A., 2005. Negligible temperature dependence of calcium isotope fractionation in 12 species of planktonic foraminifera. *Earth Planet. Sci. Lett.* 232, 51-66.
- Sime, N.G., De La Rocha, C.L., Tipper, E.T., Tripathi, A., Galy, A., Bickle, M.J., 2007. Interpreting the Ca isotope record of marine biogenic carbonates. *Geochim. Cosmochim. Acta* 71, 3979–3989.
- Simon, J.I., DePaolo, D.J., 2010. Stable calcium isotopic composition of meteorites and rocky planets. *Earth Planet. Sci. Lett.* 289, 457–466.
- Sinninghe Damsté, J.S., van Bentum, E.C., Reichart, G.J., Pross, J., Schouten, S., 2010. A CO<sub>2</sub> decrease-driven cooling and increased latitudinal temperature gradient during the mid-Cretaceous Oceanic Anoxic Event 2. *Earth Planet. Sci. Lett.* 293, 97–103.
- Sinton, C. W., Duncan, R. A., 1997. Potential links between ocean plateau volcanism and global ocean anoxia and the Cenomanian-Turonian boundary. *Econ. Geol.*, 92, 836-842.
- Snow, L.J., Duncan, R.A., Bralower, T.J., 2005. Trace element abundances in the Rock Canyon Anticline, Pueblo, Colorado, marine sedimentary section and their relationship to Caribbean plateau construction and oxygen anoxic event 2. *Paleoceanography* 20, doi:10.1029/2004PA001093.
- Takashima, R., Kawabe, F., Nishi, H., Moriya, K., Wani, R., Ando, H., 2004. Geology and stratigraphy of forearc basin sediments in Hokkaido, Japan: Cretaceous environmental events on the north-west Pacific margin. *Cretaceous Res.* 25, 365-390.
- Takashima, R., Nishi, H., Hayashi, K., Okada, H., Kawahata, H., Yamanaka, T., Fernando, A. G., Mampuku, M., 2009. Litho-, bio- and chemostratigraphy across the Cenomanian/Turonian boundary (OAE2) in the Vocontian Basin of southeast France. *Palaeogeography, Palaeoclimatology, Palaeoecology*, 273, 61-74.
- Takashima, R., Nishi, H., Yamanaka, T., Tomosugi, T., Fernando, A.G., Tanabe, K., Moriya, K., Kawabe, F., Hayashi, K., 2011. Prevailing oxic environments in the Pacific Ocean during the mid-Cretaceous Oceanic Anoxic Event 2. *Nature Comms.* 2:234 DOI:10.1038/ncomms1233.
- Tamaki, M., Itoh, Y., 2008. Tectonic implications of paleomagnetic data from upper Cretaceous sediments in the Oyubari area, central Hokkaido, Japan. *Island Arc* 17, 270-284.

- Taran, Y.A., Hedenquist, J.W., Korzhinsky, M.A., Tkachenko, S.I., Shmulovich, K.I., 1995. Geochemistry of magmatic gases from Kudryavy volcano, Iturup, Kuril Islands. *Geochim. Cosmochim. Acta* 59, 1749-1761.
- Tegner, C., Storey, M., Holm, P.M., Thorarinsson, S.B., Zhao, X., Lo, C.-H., Knudsen, M.F., 2011. Magmatism and Eureka deformation in the High Arctic Large Igneous Province:  $^{40}\text{Ar} - ^{39}\text{Ar}$  age of Kap Washington Group volcanics, North Greenland. *Earth Planet. Sci. Lett.* 303, 203-214.
- Tipper, E.T., Bickle, M.J., Galy, A., West, A.J., Pomiès, C., Chapman, H.J., 2006. The short-term climatic sensitivity of carbonate and silicate weathering fluxes: insight from seasonal variations in river chemistry. *Geochim. Cosmochim. Acta* 70, 2737-2754.
- Tipper, E.T., Gaillardet, J., Galy, A., Louvat, P., Bickle, M.J., Capmas, F., 2010. Calcium isotope ratios in the World's largest rivers: a constraint on the maximum imbalance of oceanic calcium fluxes. *Glob. Biogeochem. Cycles* 24, GB3019. doi.org/10.1029/2009GB003574.
- Tsikos, H., Jenkyns, H.C., Walsworth-Bell, B., Petrizzo, M.R., Forster, A., Kolonic, S., Erba, E., Premoli-Silva, I.P., Baas, M., Wagner, T., Sinninghe Damsté, J.S., 2004. Carbon-isotope stratigraphy recorded by the Cenomanian - Turonian Oceanic Anoxic Event: correlation and implications based on three key localities. *J. Geol. Soc. London* 161, 711-719.
- Turgeon, S.C., Creaser, R.A., 2008. Cretaceous Anoxic Event 2 triggered by a massive magmatic episode. *Nature* 454, 323-326.
- van Bentum, E.C., Hetzel, A., Brumsack, H.J., Forster, A., Reichert, G.J., Sinninghe Damsté, J.S., 2009. Reconstruction of water column anoxia in the equatorial Atlantic during the Cenomanian-Turonian oceanic anoxic event using biomarker and trace metal proxies. *Palaeogeog. Palaeoclimatol. Palaeoecol.* 280, 489-498.
- Young, E.D., Galy, A., Nagahara, H., 2002. Kinetic and equilibrium mass-dependent isotope fractionation laws in nature and their geochemical and cosmochemical significance. *Geochim. Cosmochim. Acta* 66, 1095-1104.
- Zheng X-Y., Jenkyns, H.C., Gale, A.S., Ward, D.J., Henderson, G.M., 2013. Changing ocean circulation and hydrothermal inputs during Oceanic Anoxic Event 2 (Cenomanian-Turonian): Evidence from Nd-isotopes in the European shelf sea. *Earth Planet. Sci. Lett.* <http://dx.doi.org/10.1016/j.epsl.2013.05.053i>

## Data Tables

**Table 4.1a**  $\delta^{44}\text{Ca}$  (sw) values and  $\text{CaCO}_3$  abundances for Portland #1 Core, USA, during the CTBI

Sample ID	Height (m)	$\delta^{44}\text{Ca}$ (sw) (‰)	ex. precision (‰)	Ca (g/g)	$\text{CaCO}_3$ wt%	kyr
AD107-09	6.98	-1.61	0.002	0.255	63.637	742.57
AD105-09	6.37	-1.54	0.032	0.266	66.504	681.57
AD104-09	6.07	-1.40	0.017	0.317	79.236	651.57
AD103-09	5.47	-1.53	0.003	0.235	58.832	591.57
AD102-09	5.11	-1.60	0.010	0.319	79.724	555.57
AD101-09	4.80	-1.57	0.017	0.307	76.865	524.57
AD99-09	4.17	-1.61	0.031	0.235	58.641	455.34
AD98-09	3.85	-1.54	0.008	0.299	74.804	420.18
AD96-09	3.52	-1.56	0.040	0.289	72.257	383.91
AD95-09	3.10	-1.53	0.040	0.250	62.500	337.76
AD93-09	2.40	-1.51	0.040	0.278	69.601	254.42
AD90-09	1.90	-1.49	0.040	0.192	48.105	194.90
AD89-09	1.82	-1.29	0.000	0.342	85.613	167.90
AD88-09	1.67	-1.53	0.007	0.176	44.011	167.52
AD87-09	1.50	-1.46	0.040	0.187	46.764	147.28
AD86-09	1.40	-1.32	0.012	0.313	78.336	129.28
AD84-09	1.25	-1.44	0.020	0.170	42.557	117.52
AD83-09	1.10	-1.40	0.007	0.255	63.734	99.66
AD85-09	1.00	-1.30	0.026	0.372	93.023	16.66
AD68-09	0.30	-1.41	0.040	0.292	73.023	4.42
AD69-09	0.20	-1.44	0.040	0.237	59.369	0.00
AD70-09	0.10	-1.39	0.040	0.218	54.568	-4.42
AD71-09	0.00	-1.55	0.040	0.178	44.526	-8.85
AD72-09	-0.10	-1.54	0.040	0.162	40.408	-13.27
AD73-09	-0.20	-1.49	0.040	0.223	55.850	-17.70
AD74-09	-0.30	-1.49	0.040	0.109	27.204	-22.12
AD75-09	-0.40	-1.48	0.040	0.151	37.814	-26.55
AD76-09	-0.50	-1.54	0.040	0.146	36.443	-30.97
AD77-09	-0.60	-1.50	0.040	0.155	38.666	-35.40
AD78-09	-0.70	-1.52	0.040	0.191	47.826	-39.82
AD118-09	-1.10	-1.57	0.040	0.187	46.707	-57.52
AD119-09	-1.25	-1.53	0.040	0.208	51.997	-64.16
AD79-09	-1.84	-1.50	0.040	0.220	55.043	-90.27
AD120-09	-1.98	-1.53	0.040	0.250	62.624	-96.46
AD121-09	-2.26	-1.58	0.040	0.201	50.161	-108.85
AD80-09	-2.81	-1.54	0.040	0.171	42.756	-133.19
AD122-09	-2.87	-1.58	0.040	0.169	42.338	-135.84
AD123-09	-2.95	-1.56	0.040	0.223	55.679	-139.38
AD124-09	-3.18	-1.55	0.040	0.235	58.706	-149.56
AD81-09	-3.79	-1.54	0.040	0.178	44.554	-176.55
AD126-09	-3.82	-1.53	0.040	0.188	47.073	-177.88
AD128-09	-4.25	-1.50	0.040	0.192	47.977	-196.90
AD82-09	-4.80	-1.51	0.040	0.132	33.006	-221.24
AD130-09	-5.16	-1.49	0.040	0.164	41.046	-237.17
AD132-09	-5.36	-1.56	0.040	0.139	34.689	-246.02
AD133-09	-5.59	-1.57	0.040	0.200	50.083	-256.19
501.61	-7.09	-1.53	0.040	0.163	40.662	-322.57
AD134-09	-7.26	-1.51	0.040	0.259	64.639	-330.09
505.9	-8.53	-1.49	0.040	0.165	41.212	-386.28
509.5	-9.65	-1.48	0.040	0.118	29.382	-435.84
512	-10.43	-1.49	0.040	0.115	28.660	-470.35
516	-11.65	-1.38	0.040	0.154	38.461	-524.34

Note: individual uncertainties are reported at the  $2\sigma$  level. Internal precision of measurements is  $\pm 0.02\text{‰}$  (2SEM)  
OSIL Atlantic Seawater (SW) is employed as the normalizing standard for the delta equation  
Precision for the method is continuously monitored by repeated analyses of the following standards:  
OSIL SW, NIST SRM 915a and 915b, see Table 4.2  
kyr calculated as detailed in Chapters 2 and 3, this thesis

**Table 4.1b**  $\delta^{44}\text{Ca}$  (sw) values and  $\text{CaCO}_3$  abundances for Pont d'Issole, SE France, during the CTBI

Sample ID	Height (m)	$\delta^{44}\text{Ca}$ (sw) (‰)	ex. precision (‰)	Ca (g/g)	$\text{CaCO}_3$ wt%	kyr
AD47-10	14.86	-1.45	0.04	0.121	30.260	417.56
AD67-10	10.86	-1.51	0.04	0.151	37.817	183.64
AD02-10	7.75	-1.47	0.04	0.209	52.309	96.12
AD09-10	6.35	-1.45	0.04	0.082	20.477	71.43
AD11-10	5.95	-1.45	0.04	0.208	51.930	64.37
AD13-10	5.55	-1.45	0.04	0.091	22.639	57.32
AD19-10	4.35	-1.44	0.04	0.065	16.126	36.16
AD23-10	3.55	-1.42	0.04	0.113	28.292	22.05
AD24-10	3.35	-1.37	0.04	0.200	49.875	18.52
ISL8-09	2.80	-1.39	0.04	0.088	21.919	8.82
ISL7-09	2.30	-1.40	0.04	0.212	53.008	0.00
AD27-10	-0.78	-1.45	0.04	0.213	53.354	-121.81
AD33-10	-1.84	-1.45	0.04	0.241	60.209	-232.23

Note: individual uncertainties are reported at the  $2\sigma$  level. Internal precision of measurements is  $\pm 0.02\text{‰}$  (2SEM)  
OSIL Atlantic Seawater (SW) is employed as the normalizing standard for the delta equation

Precision for the method is continuously monitored by repeated analyses of the following standards:

OSIL SW, NIST SRM 915a and 915b, see Table 4.2

kyr calculated as detailed in Chapters 2 and 3, this thesis

**Table 4.1c**  $\delta^{44}\text{Ca}$  (sw) values and  $\text{CaCO}_3$  abundances for Yezo Group, Japan, during the CTBI

Sample ID	Height (m)	$\delta^{44}\text{Ca}$ (sw) (‰)	ex. precision (‰)	Ca (g/g)	$\text{CaCO}_3$ wt%	kyr
AD110-11	29.50	-1.16	0.04	0.002	0.570	679.97
AD112-11	22.75	-1.15	0.04	0.002	0.620	594.39
AD114-11	15.80	-1.11	0.04	0.003	0.755	506.28
AD116-11	7.90	-1.11	0.04	0.003	0.685	406.12
AD118-11	0.25	-1.16	0.04	0.003	0.690	309.13
AD120-11	-7.15	-1.13	0.04	0.005	1.343	215.31
AD121-11	-11.25	-1.21	0.04	0.002	0.518	163.33
AD122-11	-15.20	-1.15	0.04	0.003	0.728	31.67
CT056	-16.15	-1.16	0.04	0.002	0.495	0.00
CT055	-17.40	-1.13	0.04	0.006	1.495	-11.72
CT053	-18.60	-1.26	0.04	0.017	4.143	-22.96
AD123-11	-19.35	-1.19	0.04	0.009	2.255	-29.99
AD124-11	-21.00	-1.24	0.04	0.008	2.110	-45.46
AD125-11	-23.25	-1.18	0.04	0.007	1.770	-66.55
AD126-11	-24.95	-1.23	0.04	0.006	1.383	-82.48
AD128-11	-28.55	-1.13	0.04	0.004	1.028	-116.23
AD130-11	-33.70	-1.17	0.04	0.005	1.338	-137.69
AD132-11	-37.10	-1.21	0.04	0.009	2.138	-151.85
AD134-11	-40.65	-1.20	0.04	0.006	1.418	-166.64
AD136-11	-44.60	-1.20	0.04	0.003	0.698	-183.10
AD138-11	-47.95	-1.18	0.04	0.003	0.695	-197.06
AD140-11	-51.25	-1.01	0.04	0.017	4.373	-210.81
AD142-11	-56.10	-1.21	0.04	0.004	0.985	-231.02
AD144-11	-59.85	-1.24	0.04	0.004	1.003	-246.64
AD146-11	-63.80	-1.15	0.04	0.006	1.560	-263.10

Note: individual uncertainties are reported at the  $2\sigma$  level. Internal precision of measurements is  $\pm 0.02\text{‰}$  (2SEM)

OSIL Atlantic Seawater (SW) is employed as the normalizing standard for the delta equation

Precision for the method is continuously monitored by repeated analyses of the following standards:

OSIL SW, NIST SRM 915a and 915b, see Table 4.2

kyr calculated as detailed in Chapters 2 and 3, this thesis

**Table 4.1d**  $\delta^{44}\text{Ca}$  (sw) values and  $\text{CaCO}_3$  abundances for Eastbourne, UK, during the CTBI

Sample ID	Height (m)	$\delta^{44}\text{Ca}$ (sw) (‰)	ex. precision (‰)	Ca (g/g)	$\text{CaCO}_3$ wt%
WCO	13.90	-1.085	0.04	-	-
WCO-2	13.90	-1.045	0.04	0.334	83.594
PM-600	12.00	-1.245	0.04	0.319	79.634
PM-500	11.00	-1.235	0.04	0.324	80.915
PM-400	10.00	-1.175	0.04	0.354	88.559
PM-300	9.00	-1.270	0.04	0.312	77.919
PM-200	8.00	-1.255	0.04	0.324	81.045
PM-100	7.00	-1.195	0.04	0.314	78.443
GC-00	6.00	-1.165	0.04	0.358	89.599
GC-100	5.00	-1.185	0.04	0.375	93.749
GC-200	4.00	-1.225	0.04	0.342	85.379
GC-300	3.00	-1.115	0.04	0.386	96.529

Note: individual uncertainties are reported at the  $2\sigma$  level. Internal precision of measurements is  $\pm 0.02\text{‰}$  (2SEM)  
 OSIL Atlantic Seawater (SW) is employed as the normalizing standard for the delta equation  
 Precision for the method is continuously monitored by repeated analyses of the following standards:  
 OSIL SW, NIST SRM 915a and 915b, see Table 4.2



# 5 Conclusion

### **1. Overview**

The late Cretaceous OAE 2 has been extensively studied, with the primary objective to understand the palaeoclimate of the period through the evaluation of ocean chemistry and the implications of palaeocirculation, volcanism and climate change to determine the controlling factors driving oceanic anoxia. In this study the application of isotope geochemistry and geochronology (Os, Ca and U-Pb) facilitates a fundamental insight into; 1) what ocean-atmosphere processes were responsible for driving OAE 2 to become synchronously widespread in multiple basinal environments in the world's oceans; 2) if key stages and the duration of the OAE 2 can be quantitatively constrained; and 3) to establish if OAE 2 was a truly global isochronous event.

The following sections provide a concise synopsis of the findings for each chapter presented in this thesis. Each chapter represents a single version of a manuscript, which at the time of this thesis submission has either been published (Chapter 2; Du Vivier et al., EPSL, 2014), is ready for submission (Chapter 3; EPSL), or being finalised for submission to a journal (Chapter 4; GCA). In addition to the chapter synopsis I suggest a focus for future research and further applications of  $^{187}\text{Os}/^{188}\text{Os}$  isotope stratigraphy beyond the realm of palaeoclimate/palaeoceanography, specifically in petroleum geology.

### **2. Global marine $^{187}\text{Os}/^{188}\text{Os}$ isotope stratigraphy reveals the interaction of volcanism and ocean circulation during Oceanic Anoxic Event 2**

The following sections provide a summary of Chapter 2 (Marine  $^{187}\text{Os}/^{188}\text{Os}$  isotope stratigraphy reveals the interaction of volcanism and ocean circulation during

Oceanic Anoxic Event 2) and Chapter 3 (Pacific  $^{187}\text{Os}/^{188}\text{Os}$  isotope chemistry and U-Pb geochronology: Implications for global synchronicity of OAE 2) combined.

### *2.1. Introduction*

High-resolution osmium (Os) isotope stratigraphy across the Cenomanian-Turonian Boundary Interval (CTBI) from 8 sections for five transcontinental settings has produced a record of seawater chemistry that demonstrates regional variability as a function of terrestrial and hydrothermal inputs, revealing the impact of palaeoenvironmental processes. Marine  $^{187}\text{Os}/^{188}\text{Os}$  isotope stratigraphy in seawater changes as a function of 2 end-members mixing (Peucker-Ehrenbrink and Ravizza, 2000). As a result, the initial  $^{187}\text{Os}/^{188}\text{Os}$  ( $\text{Os}_i$ ) record has distinct variation, which can be directly linked to ocean inputs: radiogenic Os from weathering of ancient continental material and unradiogenic Os from juvenile (submarine) hydrothermal input (Peucker-Ehrenbrink and Ravizza, 2000).

Herein, the  $\text{Os}_i$  profile of 8 selected sites (Fig. 5.1): Portland #1 core, USA (WIS; ratified bed-by-bed correlation to GSSP Pueblo); ODP Site 1260, Demerara Rise (proto-North Atlantic); Wunstorf, Germany (NW European shelf); Vocontian Basin, SE France (Western Tethys); Furlo, Italy (Western Tethys); DSDP Site 530, Angola Basin (proto-South Atlantic); Yezo Group (YG), Japan (west proto-Pacific); and the Great Valley Sequence (GVS), USA (east proto-Pacific) demonstrate the interaction of the 2 end-members and their effects on seawater chemistry during the OAE 2.

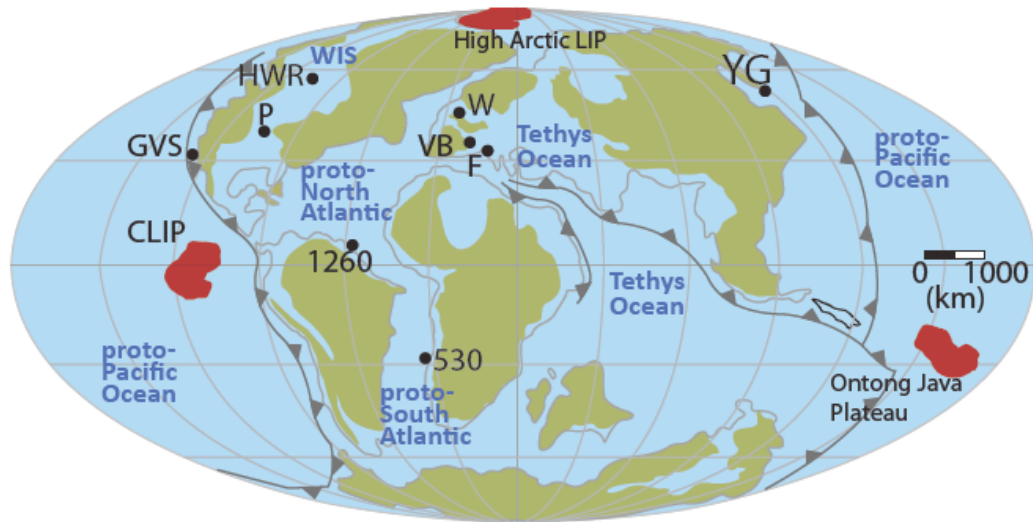


**Figure 5.1 Palaeomap of the late Cretaceous.** The sites analysed in this thesis are; P – Portland #1 Core, GVS – California, 1260 – ODP Site 1260 Demerara Rise, 530 – DSDP Site 530, W – Wunstorf, VB- Vocontian Basin, F – Furlo, YG – Japan, HWR – Canada (Appendix). The location of the Caribbean (CLIP) and High Arctic Large Igneous Province, and the Ontong Java Plateau is marked on in red.

The OAE 2 occurs as a result of a turbulent time in the ocean and atmosphere systems, which led to perturbations in the carbon cycle and during extreme intervals led to oceanic anoxic events, i.e., the OAE 2 (Jenkyns, 1980; Schlanger et al., 1987). Prior to OAE 2 atmospheric and sea surface temperatures were very high ( $\geq 33^{\circ}\text{C}$ ), which reduced the meridional temperature gradient (Jenkyns et al., 2004; Forster et al., 2007). As a result of globally higher temperatures the hydrological cycle accelerated and resulted in increased rates of continental weathering (Jenkyns, 2010). Simultaneously submarine volcanic activity at the Caribbean LIP initiated, which increased the influx of nutrients and altered the chemical composition of the seawater.

The global synchronicity of OAE 2 is a supposition of work that has previously focussed on sites from the North Atlantic, WIS and Tethyan regions. Hitherto this study the analysis of OAE 2 sections in the proto-Pacific was limited and consequently the global correlation of OAE 2 is not necessarily founded by

evidence but more broadly assumed. Therefore this study aimed to determine the true extent of OAE 2 and thus the implications of proto-Pacific circulation. In addition,  $^{206}\text{Pb}/^{238}\text{U}$  zircon geochronology was applied to from 5 volcanic tuff horizons from the YG section, Japan, to facilitate correlation to the Portland #1 core and integrate a temporal framework to quantitatively evaluate the timing and duration of events across the CTBI.

## 2.2. *Temporal framework*

An integrated timescale model is developed based on the Bayesian stratigraphy from the Portland #1 core (Meyers et al., 2012), which is the representative core for the GSSP Pueblo, ratified by bed-by-bed correlation (Sageman et al., 2006). The  $^{206}\text{Pb}/^{238}\text{U}$  zircon ages from the YG section are applied to verify an integrated timescale model for the Pacific, which highlights the non-correlative perturbations in the YG that are a function of a variable sedimentation rate. The timescale is utilised to derive the timing of the onset of OAE 2 (~94.38 Ma) relative to the CTB ( $93.90 \pm 0.15$  Ma), and to determine the timing of the onset of OAE 2 relative to the onset of activity at the Caribbean LIP. Furthermore, the synchronicity of the unradiogenic  $\text{Os}_i$  profile suggests that the magnitude of Caribbean LIP volcanism was sufficient to attenuate continental inputs and simultaneously influence the seawater chemistry of each basin; the abundance of organic-rich sediments added to the water column as a result of enhanced continental weathering permitted sequestration of hydrogenous unradiogenic Os from the contemporaneous Caribbean LIP.

### 2.3. Implications of $^{187}\text{Os}/^{188}\text{Os}$ profiles

In every section the  $^{187}\text{Os}/^{188}\text{Os}$  profiles show a comparable trend, despite minor non-correlative perturbations, that is characteristic of OAE 2 sections; radiogenic values in the lead up to OAE 2; an abrupt unradiogenic trend at the onset of OAE 2; an unradiogenic interval during the first part of OAE 2; and a return to radiogenic values towards the end of the event, above the CTB. The unradiogenic trend in  $^{187}\text{Os}/^{188}\text{Os}$  is synchronous in all sections, with the exception of GVS. Therefore the  $\text{Os}_i$  data demonstrate the impact of inputs from continental weathering and hydrothermal input. The distinct and sudden transition from radiogenic to unradiogenic Os, is indicative to the onset of volcanic activity at the Caribbean LIP, and is contemporaneous with the onset of OAE 2. Previous work suggests that activity of the Caribbean LIP was possibly an instigator of anoxia in the oceans (Turgeon and Creaser, 2008).

The  $\text{Os}_i$  profile at Portland #1 core records a brief shift to high radiogenic  $^{187}\text{Os}/^{188}\text{Os}$  values in the Western Interior Seaway before the onset of OAE 2. It is suggested that the epeiric seaway was decoupled from the open ocean and the restriction amplified the effects of high weathering rates as abundant organic-rich sediments sequestered radiogenic Os derived from the ancient continental crust. The YG section records similar time correlative radiogenic  $\text{Os}_i$  trends in the pre-OAE 2 interval, which are inferred to be the result of basin restriction and cause local variation in seawater chemistry. The evaluation of this trend suggests that a combination of factors collectively played critical roles in the initiation of OAE 2; differential input of nutrients from continental and volcanogenic sources, coupled with efficient palaeocirculation of the global ocean and epeiric seas, enhanced productivity due to higher nutrient availability, which permitted

penecontemporaneous transport of continental and LIP-derived nutrients to transcontinental basins.

The close similarity of  $Os_i$  profiles from ~50 kyr prior to the OAE 2 and throughout the syn-OAE 2 interval indicates that transgression progressed to a point where a homogeneous global seawater signal was delivered to multiple proto-transcontinental basins by active ocean circulation. Hence, it is proposed that the combined consequence of nutrients from continental weathering and hydrothermalism conditioned the oceans and helped trigger OAE 2 through an increase in productivity, with the late Cenomanian transgression being the tipping point for the development of widespread anoxia.

With regard to the GVS, despite showing the same overall trend in the  $Os_i$  profile, the sequence records high frequency oscillations compared to all other sections. The perturbations are indicative to rapidly alternating inputs; inputs from the continent are sequentially attenuated by transient inputs from the Caribbean LIP, which demonstrate the sensitivity of the Os isotope composition in seawater on the order of the residence time ( $\leq 10$  kyr). In addition, the proximity of the GVS to the Caribbean LIP has the potential to reveal the extent of activity at the LIP; combined with the application of the integrated timescale the temporal coincidence provides empirical evidence that the duration of volcanic activity at the Caribbean LIP was ~450 kyr.

The  $Os_i$  data from the Portland #1 core, Wunstorf, Vocontian Basin, Site 530, YG and GVS support the findings from Site 1260 and Furlo (Turgeon and Creaser, 2008) with regard to the synchronicity of the unradiogenic  $Os_i$  trend, indicative to activity from the Caribbean LIP. However, additional analysis of samples from Site 1260 and Furlo combined with the 6 new sections (Fig. 5.1) illustrates the

significance of the pre-OAE 2 interval, and the transgression that facilitates ocean circulation, which led to the widespread distribution of nutrients from weathering and volcanism combined that instigated ocean anoxia.

Consequently, despite regional variation, the putative seawater record remains robust; radiogenic Os suppressed by unradiogenic Os for ~200 kyr before seawater returned to radiogenic equilibrium. Hence the evidence from  $Os_i$  isotope stratigraphy, from the Atlantic, WIS, Tethys and Pacific sections constrained by new U-Pb zircon geochronology (YG section), ascertains that the OAE 2 was a globally isochronous event.

#### *2.4. Revised correlation and application of $^{187}Os/^{188}Os$ isotope stratigraphy*

The onset of OAE 2 at the YG was previously identified by the putative positive excursion in the  $\delta^{13}C$  isotope record; however, this does not correlate with the new high-resolution  $Os_i$  isotope stratigraphy. The  $^{206}Pb/^{238}U$  zircon ages (HK017  $94.436 \pm 0.093/0.14$  Ma and HK018  $93.920 \pm 0.031/0.11$  Ma) facilitate correlation and consequently I revise the onset of the OAE 2 and, in addition, the stratigraphic position of the CTB (see figures Chapter 3). The revised onset of OAE 2 is synchronous with the unradiogenic trend in the  $Os_i$  profile, and therefore contemporaneous with volcanic activity at the Caribbean LIP, which is consistent with all  $Os_i$  profiles from the Atlantic, WIS and Tethys basins (i.e. Chapter 2). The application of an OxCal age-depth model (Bronk Ramsey, 2008) justifies the correlation of the  $Os_i$  profiles from the YG and Portland #1 core, and the improved correlation of the proto-Pacific across the CTB has created a nominal correlation to the GSSP in the WIS.

### ***3. Calcium isotope stratigraphy across the Cenomanian-Turonian OAE 2: Implication on the controls of marine Ca isotope composition***

#### ***3.1. Introduction: Isotopic proxies and the OAE 2***

Chapter 4 presents  $\delta^{44}\text{Ca}$  data from 4 globally correlated OAE 2 sections; Portland #1 core, USA, Pont d'Issole section, SE France, and the Yezo Group section, Japan. As well as re-analysed data, for direct comparison with the  $\delta^{44}\text{Ca}$  data from this study, from the Eastbourne section, UK, previously reported by Blättler et al. (2011).

The OAE 2 has been studied in detail utilising multiple isotope proxies, e.g.,  $\delta^{13}\text{C}$ , Nd, U, Pb, P, Sr, Os, Li, and trace metals (Schlanger et al., 1987; Kerr, 1998; McArthur, et al., 2004; Snow et al., 2005; MacLeod et al., 2008; Turgeon and Creaser, 2008; Jenkyns, 2010; Montoya-Pino et al., 2010; Kuroda et al., 2011; Mort et al., 2011; Martin et al., 2012; Pogge von Strandmann et al., 2013; Zheng et al., 2013; Du Vivier et al., 2014). As discussed above in section 2.3, the overall interpretation of these isotope records suggests that global warming prior to the OAE 2 enhanced weathering, which led to  $\text{CO}_2$  drawdown, increased productivity and an abundance of organic-rich material. As such the oxygen minimum zone expanded and the onset of activity at submarine LIPs introduced more nutrients and  $\text{CO}_2$  to the seawater, which further increased the extent of the oxygen minimum zone and subsequently the sequestration of elements into organic-rich sediments. Global transgression was the tipping point for the development of widespread, global anoxia.

A recent addition to the proxy catalogue assessing palaeoclimate conditions during the CTBI is marine Ca. Ca is a key element involved in the long-term carbon cycle since its mobility allows for elemental transfer through geochemical reservoirs

coupled with carbon to and from the ocean. As a result Ca has the potential to record the variability of seawater chemistry as a result of perturbations to the ocean and atmosphere system during intervals of climatic instability, which influence carbonate sedimentary successions.

Multiple studies have aimed to establish the factors affecting the marine  $\delta^{44}\text{Ca}$  system (De La Rocha and DePaolo, 2000; DePaolo, 2004; Gussone et al., 2003, 2005, 2006; Böhm et al., 2006, 2009; Farkaš et al., 2007a, 2007b; Griffith et al., 2008; Fantle, 2010; Blättler et al., 2012; Holmden et al., 2012; Fantle and Tipper, 2013). The systematics of marine  $\delta^{44}\text{Ca}$  isotopes are, like many isotopes, associated with the inputs and outputs; riverine and hydrothermal inputs versus carbonate precipitation outputs. Conversely, unlike many isotopes (noted above) the variation in  $\delta^{44}\text{Ca}$  values cannot be determined through simple end-member mixing. The end-members lack isotopic leverage to differentiate between the sources of the inputs ( $-0.95\text{‰}$  for hydrothermal and  $-1.03\text{‰}$  for riverine; Holmden et al., 2012). The flux of inputs during the CTBI was higher than normal as a result of the climate perturbation. Therefore based on observations and interpretation from a number of aforementioned isotopes this study aimed to determine if the dramatic unradiogenic trend in  $\text{Os}_i$  associated with volcanism at the Caribbean LIP (reported in Chapters 2 and 3) is recorded by  $\delta^{44}\text{Ca}$  values, or if I can quantify the increase in flux of riverine Ca due to weathering as previously proposed (Blättler et al., 2011). The aim is to constrain the principal factor that is influencing the evolution of marine  $\delta^{44}\text{Ca}$  chemistry across the OAE 2.

### 3.2. *Qualitative observations and implications*

A previous study infers a negative excursion coincident with the onset of OAE 2, which suggests it is associated with an elevated weathering flux (Blättler et al., 2011). The  $\delta^{44}\text{Ca}$  values from this study show a positive excursion concurrent with the onset of OAE 2 at Portland and Pont d'Issole, which contradicts the inferred negative excursion at Eastbourne (Blättler et al., 2011). In this study I re-analysed select samples across the onset of OAE 2 from Blättler et al.'s (2011) record. The  $\delta^{44}\text{Ca}$  values show a subtle excursion and permit direct comparison with our  $\delta^{44}\text{Ca}$  values from Portland Pont d'Issole; the negative excursion is not an analytical artefact of the different analytical techniques. The analyses from the Yezo Group section do not produce a differentiable trend in the  $\delta^{44}\text{Ca}$  values as a result of the extremely low abundance of carbonate, <1 wt.%. Therefore it is unlikely that the  $\delta^{44}\text{Ca}$  values from the Yezo Group represent a robust seawater signal.

The observed positive trend in the  $\delta^{44}\text{Ca}$  values from Portland and Pont d'Issole is synchronous with the onset of OAE 2, which is interpreted by many other isotopes and trace metals as a record of hydrothermal activity contemporaneous with OAE 2, derived from volcanic activity at the Caribbean or High Arctic LIP (Schlanger et al., 1987; Kerr, 1998; McArthur, et al., 2004; Snow et al., 2005; MacLeod et al., 2008; Turgeon and Creaser, 2008; Jenkyns, 2010; Montoya-Pino et al., 2010; Kuroda et al., 2011; Mort et al., 2011; Martin et al., 2012; Pogge von Strandmann et al., 2013; Zheng et al., 2013; Du Vivier et al., 2014). In addition, significant enrichment of Ca in seawater by sublimation compared to exsolved Sr from fumarolic condensates may be indicative to Ca and Sr temporally decoupling adjacent to hydrothermalism. However, despite the qualitative observations and

temporal agreement, quantitative analysis is indicative of other factors contributing to the evolution of marine  $\delta^{44}\text{Ca}$  composition.

### 3.3. *Quantitative observations and implications*

In order to quantitatively verify the main factor influencing the  $\delta^{44}\text{Ca}$  composition and to resolve the discrepancy in the interpretation between the data in this study and in the previous record (Blättler et al., 2011), I utilised a seawater mixing model. Unlike Blättler et al. (2011), I apply modern parameters (Milliman, 1993; Holmden et al., 2012) and solve the equations analytically and numerically (for comparison) under non-steady-state. Figure 5.2 shows the discrepancy between model calculations. Blättler et al. (2011) numerically derived a curve to simulate  $\delta^{44}\text{Ca}$  composition in seawater, with combined inputs and at a fixed residence time, which I model using the modern parameters (Fig. 5.2, blue curve). However, if I numerically solve the equation, with combined inputs while allowing  $\tau_{\text{Ca}}$  to vary as  $N_{\text{Ca}}$  varies (Fig. 5.2, green curve); the output matches our analytically derived curve (Fig. 5.2, red curve). The analytical models show that in a non-steady-state model, instantaneously increasing an input flux must decrease residence time for a given initial reservoir size in order to maintain mass balance. The only real difference between steady-state and non-steady-state approaches to modelling the Ca isotope evolution of seawater is that the former assumes instantaneous shifts in  $\tau_{\text{Ca}}$  (or  $N_{\text{Ca}}$ ), whereas the latter allows  $\tau_{\text{Ca}}$  and  $N_{\text{Ca}}$  to change with time until steady-state occurs.

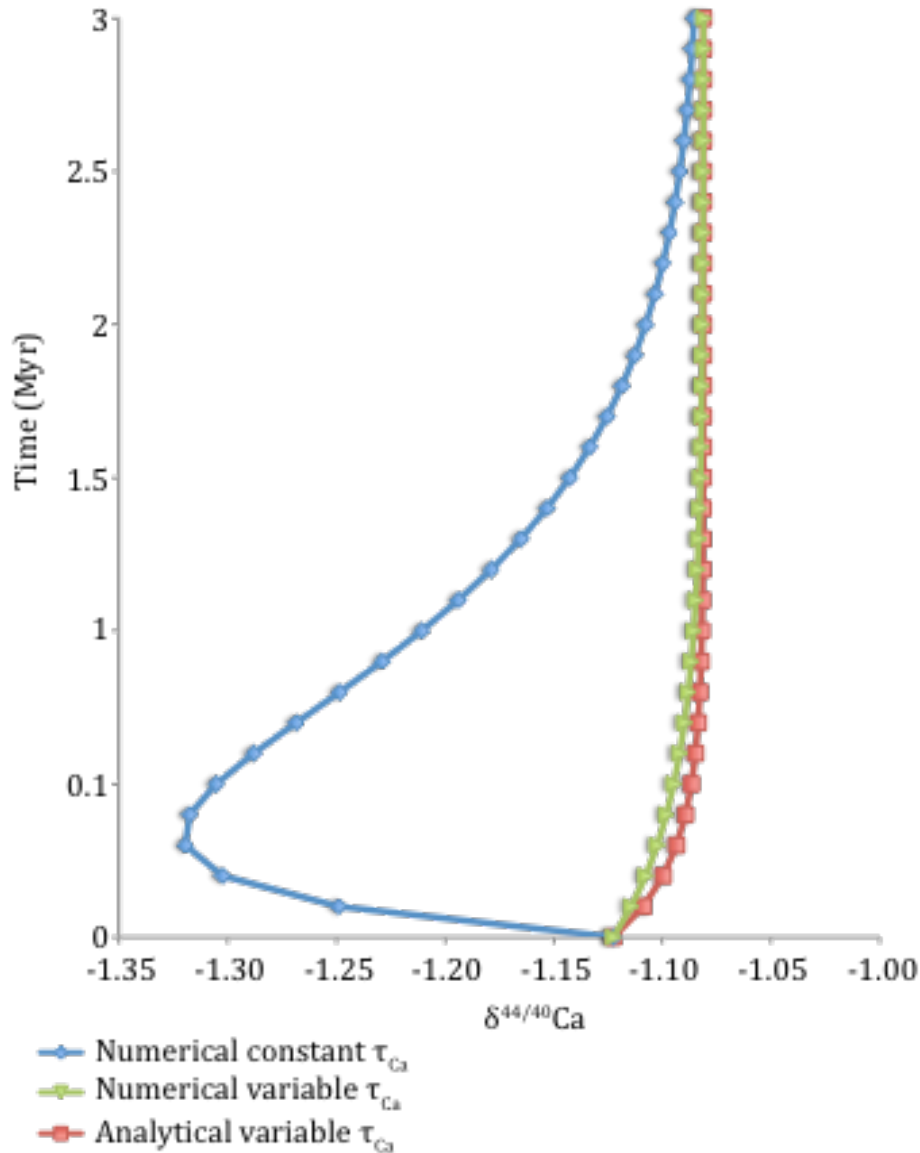


**Figure 5.2 shows analytical vs. numerically derived curves.** The blue curve slightly differs from the model results presented in Blättler et al. (2011) because I adopted different input parameters, but the overall pattern is identical.

The models simulate steady-state and 3 other scenarios of varying inputs to the ocean (see Fig. 4.7 Chapter 4). A – steady-state, B – increased hydrothermal influx ( $F_H$ ), C – increased riverine influx ( $F_R$ ), and D – change in carbonate fractionation factor ( $\Delta_C$ ). The models for B and C show no appreciable change in response to increased  $F_H$  and/or  $F_R$  since the behaviour exhibited by the modelled curves is dissimilar to the  $\delta^{44}\text{Ca}$  records at Portland and Pont d’Issole. As such,

despite the qualitative observations based on isotopic records indicative of a globally contemporaneous injection of volcanic activity at the onset of OAE 2, analytically quantitative evidence confirms that if Ca and Sr are coupled based on their similar geochemical characteristics, an increase in  $F_H$  and/or  $F_R$  is not driving the  $\delta^{44}\text{Ca}$  composition in seawater. The modelled  $\delta^{44}\text{Ca}$  curves suggest that the most tenable explanation for the variation in  $\delta^{44}\text{Ca}$  values is a change in  $\Delta_C$ .

However, the  $\Delta_C$  is a function of other variables, which need to be constrained and understood before interpretation of the marine  $\delta^{44}\text{Ca}$  isotope system can be made. Primarily the  $\Delta_C$  varies depending on carbonate precipitation. From this study I suggest that the Ca:CO<sub>3</sub> ratios in seawater may have increased due to enhanced Ca inputs as well as elevated dissolved CO<sub>2</sub>, associated with an increased  $F_H$ , which lead to ocean acidification, which caused carbonate dissolution. Therefore an increased  $F_H$  is not directly recorded by the  $\delta^{44}\text{Ca}$  values, as the modelled data shows. However, they respond to the decrease in carbonate precipitation due to ocean acidification and therefore a change in the  $\Delta_C$ .

Finally, I surmise that the discrepancy between the trends in  $\delta^{44}\text{Ca}$  values from this study versus the previous study (Blättler et al., 2011) may have been caused by the contrasting stratigraphy; Portland and Pont d'Issole are more varied and marl-rich, whereas Eastbourne and South Ferriby are predominately chalk-rich with sparsely interbedded marl-rich horizons. Given that the  $\Delta_C$  is a function of carbonate precipitation, it seems tenable that the changeable  $\Delta_C$  is determined by the mineralogical composition of the different lithological sequences, which are a function of the regional seawater chemistry. Herein, I suggest that the marine  $\delta^{44}\text{Ca}$  profiles are regionally disparate on a global scale as a function of varying  $\Delta_C$ .

#### 4. Future research and implications

The data recorded in this thesis has shown the utilisation of Os isotope stratigraphy as a reliable palaeoproxy. The  $Os_i$  profiles are valuable correlation tools and record regional and global variation in seawater chemistry on the order of Os residence time. The extent of regional variability and what factors influence local variation is an area for future research, which should aim to investigate the open ocean basins compared to restricted ocean basins; for example the Angus Core, WIS, USA; Tarfaya Core, proto-North Atlantic; and the Eagleford Core, WIS, USA (Fig. 5.3).

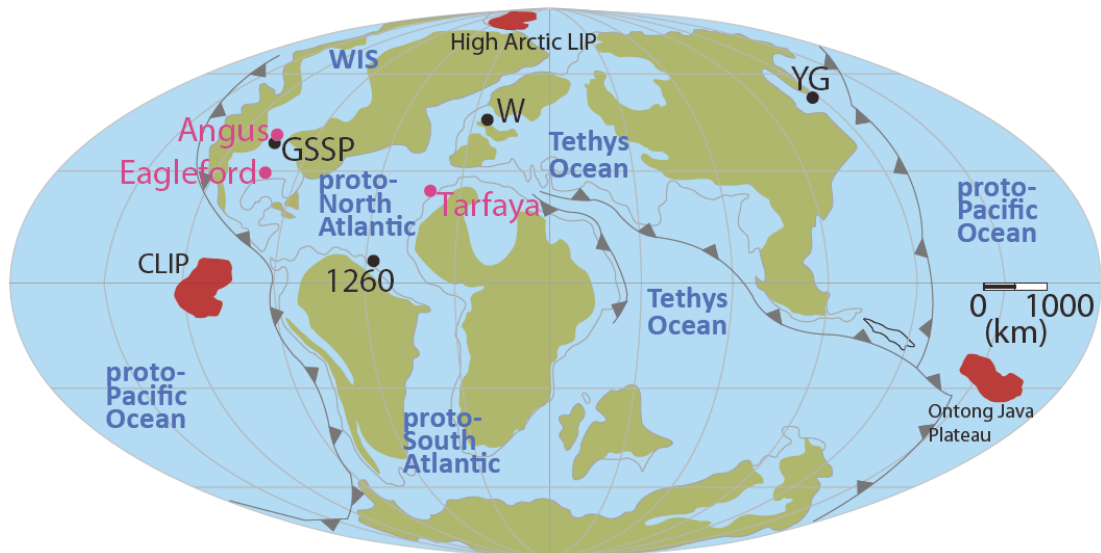


**Figure 5.3 Palaeomap of the late Cretaceous, sites proposed for future work are in pink.** Angus and Eagleford Cores in the WIS, Tarfaya Core in the proto-North Atlantic. GSSP – illustrates the proximity of the GSSP Pueblo (Portland #1 Core) to the Angus Core. 1260 – ODP Site 1260, Demerara Rise, W – Wunstorf, and YG – Yezo Group, Japan are left on for reference. The location of the Caribbean (CLIP) and High Arctic Large Igneous Province, and the Ontong Java Plateau are marked on in red.

The application of Os as a palaeoproxy to additional sites will improve our understanding of Re-Os systematics in open and restricted ocean basins. Based on the disparate  $Os_i$  isotope profiles of Portland #1 core and Site 1260 for ~200 kyr before the onset of OAE 2, the  $Os_i$  profiles will either support, or not, the conclusion

that epeiric sea  $Os_i$  records (e.g., Portland #1 core) are decoupled from deep/open ocean  $Os_i$  records and may be more strongly influenced by local weathering inputs and changes in mixing between basins. Thus further study of other cores in the same setting (i.e., Angus Core and Eagleford Core in the WIS; Fig. 5.3) will empirically determine if the regional differences in  $Os_i$  are robust. The Eagleford in particular, which is located at the south (the opening *per se*) of the WIS, could determine the extent of basin restriction in the WIS if the  $Os_i$  record was indicative to high continental inputs driving the radiogenic Os signal until transgression relieved basin restriction. Alternatively, if the  $Os_i$  record showed that seawater chemistry was susceptible to fluctuations analogous to the  $Os_i$  profile of the GVS, important implications on regional palaeocirculation may be inferred given the proximity to the Caribbean LIP.

The  $^{187}Os/^{188}Os$  isotope composition of Site 1260 is regarded as a record for an open ocean site and frequently analysed to determine circulation using  $\epsilon_{Nd}$  isotopes. Additional analysis of the Tarfaya Core, for example, will provide further implications on palaeocirculation as well as Os residence time. Similarly Site 530 is an open ocean section, yet due to poor core recovery the sample resolution in the pre-OAE 2 interval is limiting. An important oceanographic parameter of circulation is basin depth; further study within the WIS and the North Atlantic may result in comparatively heterogeneous  $Os_i$  records relative to the sites in similar settings from this study. Consequently the discontinuity of  $Os_i$  profiles within the basins may be indicative of poor vertical mixing of  $^{187}Os/^{188}Os$  in seawater.

This study has verified that submarine volcanic activity is globally contemporaneous with the OAE 2. Herein, I infer that the unradiogenic Os is

derived from the Caribbean LIP. Most recently however, activity from the High Arctic LIP has been implicated as contemporaneous with OAE 2 (Fig. 5.3). But the constraints on timing and duration of activity are very broad to-date, spanning 130 – 80 Ma, and in the most part suggest that the main pulse of activity occurred before the late Cretaceous (Tegner et al., 2011): why is this activity not recorded in  $Os_i$  record throughout the Cenomanian? Currently preliminary  $Os_i$  records from the Arctic (Greenland) confirm contemporaneous volcanic activity, synchronous with  $Os_i$  records from this study (Herrle et al., *EGU abs.* 2014). Therefore the extent of dispersion of unradiogenic Os associated with submarine volcanism is global across latitude, as well as longitude. If activity from the High Arctic can be constrained the impact on seawater chemistry caused by the main pulses of activity will have implications on circulation, particularly in the WIS.

Development of  $^{187}Os/^{188}Os$  isotope stratigraphy combined with U-Pb zircon geochronology of the YG section from this study demonstrates the application of  $Os_i$  as a palaeoproxy to transcontinental sections; where the onset of the OAE 2 and the CTB are revised. Future work ought to focus on improving the resolution of biostratigraphy and to develop the catalogue of chemostratigraphic proxies. The addition of higher precision and higher resolution U-Pb zircon ID-TIMS geochronology, compared to what was previously available for Pacific OAE 2 sections, provides a foundation of data that has the potential to establish the YG section as a proposed reference section for the CTBI in the Pacific Ocean.

The  $\delta^{44}Ca$  values produced in this study indicate that a change in fractionation factor is the principal factor influencing the evolution of  $\delta^{44}Ca$

composition in seawater. I suggest that the fractionation factor is a function of ocean acidification associated with increased volcanic activity during the CTBI from LIPs. I also briefly discuss a number of other factors, temperature, lithology, diagenesis, which have been suggested to influence the variability of  $\delta^{44}\text{Ca}$  values. As such there is a large scope for more research utilising this proxy, for example, from sections adjacent to a hydrothermal source and/or a riverine source, also from sections out with the temperate zone of the Northern Hemisphere.

### ***5. Application of $^{187}\text{Os}/^{188}\text{Os}$ isotope stratigraphy to petroleum geology***

In addition to the implications of OAE 2 and the relationships between palaeocirculation and submarine volcanism, the  $\text{Os}_i$  isotope stratigraphy presented here may facilitate source-oil correlation for OAE 2 sections that have generated oil.

Oil is derived from organic-rich source rocks, similar to the organic-rich sediments (ORS) of the OAE 2 horizons. The  $\text{Os}$  isotope composition is inherited from the source rock and captured in the oil at the time of maturation and transferred to the generated oil (Selby and Creaser, 2005, Selby et al., 2005, 2007; Finlay et al., 2010; Rooney et al., 2012). Over time oil migrates to new horizons. As discussed above, and in Chapters 2 and 3, the OAE 2 interval possesses distinct  $\text{Os}_i$  profiles. In addition, as a result of the units Re-Os abundances and variable  $\text{Os}_i$  isotope composition, the OAE 2 interval will continue to possess a distinct profile at the time of oil generation if oil is derived from the ORS (Fig. 5.4).

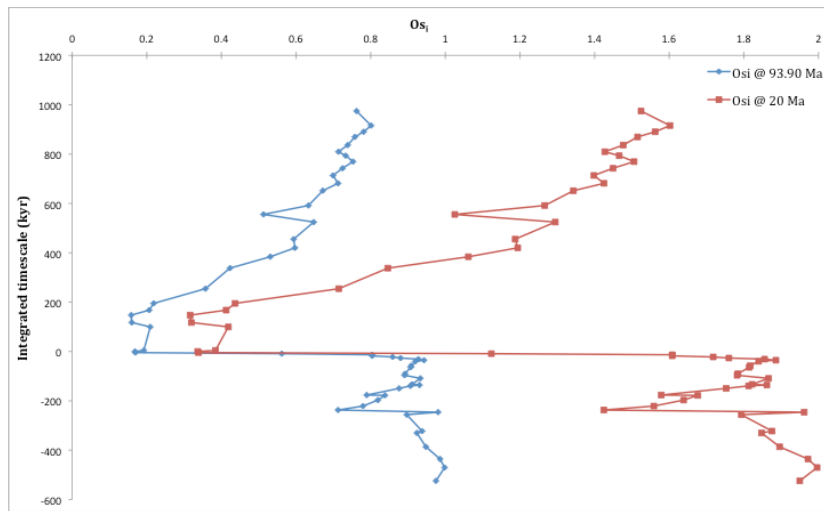


**Figure 5.4 Distinct  $Os_i$  isotope profile of CTBI and after radiogenic growth.**  $Os_i$  profile at 93.90 Ma (blue) and at 20 Ma (red) vs. integrated timescale (kyr).

Figure 5.4 illustrates the distinct  $Os_i$  profile of the CTBI. As such if I consider that ORS of the OAE 2 underwent thermal maturation  $\sim 70$  Myr after deposition, the distinct  $Os_i$  profile at  $\sim 93.90$  Ma (blue) remains intact at  $\sim 20$  Ma (red). The trend in  $Os_i$  data will be identical yet more radiogenic as a result of radiogenic growth. Consequently the unradiogenic  $Os$  isotope composition in oils from the basal OAE 2 will be distinct from the majority of all oils generated from other Cretaceous ORS as the  $Os_i$  is commonly radiogenic,  $>0.5$  (see Peucker-Ehrenbrink and Ravizza, 2000; Gradstein et al., 2012), thus over time generating oils with  $Os_i > 1.0$  (Fig. 5.4) such as before and after the OAE 2 interval (Finlay et al., 2011).

Furthermore, due to the unradiogenic initial,  $\sim 0.12$  (close to chondritic values) and low  $Re/Os$  at the onset and for  $\sim 200$  kyr of OAE 2, the  $Os_i$  at  $\sim 20$  Ma will remain unradiogenic (Fig. 5.4). The syn-OAE 2 period coincides with organic preservation during sediment accumulation of ORS, therefore if this interval is to generate oil the oil will have an exclusive unradiogenic composition unlike the  $Os_i$

values of the pre-OAE 2 interval and after ~200 kyr of the syn-OAE 2 interval. This hypothesis could also be applied to similar records from OAE 1a (Bottini et al., 2012), which may also be a useful tool for fingerprinting oil to its source. As such, oils from an unknown source can be linked using the Os isotope composition, a process known as fingerprinting (Finlay et al., 2011). For example, the Os isotope stratigraphy of Site 530, from the Angola Basin, South Atlantic could be combined with Re-Os oil geochronology and applied to evaluate the evolution of oils and facilitate mapping of the petroleum systems in the Angola Basin.

## REFERENCES

- Blättler, C. L., Jenkyns, H. C., Reynard, L. M., Henderson, G. M., 2011. Significant increases in global weathering during Oceanic Anoxic Events 1a and 2 indicated by calcium isotopes. *Earth Planet. Sci. Letts.* 309, 77-88.
- Blättler, C.L., Henderson, G.M., Jenkyns, H.C., 2012. Explaining the Phanerozoic Ca isotope history of seawater. *Geology* 40, 843-846.
- Böhm, F., Gussone, N., Eisenhauer, A., Dullo, W-C., Reynaud, S., Paytan, A., 2006. Ca isotope fractionation in modern corals. *Geochim. Cosmochim. Acta* 70, 4452–4462.
- Böhm, F., Eisenhauer, A., Rausch, S., Bach, W., & Klügel, A., 2009. Calcium isotope systematics of low temperature alteration carbonates in the ocean crust. *Geochim. Cosmochim. Acta* 71, 2524-2546.
- Bottini, C., Cohen, A. S., Erba, E., Jenkyns, H. C., & Coe, A. L., 2012. Osmium-isotope evidence for volcanism, weathering, and ocean mixing during the early Aptian OAE 1a. *Geology*, 40(7), 583-586.
- Bronk Ramsey, C., 2008. Deposition models for chronological records. *Quaternary Science Reviews* 27, 42-60.
- De La Rocha, C.L., DePaolo, D.J., 2000. Isotopic evidence for variations in the marine calcium cycle over the Cenozoic. *Science* 289, 1176–1178.
- DePaolo, D.J., 2004. Calcium isotopic variations produced by biological, kinetic, radiogenic and nucleosynthetic processes. *Rev. Mineral. Geochem.* 55, 255–288.
- Du Vivier, A.D.C., Selby, D., Sageman, B.B., Jarvis, I., Grocke, D.R., Voigt, S., 2014. Marine  $^{187}\text{Os}/^{188}\text{Os}$  isotope stratigraphy reveals the interaction of volcanism and

- ocean circulation during Oceanic Anoxic Event 2. *Earth Planet. Sci. Lett.* 389, 23-33.
- Fantle, M.S., 2010. Evaluating the Ca isotope proxy. *Am. J. Sci.* 310, 194–230.
- Fantle, M.S., Tipper, E.T., 2013. Calcium isotopes in the global biogeochemical Ca cycle: Implications for development of a Ca isotope proxy. *Earth-Science Reviews* doi:10.1016/j.earscirev.2013.10.004
- Farkaš, J., Böhm, F., Wallmann, K., Blenkinsop, J., Eisenhauer, A., Van Geldern, R., Veizer, J., 2007b. Calcium isotope record of Phanerozoic oceans: Implications for chemical evolution of seawater and its causative mechanisms. *Geochim. Cosmochim. Acta* 71(21), 5117-5134.
- Farkaš, J., Buhl, D., Blenkinsop, J., Veizer, J., 2007a. Evolution of the oceanic calcium cycle during the late Mesozoic: Evidence from  $\delta^{44/40}\text{Ca}$  of marine skeletal carbonates. *Earth Planet. Sci. Lett.* 253(1), 96-111.
- Finlay, A.J., Selby, D., Osborne, M.J., 2011. Re-Os geochronology and fingerprinting of United Kingdom Atlantic margin oil: Temporal implications for regional petroleum systems. *Geology* 39(5), 475-478.
- Finlay, A.J., Selby, D., Osborne, M.J., Finucane, D., 2010. Fault charged mantle-fluid contamination of U.K. North Sea oils: Insights from Re-Os isotopes: *Geology* 38, 979–982 doi: 10.1130/G31201.1.
- Forster, A., Schouten, S., Moriya, K., Wilson, P.A., Sinninghe Damsté, J.S., 2007. Tropical warming and intermittent cooling during the Cenomanian/Turonian oceanic anoxic event 2: Sea surface temperature records from the equatorial Atlantic. *Paleoceanography*, 22, PA1219. doi:10.1029/2006PA001349.
- Gradstein, F.M., Ogg, J.G., Schmitz, M., eds., 2012. *The Geologic Time Scale 2012*, 2-volume set. Elsevier.
- Griffith, E.M., Paytan, A., Kozdon, R., Eisenhauer, A., Ravelo, A.C., 2008, Influences on the fractionation of calcium isotopes in planktonic foraminifera: *Earth and Planetary Science Lett.* 268, 124–136, doi:10.1016/j.epsl.2008.01.006
- Gussone, N., Eisenhauer, A., Heuser, A., Dietzel, M., Bock, B., Böhm, F., Spero, H.J., Lea, D.W., Buma, J., Nägler, T.F., 2003. Model for kinetic effects on calcium isotope fractionation ( $\delta^{44}\text{Ca}$ ) in inorganic aragonite and cultured planktonic foraminifera. *Geochim. Cosmochim. Acta* 67, 1375–1382.
- Gussone, N., Böhm, F., Eisenhauer, A., Dietzel, M., Heuser, A., Teichert, B.M.A., Reitner, J., Worheide, G., Dullo, W-C., 2005. Calcium isotope fractionation in calcite and aragonite. *Geochim. Cosmochim. Acta* 69, 4485-4494.

- Gussone, N., Langer, G., Thoms, S., Nehrke, G., Eisenhauer, A., Riebesell, U., Wefer, G., 2006. Cellular calcium pathways and isotope fractionation in *Emiliania huxleyi*. *Geology* 34, 625–628.
- Herrle, J., Schröder-Adams, C., Selby, D., Du Vivier, A., Flögel, S., McAnena, A., Davis, W., Pugh, A., Galloway, J., Hofmann, P., Wagner, T. High Arctic Paleoenvironmental and paleoclimatic changes in the Mid-Cretaceous. *Geophysical Research Abstracts*, EGU General Assembly 2014.
- Holmden, C., Papanastassiou, D.A., Blanchon, P., Evans, S., 2012.  $\delta^{44/40}\text{Ca}$  variability in shallow water carbonates and the impact of submarine groundwater discharge on Ca-cycling in marine environments. *Geochim. Cosmochim. Acta* 83, 179–194.
- Jenkyns, H.C., 1980. Cretaceous anoxic events: from continents to oceans. *J. Geol. Soc. London* 137, 171–188.
- Jenkyns, H.C., 2010. Geochemistry of oceanic anoxic events. *Geochem. Geophys. Geosys.* 11(3).
- Jenkyns, H.C., Forster, A., Schouten, S., Sinninghe Damste, J.S., 2004. High temperatures in the Late Cretaceous Arctic Ocean. *Nature* 432, 888 -892.
- Kerr, A.C., 1998. Oceanic plateau formation: a cause of mass extinction and black shale deposition around the Cenomanian–Turonian boundary? *J. Geol. Soc.* 155, 619-626.
- Kuroda, J., Tanimizu, M., Hori, R.S., Suzuki, K., Ogawa, N.O., Tejada, M.L., Ohkouchi, N., 2011. Lead isotopic record of Barremian–Aptian marine sediments: Implications for large igneous provinces and the Aptian climatic crisis. *Earth Planet. Sci. Lett.* 307, 126-134.
- MacLeod, K. G., Marin, E. E., Blair, S. W., 2008. Nd excursions across the Cretaceous oceanic anoxia event 2 (Cenomanian-Turonian) in the tropical North Atlantic. *Geology* 36, 811-814.
- Martin, E. E., MacLeod, K. G., Jimenez Berroco, A., Bourbon, E., 2012. Water mass circulation on Demerara Rise during the Late Cretaceous based on Nd isotopes. *Earth Planet. Sci. Lett.*, 327-328, 111-120.
- McArthur, J.M., Howarth, R.J., Bailey, T., 2004. Strontium isotope stratigraphy. In: Gradstein, F., Ogg, J., Smith, A., (Eds.) *A Geological Time Scale 2004*. Cambridge University Press, Cambridge, U.K., pp. 96–105.
- Meyers, S.R., Siewert, S.E., Singer, B.S., Sageman, B.B., Condon, D.J., Obradovich, J.D., Jicha, B.R., Sawyer, D.A., 2012. Intercalibration of radioisotopic and astrochronologic time scales for the Cenomanian-Turonian boundary interval, Western Interior Basin, USA. *Geology* 40, 7-10.
- Milliman J.D., 1993. Production and accumulation of  $\text{CaCO}_3$  in the ocean: budget of a non-steady state. *Global Biogeochem. Cy.* 7, 927–957.

- Mitchell, S.F., Ball, J.D., Crowley, S.F., Marshall, J.D., Paul, C.R., Veltkamp, C.J., Samir, A. 1997. Isotope data from Cretaceous chalks and foraminifera: Environmental or diagenetic signals? *Geology* 25, 691-694.
- Montoya-Pino, C., Weyer, S., Anbar, A.D., Pross, J., Oschmann, W., van de Schootbrugge, B., Arz, H.W., 2010. Global enhancement of ocean anoxia during Oceanic Anoxic Event 2: A quantitative approach using U isotopes. *Geology*, 38, 315-318.
- Mort, H. P., Adatte, T., Follmi, K. B., Keller, G., Steinmann, P., Matera, V., Berner, Z., Stüben, D., 2011. Phosphorus and the roles of productivity and nutrient recycling during Oceanic Anoxic Event 2. *Geology*, 35, 6; 483-486.
- Paul, C.R.C., Lamolda, M.A., Mitchell, S.F., Vaziri, M.R., Gorostidi, A., Marshall, J.D., 1999. The Cenomanian–Turonian boundary at Eastbourne (Sussex, UK): a proposed European reference section. *Palaeogeog. Palaeoclimatol. Palaeoecol.* 150, 83–122.
- Peucker-Ehrenbrink, B., Ravizza, G., 2000. The marine osmium isotope record. *Terra Nova* 12, 205-219.
- Pogge von Strandmann, P.A.P., Jenkyns, H.C., Woodfine, R.G., 2013. Lithium isotope evidence for enhanced weathering during Oceanic Anoxic Event 2. *Nature Geoscience*, 6, 668-672.
- Rooney, A.D., Selby, D., Lewan, M.D., Lillis, P.G., Houzay, J-P., 2012. Evaluating Re-Os systematics in organic-rich sedimentary rocks in response to petroleum generation using hydrous pyrolysis experiments. *Geochim. Cosmochim. Acta* 77, 275.
- Sageman, B.B., Meyers, S.R., Arthur, M.A., 2006. Orbital time scale and new C-isotope record for Cenomanian–Turonian boundary stratotype. *Geology* 34, 125–128.
- Schlanger, S.O., Arthur, M.A., Jenkyns, H.C., Scholle, P.A. 1987. The Cenomanian/Turonian Oceanic Anoxic Event, I. Stratigraphy and distribution of organic carbon-rich beds and the marine  $\delta^{13}\text{C}$  excursion. In: Brooks, J. & Fleet, A.J. (eds) *Marine Petroleum Source Rocks*. Geological Society London, Spec. Publ., 26, 371–399.
- Selby, D., Creaser, R.A., 2005. Direct radiometric dating of hydrocarbon deposits using rhenium-osmium isotopes: *Science* 308, 1293–1295, doi: 10.1126/science.1111081.
- Selby, D., Creaser, R.A., Dewing, K., Fowler, M., 2005. Evaluation of bitumen as a  $^{187}\text{Re}$ - $^{187}\text{Os}$  geochronometer for hydrocarbon maturation and migration: A test case from the Polaris MVT deposit, Canada. *Earth Planet. Sci. Lett.* 235, 1–15, doi: 10.1016/j.epsl.2005.02.018.
- Selby, D., Creaser, R.A., Fowler, M.G., 2007. Re-Os elemental and isotopic systematics in crude oils. *Earth Planet. Sci. Lett.* 71, 378–386, doi: 10.1016/j.gca.2006.09.005.
- Snow, L. J., Duncan, R. A., Bralower, T. J., 2005. Trace element abundances in the Rock Canyon Anticline, Pueblo, Colorado, marine sedimentary section and their

relationship to Caribbean plateau construction and oxygen anoxic event 2. *Paleoceanography* 20, doi:10.1029/2004PA001093.

Tegner, C., Storey, M., Holm, P.M., Thorarinsson, S.B., Zhao, X., Lo, C.-H., Knudsen, M.F., 2011. Magmatism and Eureka deformation in the High Arctic Large Igneous Province:  $^{40}\text{Ar} - ^{39}\text{Ar}$  age of Kap Washington Group volcanics, North Greenland. *Earth Planet. Sci. Lett.* 303, 203-214.

Turgeon, S.C., Creaser, R.A., 2008. Cretaceous Anoxic Event 2 triggered by a massive magmatic episode. *Nature* 454, 323–326.

Zheng X-Y., Jenkyns, H.C., Gale, A.S., Ward, D.J., Henderson, G.M., 2013. Changing ocean circulation and hydrothermal inputs during Oceanic Anoxic Event 2 (Cenomanian-Turonian): Evidence from Nd-isotopes in the European shelf sea. *Earth Planet. Sci. Lett.* <http://dx.doi.org/10.1016/j.epsl.2013.05.053>

## **Appendix I: Highwood River, Alberta, Canada**

## ***1. Introduction***

This site was chosen for comparison with the other OAE 2 section in the Western Interior Seaway (WIS), the Portland #1 Core (Du Vivier et al., 2014; Chapter 2, this thesis). The work was carried out in collaboration with G. Plint (Ontario) and D. Gröcke (Durham). At the time of sampling and laboratory analysis, the Highwood River section in Alberta, Canada was considered the most complete OAE 2 section in the Northern WIS, according to unpublished stratigraphic data (Plint). However, continued stratigraphic analysis of samples at University of Western Ontario from other sections in the Canadian Foreland basin yielded complexities previously undetermined in the Highwood River section, whilst samples from Highwood River were analysed for Re-Os geochemistry at Durham University. Consequently continued stratigraphic analysis has established that Highwood River is missing an undetermined amount of stratigraphy. Therefore the examined section to the North of Highwood River, the Bighorn River section, is a more suitable section to facilitate correlation of OAE 2 in the Northern WIS with the Portland #1 core, the representative core of GSSP Pueblo, which is ratified by bed-by-bed correlation to the GSSP Pueblo (Sageman et al., 2006).

In addition, detailed age control of the WIS (Meyers et al., 2012) was not complete at the time of sampling and laboratory analysis (in 2010). Therefore the correlation of Highwood River with the GSSP was based on  $\delta^{13}\text{C}_{\text{org}}$  isotope data and existing chronology (Barker et al., 2011). The  $\sim 1.5\text{‰}$   $\delta^{13}\text{C}_{\text{org}}$  excursion is characteristic of the onset of OAE 2, thus it was identified as the marker horizon for the onset of OAE 2 in Highwood River.

The more complete section (Bighorn River) is still undergoing analysis (Plint and Gröcke) and remains a long way off completion. I am not permitted by

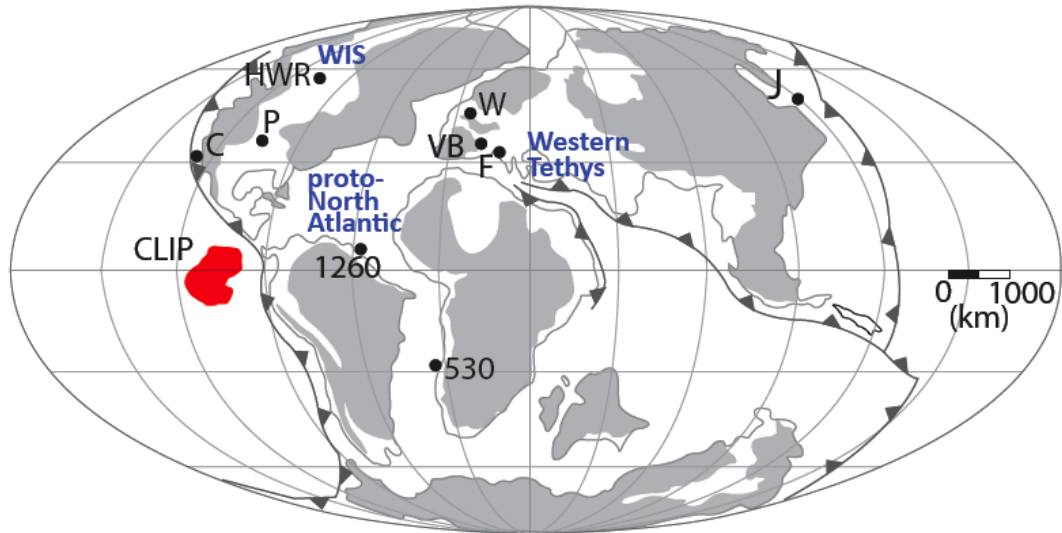
collaborators to use their preliminary findings based on new stratigraphy as evidence to support the high-resolution initial  $^{187}\text{Os}/^{188}\text{Os}$  ( $\text{Os}_i$ ) data produced during this PhD study, which infers a revision to the interpretation of the  $\delta^{13}\text{C}_{\text{org}}$  isotope curve and the timing of the OAE 2 onset. As a result of the aforementioned complexities, Plint and Gröcke will publish the  $\text{Os}_i$  data in a paper on completion of bio, litho- and chemostratigraphy analysis of the Bighorn River section. The analysis is included as an appendix here since the analysis was undertaken during this PhD study.

## ***2. Geological background***

The Highwood River section is located southwest of Calgary, Alberta, Canada;  $50^{\circ} 33'428$  N,  $114^{\circ}20'56$  W (Appendix Fig. 1). The site was chosen for analysis because it was believed to represent a complete carbon record with well constrained stratigraphy, and a dated volcanic tuff horizon. The site consists of a 25 m long section of the Cenomanian-Turonian Boundary Interval, composed of fine grained muddy-shale interbedded by less fine grain marly-siltstone. The primary feature of this section is a 43 cm tuff horizon, the Bighorn River Bentonite, which has a  $^{206}\text{Pb}/^{238}\text{U}$  weighted-mean age of  $94.29 \pm 0.28$  Ma, MSWD 2.4 (Barker et al., 2011). The recently recalculated  $^{40}\text{Ar}/^{39}\text{Ar}$  age of  $94.11 \pm 0.14$  Ma (Singer et al., 2009) is in agreement with the U-Pb age, within uncertainty, since the  $^{40}\text{Ar}/^{39}\text{Ar}$  radiometric methods and the astrochronologically-calibrated age of 28.201 Ma for the Fish Canyon sanidine standard (Kuiper et al., 2008) were used to reduce the discrepancy between  $^{40}\text{Ar}/^{39}\text{Ar}$  and U-Pb results. The bentonite has been mapped extensively from the Southern Alberta Foothills and with no other large regional bentonite present the tuff may be time correlative with the B bentonite of the basal Turonian GSSP Pueblo Rock Canyon (Sageman et al., 2006; Barker et al., 2011).

The B bentonite has a  $^{206}\text{Pb}/^{238}\text{U}$  age of  $94.01 \pm 0.14$  Ma and  $^{40}\text{Ar}/^{39}\text{Ar}$  age of  $94.10 \pm 0.27$  Ma (Meyers et al., 2012). The  $\delta^{13}\text{C}_{\text{org}}$  record expresses a  $\sim 1.5\%$  positive excursion interpreted to represent the marker horizon of the onset of OAE2, which is coincident with the Bighorn River tuff. Therefore the correlation is currently based on carbon stratigraphy and U-Pb dating of the bentonites within uncertainty.

Highwood river section was deposited from the Western Interior Seaway (WIS). In the west of the WIS the deposits are consistent with clay-rich alluvial and near shore facies, grading eastwards in to shallow water marine siltstones and claystones. The stratigraphic architecture reflects a transgressive-regressive sequence, where transgressive surfaces mark the upper and lower extents of these packages (Barker et al., 2011). There is evidence of consistent sea level rise preserved in depositional sequences; rusty-weathering pyritic siltstone/sandstone and mudstone shelf facies to finely laminated grey weathering/ calcareous siltstones and claystones. Biostratigraphic observations confirm body and trace fossils as typically marine and fluctuations in fossil abundance suggests intermittent periods of higher benthic oxygenation (Tsujita, 1998).



**Appendix Figure 1 Palaeogeographic map of the late Cretaceous.** Shows the location of the Highwood river section (HWR) in the northern region of the Western Interior Seaway.

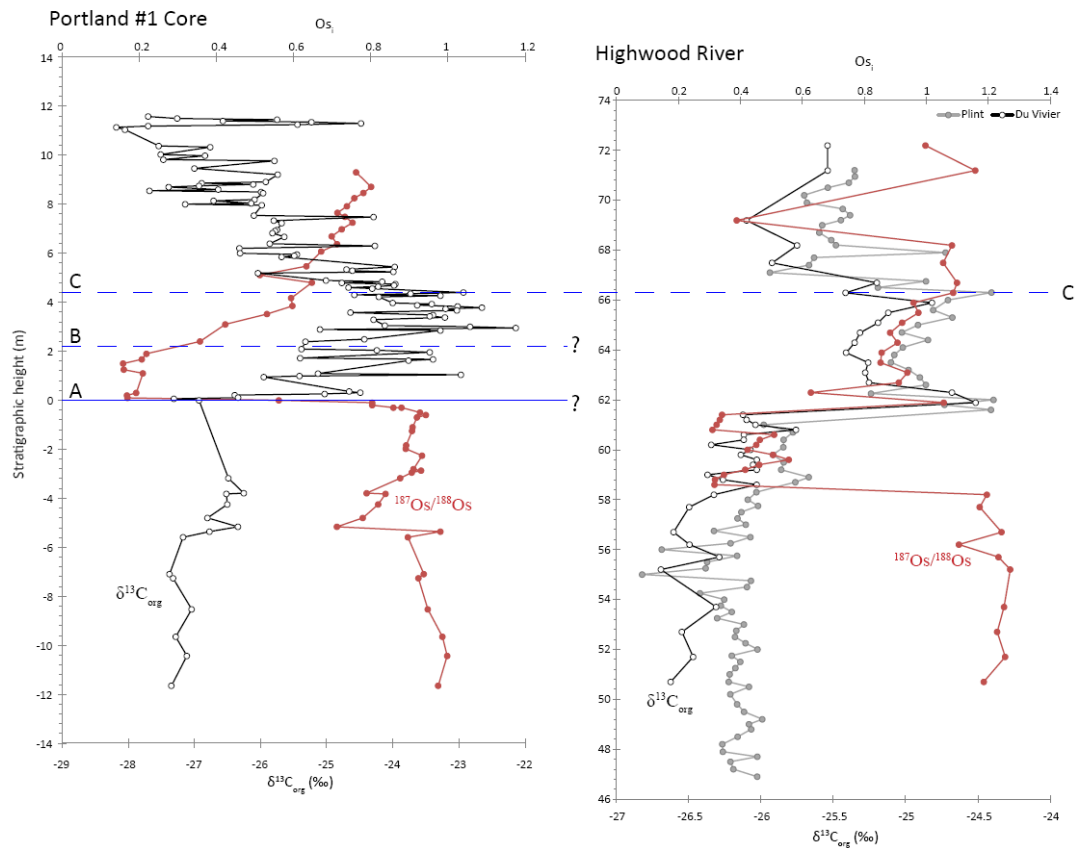
### 3. Results

#### 3.1. $Os_i$ profile Highwood River

Highwood River records high radiogenic  $Os_i$  values (1.1-1.3) from 50.7 – 58.2 m (Appendix Fig. 2; Appendix Table 1). The radiogenic values are relatively homogeneous and have more radiogenic  $Os_i$  values than other analysed sections (Chapter 2 and 3; Du Vivier et al., 2014). The sudden unradiogenic trend at 58.2 m goes from 1.2 to 0.32 within 40 cm. The unradiogenic  $Os_i$  values fluctuate between 0.31 and 0.56 up to 61 m. At this point the  $Os_i$  values instantaneously return to radiogenic values (1.06) by ~62 m. The  $\delta^{13}C_{org}$  remains depleted (~ -26‰) during the trend to unradiogenic  $Os_i$  values (Appendix Fig. 2; Appendix Table 2).

The ~1.5‰ positive excursion in the  $\delta^{13}C_{org}$ , which is characteristic with the onset of OAE2, coincides with the return to radiogenic  $Os_i$  values, at ~61.5 m (Appendix Fig. 2). The overall trend of the  $Os_i$  profile is agreeable with other basins. However, the relationship between the  $\delta^{13}C_{org}$  and the  $Os_i$  excursions do not correlate

as elsewhere, i.e., Portland (Appendix Fig. 2; Du Vivier et al., 2014; Chapters 2, 3, this thesis).



**Appendix Figure 2.  $Os_i$  data (red) with  $\delta^{13}C_{org}$  (black and grey) vs. stratigraphic height (m).** The blue lines ‘A’, ‘B’ and ‘C’ are the correlative datum levels, defined by Pratt et al. (1985) and Tsikos et al. (2004). ‘A’ marks the onset of OAE 2 in Portland, which does not correlate with Highwood River based on  $Os_i$  isotope stratigraphy combined with the  $\delta^{13}C_{org}$ . ‘B’ is also uncertain, however ‘C’ is hypothesised.

#### 4. Discussion

The high-resolution  $Os_i$  profile generated for Highwood River highlights issues of correlation, of which there are two significant differences between the WIS sections. Firstly, the unradiogenic trend in the  $Os_i$  values at Highwood River is ~4 m below the positive excursion in the  $\delta^{13}C_{org}$ , whereas in the Portland core the unradiogenic  $Os$  trend is synchronous with the positive excursion in the  $\delta^{13}C_{org}$  record (Appendix Fig. 2). Secondly, the trend in  $Os_i$  values return to radiogenic  $Os$  is

abrupt relative to the gradual trend at the Portland core and coincides with the positive excursion in the  $\delta^{13}\text{C}_{\text{org}}$  (Appendix Fig. 2).

Based on  $\text{Os}_i$  work to date the unradiogenic trend in the  $\text{Os}_i$  data is interpreted to represent the marker horizon of the onset of OAE 2 (Du Vivier et al., 2014; Chapters 2, 3, this thesis) but in the Highwood River section the onset of OAE 2 is determined by the positive excursion in the  $\delta^{13}\text{C}_{\text{org}}$ , which coincides with the volcanic tuff horizon,  $94.29 \pm 0.28$  Ma (Barker et al., 2011). However, since the original interpretation of the positive excursion in  $\delta^{13}\text{C}_{\text{org}}$  record and the single grain U-Pb analysis (Barker et al., 2011), further geochronological analysis of the WIS yields a revised age control for the CTB interval (Meyers et al., 2012; Du Vivier et al., 2014).

The Portland core derives the age of the onset of OAE 2 at  $\sim 94.38 \pm 0.15$  Ma (Meyers et al., 2012; Du Vivier et al., 2014; Chapter 2, this thesis), which is  $\sim 100$  kyr older than the excursion in the  $\delta^{13}\text{C}_{\text{org}}$  record and the dated Bighorn bentonite,  $94.29 \pm 0.28$  Ma (Barker et al., 2011). Preliminary findings from the stratigraphy at the Bighorn River section (Plint and Gröcke) infer that the tuff was deposited on an erosional flooding surface, which is indicative of a hiatus. A hiatus would explain the abrupt trend to radiogenic values in the  $\text{Os}_i$  profile, and a dramatic artificial excursion in the  $\delta^{13}\text{C}_{\text{org}}$  record. Therefore by inference  $\sim 100$  kyr of stratigraphy is missing from Highwood River, which is accounted for in preliminary evaluation of the Bighorn River section (Plint *pers comm.*). Consequently the  $\text{Os}_i$  profile and geochronology combined with new stratigraphy imply that the onset of OAE 2 in Highwood River is revised.

## 5. *Conclusions and future work*

The positive excursion interpreted as the onset of OAE 2 is tenable with the other sections based on  $\delta^{13}\text{C}_{\text{org}}$  data alone. However, based on preliminary findings from further stratigraphic examination combined with osmium isotope analysis and a revised age control of the WIS, the previously identified onset according to  $\delta^{13}\text{C}_{\text{org}}$  is interpreted to represent a hiatus in the Highwood River section. Therefore, the onset of the OAE 2 is synchronous with the trend to unradiogenic  $\text{Os}_i$  values, which is consistent with the global hypothesis as discussed in this thesis (Chapters 2 and 3).

The analysis presented here will be published in due course, alongside  $\delta^{13}\text{C}_{\text{org}}$  data gathered from multiple sites throughout the Albertan WIS (including the aforementioned Bighorn River section). The evaluation of the  $\text{Os}_i$  profile presented here is not presented in Chapter 2 since the interpretation of the  $\text{Os}_i$  profile is based on the assessment of bio- and lithostratigraphy and  $\delta^{13}\text{C}_{\text{org}}$  data from other Albertan OAE 2 sections. Currently, without the publication of these data I am unable to justify the discussion and hypothesised revision above.

## REFERENCES

- Barker, I.R., Moser, D.E., Kamo, S.L., Plint, A.G., 2011. High-precision U-Pb zircon ID-TIMS dating of two regionally extensive bentonites: Cenomanian Stage, Western Canada Foreland Basin. *Canadian Journal of Earth Sciences* 48, 543-556.
- Du Vivier, A.D.C., Selby, D., Sageman, B.B., Jarvis, I., Grocke, D.R., Voigt, S., 2014. Marine  $^{187}\text{Os}/^{188}\text{Os}$  isotope stratigraphy reveals the interaction of volcanism and ocean circulation during Oceanic Anoxic Event 2. *Earth Planet. Sci. Lett.* 389, 23-33.
- Kuiper, K.F., Deino, A., Hilgen, F.J., Krijgsman, W., Renne, P.R., and Wijbrans, J.R. 2008. Synchronizing Rock Clocks of Earth History. *Science* 320, 500-504.
- Meyers, S.R., Siewert, S.E., Singer, B.S., Sageman, B.B., Condon, D.J., Obradovich, J.D., Jicha, B.R., Sawyer, D.A., 2012. Intercalibration of radioisotopic and

- astrochronologic time scales for the Cenomanian-Turonian boundary interval, Western Interior Basin, USA. *Geology* 40, 7-10.
- Pratt, L.M., Kauffman, E.G., Zelt, F.B., 1985. Fine-grained deposits and biofacies of the Cretaceous Western Interior Seaway: evidence for cyclic sedimentary processes. *Soc. Econ. Paleont. Miner. Field Trip Guidebook* 4, 1985 Midyear Meeting, Golden, Colorado.
- Sageman, B.B., Meyers, S.R., Arthur, M.A., 2006. Orbital time scale and new C-isotope record for Cenomanian–Turonian boundary stratotype. *Geology* 34, 125–128.
- Singer, B.S., Sageman, B.B., Siewert, S.E., Condon, D., Obradovich, J.D., Jicha, B.R., Sawyer, D.A., and Meyers, S.R. 2009. Implications of New  $^{40}\text{Ar}/^{39}\text{Ar}$  ages for the Cenomanian-Turonian OAE 2. *Geological Society of America, Program with Abstracts* 41, 421.
- Tsikos, H., Jenkyns, H.C., Walsworth-Bell, B., Petrizzo, M.R., Forster, A., Kolonic, S., Erba, E., Premoli-Silva, I.P., Baas, M., Wagner, T., Sinninghe Damsté, J.S., 2004. Carbon-isotope stratigraphy recorded by the Cenomanian - Turonian Oceanic Anoxic Event: correlation and implications based on three key localities. *J. Geol. Soc. London* 161, 711-719.
- Tsujita, C.J., Westermann, G.E.G., 1998. Ammonoid habitats and habits in the Western Interior Seaway: a case study from the Upper Cretaceous Bearpaw Formation of southern Alberta, Canada. *Palaeogeog. Palaeoclimatol. Palaeoecol.* 144, 135-160.

Data Tables

Appendix Table 1: Re-Os geochronological data for Highwood River section, Alberta, Canada

Sample ID	Depth (m)	<sup>187</sup> Os	$\delta$	<sup>187</sup> Os	$\delta$	<sup>187</sup> Re/ <sup>188</sup> Os	$\delta$	<sup>187</sup> Re/ <sup>188</sup> Os	$\delta$	<sup>187</sup> Os	$\delta$	D <sub>95</sub>	$\delta$
AD0162-10	72.19	14.71	0.052	172.82	1.55	488.47	4.461	1.78	0.017	58.71	1.89	0.007	
AD0166-10	71.19	6.75	0.030	137.13	1.252	282.99	2.954	1.89	0.027	47.48	1.35	0.013	
AD0176-10	69.19	16.22	0.061	315.72	1.991	269.61	3.285	0.81	0.008	119.68	0.79	0.003	
AD0174-10	68.19	4.90	0.025	87.91	1.010	319.35	6.251	1.58	0.037	30.59	1.88	0.016	
AD0172-10	67.49	3.06	0.026	69.07	0.879	458.66	9.281	1.72	0.045	25.69	1.85	0.018	
AD0168-10	66.89	71.11	0.235	433.28	2.587	1007.34	5.984	2.88	0.016	140.82	1.39	0.005	
AD0168-10	66.29	61.82	0.282	423.53	5.695	934.88	10.313	2.43	0.058	132.09	1.89	0.016	
AD0164-10	65.89	48.67	0.190	382.83	2.015	1019.75	7.946	2.26	0.020	94.95	0.96	0.005	
AD0162-10	65.49	59.95	0.196	349.46	2.409	1198.38	8.917	2.76	0.024	169.63	0.97	0.006	
AD0168-10	65.09	77.92	0.254	413.41	2.248	1232.36	7.411	2.84	0.016	136.71	0.82	0.004	
AD0158-10	64.89	80.11	0.281	468.03	2.412	1095.40	6.099	2.88	0.013	145.50	0.88	0.003	
AD0164-10	64.29	71.64	0.235	431.98	2.318	979.27	5.414	2.44	0.012	143.54	0.91	0.003	
AD0154-10	63.89	75.37	0.280	497.94	2.566	938.45	5.320	2.33	0.012	159.77	0.86	0.003	
AD0152-10	63.49	69.79	0.225	464.45	16.629	928.73	37.996	2.31	0.151	149.51	0.85	0.030	
AD0148-10	63.09	75.69	0.240	462.12	2.317	1007.94	5.494	2.52	0.012	143.44	0.94	0.003	
AD0148-10	62.89	63.85	0.227	417.68	2.295	933.78	5.988	2.41	0.014	132.90	0.81	0.004	
AD0148-10	62.29	15.20	0.055	139.11	0.980	633.36	6.418	1.62	0.017	48.88	0.63	0.005	
AD0144-10	61.89	17.77	0.061	193.68	1.389	545.26	4.983	1.91	0.020	64.85	1.86	0.007	
AD0184-10	61.49	34.78	0.113	413.63	1.397	431.64	1.937	1.88	0.004	193.19	0.34	0.001	
AD0185-10	61.29	20.51	0.069	203.89	1.402	357.68	2.386	0.88	0.007	104.09	0.33	0.002	
AD0186-10	61.09	17.59	0.058	249.73	1.089	383.39	2.145	0.89	0.006	98.28	0.22	0.001	
AD0187-10	60.89	7.16	0.031	47.45	0.654	874.36	23.038	1.88	0.046	16.28	0.21	0.006	
AD0184-10	60.69	4.47	0.019	188.69	0.857	216.83	2.918	0.85	0.015	41.81	0.51	0.006	
AD0188-10	60.49	6.47	0.035	131.91	1.636	237.26	6.098	0.87	0.027	50.85	0.46	0.009	
AD0196-10	60.29	4.90	0.020	96.82	0.858	288.24	4.153	0.87	0.018	36.28	0.43	0.006	
AD0193-10	60.09	19.52	0.070	340.63	2.471	303.82	3.555	0.80	0.014	127.76	0.42	0.004	
AD0182-10	59.89	7.41	0.027	129.48	0.914	369.26	3.470	0.89	0.014	47.85	0.51	0.005	
AD0193-10	59.69	3.19	0.038	179.63	2.147	212.87	4.800	0.89	0.027	67.46	0.56	0.010	
AD0194-10	59.49	13.46	0.045	262.38	1.290	271.66	1.297	0.89	0.008	98.37	0.46	0.003	
AD0195-10	59.29	25.08	0.077	306.78	1.978	241.37	1.576	0.78	0.005	198.21	0.42	0.002	
AD0196-10	59.09	32.67	0.106	376.78	2.051	212.89	0.856	0.88	0.002	209.47	0.35	0.001	
AD0197-10	58.89	26.87	0.125	323.37	2.285	283.86	1.216	0.73	0.003	278.77	0.32	0.001	
AD0198-10	58.69	26.05	0.085	194.13	2.115	175.33	0.735	0.59	0.002	395.53	0.32	0.001	
AD0198-10	58.29	2.41	0.014	47.81	0.690	299.34	7.489	1.65	0.053	16.47	1.29	0.025	
AD0202-10	57.79	1.77	0.015	31.24	0.310	329.88	10.099	1.87	0.062	10.73	1.17	0.028	
AD0202-10	56.79	1.92	0.015	40.44	0.422	258.85	4.529	1.64	0.028	14.97	1.24	0.015	
AD0202-10	56.29	2.24	0.021	49.24	1.147	239.44	12.891	1.53	0.095	17.19	1.11	0.040	
AD0204-10	55.79	2.26	0.014	51.35	0.458	254.86	3.934	1.63	0.024	17.32	1.23	0.013	
AD0205-10	55.29	1.15	0.019	22.84	0.668	292.31	19.214	1.73	0.131	7.90	1.27	0.064	
AD0206-10	55.79	2.60	0.021	54.95	1.279	232.86	12.747	1.68	0.100	18.87	1.25	0.048	
AD0210-10	52.79	1.29	0.019	38.11	0.931	239.37	12.241	1.68	0.100	13.19	1.23	0.050	
AD0212-10	51.79	2.71	0.021	47.44	1.154	324.89	15.898	1.78	0.111	16.11	1.23	0.049	
AD0214-10	50.79	0.84	0.007	23.26	0.906	291.48	16.638	1.59	0.173	8.32	1.19	0.084	

Note: Individual ratio uncertainties are given in the  $\delta$  level. The uncertainties are determined through full reconstruction of uncertainties in Re & Os mass spectrometry; error: 1-sigma and red Re & Os isotope values

**Appendix Table 2:  $\delta^{13}C_{org}$  data for Highwood River section, Alberta, Canada**

PLINT SAMPLES		Du Vivier SAMPLES	
Height (cm)	$\delta^{13}C_{org}$ (‰)	Height (cm)	$\delta^{13}C_{org}$ (‰)
71.2	-25.55	72.09	-25.54
70.95	-25.55	71.09	-25.54
70.7	-25.59	69.09	-26.00
70.5	-25.54	68.09	-25.55
70.2	-25.70	67.49	-25.92
69.9	-25.68	66.89	-25.20
69.65	-25.43	66.29	-25.42
69.4	-25.58	65.89	-24.82
69.2	-25.45	65.49	-25.02
69	-25.58	65.09	-25.09
68.7	-25.60	64.69	-25.31
68.4	-25.51	64.29	-25.35
68.2	-25.48	63.89	-25.41
67.9	-24.72	63.49	-25.26
67.7	-25.63	63.09	-25.28
67.4	-25.67	62.69	-25.25
67.1	-25.94	62.29	-24.68
66.75	-24.86	61.89	-24.52
66.5	-25.19	61.49	-26.02
66.3	-24.41	61.29	-26.00
66	-24.71	61.09	-26.04
65.6	-24.81	60.89	-25.76
65.3	-24.68	60.69	-26.02
65	-24.91	60.49	-26.02
64.7	-25.03	60.29	-26.34
64.4	-24.84	60.09	-26.07
64.1	-25.02	59.89	-26.04
63.8	-25.08	59.69	-26.03
63.5	-25.10	59.49	-26.06
63.2	-24.98	59.29	-26.03
62.9	-24.90	59.09	-26.37
62.6	-24.86	58.89	-26.26
62.25	-25.24	58.69	-26.07
62	-24.59	58.29	-26.33
61.8	-24.75	57.79	-26.50
61.6	-24.41	56.79	-26.60
61	-25.98	56.29	-26.49
60.7	-25.78	55.79	-26.29
60.4	-25.84	55.29	-26.69
60.1	-25.85	53.79	-26.31
59.8	-25.92	52.79	-26.55
59.5	-25.84	51.79	-26.47
59.2	-25.86	50.79	-26.62
58.9	-25.67		
58.7	-25.76		
58.3	-26.03		
58	-26.09		
57.75	-26.02		
57.5	-26.14		
57.25	-26.16		
57	-26.10		
56.75	-26.33		
56.5	-26.07		
56.25	-26.21		
56	-26.69		
55.75	-26.17		
55.5	-26.37		
55.25	-26.38		
55	-26.82		
54.75	-26.07		
54.5	-26.10		
54.25	-26.42		
54	-26.25		
53.75	-26.28		
53.5	-26.20		
53.25	-26.30		
53	-26.12		
52.75	-26.17		
52.5	-26.18		
52.25	-26.11		
52	-26.02		
51.75	-26.20		
51.5	-26.14		
51.25	-26.18		
51	-26.22		
50.7	-26.22		
50.5	-26.08		
50.2	-26.21		
49.8	-26.16		
49.5	-26.12		
49.2	-25.99		
49	-26.08		
48.8	-26.07		
48.5	-26.16		
48.2	-26.27		
47.9	-26.26		
47.7	-26.03		
47.5	-26.21		
47.2	-26.19		
46.9	-26.03		

\* values reported permil (‰) relative to the VPDB standard  
 Plint samples were analysed at Western Ontario University  
 Du Vivier samples were analysed at Durham University